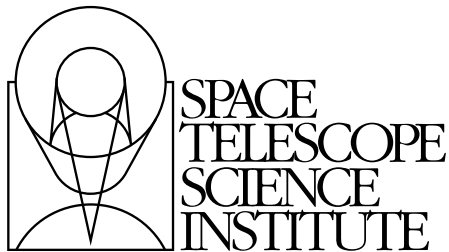

Version 6.0
October 2005

Advanced Camera for Surveys Instrument Handbook for Cycle 15



Space Telescope Science Institute
3700 San Martin Drive
Baltimore, Maryland 21218
help@stsci.edu

User Support

For prompt answers to any question, please contact the STScI Help Desk.

- **E-mail:** help@stsci.edu
- **Phone:** (410) 338-1082
(800) 544-8125 (U.S., toll free)

World Wide Web

Information and other resources are available on the ACS Web site:

- **URL:** <http://www.stsci.edu/hst/acs>

Revision History

| Version | Date | Editors |
|----------------|--------------|--------------------------|
| 6.0 | October 2005 | Gonzaga, S., et al. |
| 5.0 | October 2004 | Pavlovsky, C., et al. |
| 4.0 | October 2003 | Pavlovsky, C., et al. |
| 3.0 | October 2002 | Pavlovsky, C., et al. |
| 2.1 | July 2001 | Pavlovsky, C., et al. |
| 2.0 | June 2001 | Suchkov, A., et al. |
| 1.0 | June 2000 | Jedrzejewski, R., et al. |

Citation

In publications, refer to this document as:

Gonzaga, S., et al. 2005, "ACS Instrument Handbook", Version 6.0, (Baltimore: STScI).

Send comments or corrections to:
Space Telescope Science Institute
3700 San Martin Drive
Baltimore, Maryland 21218
E-mail: help@stsci.edu

Acknowledgments

The technical and operational information contained in this Handbook is the summary of the experience gained by members of the STScI ACS Team, the ACS group at ST-ECF, and by the ACS IDT.

Members of the STScI ACS Team are Ken Sembach (lead), John Biretta, Ralph Bohlin, Marco Chiaberge (ESA), Colin Cox, Linda Dressel, Andrew Fruchter, Mauro Giavalisco, Ron Gilliland, Shireen Gonzaga, Inge Heyer, Anton Koekemoer, Ray Lucas, Jennifer Mack, Jesus Maiz-Apellaniz (ESA), Max Mutchler, Cheryl Pavlovsky, Vera Platais, Charles Profit, Adam Riess, Kailash Sahu, Marco Sirianni (ESA), Roeland van der Marel, and Nolan Walborn.

The ST-ECF ACS group is Richard Hook, Martin Kuemmel, Soeren Larsen, and Jeremy Walsh.

The ACS IDT is Holland Ford (PI), Garth Illingworth (Deputy PI), George Hartig, Mark Rafal, Frank Bartko, Tom Broadhurst, Bob Brown, Chris Burrows, Ed Cheng, Mark Clampin, Jim Crocker, Paul Feldman, Marijn Franx, David Golimowski, Randy Kimble, John Krist, Tom La Jeunesse, Mike Lesser, Doug Leviton, George Miley, Marc Postman, Piero Rosati, Bill Sparks, Pam Sullivan, Zlatan Tsvetanov, Paul Volmer, Rick White, Bob Woodruff, David Ardila, Narciso Benitez, John Blakeslee, Rychard Bouwens, Larry Bradley, Nicholas J.G. Cross, Ricardo Demarco, Tomotsugu Goto, Caryl Gronwall, Brad Holden, Nicole Homeier, André Martel, Simona Mei, Felipe Menanteau, Gerhardt Meurer, Veronica Motta, Marco Sirianni, and Hien Tran.

The contributions of Warren Hack, Alan Welty, Tom Wheeler, and Susan Rose are greatly appreciated.

Table of Contents

| | |
|---|-----|
| Acknowledgments | iii |
| Chapter 1: Introduction | 1 |
| Chapter 2: Special Considerations for Cycle 15 | 5 |
| 2.1 Two-gyro Guiding..... | 5 |
| Chapter 3: Introduction to ACS | 7 |
| 3.1 ACS Location in the HST Focal Plane..... | 7 |
| 3.2 Instrument Capabilities | 9 |
| 3.3 Instrument Design..... | 10 |
| 3.3.1 Detectors | 10 |
| 3.3.2 ACS Optical Design..... | 11 |
| 3.4 Basic Instrument Operations..... | 13 |
| 3.4.1 Target Acquisitions | 13 |
| 3.4.2 Typical ACS Observing Sequence | 14 |
| 3.4.3 Data Storage and Transfer | 14 |
| 3.5 ACS Quick Reference Guide | 15 |
| Chapter 4: Detector Performance | 21 |
| 4.1 Overview | 21 |
| 4.2 The CCDs | 21 |
| 4.2.1 Detector Properties..... | 21 |
| 4.2.2 CCD Spectral Response | 22 |
| 4.2.3 Quantum Efficiency Hysteresis..... | 23 |
| 4.2.4 CCD Long-Wavelength Fringing..... | 23 |
| 4.2.5 Readout Format..... | 24 |
| 4.2.6 Analog-To-Digital Conversion..... | 24 |
| 4.2.7 Flat Fields | 25 |

| | |
|--|-----------|
| 4.3 CCD Operations and Limitations..... | 27 |
| 4.3.1 CCD Saturation: the CCD Full Well | 27 |
| 4.3.2 CCD Shutter Effects on Exposure Times | 28 |
| 4.3.3 Readnoise | 28 |
| 4.3.4 Dark Current | 29 |
| 4.3.5 Warm and Hot Pixels | 32 |
| 4.3.6 Cosmic Rays..... | 37 |
| 4.3.7 Charge Transfer Efficiency | 38 |
| 4.3.8 UV Light and the HRC CCD | 41 |
| 4.4 The SBC MAMA | 41 |
| 4.4.1 MAMA Properties..... | 41 |
| 4.4.2 SBC Spectral Response | 43 |
| 4.4.3 Optical Performance | 44 |
| 4.5 SBC Operations and Limitations | 45 |
| 4.5.1 SBC Scheduling Policies | 45 |
| 4.5.2 MAMA Overflow of the 16 Bit Buffer | 45 |
| 4.5.3 MAMA Darks..... | 45 |
| 4.5.4 SBC Signal-to-Noise Ratio Limitations | 47 |
| 4.5.5 SBC Flatfield..... | 47 |
| 4.5.6 SBC Nonlinearity | 48 |
| 4.6 SBC Bright-Object Limits..... | 49 |
| 4.6.1 Overview..... | 49 |
| 4.6.2 Observational Limits | 49 |
| Chapter 5: Imaging..... | 51 |
| 5.1 Imaging Overview | 51 |
| 5.2 Important Considerations for ACS Imaging | 56 |
| 5.2.1 Optical Performance | 58 |
| 5.2.2 Throughputs and Limiting Magnitudes | 58 |
| 5.2.3 Limiting Magnitudes..... | 58 |
| 5.2.4 Signal-To-Noise Ratios..... | 59 |
| 5.2.5 Saturation | 60 |
| 5.3 Wide Field Optical CCD Imaging | 60 |
| 5.3.1 Filter Set | 60 |
| 5.4 High-Resolution Optical and UV Imaging..... | 62 |
| 5.4.1 Filter Set | 62 |
| 5.4.2 Multiple Electron Events | 63 |
| 5.4.3 Red Leaks..... | 63 |

| | |
|--|----|
| 5.5 Ultraviolet Imaging with the SBC..... | 64 |
| 5.5.1 Filter Set | 64 |
| 5.5.2 Red Leaks..... | 64 |
| 5.5.3 SBC Imaging Filter Shifts..... | 64 |
| 5.6 ACS Point Spread Functions | 65 |
| 5.6.1 CCD Pixel Response Function | 65 |
| 5.6.2 Model PSFs | 66 |
| 5.6.3 Encircled Energy..... | 67 |
| 5.6.4 Geometric Distortions | 68 |
| 5.6.5 PSFs at Red Wavelengths and the UV | 70 |
| 5.6.6 Residual Aberrations | 72 |

Chapter 6: Polarimetry, Coronagraphy and Prism/Grism Spectroscopy.....

| | |
|---|-----|
| 6.1 Polarimetry..... | 75 |
| 6.2 Coronagraphy | 81 |
| 6.2.1 Coronagraph Design | 82 |
| 6.2.2 Acquisition Procedure and Pointing Accuracy..... | 85 |
| 6.2.3 Vignetting and Flat Fields | 86 |
| 6.2.4 Coronagraphic Performance | 87 |
| 6.2.5 Residual Light Subtraction..... | 90 |
| 6.2.6 The Off-Spot PSF | 95 |
| 6.2.7 Occulting Spot Motions..... | 96 |
| 6.2.8 Planning ACS Coronagraphic Observations | 97 |
| 6.2.9 Choice of Filters for Coronagraphic Observations | 100 |
| 6.3 Grism/Prism Spectroscopy | 101 |
| 6.3.1 WFC G800L..... | 102 |
| 6.3.2 HRC G800L | 104 |
| 6.3.3 HRC PR200L..... | 106 |
| 6.3.4 SBC PR110L | 107 |
| 6.3.5 SBC PR130L | 108 |
| 6.3.6 Observation Strategy | 108 |
| 6.3.7 Extraction and Calibration of Spectra | 110 |

| | |
|---|-----|
| Chapter 7: Observing Techniques | 113 |
| 7.1 Designing an ACS Observing Proposal..... | 113 |
| 7.1.1 Identify Science Requirements and Define ACS Configuration..... | 115 |
| 7.1.2 Use of Available-but-Unsupported Capabilities | 116 |
| 7.1.3 Determine Exposure Time and Check Feasibility | 117 |
| 7.1.4 Identify Need for Additional Exposures | 118 |
| 7.1.5 Data Volume Constraints..... | 118 |
| 7.1.6 Determine Total Orbit Request..... | 119 |
| 7.1.7 Charge Transfer Efficiency | 119 |
| 7.2 SBC Bright Object Protection..... | 120 |
| 7.2.1 How Do You Determine if You Violate a Bright Object Limit for SBC Exposures? | 120 |
| 7.2.2 Policy and Observers' Responsibility in Phase I and Phase II | 121 |
| 7.2.3 Bright-Object Protection for Solar System Observations | 124 |
| 7.2.4 Prime and Parallel Observing with the SBC | 125 |
| 7.3 Operating Modes..... | 126 |
| 7.3.1 WFC ACCUM Mode | 126 |
| 7.3.2 HRC ACCUM Mode..... | 129 |
| 7.3.3 SBC ACCUM Mode | 130 |
| 7.3.4 HRC ACQ Mode | 130 |
| 7.4 Patterns and Dithering..... | 131 |
| 7.5 A Road Map for Optimizing Observations..... | 132 |
| 7.6 CCD Gain Selection | 134 |
| 7.6.1 WFC Gain | 134 |
| 7.6.2 HRC Gain | 135 |
| 7.7 ACS Apertures | 136 |
| 7.7.1 WFC Apertures..... | 136 |
| 7.7.2 Ramp Filter Apertures..... | 137 |
| 7.7.3 The Small Filter Apertures..... | 139 |
| 7.7.4 Polarizer Apertures..... | 142 |
| 7.7.5 HRC Apertures | 142 |
| 7.7.6 SBC Apertures..... | 144 |
| 7.8 Specifying Orientation on the Sky..... | 144 |
| 7.8.1 Determining Orientation for Phase II | 148 |
| 7.9 Parallel Observations | 148 |
| 7.9.1 Parallel Observing | 148 |
| 7.10 Pointing Stability for Moving Targets | 154 |

| | |
|--|-----|
| Chapter 8: Overheads and Orbit-Time Determination | 155 |
| 8.1 Overview | 155 |
| 8.2 ACS Exposure Overheads..... | 156 |
| 8.2.1 Subarrays | 159 |
| 8.3 Orbit Use Determination Examples | 160 |
| 8.3.1 Sample Orbit Calculation 1:..... | 160 |
| 8.3.2 Sample Orbit Calculation 2:..... | 161 |
| 8.3.3 Sample Orbit Calculation 3:..... | 162 |
| 8.3.4 Sample Orbit Calculation 4:..... | 162 |
| 8.3.5 Sample Orbit Calculation 5:..... | 164 |
| | |
| Chapter 9: Exposure-Time Calculations | 165 |
| 9.1 Overview | 165 |
| 9.1.1 The ACS Exposure Time Calculator..... | 165 |
| 9.2 Determining Count Rates from Sensitivities..... | 166 |
| 9.2.1 Imaging..... | 169 |
| 9.2.2 Spectroscopy..... | 171 |
| 9.3 Computing Exposure Times | 172 |
| 9.3.1 Calculating Exposure Times for a Given Signal-to-Noise..... | 172 |
| 9.3.2 Exposure Time Estimates for Red Targets in F850LP | 173 |
| 9.4 Detector and Sky Backgrounds..... | 175 |
| 9.4.1 Detector Backgrounds | 175 |
| 9.4.2 Sky Background | 175 |
| 9.5 Extinction Correction | 180 |
| 9.6 Exposure-Time Examples..... | 181 |
| 9.6.1 Example 1: WFC Imaging a Faint Point Source | 181 |
| 9.6.2 Example 2: SBC Objective Prism Spectrum of a UV Spectrophotometric Standard Star..... | 182 |
| 9.6.3 Example 3: WFC VIS Polarimetry of the Jet of M87 | 183 |
| 9.6.4 Example 4: SBC imaging of Jupiter’s Aurora at Lyman-alpha..... | 184 |
| 9.6.5 Example 5: Coronagraphic imaging of the Beta-Pictoris Disk..... | 184 |
| 9.7 Tabular Sky Backgrounds..... | 185 |

Chapter 10: Imaging Reference

| | |
|--|-----|
| Material | 187 |
| 10.1 Introduction..... | 188 |
| 10.2 Using the Information in this Chapter | 188 |
| 10.2.1 Sensitivity Units and Conversions | 188 |
| 10.2.2 Signal-To-Noise | 189 |
| 10.2.3 Point Spread Functions | 190 |
| 10.3 Distortion in the ACS..... | 236 |
| 10.3.1 WFC..... | 237 |
| 10.3.2 HRC | 239 |
| 10.3.3 SBC | 240 |
| 10.3.4 Summary | 242 |
| Glossary | 243 |
| Index | 247 |

Introduction

The Advanced Camera for Surveys (ACS), a third-generation instrument, was installed in the Hubble Space Telescope during Servicing Mission 3B (http://www.stsci.edu/hst/HST_overview/servicing_missions) on March 7, 2002. Its primary purpose is to increase HST imaging discovery efficiency by about a factor of 10, with a combination of detector area and quantum efficiency that surpasses previous instruments.

ACS has three independent cameras that provide wide-field, high resolution, and ultraviolet imaging capabilities respectively, using a broad assortment of filters designed to address a large range of scientific goals. In addition, coronagraphic, polarimetric, and grism capabilities make this a versatile and powerful instrument.

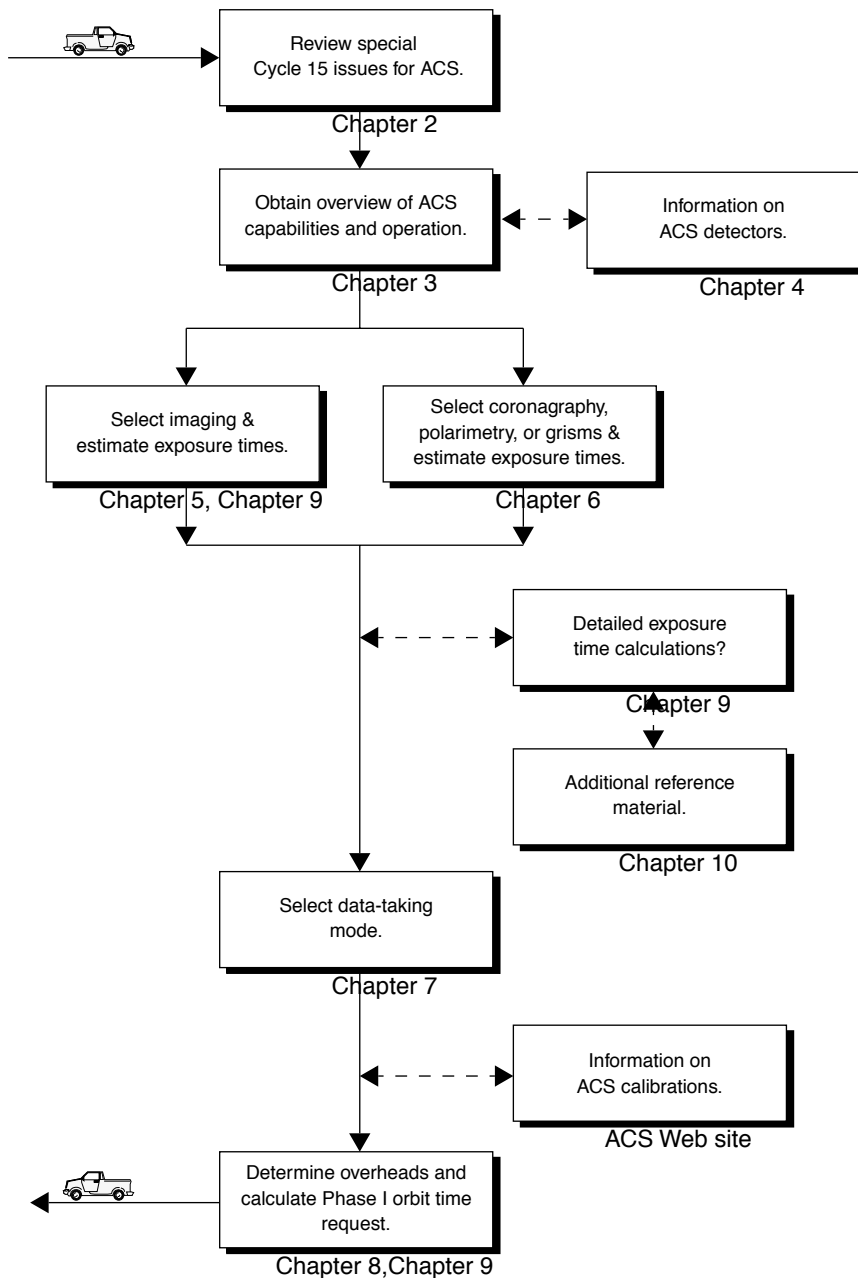
The *ACS Instrument Handbook*, which is maintained by the ACS team at STScI, describes the instrument properties, performance, operations, and calibration. It is the basic technical reference manual for the instrument, and should be used with other documents (listed in Table 1.1) for writing Phase I proposals, detailed Phase II programs, and for data analysis. (See Figure 1.1).


The documents in Table 1.1 can be downloaded from the ACS STScI Web site, <http://www.stsci.edu/hst/acs>. Paper copies can be requested by sending a message to help@stsci.edu or by calling 410-338-1082. European users may also contact the Space Telescope European Coordinating Facility (ST ECF) at Garching, Germany (+49-89-320 06-291, stdesk@eso.org.)

Table 1.1: Useful documents

| Purpose | Document or resource |
|---------------------------------|--|
| General observatory information | HST Primer http://www.stsci.edu/hst/proposing/docs/proposing/documents/cp/primer.pdf |
| Phase I proposals | Proposing Overview http://www.stsci.edu/hst/proposing/docs/proposingOverview Call for Proposals http://www.stsci.edu/hst/hst/proposing/documents/cp/cp_cover.html |
| Phase II programs | Phase II Proposal Instructions http://www.stsci.edu/hst/programs/hst/proposing/docs/p2pi.html Astronomer's Proposal Tool (APT) for Phase II preparations http://apt.stsci.edu/ Two-Gyro Web site http://www.stsci.edu/hst/HST_overview/TwoGyroMode Two-Gyro Handbook http://www.stsci.edu/hst/HST_overview/TwoGyroMode/handbook/cover.html |
| Data analysis | ACS Data Handbook http://www.stsci.edu/hst/acs/documents/handbooks/DataHandbookv4/ACS_longdnhbcover.html Dither Handbook http://www.stsci.edu/instruments/wfpc2/Wfpc2_driz/dither_handbook.html Space Telescope Analysis Newsletter http://www.stsci.edu/hst/acs/documents/isrs/hst/acs/documents/newsletters Instrument Science Reports http://www.stsci.edu/hst/acs/documents/isrs Calibration and Pipeline Information http://www.stsci.edu/hst/Post-observation |

Figure 1.1: Handbook roadmap for proposal preparation.





CHAPTER 2:

Special Considerations for Cycle 15

In this chapter . . .

| |
|--------------------------|
| 2.1 Two-gyro Guiding / 5 |
|--------------------------|

2.1 Two-gyro Guiding

HST was originally designed to use three rate-sensing gyroscopes to provide fine pointing control of the observatory during science observations. In order to conserve the lifetime of the HST gyros, the HST Project has decided to turn one of the functioning gyros off and to upload a new attitude control system that functions with only two gyros in the fine pointing control loop. This new two-gyro control mode was tested extensively during the past year and will be used during Cycle 15. Tests of the HST pointing capabilities while guiding with the new attitude control algorithms in place indicate that the pointing performance in two-gyro mode is essentially indistinguishable from previous performance in three-gyro mode.

The differences in the ACS point spread function (PSF) properties in two-gyro mode and three-gyro mode are so small that the information in this Instrument Handbook is applicable to either two-gyro or three-gyro operations. The formal changeover to 2-gyro operations occurred on August 28, 2005. To keep up to date with the status and performance of this new guiding mode, please check the Two-Gyro Science Mode Web site:

[http://www.stsci.edu/hst/HST_overview/TwoGyroMode,](http://www.stsci.edu/hst/HST_overview/TwoGyroMode)

6 ■ Chapter 2: Special Considerations for Cycle 15

for up to date information about HST pointing in this mode. Details about the visibility and scheduling of observations in two-gyro mode can be found in the HST Two-Gyro Handbook at:

http://www.stsci.edu/hst/HST_overview/TwoGyroMode/handbook/cover.html.

Additional information and restrictions on observations can be found in the Cycle 15 Call for Proposals at:

<http://www.stsci.edu/hst/hst/proposing/documents/cp/>.

Introduction to ACS

In this chapter . . .

| |
|---|
| 3.1 ACS Location in the HST Focal Plane / 7 |
| 3.2 Instrument Capabilities / 9 |
| 3.3 Instrument Design / 10 |
| 3.4 Basic Instrument Operations / 13 |
| 3.5 ACS Quick Reference Guide / 15 |

3.1 ACS Location in the HST Focal Plane

ACS is mounted in one of the instrument bays behind the HST primary mirror. The relative locations of the science instruments in the focal plane and their fields of view are shown schematically in Figure 3.1. When referring to the HST and its focal plane, we use a coordinate system that is fixed to the telescope and consists of three orthogonal axes: U1, U2 and U3. U1 lies along the optical axis, U2 is parallel to the solar-array rotation axis, and U3 is perpendicular to the solar-array axis. (Note: Some HST documentation uses the alternative V1, V2, V3 coordinate system for which $V1=U1$, $V2=-U2$ and $V3=-U3$.)

Figure 3.1: The HST field of view with the locations of the SI and the FGS apertures in the (U₂,U₃) focal plane. The scale in arcsec is indicated.

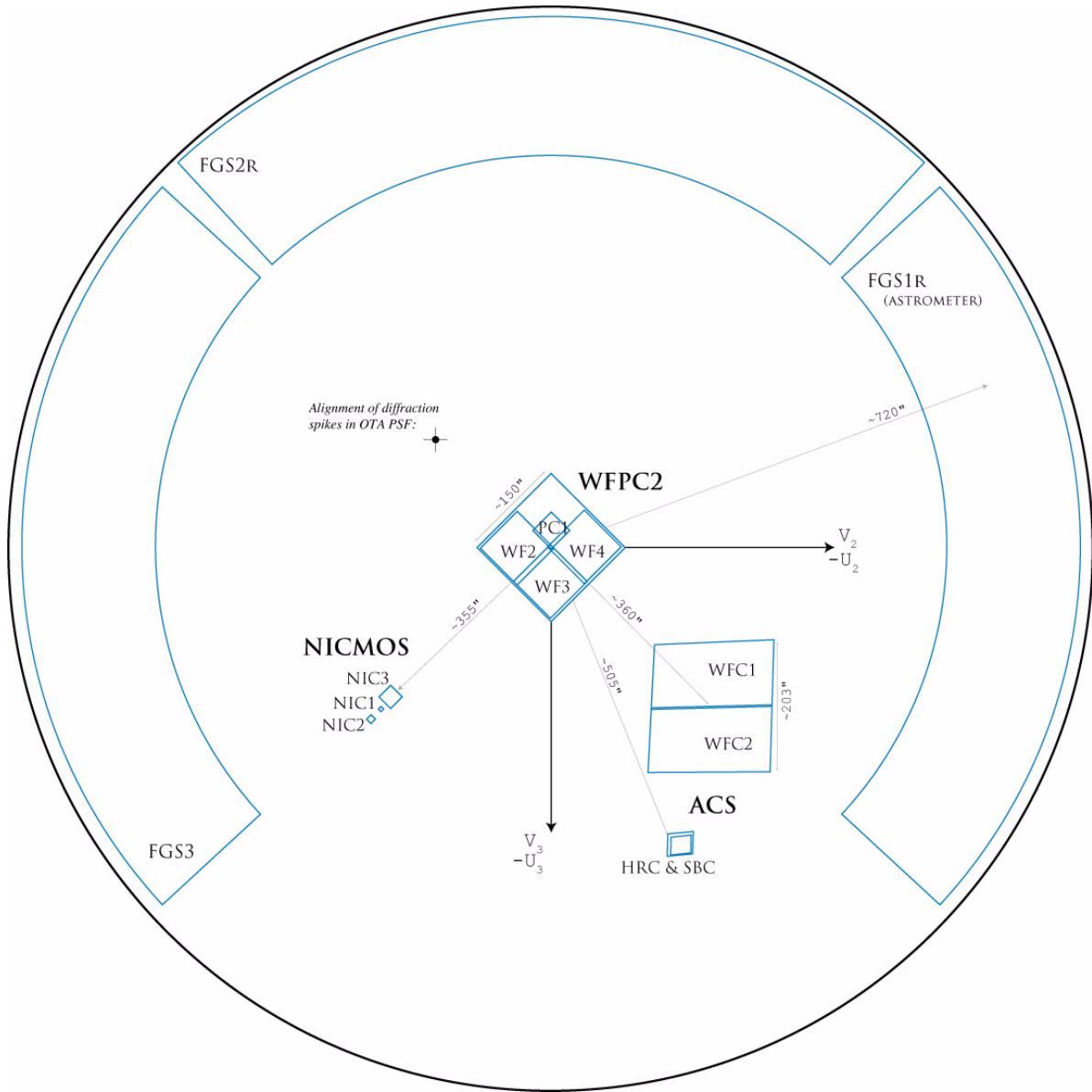


Figure 3.1 shows the layout of the instrument entrance apertures in the telescope focal plane as projected onto the sky.

3.2 Instrument Capabilities

ACS is a versatile instrument that can be applied to a broad range of scientific programs. The three prime capabilities of ACS are:

- Deep, wide-field imaging from visible to near-IR wavelengths.
- High spatial resolution imaging from near-UV to near-IR wavelengths.
- Solar blind UV imaging.

ACS has three channels, each optimized for a specific goal:

- Wide Field Channel (WFC): 202 x 202 arcsecond field of view from 3500 Å to 11,000 Å, and peak efficiency of 48% (including the Optical Telescope Assembly (OTA)). The plate scale of ~ 0.05 arcseconds/pixel provides critical sampling at 11,600 Å.
- High Resolution Channel (HRC): 29 x 26 arcsecond field of view from 1700 Å to 11,000 Å, and peak efficiency of 29%. The plate scale of ~ 0.027 arcseconds/pixel provides critical sampling at 6300 Å.
- Solar Blind Channel (SBC): 35 x 31 arcsecond field of view from 1150 Å to 1700 Å, plate scale of ~ 0.032 arcseconds/pixel, and peak efficiency of 7.5%.

In addition to these three prime capabilities, ACS also provides:

- Grism spectroscopy: Low resolution ($R \sim 100$ @ 8000 Å) wide field spectroscopy from 5500 Å to 10,500 Å available in both the WFC and the HRC.
- Prism spectroscopy: Low resolution ($R = 59$ @ 2500 Å) near-UV spectroscopy from 1700 Å to 3900 Å available in the HRC.
- Prism spectroscopy: Low resolution ($R \sim 100$ @ 1500 Å) far-UV spectroscopy from 1250 Å to 1800 Å available in the SBC.
- Coronagraphy: Aberrated beam coronagraphy in the HRC from 2000 Å to 11,000 Å with 1.8 arcsecond and 3.0 arcsecond diameter occulting spots.
- Imaging Polarimetry: Polarimetric imaging in the HRC and WFC with relative polarization angles of 0°, 60°, and 120°.

3.3 Instrument Design

3.3.1 Detectors

ACS uses the following detectors in each channel:

- The WFC employs a mosaic of two 4096 x 2048 Scientific Imaging Technologies (SITE) CCDs. The 15 x 15 μm pixels provide ~ 0.05 arcseconds/pixel spatial resolution, with critical sampling at 11,600 \AA , resulting in a nominal 202 x 202 arcsecond field of view (FOV). The spectral sensitivity of the WFC ranges from 3500 \AA to 11,000 \AA , with a peak efficiency of 48% at ~ 7000 \AA (including OTA).
- The HRC detector is a 1024 x 1024 SITE CCD, with 21 x 21 μm pixels that provide $\sim 0.028 \times 0.025$ arcsecond/pixel spatial resolution with critical sampling at 6300 \AA . This gives the HRC a nominal 29 x 26 arcsecond field of view. The spectral response of the HRC ranges from ~ 1700 \AA to 11,000 \AA , and it has a peak efficiency of 29% at ~ 6500 \AA (including OTA).
- The SBC detector is a solar-blind CsI microchannel plate (MCP) with Multi-Anode Microchannel Array (MAMA) readout. It has 1024 x 1024 pixels, each 25 x 25 μm in size. This provides a spatial resolution of $\sim 0.034 \times 0.030$ arcseconds/pixels, producing a nominal FOV of 35 x 31 arcseconds. The SBC UV spectral response ranges from 1150 \AA to 1700 \AA with a peak efficiency of 7.5% at 1250 \AA .

The WFC & HRC CCDs

The ACS CCDs are thinned, backside-illuminated full-frame devices cooled by thermo-electric cooler (TEC) stacks housed in sealed, evacuated dewars with fused silica windows. The spectral response of the WFC CCDs is optimized for imaging at visible to near-IR wavelengths, while the HRC CCD spectral response is optimized specifically for near-UV wavelengths. Both CCD cameras produce a time-integrated image in the ACCUM data-taking mode. As with all CCD detectors, there is noise (readout noise) and time (read time) associated with reading out the detector following an exposure.

The minimum exposure time is 0.1 seconds for the HRC and 0.5 seconds for the WFC. Between successive identical exposures, the minimum time is 45 seconds for the HRC, and 135 seconds for the WFC, for full-frame readouts. However, this can be reduced to as little as ~ 35 seconds for WFC subarray readouts. The dynamic range for a single exposure is ultimately limited by the depth of the CCD full well ($\sim 85,000 e^-$ for the WFC and 155,000 e^- for the HRC), which determines the total amount of charge that Section 7.2 can accumulate in any one pixel

during an exposure without saturation. Cosmic rays will affect all CCD exposures. CCD observations should be broken into multiple exposures whenever possible to allow removal of cosmic rays in post-observation data processing. During Phase II you can use the CR-SPLIT optional parameter or dithering to do this (See Section 4.3.6).

The SBC MAMA

The SBC MAMA is a photon-counting detector which provides a two-dimensional ultraviolet capability. It can only be operated in ACCUM mode. In order to preserve its functionality, the SBC MAMA detector is subject to both scientific and absolute brightness limits. At high local (≥ 50 counts/second/pixel) and global ($> 200,000$ counts/second) illumination rates, counting becomes nonlinear in a way that is not correctable. At only slightly higher illumination rates, the MAMA detectors are subject to damage. We have therefore defined absolute local and global count rate limits, which translate to a set of configuration-dependent bright-object screening limits. Sources which violate the screening limits in a given configuration cannot be observed in those configurations, as discussed in Section 4.6 and Section 7.2.

3.3.2 ACS Optical Design

The ACS design incorporates two main optical channels: one for the WFC, and one which is shared by the HRC and SBC. Each channel has independent corrective optics to compensate for spherical aberration in the HST primary mirror. The WFC has three silver-coated optics to optimize instrument throughput in the visible and near-IR. The silver coatings cut off at wavelengths shortward of 3700 \AA . The WFC has two filter wheels which it shares with the HRC, offering the possibility of internal WFC/HRC parallel observing for some filter combinations (Section 7.9). The optical design of the WFC is shown schematically in Figure 3.2. The HRC/SBC optical chain comprises three aluminized mirrors overcoated with MgF_2 , shown schematically in Figure 3.3. The HRC or SBC channels are selected by means of a plane fold mirror (M3 in Figure 3.3). The HRC is selected by inserting the fold mirror into the optical chain so that the beam is imaged onto the HRC detector through the WFC/HRC filter wheels. The SBC channel is selected by moving the fold mirror out of the beam to yield a two mirror optical chain that focuses light through the SBC filter wheel onto the SBC detector. The aberrated beam coronagraph is accessed by inserting a mechanism into the HRC optical chain. This mechanism positions a substrate with two occulting spots at the aberrated telescope focal plane and an apodizer at the re-imaged exit pupil.

While there is no mechanical reason why the coronagraph could not be used with the SBC, for health and safety reasons, use of the coronagraph is forbidden with the SBC.

Figure 3.2: ACS optical design: wide field channel.

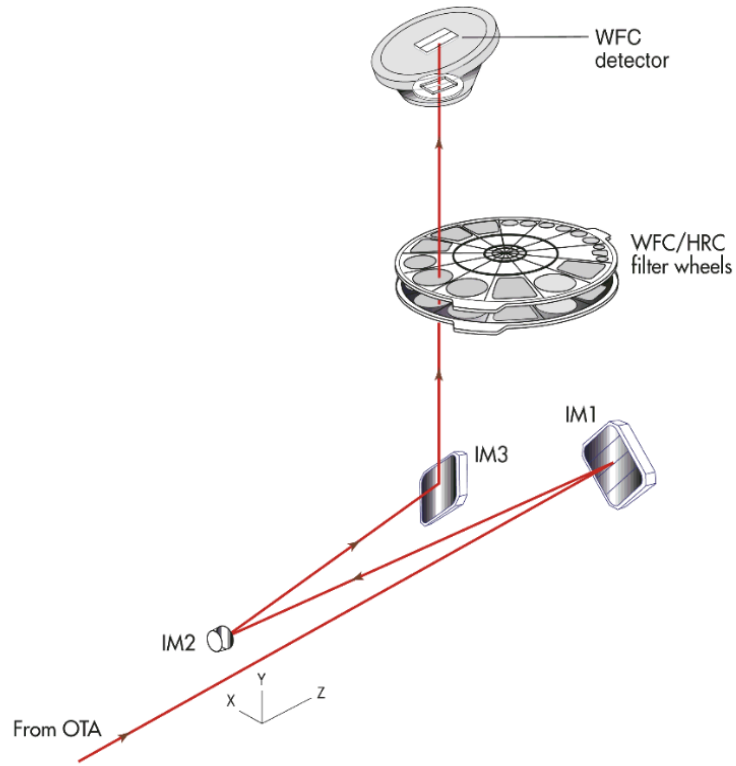
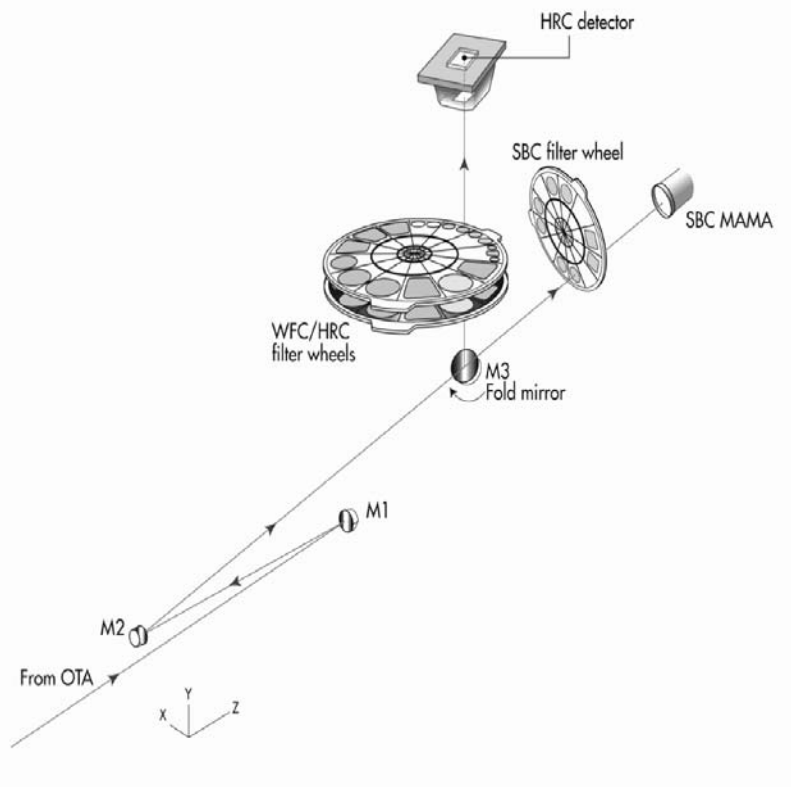


Figure 3.3: ACS optical design: high resolution/solar blind channels



Filter Wheels

ACS has three filter wheels: two shared by the WFC and HRC, and a separate wheel dedicated to the SBC. The WFC/HRC filter wheels contain the major filter sets. Each wheel also contains one clear WFC aperture and one clear HRC aperture (see Chapter 5 for more on filters). Parallel WFC and HRC observations are possible for some filter combinations and these are automatically added by the Astronomer's Proposal Tool (APT) (<http://apt.stsci.edu/>) in Phase II, unless the user disables this option via the PAREXP optional parameter, or if adding the parallel observations cannot be done due to timing considerations. Because the filter wheels are shared, it is not possible to independently select the filter for WFC and HRC parallel observations.

Calibration-Lamp Systems

ACS has a calibration subsystem consisting of tungsten lamps and a deuterium lamp for internally flat fielding each of the optical chains. The calibration subsystem illuminates a diffuser on the rear surface of the ACS aperture door, which must be closed for calibration exposures. Under normal circumstances, users are not allowed to use the internal calibration lamps.

In addition, a post-flash capability was added to the instrument to provide the means of mitigating the effects of Charge Transfer Efficiency (CTE) degradation. We do not expect to use this facility at present (except for calibration and characterization) but in later years, as radiation damage of the CCDs causes the CTE to degrade, it is possible that some users will want to avail themselves of this facility. Since we are not yet at a stage where use of post-flash is expected to be useful for any science observations, we do not provide an extensive discussion related to it.

3.4 Basic Instrument Operations

3.4.1 Target Acquisitions

For the majority of ACS observations target acquisition is simply a matter of defining the appropriate aperture for the observation. Once the telescope acquires its guide stars, your target will be within ~ 1 to 2 arcseconds of the specified pointing. For observations with the ramp filters, one must specify the desired central wavelength for the observation. For the special case of coronagraphic observations, an onboard target acquisition will need to be specified. The nominal accuracy of the onboard target acquisition process is ~ 6 milliarcseconds.

3.4.2 Typical ACS Observing Sequence

ACS is expected to be used primarily for deep, wide-field survey imaging. Important issues for observers to consider will be the “packaging” of their observations, how observations are CR-SPLIT to mitigate the impact of cosmic rays, how sub-stepping or “dithering” of images for removal of hot pixels is implemented, and how, if necessary, to construct a mosaic pattern to map the target. HRC observations and narrowband observations with the WFC are more likely to be read-noise limited, requiring consideration of optimum CR-SPLIT times. Observations with the MAMA detectors are not affected by cosmic rays or read noise, but long integration times will often be needed to obtain sufficient signal-to-noise.

A typical ACS observing sequence is expected to consist of a series of 10 to 20 minute CR-SPLIT and dithered exposures for each program filter. Coronagraphic observations will require an initial target acquisition observation to permit centering of the target under the occulting mask. Observers will generally not take their own calibration exposures. See Chapter 7 for more details about observing strategies.

3.4.3 Data Storage and Transfer

At the conclusion of each exposure, the science data are read out from the detector and placed in ACS’s internal buffer memory, where it is stored until it can be transferred to the HST solid state data recorder (and thereafter to the ground). The internal buffer memory is large enough to hold one WFC image, or sixteen HRC or SBC images, and so the buffer will typically need to be dumped before or during the following WFC exposure. If the following exposure is longer than ~339 seconds, then the buffer dump from the preceding exposure will be performed during integration (see Section 8.2 for a more complete discussion).

ACS’s internal buffer stores the data in a 16 bit-per-pixel format. This structure imposes a maximum of 65,535 counts per pixel. For the MAMA detectors this maximum is equivalent to a limit on the total number of detected photons per pixel which can be accumulated in a single exposure. For the WFC and HRC, the 16 bit buffer format (and not the full well) limits the photons per pixel which can be accumulated without saturating in a single exposure when GAIN=1 for WFC, and GAIN=2 for the HRC is selected. See Chapter 4 and Chapter 7 for a detailed description of ACS instrument operations.

3.5 ACS Quick Reference Guide

Table 3.1: Instrument characteristics.

| | WFC | HRC | SBC |
|---------------------|--|--|--|
| Field-of-View | 202" × 202" | 29" × 26" | 34.6" × 30.8" |
| Plate Scale | ~0.05"/pixel | ~0.028 × 0.025"/pixel | ~0.034 × 0.030"/pixel |
| Pixel Size | 15 × 15 μm | 21 × 21 μm | 25 × 25 μm |
| Image Format | 2 × 2048 × 4096 pixels | 1024 × 1024 pixel | 1024 × 1024 pixel |
| Spectral Response | ~3500 Å to 11,000 Å | ~1700 Å to 11,000 Å | ~1150 Å to 1700 Å |
| Detector | SITe CCDs | SITe CCD | CsI MCP with MAMA readout |
| Detector Efficiency | ~77% at 4000 Å ~83% at 6000 Å ~67% at 8000 Å | ~33% at 2500 Å ~69% at 6000 Å ~53% at 8000 Å | ~19.2% @ 1216 Å |
| Peak Efficiency | 48% at ~7000 Å | 29% at ~6500 Å | 7.5% at ~1250 Å |
| Read Noise | 5.0 e ⁻ | 4.7 e ⁻ | 0 counts |
| Dark Current | 0.0032 e ⁻ /s/pixel | 0.0036 e ⁻ /s/pixel | 1.241 × 10 ⁻⁵ e ⁻ /s/pixel |
| Full Well | 84,700 e ⁻ | 155,000 e ⁻ | ¹ Detector count rate linearity limit: 200,000 counts/second Pixel count-rate linearity limit: ~22 counts/second/pixel |
| Gain | 1,2,4 and 8 e ⁻ /DN (Max 65,535 DN) | 1,2,4 and 8 e ⁻ /DN (Max 65,535 DN) | n/a |

1. Loss of linearity occurs at count rates larger than these values. For more information, please see Section 4.5.6.

Table 3.2: Calibration accuracies.

| Attribute | WFC | HRC | SBC | Limiting factor |
|--|---|---|----------------|--|
| Distortion Solution Accuracy | 0.1 pixel | 0.1 pixel | 0.25 pixel | Calibration & stability of geometric distortion ¹ |
| Absolute Astrometry | 0.5" to 1" | 1" | 1" | Guide Star Catalog uncertainties ² |
| Absolute Photometry | 3% | 2% | 5% | Absolute calibration, standards |
| Relative Photometry within an Image | 1% | 1% | 2% | Flat-field characterization or characterization of geometric distortion. |
| Repeated Photometry of Same Star | 0.3% | 0.3% | 1% | Stability of flat field |
| Transformation to Standard Magnitude Systems | 0.02 mag SDSS 0.025 mag WFPC2 0.03 mag BVRI | 0.02 mag SDSS 0.025 mag WFPC2 0.03 mag BVRI | n/a | DQE curve determination Color terms |
| Polarimetry | 1% | 1% | n/a | |
| Wavelength Calibration | 20 Å grism | 12 Å grism | 1 pixel prisms | Accuracy of dispersion solution |
| Spectrophotometry | 6% (Grism) | 10% (Grism) | 20% (Prism) | |

1. Anderson & King, ISR 04-15 (<http://www.stsci.edu/hst/acs/documents/isrs/isr0415.pdf>)

2. Koekemoe, et. al., ISR 05-06 (<http://www.stsci.edu/hst/acs/documents/isrs/isr0506.pdf>)

Table 3.3: ACS filters.

| Filter type | Filter description | Camera |
|---------------|--|-------------------------|
| Broadband | Sloan Digital Sky Survey (SDSS): F475W, F625W, F775W, F850LP | WFC/HRC |
| | B, V, Medium V, Wide V, I: F435W, F555W, F550M, F606W, F814W | WFC/HRC |
| | Near-UV: F220W, F250W, F330W | HRC |
| | No Filter: CLEAR | WFC/HRC |
| Narrowband | H α (2%), [OIII] (1%), [NII] (1%): F658N, F502N, F660N | WFC/HRC |
| | NeV (3440 Å): F344N | HRC |
| | Methane (8920 Å): F892N | HRC/[WFC ¹] |
| Ramp filters | 2% bandpass (3700-10,700 Å): FR388N, FR505N, FR656N | WFC/HRC |
| | 2% bandpass (3700-10,700 Å): FR423N, FR462N, FR716N, FR782N, FR853N, FR931N, FR1016N, FR551N, FR601N | WFC |
| | 9% bandpass (3700-10,700 Å): FR459M, FR914M | WFC/HRC |
| | 9% bandpass (3700-10,700 Å): FR647M | WFC |
| Spectroscopic | Grism: G800L | WFC/HRC |
| | Prism: PR200L | HRC |
| Polarizers | Visible (0°, 60°, 120°): POL0V, POL60V, POL120V | HRC/[WFC ¹] |
| | Near-UV (0°, 60°, 120°): POL0UV, POL60UV, POL120UV | HRC/[WFC ¹] |
| Medium Band | Lyman-Alpha: F122M | SBC |
| Long Pass | MgF2, CaF2, BaF2, Quartz, Fused Silica: F115LP, F125LP, F140LP, F150LP, F165LP | SBC |
| Prisms | LiF, CaF2: PR110L, PR130L | SBC |

1. Limited field of view (72" x 72") for these filters using WFC

Table 3.4: ACS polarizers.

| Polarizer set | Filters | Filter comments |
|---------------------------|---------|-----------------|
| POL0UV, POL60UV, POL120UV | F220W | HRC NUV short |
| | F250W | HRC NUV long |
| | F330W | HRC U |
| | F435W | Johnson B |
| | F814W | Broad I |
| POL0V, POL60V, POL120V | F475W | SDSS g |
| | F606W | Johnson V |
| | F625W | SDSS r |
| | F658N | H α |
| | F775W | SDSS i |

Table 3.5: ACS dispersers.

| Disperser | Channel | Wavelength range (Å) | Resolving power |
|-----------|---------|---------------------------|-----------------|
| G800L | WFC | 1st order: 5500 to 10,500 | 100 @8000 Å |
| G800L | WFC | 2nd order: 5000 to 8500 | 200 @8000 Å |
| G800L | HRC | 1st order: 5500 to 10,500 | 140 @8000 Å |
| G800L | HRC | 2nd order: 5500 to 8500 | 280 @8000 Å |
| PR200L | HRC | 1700 to 3900 | 59 @2500 Å |
| PR110L | SBC | 1150 to 1800 | 79 @1500 Å |
| PR130L | SBC | 1250 to 1800 | 96 @1500 Å |

Table 3.6: Useful tables and figures list.

| Topics | Tables |
|--|--|
| Proposal Preparation Tips | <p>Table 6.1: Examples of polarizer and non-polarizer exposures in a Phase II proposal.</p> <p>Table 7.1: Science decision guide.</p> <p>Table 7.2: Science feasibility guide.</p> <p>Table 9.1: Useful quantities for the ACS WFC.</p> <p>Table 9.2: Useful quantities for the ACS HRC.</p> <p>Table 9.3: Useful quantities for the ACS SBC.</p> |
| Overheads | <p>Table 8.1: Science exposure overheads: general.</p> <p>Table 8.2: ACS science exposure overhead times (minutes).</p> |
| Autoparallels | <p>Table 7.11: Filter combinations for auto-parallels in the two cases of (i) HRC camera prime and (ii) WFC camera prime.</p> <p>Table 7.12: Minimum primary exposure time (seconds) to attach an auto-parallel for CR-SPLIT=n.</p> |
| Aperture Parameters | <p>Table 7.6: WFC aperture parameters.</p> <p>Table 7.7: Ramp filter apertures.</p> <p>Table 7.8: HRC aperture parameters.</p> <p>Table 7.9: SBC aperture parameters</p> <p>Table 7.10: Plate scales and axis angles for the 3 ACS channels.</p> <p>Figure 3.1: The HST field of view with the locations of the SI and the FGS apertures in the (U2,U3) focal plane. The scale in arcsec is indicated.</p> <p>Figure 7.7: Aperture and image feature orientation.</p> <p>Figure 7.8: ACS apertures in the V2/V3 reference frame.</p> |
| Detector Characteristics | <p>Table 3.1: Instrument characteristics.</p> <p>Table 4.1: ACS CCD detector performance characteristics.</p> <p>Table 4.2: CCD gain and readout noise.</p> <p>Table 4.7: SBC detector performance characteristics.</p> |
| SBC Bright Object Protection Limits | <p>Table 7.3: Absolute SBC count rate screening limits for nonvariable and variable objects.</p> <p>Table 7.4: Bright limit V-band magnitudes for observations with the SBC filters and prisms (no reddening).</p> <p>Table 7.5: Bright object protection policy for SBC observations.</p> |

| Topics | Tables |
|---|--|
| Hot and Warm Pixels | <p>Table 4.3: Creation rate of new hot pixels (pixel/day).</p> <p>Table 4.4: Permanent warm and hot pixel growth (%/yr).</p> <p>Figure 4.9: Growth of permanent warm and hot pixel population as a function of time (WFC top, HRC bottom).</p> |
| Charge Transfer Efficiency | <p>Table 4.5: Charge transfer efficiency measurements for the ACS CCDs at installation time (Fe55 test at 1620 e⁻).</p> <p>Table 4.6: Example of science applications and their assumed parameters.</p> <p>Figure 4.12: Projected CTE losses in WFC (and equivalently, the size of corrections).</p> |
| Geometric Distortion | <p>Figure 10.127: Non-linear component of the WFC Distortion.</p> <p>Figure 10.128: Variation of the WFC effective pixel area with position in detector coordinates.</p> <p>Figure 10.129: HRC distortion.</p> <p>Figure 10.130: Variation of the HRC effective pixel area with position in detector coordinates.</p> |
| Encircled Energy | <p>Table 5.4: Encircled energy measurements for the ACS channels.</p> <p>Table 9.4: Encircled energy comparison for WFC/F850LP.</p> <p>Figure 4.15: MAMA point spread function.</p> <p>Figure 5.9: Encircled energy for the CCD channels.</p> <p>Figure 5.10: Encircled energy for the SBC.</p> |
| PSF | <p>Figure 5.8: Kernels representing CCD pixel functions for HRC and WFC.</p> <p>Table 5.10: Model ACS SBC PSFs.</p> <p>Figure 5.9: Model ACS CCD PSFs.</p> |
| Plate Scale | <p>Table 7.10: Plate scales and axis angles for the 3 ACS channels.</p> |
| Filters | <p>Table 3.3: ACS filters.</p> <p>Table 3.5: ACS dispersers.</p> <p>Table 5.1: ACS WFC/HRC filters in Filter Wheel #1.</p> <p>Table 5.2: ACS WFC/HRC filters in Filter Wheel #2.</p> <p>Table 5.3: ACS SBC filter complement.</p> <p>Table 5.6: In-band flux as a percentage of the total flux.</p> <p>Table 5.7: Visible-light rejection of the SBC F115LP imaging mode.</p> |
| Polarizers: | <p>Table 3.4: ACS polarizers.</p> <p>Table 6.1: Examples of polarizer and non-polarizer exposures in a Phase II proposal.</p> <p>Table 6.2: Filters that can be used in conjunction with the ACS polarizers.</p> |
| Photometry | <p>Table 5.5: V detection limits for ACS, HRC, and SBC direct imaging.</p> <p>Table 9.1: Useful quantities for the ACS WFC.</p> <p>Table 9.2: Useful quantities for the ACS HRC.</p> <p>Table 9.3: Useful quantities for the ACS SBC.</p> <p>Table 10.1: Color corrections AB_n to go from Johnson V magnitude to AB magnitude for the WFC.</p> <p>Table 10.2: Color corrections AB_n to go from Johnson V magnitude to AB magnitude for the HRC.</p> <p>Table 10.3: Color corrections AB_n to go from Johnson V magnitude to AB magnitude for the SBC.</p> |
| Limiting Magnitudes for Direct Imaging | <p>Table 5.5: V detection limits for ACS, HRC, and SBC direct imaging.</p> |

| Topics | Tables |
|-------------------------------|---|
| Spectroscopy | <p>Table 6.3: Optical parameters of ACS dispersers.</p> <p>Table 6.4: V detection limits for the ACS grism/prism modes.</p> <p>Figure 6.15: Sensitivity versus wavelength for WFC G800L.</p> <p>Figure 6.16: Sensitivity versus pixel position for WFC G800L.</p> <p>Figure 6.18: Sensitivity versus wavelength for HRC G800L.</p> <p>Figure 6.19: Sensitivity versus pixel position for HRC G800L.</p> <p>Figure 6.21: Sensitivity versus wavelength for HRC/PR200L.</p> <p>Figure 6.22: Sensitivity versus wavelength for SBC PR110L.</p> <p>Figure 6.23: Sensitivity versus wavelength for SBC/PR130L.</p> |
| Sky Backgrounds | <p>Table 9.5: Approximate zodiacal sky background as a function of ecliptic latitude and ecliptic longitude (in V magnitudes per square arcseconds).</p> <p>Table 9.6: Geocoronal emission lines.</p> <p>Table 9.7: High sky backgrounds.</p> <p>Figure 9.1: High sky background intensity as a function of wavelength.</p> <p>Figure 9.2: Background contributions in V magnitude per arcseconds² due to the zodiacal light, Moon, and the sunlit Earth, as a function of angle between the target and the limb of the Earth or Moon.</p> <p>Figure 9.3: Extinction versus wavelength.</p> |
| Calibration Accuracies | <p>Table 3.2: Calibration accuracies.</p> <p>Figure 4.5: Dark rate trend with time for the ACS CCDs (HRC, WFC1, WFC2).</p> |

Detector Performance

In this chapter . . .

| |
|---|
| 4.1 Overview / 21 |
| 4.2 The CCDs / 21 |
| 4.3 CCD Operations and Limitations / 27 |
| 4.4 The SBC MAMA / 41 |
| 4.5 SBC Operations and Limitations / 45 |
| 4.6 SBC Bright-Object Limits / 49 |

4.1 Overview

ACS employs two fundamentally different types of detectors: CCDs for use from the near UV to the near IR, and a Multi-Anode Microchannel Array detector known as a MAMA for use in the ultraviolet. The CCD and the MAMA detectors are used in different ways and impose their own unique limitations on the feasibility of observations performed with them. This chapter covers the properties of the ACS detectors, descriptions of how to use them to optimize scientific programs, and steps needed to ensure the feasibility of observations.

4.2 The CCDs

4.2.1 Detector Properties

WFC Properties

The WFC/CCD consists of two 4096 x 2048 charge-coupled devices that are sensitive from the near UV to the near IR. They are thinned,

backside-illuminated devices manufactured by Scientific Imaging Technologies (SITe). They are butted together along their long dimension to create an effective 4096×4096 array with a gap corresponding to approximately 50 pixels between the chips. The CCD camera design incorporates a warm dewar window, designed to prevent buildup of contaminants on the window that cause a loss of UV throughput.

A summary of the ACS CCD performance is given in Table 4.1.

Table 4.1: ACS CCD detector performance characteristics.

| Characteristic | WFC performance | HRC performance |
|----------------------------|---|---|
| Architecture | Thinned, backside illuminated anti-reflection coated multi-phase pinned | Thinned, backside illuminated anti-reflection coated multi-phase pinned |
| Wavelength range | 3700 Å to 11,000 Å | 2000 Å to 11,000 Å |
| Pixel Format | 2 butted 2048×4096 | 1024×1024 |
| Field of View | $202'' \times 202''$ | $29'' \times 26''$ |
| Pixel Size | $15 \mu\text{m} \times 15 \mu\text{m}$ | $21 \mu\text{m} \times 21 \mu\text{m}$ |
| Pixel Plate Scale | 0.05" | 0.027" |
| Quantum Efficiency | ~77% @ 4000 Å ~83% @ 6000 Å ~67% @ 8000 Å | ~33% @ 2500 Å ~69% @ 6000 Å ~53% @ 8000 Å |
| Dark Count (as of July'05) | ~0.0038 e ⁻ /second/pixel | 0.0044 e ⁻ /second/pixel |
| Read Noise | ~5 e ⁻ rms | ~4.7 e ⁻ rms |
| Full Well | ~84,700 e ⁻ | ~155,000 e ⁻ |
| Gain (max. 65, 535 DN) | 1, 2, 4, and 8 electrons/DN | 1, 2, 4, and 8 electrons/DN |
| Operating Temperature* | -77°C | -81°C |

* Average temperature value for WFC1 and WFC2

HRC

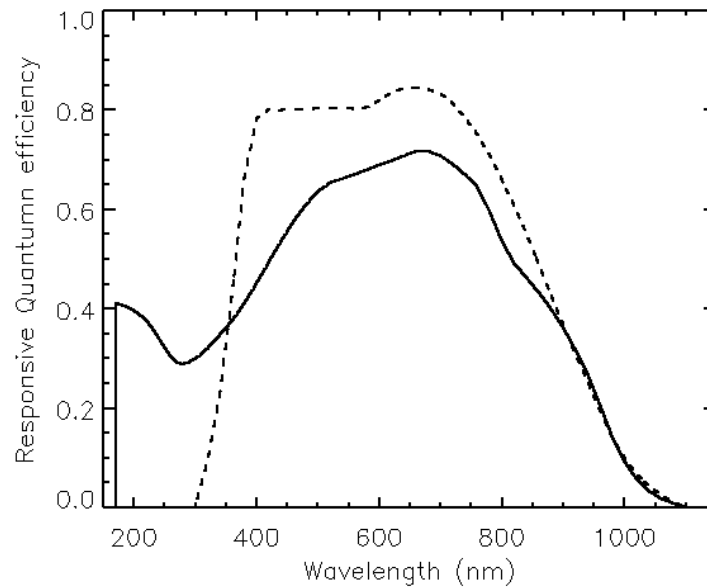
The HRC CCD is a flight-spare STIS 1024×1024 CCD, also manufactured by SITe. It is a thinned, backside-illuminated device, but is coated using a process developed by SITe to provide good quantum efficiency in the near-ultraviolet. The performance characteristics and specifications are given in Table 4.1

4.2.2 CCD Spectral Response

The responsive quantum efficiency (RQE) of the WFC and HRC CCDs is shown in Figure 4.1; it includes corrections needed to reproduce the instrument sensitivity measured on orbit ([ACS ISR 2004-08](#)). The total

spectral response of the camera (see Figure 5.7) is given by the convolution of the RQEs shown here and the throughput of optical elements of the camera. For example, the WFC silver coated mirrors, while enhancing the reflectivity in the near-IR, impose a violet cutoff below 370 nm.

Figure 4.1: Responsive quantum efficiency of the HRC CCD (solid line) and WFC CCDs (dashed line).



4.2.3 Quantum Efficiency Hysteresis

Based on current data, the ACS CCDs do not suffer from quantum efficiency hysteresis (QEH). The CCDs respond in the same way to light levels over their whole dynamic range, irrespective of the previous illumination level.

4.2.4 CCD Long-Wavelength Fringing

Like most thinned CCDs, the ACS CCDs exhibit fringing in the red, longward of $\sim 7500 \text{ \AA}$. The amplitude of the fringes is a strong function of wavelength and spectral resolution. The fringe pattern can be corrected by rectification with an appropriate flat field. The fringe pattern is a convolution of the contours of constant distance between the front and back surfaces of the CCD, and the wavelength of light on a particular part of the CCD. The fringe pattern has been shown to be very stable in similar devices, as long as the wavelength of light on a particular part of the CCD stays constant. In practice, this means that the fringe pattern is dependent on the spectrum of the light incident on the detector, with the sensitivity to the source spectrum a function of the bandwidth of the filter.

4.2.5 Readout Format

WFC

Each CCD chip is read out as a 4144×2068 array, including physical and virtual overscans. Two different amplifiers are used to read out each half of the chip. The final images consist of 24 columns of physical overscan, 4096 columns of pixel data, and another 24 columns of physical overscan. Each column consists of 2048 rows of pixel data followed by 20 rows of virtual overscan. The orientation of the chip is such that for the grism spectra, the dispersed images have wavelength increasing from left to right in the positive x-direction.

HRC

The HRC CCD is read out as a 1062×1044 array, including physical and virtual overscans. There are 19 columns of physical overscan, followed by 1024 columns of pixel data, and then 19 more columns of physical overscan. Each column consists of 1024 rows of pixel data followed by 20 rows of virtual overscan. As with the WFC, the orientation of the chip was chosen so that grism images have wavelength increasing from left to right.

4.2.6 Analog-To-Digital Conversion

Electrons which accumulate in the CCD wells are read out and converted to data numbers (DN) by the analog-to-digital converter (ADC). The ADC output is a 16 bit number, producing a maximum of 65,535 DN in one pixel.

The CCDs are capable of operating at gains of 1, 2, 4 or 8 electrons/DN. In principle, use of a lower gain value can increase the dynamic range of faint source observations by reducing the quantization noise; however, in practice this improvement is not significant. Table 4.2 shows the actual gain levels and readout noise in electrons for the four WFC amps, and the default C amp used for the HRC.

Table 4.2: CCD gain and readout noise.

| Chip | Amp | Gain=1 | | Gain=2 (default) | | Gain=4 | |
|------|-----|--------|-------|------------------|-------|--------|-------|
| | | Gain | Noise | Gain | Noise | Gain | Noise |
| WFC1 | A | 1.000 | 5.57 | 2.002 | 5.84 | 4.01 | --- |
| WFC1 | B | 0.972 | 4.70 | 1.945 | 4.98 | 3.90 | --- |
| WFC2 | C | 1.011 | 5.18 | 2.028 | 5.35 | 4.07 | --- |
| WFC2 | D | 1.018 | 4.80 | 1.994 | 5.27 | 4.00 | --- |
| HRC | C | 1.163 | 4.46 | 2.216 | 4.80 | 4.235 | 5.86 |

For the WFC, gain factors of 1 and 2 are fully supported, as are gain values of 2 and 4 for the HRC. The remaining two gain factors for each camera are available but unsupported so users of those modes must plan their own calibration. **GAIN=2 is the default configuration for the WFC for observations in Cycle 14 and later cycles.** The readout noise associated with GAIN=2 is on average only $0.28 e^-$ higher per amplifier than that of GAIN=1. The noise increase brought about by the use of GAIN=2 is equivalent to that produced by adding a mere $1.7 e^-$ of noise in quadrature to the noise of the GAIN=1 configuration; when the number of detected photons is larger than 3, the Poisson noise alone on the combination of source and sky would exceed this level. Thus, in terms of readout noise, the advantage of using GAIN=1 is minimal, whereas by adopting GAIN=2, the ability to do accurate photometry before saturation is extended by 0.32 magnitudes. In addition, more bright unsaturated sources could become available for cross-image registration, and for point sources, it may be possible to perform photometry several magnitudes beyond saturation for some cases. Further information about gain values can be found in [ACS ISR 2002-03](#) and [ACS ISR 2004-01](#).

4.2.7 Flat Fields

WFC

The flat fields for the WFC combine information from two sources. Ground-based flats were obtained for all filters at a signal-to-noise of ~ 300 per pixel. To refine the low-frequency domain of the ground flats, inflight observations of a rich stellar field with large scale dithers have been analyzed (see [ACS ISR 2002-08](#) and [2003-10](#)). The required L-flat correction is a corner-to-corner gradient of 10 to 18%, dependent on wavelength. The resulting flat field supports photometry to $\sim 1\%$ over the full WFC field of view.

Figure 4.2 shows the corrected WFC ground flats for several broadband filters. **Note: the 50 pixel gap seen in external images, between the top and bottom chips, is not shown here.** Since the two CCDs were cut from the same Si wafer, and have undergone similar treatments, there is a significant continuity in the response across the gap. The central donut-like structure is wavelength dependent, where pixels in the central region are less sensitive than surrounding pixels in the blue F435W filter, for example, and more sensitive in the red F850LP filter. For further discussion of WFC flat fields, see ACS ISRs [2001-11](#), [2002-04](#), [2003-10](#), [2003-11](#), [2005-02](#), and [2005-09](#).

HRC

As for the WFC, the HRC ground flats were refined using in-flight observations of a rich stellar field with large scale dithers to determine the low-frequency domain of the flat fields. The correction required for the

visible filters is a corner-to-corner gradient of 6% to 12%, dependent on wavelength. For the NUV filters, flats were taken in-flight using observations of the bright earth (see [ACS ISR 2003-02](#)) and include both the pixel-to-pixel and low-frequency structure of the detector response.

Currently, HRC flat fields have a signal-to-noise of ~ 300 per pixel and support photometry to $\sim 1\%$ over the full HRC field of view. Figure 4.3 shows the corrected HRC ground flats, derived for 6 broadband optical filters. The donut-like structure seen in the WFC response is not found in the HRC flats. For further discussion of HRC flat fields, see ACS ISRs [2001-11](#) and [2002-04](#).

Figure 4.2: WFC flat field.

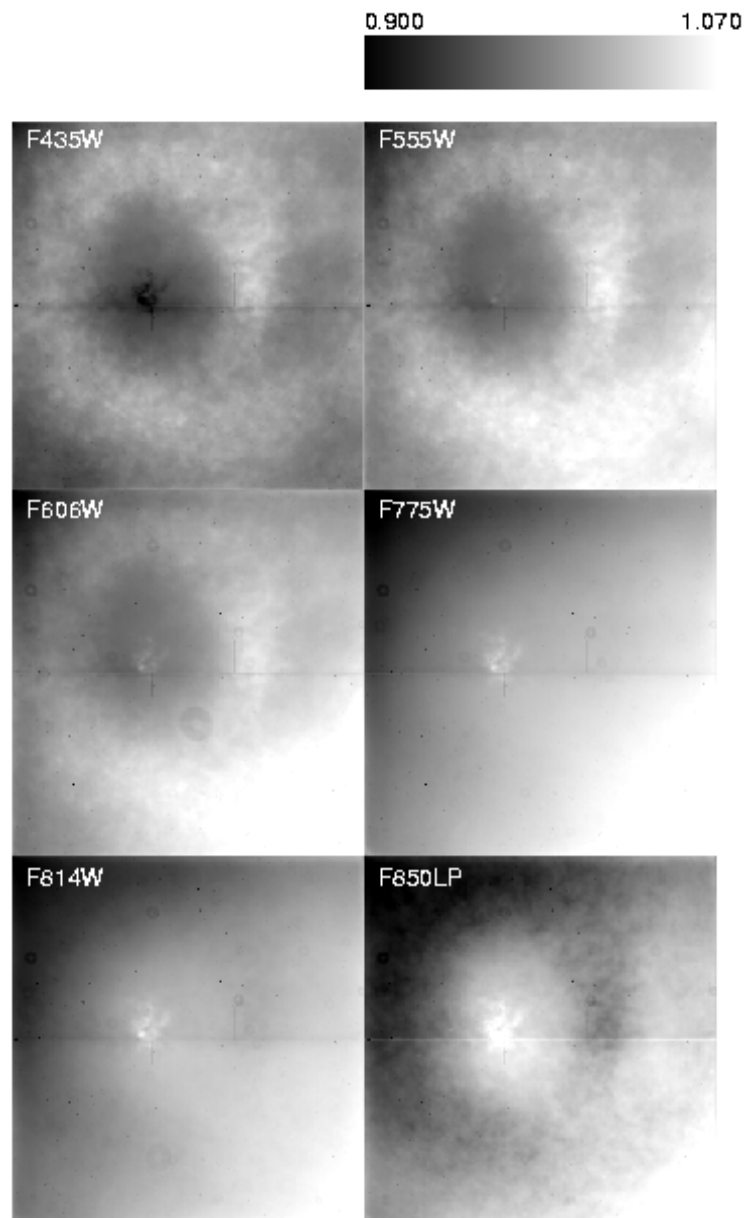
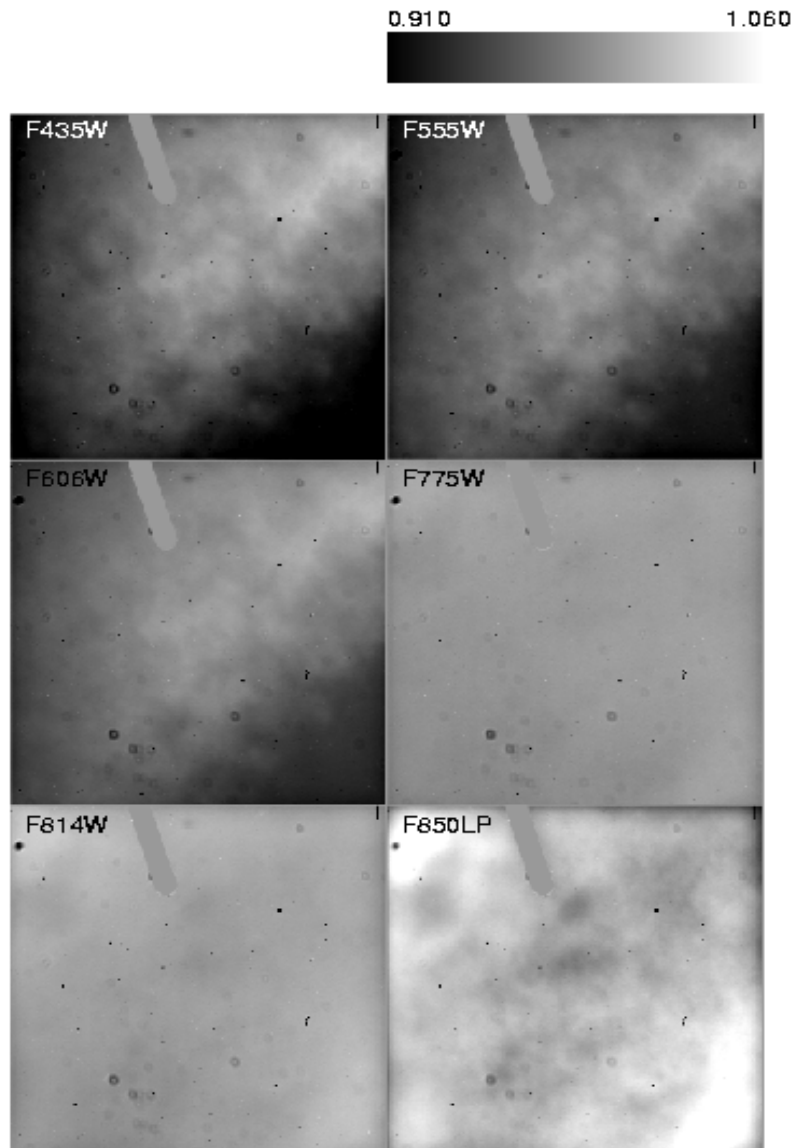


Figure 4.3: HRC flat field.



4.3 CCD Operations and Limitations

4.3.1 CCD Saturation: the CCD Full Well

The full well capacity for the ACS CCDs is given in Table 4.1 as $84,700 e^-$ for the WFC and $155,000 e^-$ for the HRC. This is somewhat dependent on the position on the chip, with variations of the order 10% and 18% across the field of view for the WFC and the HRC, respectively. If the CCD is over-exposed, blooming will occur. This happens when a pixel

becomes full, so excess charge flows into the next pixels along the column. However, extreme overexposure is not believed to cause any long-term damage to the CCDs, so there are no bright object limits for the ACS CCDs. When using $GAIN=2$ on the WFC and $GAIN=4$ on the HRC, it has been shown that the detector response remains linear to well under 1% up to the point when the central pixel reaches the full well depth. On-orbit tests have demonstrated that when using aperture photometry and summing over the surrounding pixels affected by bleeding, linearity to $\leq 1\%$ holds even for cases in which the central pixel has received up to 10 times the full well depth (see [ACS ISR 2004-01](#) for details).

4.3.2 CCD Shutter Effects on Exposure Times

The ACS camera has a very high-speed shutter; even the shortest exposure times are not significantly affected by the finite traversal time of the shutter blades. On-orbit testing reported in [ACS ISR 2003-03](#) has verified that shutter shading corrections are not necessary to support 1% photometry for either the HRC or WFC.

A total of 4 exposure times are known to be in error by up to 4.1%; the nominal 0.1 seconds HRC exposure is really 0.1041 seconds (updates for reference files have been made to use the correct values in pipeline processing). No significant differences exist between exposure times controlled by the two shutters (A and B), with the possible exception of non-repeatability up to $\sim 1\%$ on the WFC for exposures in the 0.7 to 2.0 second range. The HRC provides excellent shutter time repeatability.

4.3.3 Readnoise

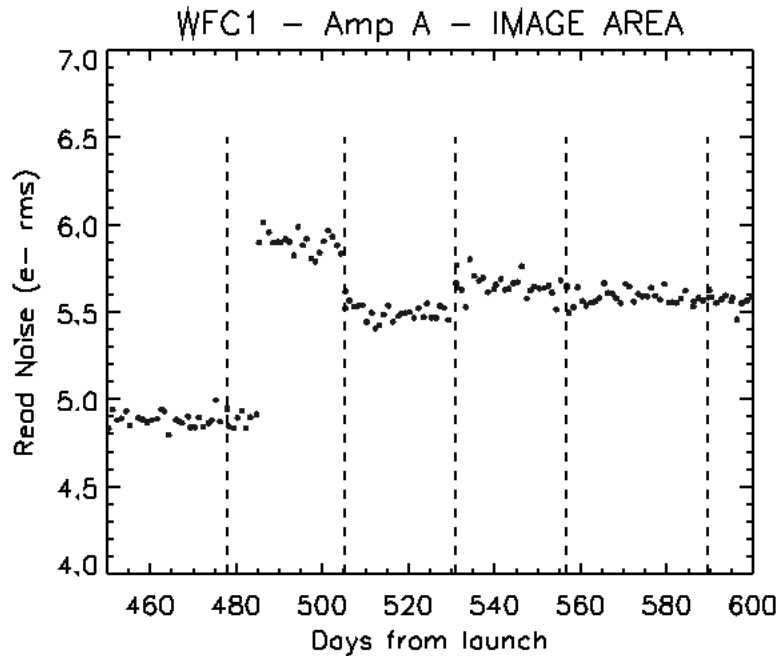
WFC

We measured the read noise level in the active area and overscan regions for all the amplifiers at the default gain settings. In general the read noise has been constant with time. On June 29, 2003, just after a transit through the South Atlantic Anomaly (SAA) the readnoise in Amp A changed from ~ 4.9 to ~ 5.9 electrons rms. Although the telemetry did not show any anomaly in any component of the camera, it is likely that the read noise jump was due to some sort of radiation damage. Amp A is the only amplifier that showed this anomaly. The amplitude of the variation ($\sim 1 e^-$) was the same for $GAIN 1$ and 2 . After the following anneal date the readnoise dropped to $\sim 5.5 e^-$ and it remained constant for 27 days. After the following two anneal cycles the read noise reached stability at $\sim 5.6 e^-$ rms, approximately $0.7 e^-$ higher than before the change, and has remained constant since then. Figure 4.4 shows the read noise in the image area for amplifier A during the “instability” period. The readnoise of all the other amplifiers have been very stable since launch with post-launch figures

almost unchanged from the pre-launch measurements made during ground testing.

Even with a slightly higher read noise in Amp A most of the WFC broadband science observations are sky limited, while narrowband observations are primarily read noise limited.

Figure 4.4: Readnoise jump in WFC Amp A (occurred on June 29, 2003).



The vertical dashed lines indicate the annealing dates. See Table 4.2 for CCD gain and readout noise values.

HRC

The read noise is monitored only for the default readout amplifier C at the default gain setting ($2 e^-/\text{DN}$). No variations have been observed with time. The read noise measured in the image area ($4.80 \pm 0.12 e^-$) is in agreement with the read noise measured in the two overscan regions, and it is comparable to the pre-flight value of $4.74 e^-$.

4.3.4 Dark Current

All ACS CCDs are buried channel devices which have a shallow n-type layer implanted below the surface to store and transfer the collected signal charge away from the traps associated with the Si-SiO₂ interface. Moreover, ACS CCDs are operated in Multi Pinned Phases (MPP) mode so that the silicon surface is inverted and the surface dark current is suppressed. ACS CCDs therefore have very low dark current. The WFC CCDs are operated in MPP mode only during integration, so the total dark

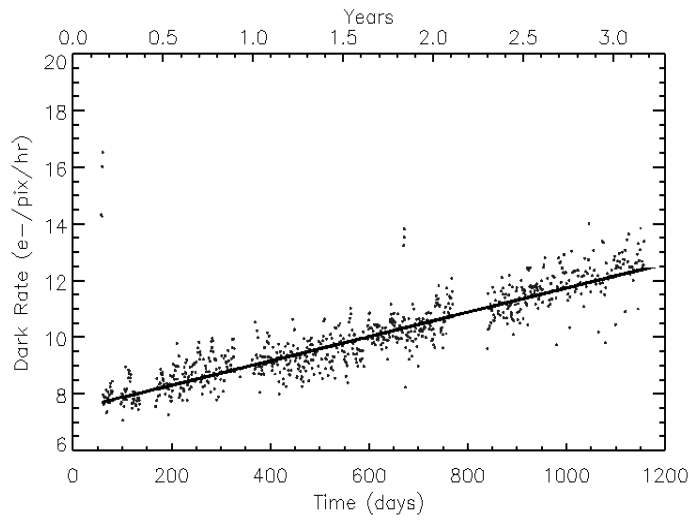
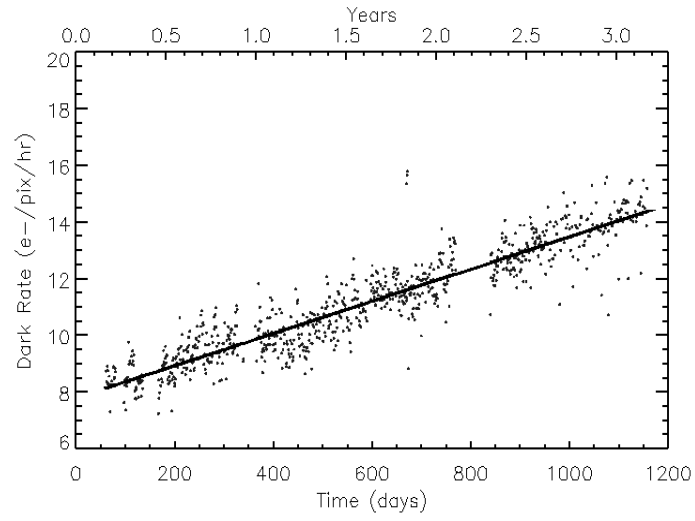
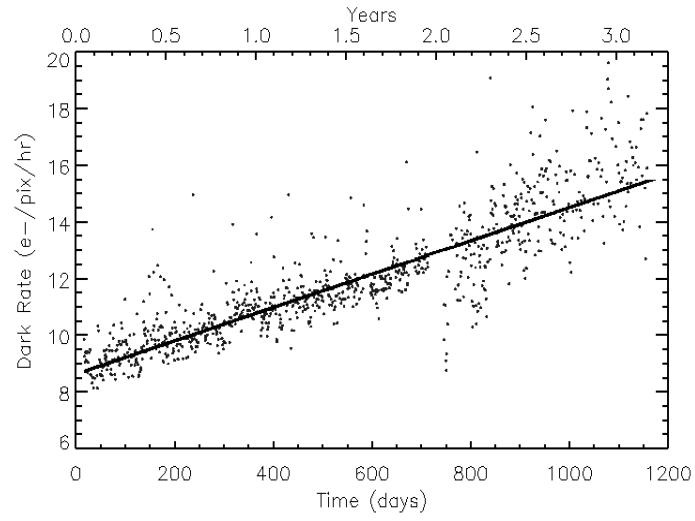
current figure for WFC includes a small component of surface dark current accumulated during the readout time.

Like all CCDs operated in a low earth orbit radiation environment, the ACS CCDs are subject to radiation damage by energetic particles trapped in the radiation belts. Ionization damage and displacement damage are two types of damage caused by protons in silicon. The MPP mode is very effective in mitigating the damage due to ionization such as the generation of surface dark current due to the creation of trapping states in the Si-SiO₂ interface. Although only a minor fraction of the total energy is lost by a proton via nonionizing energy loss, the displacement damage can cause significant performance degradation in CCDs by decreasing the charge transfer efficiency (CTE), increasing the average dark current, and introducing pixels with very high dark current (hot pixels). Displacement damage to the silicon lattice occurs mostly due to the interaction between low energy protons and silicon atoms. The generation of phosphorous-vacancy centers introduces an extra level of energy between the conduction band and the valence band of the silicon. New energetic levels in the silicon bandgap have the direct effect of increasing the dark current as a result of carrier generation in the bulk depletion region of the pixel. As a consequence, the dark current of CCDs operated in a radiative environment is predicted to increase with time.

Ground testing of the WFC CCDs, radiated with a cumulative fluence equivalent to 2.5 and 5 years of on-orbit exposure, predicted a linear growth of $\sim 1.5 \text{ e}^-/\text{pixel}/\text{hour}/\text{year}$. During the ground tests the WFC CCDs were operated at $\sim 81 \text{ }^\circ\text{C}$, about 4° cooler than the operating temperature on orbit.

The dark current in ACS CCDs is monitored four days per week with the acquisition of four 1000 seconds dark frames (totaling 16 images per week). Dark frames are used to create reference files for the calibration of scientific images, and to track and catalog hot pixels as they evolve. The four daily frames are combined together to remove cosmic rays and to extract hot pixel information for any specific day. The dark reference files are generated by combining two weeks of daily darks in order to reduce the statistical noise. The hot pixel information for a specific day is then added to the combined bi-weekly dark. In order to study the evolution of the dark current with time, the modal dark current value in the cosmic-ray free daily darks is calculated. As expected, the dark current increases with time (Figure 4.5). The observed linear growth rates of dark current are 2.1 and $1.6 \text{ e}^-/\text{pixel}/\text{hour}/\text{year}$ for WFC1 and WFC2 respectively, and $2.1 \text{ e}^-/\text{pixel}/\text{hour}/\text{year}$ for the HRC CCD. These rates are in general agreement with the ground test predictions.

Figure 4.5: Dark rate trend with time for the ACS CCDs (HRC, WFC1,WFC2).



4.3.5 Warm and Hot Pixels

In the presence of a high electric field, the dark current of a single pixel can be greatly enhanced. Such pixels are called dark spikes or hot pixels. Although the increase in the mean dark current with proton irradiation is important, of greater consequence is the large increase in dark current nonuniformity.

We have chosen to classify the field-enhanced dark spikes into two categories: warm and hot pixels. The definition of “warm” and “hot” pixel is somewhat arbitrary. We have chosen a limit of $0.08 \text{ e}^-/\text{pixel}/\text{seconds}$ as a threshold above which we consider a pixel to be “hot”. We identify “warm” pixels as those which exceed by about 5σ ($\sim 0.02 \text{ e}^-/\text{pixel}/\text{second}$) the normal distribution of the pixels in a dark frame up to the threshold of the hot pixels (See Figure 4.8) for a typical dark rate pixel distribution)

Warm and hot pixels accumulate as a function of time on orbit. Defects responsible for elevated dark rate are created continuously as a result of the ongoing displacement damage on orbit. The number of new pixels with a dark current higher than the mean dark date increases every day by few to several hundreds depending on the threshold.

Table 4.3: Creation rate of new hot pixels (pixel/day).

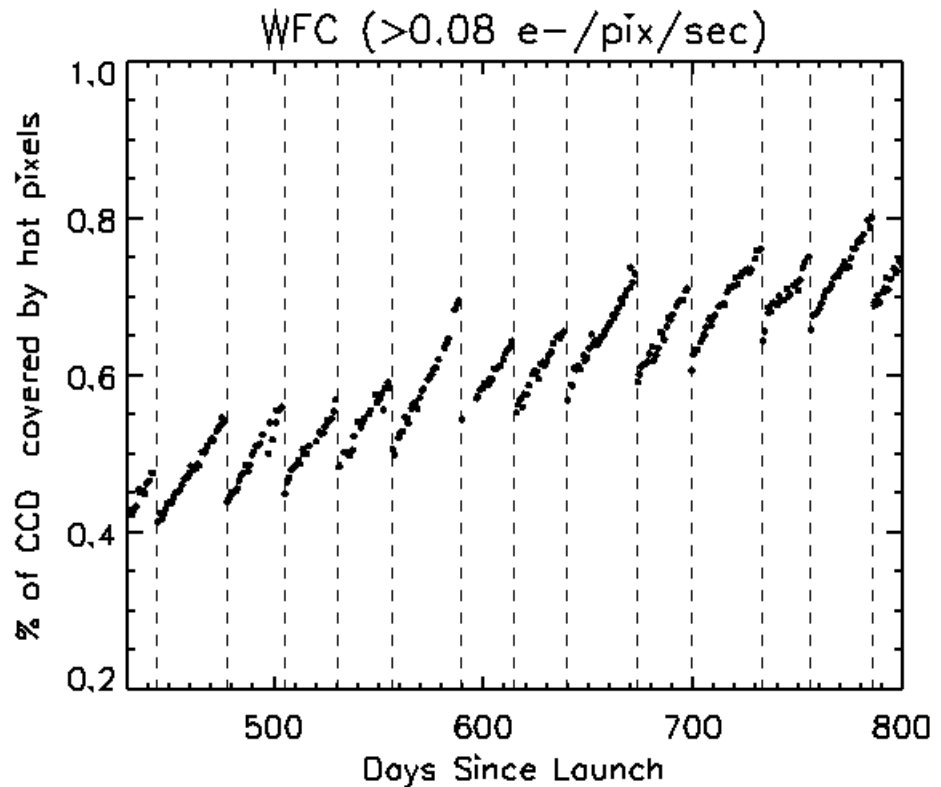
| Threshold ($\text{e}^-/\text{pixel}/\text{second}$) | WFC | HRC |
|--|--------------|--------------|
| 0.02 | 815 ± 56 | 125 ± 12 |
| 0.04 | 616 ± 22 | 96 ± 2 |
| 0.06 | 480 ± 13 | 66 ± 1 |
| 0.08 | 390 ± 9 | 48 ± 1 |
| 0.10 | 328 ± 8 | 35 ± 1 |
| 1.00 | 16 ± 1 | 1 ± 0.5 |

Most of these new hot pixels are transient. Like others CCDs on HST, the ACS devices undergo a monthly annealing process. The CCDs and the thermal electric coolers (TECs) are turned off and the heaters are turned on to warm the chips to $\sim 19^\circ \text{C}$. Although the annealing mechanism at such low temperatures is not yet understood, after this “thermal cycle” the population of hot pixels is greatly reduced (see Figure 4.6). The anneal rate depends on the dark current rate with very hot pixels being annealed easier than warmer pixels. For pixels classified as “hot” (those with dark rate $> 0.08 \text{ e}^-/\text{pix}/\text{sec}$) the anneal rate is $\sim 82\%$ for WFC and $\sim 86\%$ for HRC.

Annealing has no effect on the normal pixels that are responsible for the increase in the mean dark current rate. Such behavior is similar to what is

seen with STIS SITe CCD and WFC3 CCDs during ground radiation testing.

Figure 4.6: Hot pixel growth in the WFC CCDs.

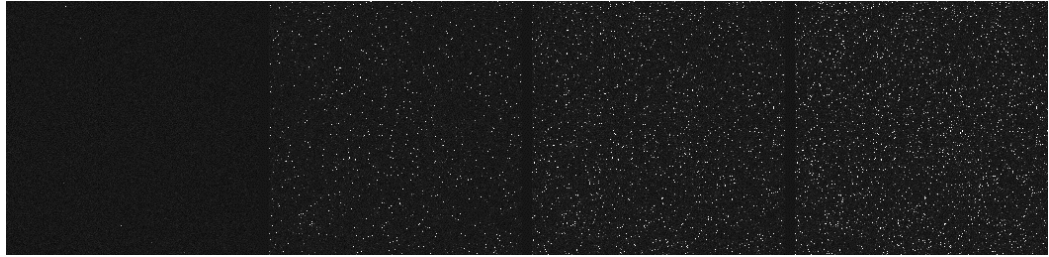


The vertical dashed lines indicate the annealing dates.

During early annealing episodes the ACS CCDs were warmed up for 24 hours. But the annealing time was reduced to 6 hours in spring of 2004 to allow better scheduling of HST time. Even with a shorter cycle the effectiveness of the anneal in ACS CCDs has remained the same. It is interesting to note that since ACS launch, four HST safing events have occurred; after each event the population of hot pixels was reduced as if a normal anneal cycle has occurred. During the safing events the CCDs and the TECs were turned off. Since the heaters were not turned on, the CCDs warmed-up to only about -10°C . After a period of time ranging from 24 to 48 hours, HST resumed normal operation. The dark frames taken after the safing events showed a reduction in hot pixel population similar to those observed during normal annealing cycles.

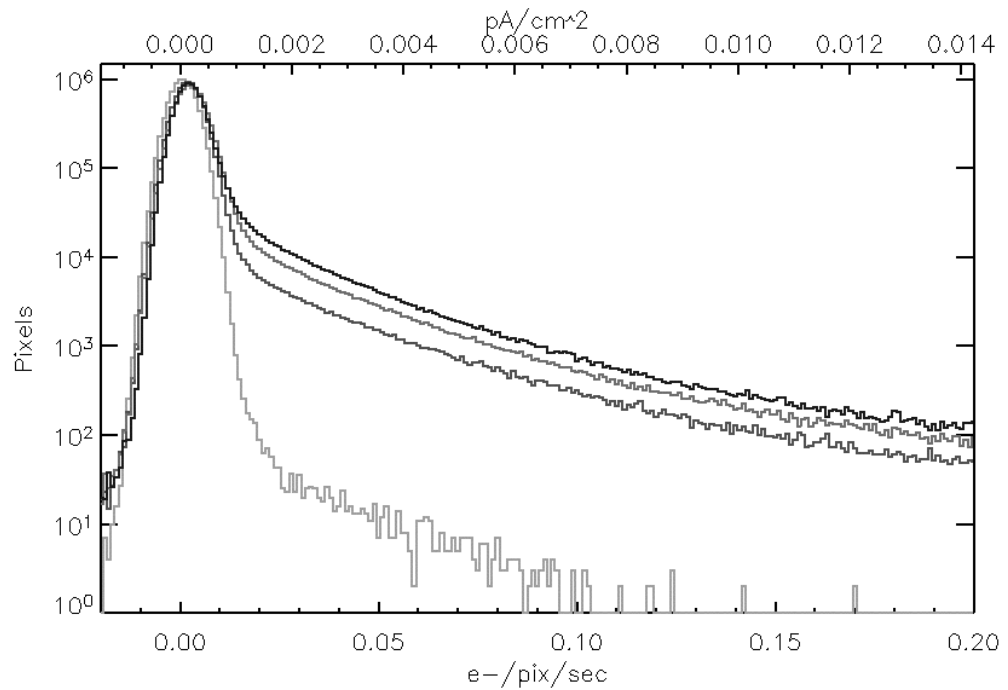
Since the anneals cycle do not repair 100% of the hot pixels, there is a growing population of permanent hot pixels (see Figure 4.7 and Figure 4.8).

Figure 4.7: A subsection of WFC1 dark frames taken at different epochs showing the increasing population of hot pixels.



From left to right: before launch, and after 1, 2 and 3 years on orbit.

Figure 4.8: Histogram of WFC dark frames taken at different epochs.



Epochs pre-launch, and after 1,2, and 3 years on orbit. Both the mean dark rate increase and the growing population of permanent hot pixels are visible.

According to the current trend, about 0.3% of WFC (0.22% of HRC) pixels became permanently hot every year (see Table 4.4). In a typical 1000 second exposure the percentage of pixels contaminated by cosmic rays ranges between 1.5% and 3% of the total. By spring of 2007 the contamination from hot pixels will impact about 2% of the pixels (See Figure 4.9).

Table 4.4: Permanent warm and hot pixel growth (%/yr).

| Threshold ($e^-/\text{pix}/\text{sec}$) | WFC | HRC |
|--|------|------|
| 0.02 | 174 | 1.52 |
| 0.04 | 0.86 | 0.50 |
| 0.06 | 0.50 | 0.31 |
| 0.08 | 0.30 | 0.22 |
| 0.10 | 0.25 | 0.18 |
| 1.00 | 0.04 | 0.03 |

In principle, warm and hot pixels could be eliminated by the superdark subtraction. However, some pixels show a dark current that is not stable with time but switches between well defined levels. These fluctuations may have timescales of a few minutes and have the characteristics of random telegraph signal (RTS) noise. The dark current in field-enhanced hot pixels can be dependent on the signal level, so the noise is much higher than the normal shot noise. As a consequence, since the locations of warm and hot pixels are known from dark frames, they are flagged in the data quality. The hot pixels can be discarded during image combination if multiple exposures have been dithered.

While the standard CR-SPLIT approach allows for cosmic ray subtraction, without additional dithering, it will not eliminate hot pixels in post-observation processing.



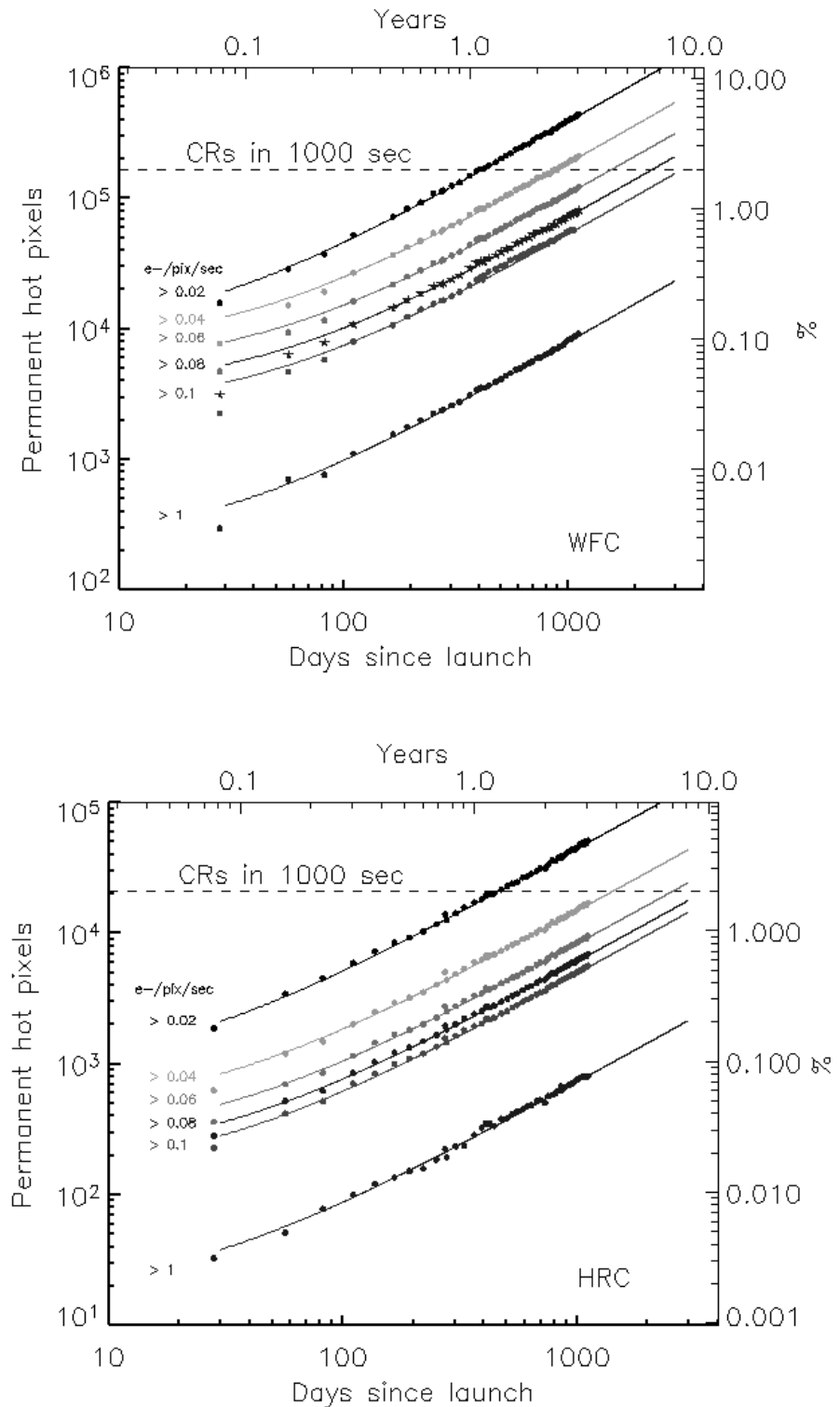
We recommend that observers who would have otherwise used a simple CR-SPLIT now use some form of dithering instead. Any form of dithering providing a displacement of at least a few pixels can be used to simultaneously remove the effects of cosmic ray hits and hot pixels in post-observation processing.

For example, a simple ACS-WFC-DITHER-LINE pattern has been developed, based on integer pixel offsets, which shifts the image by 2 pixels in X and 2 pixels in Y along the direction that minimizes the effects of scale variation across the detector. The specific parameter values for this pattern are given in the *Phase II Proposal Instructions*.

Given the transient nature of hot pixels, users are reminded that few hot pixels may not be properly flagged in the data quality array (because they spontaneously “healed” or because their status changed in the period

spanning the reference file and science frame acquisition), and therefore could create false positive detections in some science programs.

Figure 4.9: Growth of permanent warm and hot pixel population as a function of time (WFC top, HRC bottom).



The contamination level due to cosmic rays accumulated in a 1000 second exposure is shown with a dashed line.

4.3.6 Cosmic Rays

Initial studies have been made of the characteristics of cosmic ray impacts on the HRC and WFC. The fraction of pixels affected by cosmic rays varies from 1.5% to 3% during a 1000 second exposure for both cameras, similar to what was seen on WFPC2 and STIS. This number provides the basis for assessing the risk that the target(s) in any set of exposures will be compromised. The affected fraction is the same for the WFC and HRC despite their factor of two difference in pixel areas because the census of affected pixels is dominated by charge diffusion, not direct impacts. Observers seeking rare or serendipitous objects, as well as transients, may require that every single WFC pixel in at least one exposure among a set of exposures is free from cosmic ray impacts. For the cosmic ray fractions of 1.5% to 3% in 1000 seconds, a single ~ 2400 second orbit must be broken into 4 exposures (4 CR-SPLITS of 500 to 600 seconds each) to reduce the number of uncleanable pixels to 1 or less. (We recommend that users dither these exposures to remove hot pixels as well.)

The flux deposited on the CCD from an individual cosmic ray does not depend on the energy of the cosmic ray but rather the length it travels in the silicon substrate. The electron deposition due to individual cosmic rays has a well defined cut-off with negligible events of less than $500 e^-$ and a median of $\sim 1000 e^-$ (see Figure 4.10 and Figure 4.11).

Figure 4.10: Electron deposition by cosmic rays on WFC.

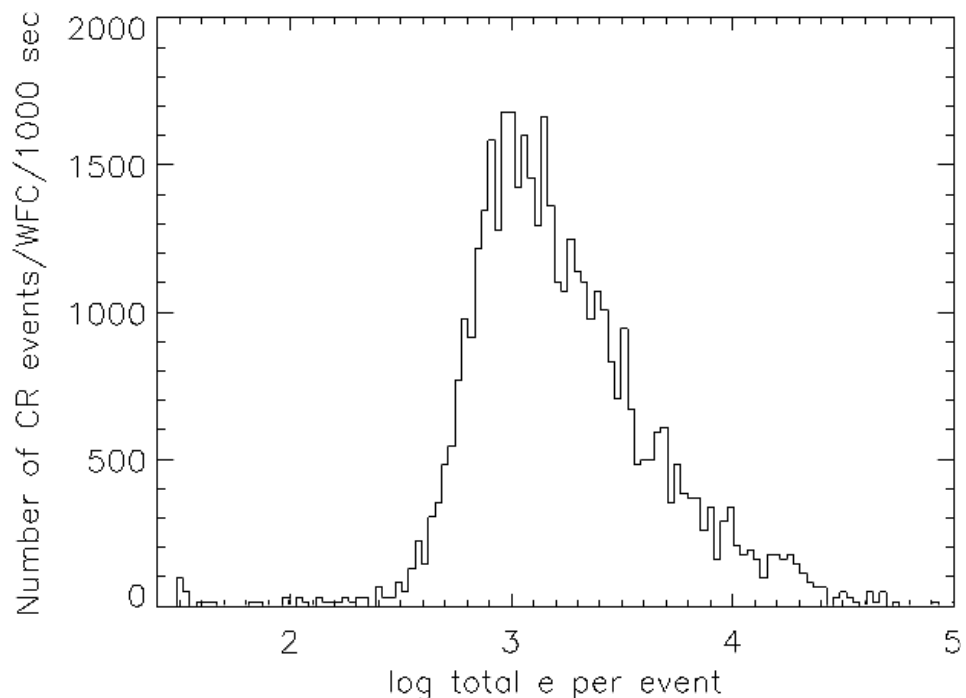
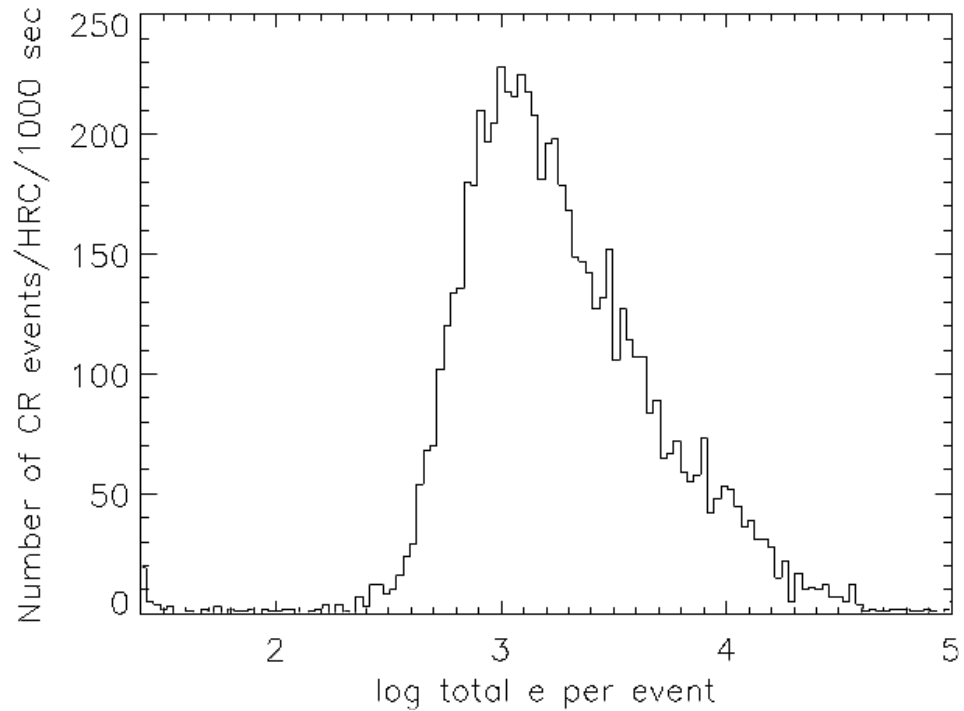


Figure 4.11: Electron deposition of cosmic rays on HRC.



The distribution of the number of pixels affected by a single cosmic ray is strongly peaked at 4 to 5 pixels. Although a few events are seen which encompass only one pixel, examination of these events indicate that at least some, and maybe all of these sources are actually transient hot pixels or unstable pixels which can appear hot in one exposure (with no charge diffusion) and normal in the next. Such pixels are very rare but do exist. There is a long tail in the direction towards increasing numbers of attached pixels.

Distributions of sizes and anisotropies can be useful for distinguishing cosmic rays from astrophysical sources in a single image. The size distribution for both chips peaks near 0.4 pixels as a standard deviation (or 0.9 pixels as a FWHM). This is much narrower than for a PSF and is thus a useful discriminant between unresolved sources and cosmic rays.

4.3.7 Charge Transfer Efficiency

Charge transfer efficiency (CTE) is a measure of how effective the CCD is at moving charge from one pixel location to the next when reading out the chip. A perfect CCD would be able to transfer 100% of the charge as the charge is shunted across the chip and out through the serial register. In practice, small traps in the silicon lattice compromise this process by holding on to electrons, releasing them at a later time. (Depending on the trap type, the release time ranges from a few microseconds to several seconds). For large charge packets (several thousands of electrons), losing

a few electrons along the way is not a serious problem, but for smaller ($\sim 100 e^-$ or less) signals, it can have a substantial effect.

CTE is typically measured as a pixel transfer efficiency, and would be unity for a perfect CCD. The CTE numbers for the ACS CCDs at the time of installation are given in Table 4.5. While the numbers look impressive, remember that reading out the WFC CCD requires 2048 parallel and 2048 serial transfers, so that almost 2% of the charge from a pixel in the corner opposite the readout amplifier is lost.

Table 4.5: Charge transfer efficiency measurements for the ACS CCDs at installation time (Fe55 test at 1620 e^-).

| Chip | Parallel | Serial |
|------|----------|----------|
| WFC1 | 0.999995 | 0.999999 |
| WFC2 | 0.999995 | 0.999999 |
| HRC | 0.999983 | 0.999994 |

Also, the CTE numbers are significantly different for images where the pixels have a low intensity compared to those where the intensity is high.

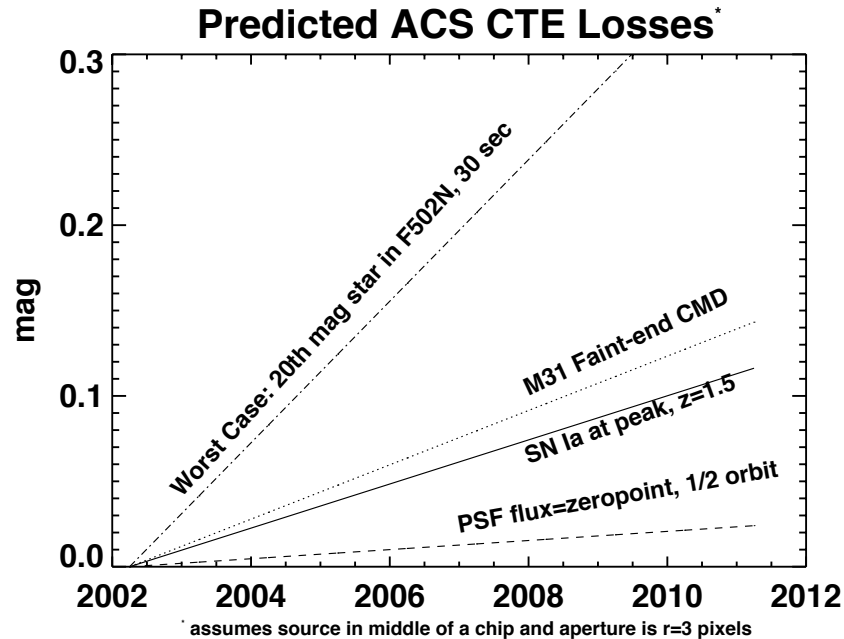
Both the WFPC2 and STIS CCDs have been found to suffer from a significant degradation in CTE since their installation in 1993 and 1997, respectively. At the end of Cycle 11 we performed the first on-orbit calibration of the photometric losses due to imperfect CTE on ACS HRC and WFC. We used images of 47 Tucanae from a CTE calibration program to measure the dependence of stellar photometry on the number of parallel and serial transfers. The results are described by Riess et al. ([ACS ISR 2003-09](#)) and are summarized here. For WFC, significant photometric losses are apparent for stars undergoing numerous parallel transfers (y-direction) and are ~ 1 to 2% for typical observing parameters, rising to $\sim 10\%$ in worst cases (faint stars, low background). The size of the photometric loss appears to have a strong power-law dependence on the stellar flux, as seen for other CCDs flown on HST.

The dependence on background is significant but there is little advantage to increasing the background intentionally (e.g., by post-flashing) due to the added shot noise. No losses are apparent for WFC due to serial transfers (x-direction). For HRC, significant photometric losses also arise from parallel transfer ($\sim 1\%$ for typical observations, $\sim 5\%$ for worst case) but are not seen for serial transfer. Correction formulae are presented in [ACS ISR 2004-06](#) to correct photometric losses as a function of a source's position, flux, background, time, and aperture size.

Figure 4.12 shows the predicted photometric losses for the WFC due to imperfect parallel CTE as a function of time. These curves require extreme extrapolation and should be used for planning purposes only. Four specific science applications are shown as examples: the measurement of the faint

end of M31's CMD (GO 9453), the measurement of high-redshift supernovae (GO 9528), the measurement of any PSF whose brightness is the zeropoint (i.e., $1 \text{ e}^-/\text{second}$), and photometry of a 20^{th} magnitude star in a narrow band.

Figure 4.12: Projected CTE losses in WFC (and equivalently, the size of corrections).



Projected CTE losses in WFC for sample science applications described in Table 4.6. The precision of measurements is not limited by the size of the loss but rather its uncertainty. As a rule of thumb we suggest that the ultimate limit of precision will be $\sim 25\%$ of the loss after correction.

Table 4.6: Example of science applications and their assumed parameters.

| Science application | Source flux (e^-) | Sky (e^-) |
|--|------------------------------|----------------------|
| SN Ia at peak $z = 1.5$ | 100 | 30 |
| M31 faint-end of CMD | 40 | 100 |
| PSF e^-/sec , 1/2 orbit | 1000 | 40 |
| F502N, 30 sec, 20^{th} mag star | 258 | 0.1 |

When observing a single target significantly smaller than a single detector, it is possible to place it near an amplifier to reduce the impact of imperfect CTE. This is easy to accomplish by judicious choice of aperture and target position, or by utilizing POS TARG commands. However, be aware that large POS TARGs are not advisable because they change the fractional pixel shifts of dither patterns due to the geometric distortion of

ACS. An alternative means to achieve the placement of a target near the amplifier is by using some of the subarray apertures. For example, WFC1-512 (target will have 256 transfers in X and Y), WFC1-1K, and WFC1-2K place the target near the B amplifier (or WFC2-2K for the C amplifier).

4.3.8 UV Light and the HRC CCD

In the optical, each photon generates a single electron. However, in the near UV, shortward of $\sim 3200 \text{ \AA}$ there is a finite probability of creating more than one electron per UV photon (see Christensen, O., *J. App. Phys.* **47**,689, 1976). At room temperature the theoretical quantum yield (i.e., the number of electrons generated for a photon of energy $E > 3.5 \text{ eV}$ ($\lambda \sim 3500 \text{ \AA}$)), is $N_e = E(\text{eV})/3.65$. The HRC CCDs quantum efficiency curve has not been corrected for this effect. The interested reader may wish to see the *STIS Instrument Handbook* for details on the signal-to-noise treatment for the STIS CCDs.

4.4 The SBC MAMA

4.4.1 MAMA Properties

The ACS MAMA detector is the STIS flight spare STF7. It provides coverage from 1150 \AA to 1700 \AA . The MAMA detector is a photon-counting device which processes events serially. The ACS MAMA only operates in the accumulate (ACCUM) mode, in which a time-integrated image is produced. Unlike the STIS MAMAs, the ACS does not offer the high-resolution (2048×2048) mode or time-tagged data acquisition. The primary benefits afforded by the STIS and ACS MAMAs, in comparison with previous HST UV spectroscopic detectors such as those in the GHRS and FOS, are high spatial resolution, two-dimensional imaging over a relatively large field of view, and low background for point sources.

Figure 4.13: Design of the SBC MAMA.

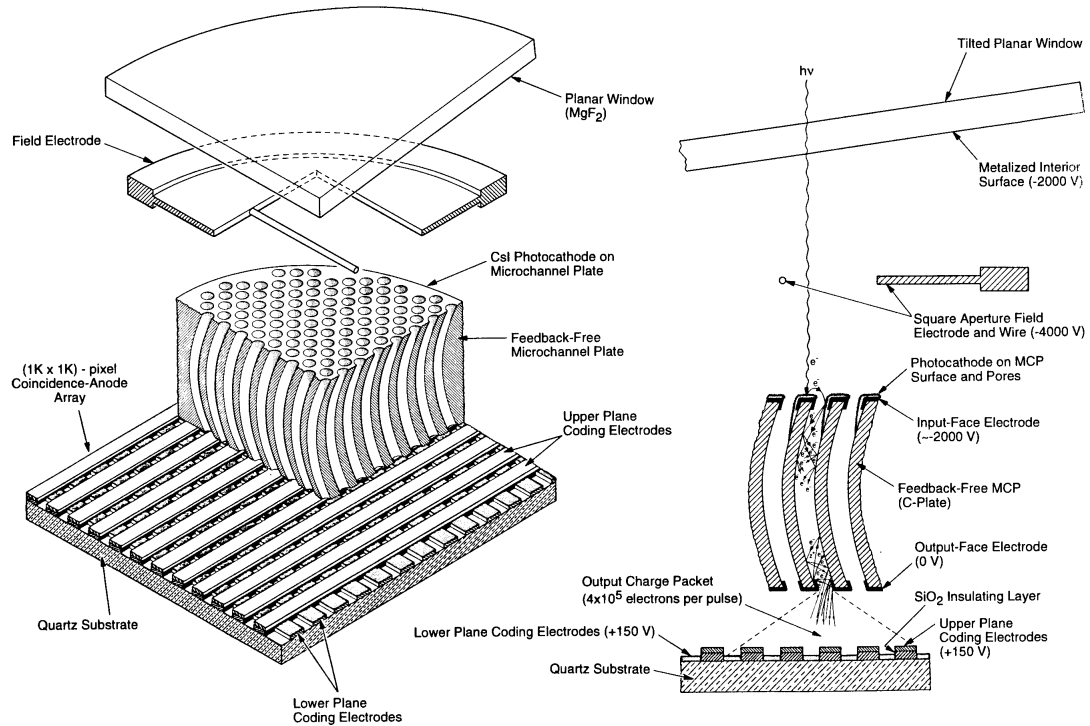


Figure 4.13 illustrates the design of the MAMA, which has an opaque CsI photocathode deposited directly on the face of the curved microchannel plate (MCP). Target photons strike the photocathode, liberating single photoelectrons which pass into the MCP. There they are multiplied to a pulse of $\sim 4 \times 10^5 e^-$. The pulse is recorded by an anode array behind the photocathode, and detected by the MAMA electronics which rejects false pulses and determines the origin of the photon event on the detector.

The field electrode, or *repeller wire*, repels electrons emitted away from the microchannel plate back into the channels. This provides an increase in quantum efficiency of the detector at the price of an increase in the detector point spread function halo. The repeller wire voltage is always on for SBC observations.

Table 4.7: SBC detector performance characteristics.

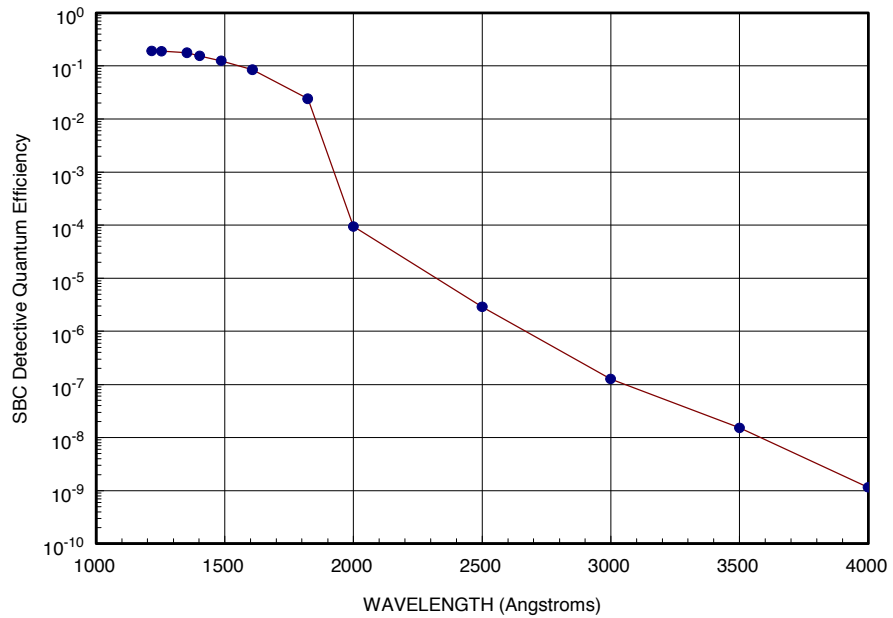
| Characteristic | SBC MAMA performance |
|--|--|
| Photocathode | CsI |
| Wavelength range | 1150 to 1700 Å |
| Pixel format | 1024 × 1024 |
| Pixel size | 25 × 25 μm |
| Plate scale | 0.034 × 0.030 "/pixel |
| Field of view | 34.6" x 30.8" |
| Quantum efficiency | 19.2% @ 1216 Å |
| Dark count | 1.2 × 10 ⁻⁵ counts/second/pixel |
| Global count-rate linearity limit ¹ | 360,000 counts/second |
| Local count-rate linearity limit | ~350 counts/second/pixel |
| Visible light DQE | < 1.2 × 10 ⁻⁹ above 400 nm |

1. Rate at which counting shows 10% deviation from linearity. These count rates are well above the bright-object screening limits.

4.4.2 SBC Spectral Response

The spectral response of the unfiltered SBC is illustrated in Figure 4.14. The peak photocathode response occurs at Lyman- α . Its spectral response is defined by the cutoff of the MgF₂ window at 1150 Å at short wavelengths, and by the relatively steep decline of the CsI photocathode at long wavelengths. Out-of-band QE at longer wavelengths (> 4000 Å) is < 10⁻⁸, yielding excellent solar-blind performance.

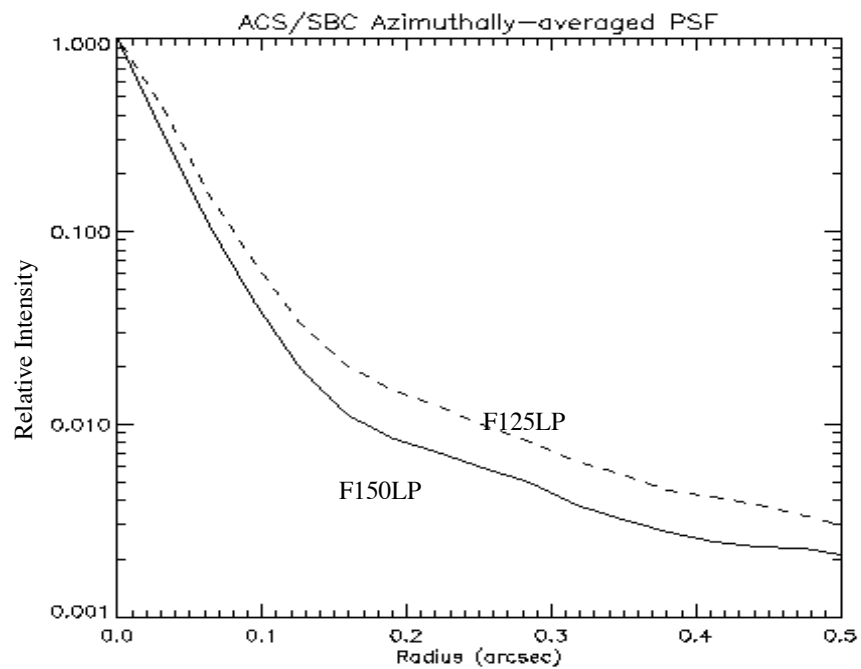
Figure 4.14: ACS SBC detector quantum efficiency.



4.4.3 Optical Performance

The SBC exhibits low-level extended wings in the detector point-spread function (PSF). Sample MAMA detector PSF profiles are shown in Figure 4.15.

Figure 4.15: MAMA point spread function.



4.5 SBC Operations and Limitations

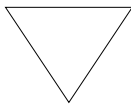
4.5.1 SBC Scheduling Policies

The STIS MAMA control electronics are subject to resets due to cosmic-ray upsets. Therefore, STIS MAMAs were operated only during the contiguous orbits of each day that are free of the South Atlantic Anomaly (SAA). Even though the design of the ACS MAMA control electronics in the SBC was modified so that they would not be susceptible to cosmic-ray hits, the background count rate still exceeds the bright object limits for the SBC during SAA passage. Consequently, the SBC will in general only be scheduled for use during SAA-free orbits.

4.5.2 MAMA Overflow of the 16 Bit Buffer

The MAMA is a photon-counting detector: as each photon is recorded, it is placed into buffer memory. The buffer memory stores values as 16 bit integers; hence the maximum number it can accommodate is 65,535 counts per pixel in a given ACCUM mode observation. When accumulated counts per pixel exceed this number, the values will wrap. As an example, if you are counting at 25 counts/second/pixel, you will reach the MAMA “accumulation” limit in ~44 minutes.

One can keep accumulated counts per pixel below this value by breaking individual exposures into multiple identical exposures, each of which is short enough that fewer than 65,535 counts are accumulated per pixel. There is no read noise for MAMA observations, so no penalty is paid in lost signal-to-noise ratio when exposures are split. There is only a small overhead for each MAMA exposure (see Section 8.2).



Keep the accumulated counts per SBC pixel below 65,535 by breaking single exposures into multiple exposures, as needed.

4.5.3 MAMA Darks

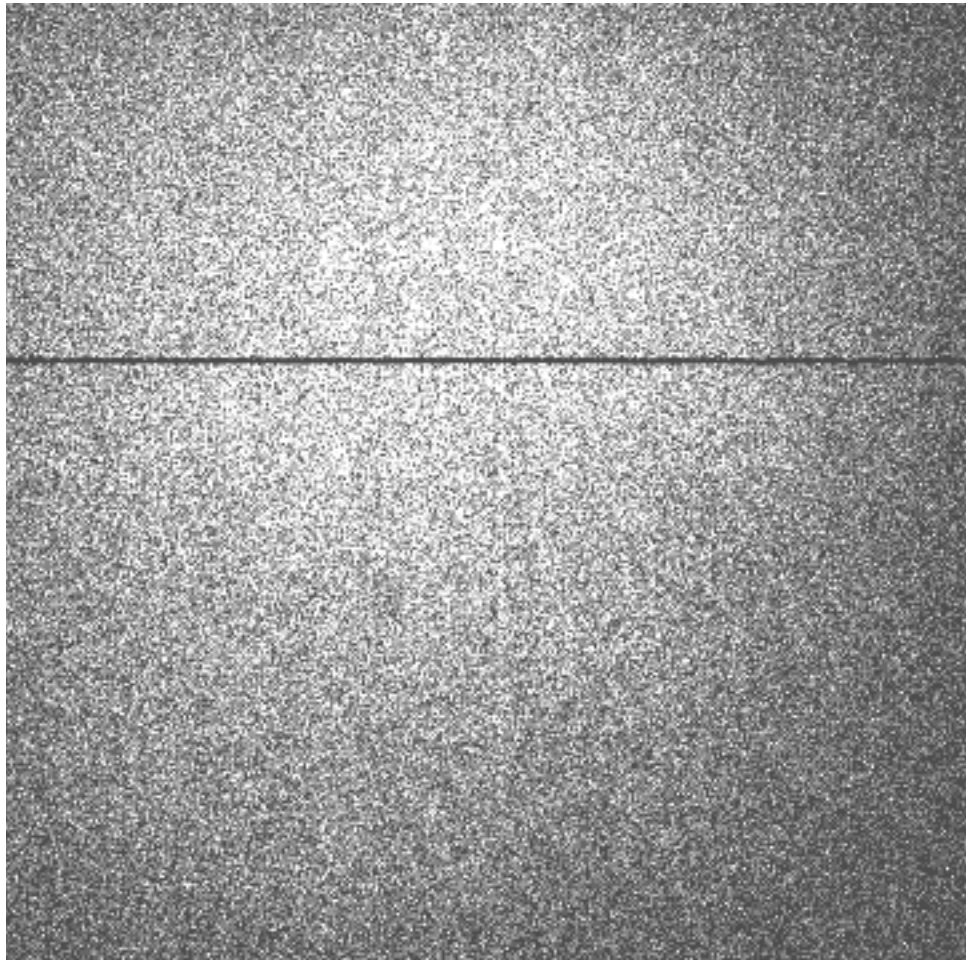
MAMA detectors have intrinsically low dark currents. Ground test measurements of the ACS MAMA showed count rates in the range of 10^{-5} to 10^{-4} counts per pixel per second as the temperature varied from 28 °C to 35 °C degrees. The count rate increased by about 30% for one degree increase in temperature. In-flight measurements, taken weekly throughout June and July 2002, show count rates between 8×10^{-6} and 10^{-5} . These measurements were taken as soon as the MAMA was turned on and were

therefore at the lower end of the temperature range. A 10 hour observation in SMOV, long enough for nominal temperatures to be reached, yielded a dark current of 1.2×10^{-5} counts per second per pixel. Monthly monitoring shows the in-flight dark current to be about 9×10^{-6} counts per second per pixel. For typical SBC operations in which the detector is turned on for less than two hours, a dark image collected at lower temperatures is more suitable and replaces the current calibration image. This has a mean dark rate of 10^{-5} counts per second per pixel.

The ACS MAMA has a broken anode which disables rows 599 to 605. There are three dark spots smaller than 50 microns at positions (334,977), (578,964), and (960,851), as well as two bright spots at (55,281) and (645,102) with fluctuating rates that are always less than 3 counts per second. The reference pixel has been moved to (512,400) to avoid these areas (see Table 7.9)

An example of the dark current variation across the detector can be seen in Figure 4.16 below.

Figure 4.16: MAMA dark image.

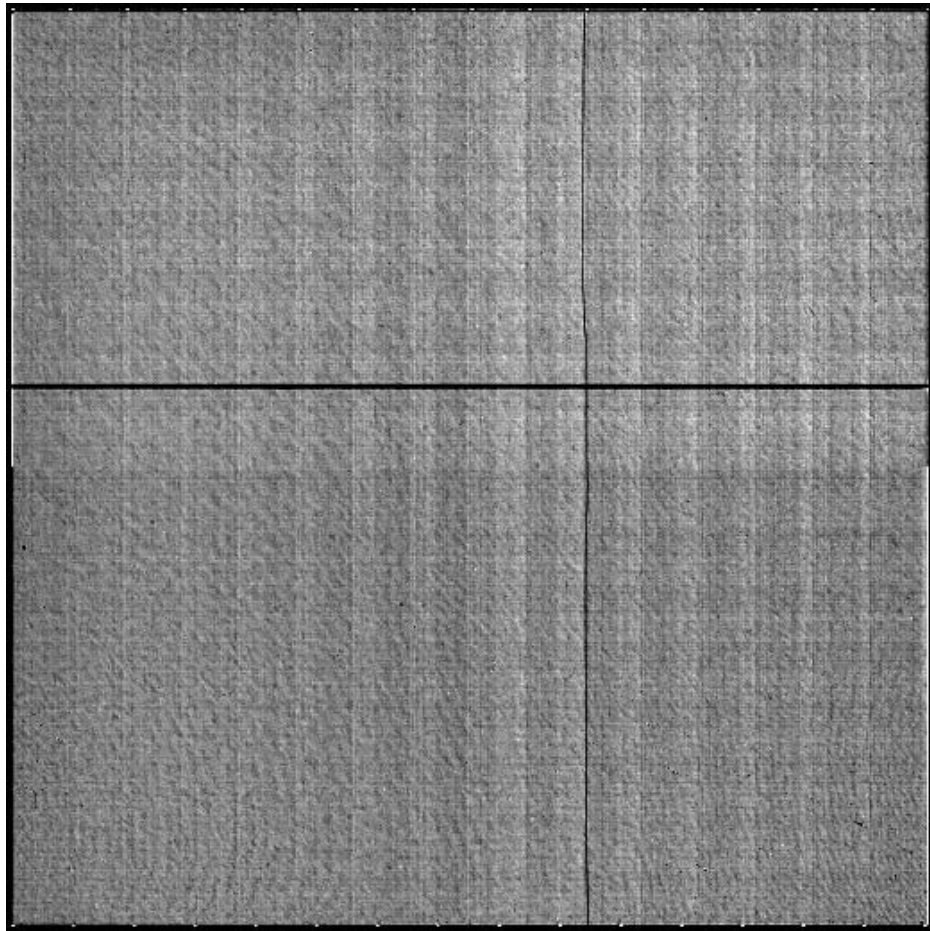


4.5.4 SBC Signal-to-Noise Ratio Limitations

MAMA detectors are capable of delivering signal-to-noise ratios on the order of 100:1 per resolution element (2×2 pixels) or even higher. Tests in orbit have demonstrated that such high S/N is possible with STIS (Kaiser et al., *PASP*, 110, 978; Gilliland, *STIS ISR 1998-16*). For targets observed at a fixed position on the detector, the signal-to-noise ratio is limited by systematic uncertainties in the small-scale spatial and spectral response of the detector. The MAMA flats show a fixed pattern that is a combination of several effects including beating between the MCP array and the anode pixel array, variations in the charge-cloud structure at the anode, and low-level capacitive cross-coupling between the fine anode elements. Intrinsic pixel-to-pixel variations are of order 6% but are stable to $< 1\%$.

4.5.5 SBC Flatfield

Figure 4.17: MAMA flat field.



The SBC requires two types of flat fields: the "pixel-to-pixel flats" (or P-flats) which take care of the high-frequency structures in the detector

sensitivity, and the "low-order flats" (or L-flats) which handle the low-frequency components. Current P-flats were recently derived by Bohlin & Mack ([ACS ISR 2005-04](#)) using the on-board deuterium lamp, and found to be independent of wavelength. The P-flat in Figure 4.17 shows the effect of the disabled broken anode (rows 601 to 605) and of the shadow of the repeller wire (around column 577).

Low-frequency flatfield corrections for the SBC imaging modes have recently been derived using multiple exposures of the globular cluster NGC6681 (Mack, et. al., ISR in prep.). Variations of $\pm 6\%$ (full range) were found for the F115LP and F125LP filters, $\pm 8\%$ for the F140LP and F150LP filters, and $\pm 14\%$ for the F165LP filter. (The F122M filter was not included in this analysis due to lack of sufficient data). The L-flat shows a similar general pattern in all filters, with the required correction increasing with wavelength. While performing the L-flat analysis, a decline in the UV sensitivity with time was detected at a level of 2 to 4%/yr over the first 1.6 years of operation. The sensitivity appears to have leveled off after this time. A slight sensitivity loss as a function of temperature ($\sim 0.1\%/degree$) was also discovered. These effects were detected for the STIS FUV-MAMA detector (see [STIS ISRs 2003-01](#) and [2004-04](#)).

4.5.6 SBC Nonlinearity

Global

The MAMA detector begins to experience nonlinearity (photon impact rate not equal to photon count rate) at global (across the entire detector) count rates of 200,000 counts/second. The nonlinearity reaches 10% at 360,000 counts/second and can be corrected for in post-observation data processing at the price of a loss of photometric reliability. Additionally, the MAMA detector plus processing software are not able to count reliably at rates exceeding 285,000 counts/second. For this reason, and to protect the detectors, observations beyond this rate are not allowed (see Section 4.6).

Local

The MAMA detector remains linear to better than 1% up to ~ 22 counts/second/pixel. At higher rates, it experiences local (at a given pixel) nonlinearity. The nonlinearity effect is image dependent—that is, the nonlinearity observed at a given pixel depends on the photon rate affecting neighboring pixels. This property makes it impossible to correct reliably for the local nonlinearity in post-observation data processing. In addition, MAMA detectors are subject to damage at high local count rates (see Section 4.6).

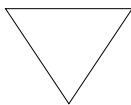
4.6 SBC Bright-Object Limits

STScI has responsibility to ensure that the MAMA detectors are not damaged through over-illumination. Consequently, we have developed procedures and rules to protect the MAMA. We ask all potential users to share in this responsibility by reading and taking note of the information in this section, and designing observing programs which operate in the safe regime for these detectors.

4.6.1 Overview

The SBC detector is subject to catastrophic damage at high global and local count rates, and cannot be used to observe sources which exceed the defined safety limits. The potential detector damage mechanisms include over-extraction of charge from the microchannel plates causing permanent reduction of response, ion feedback from the microchannel plates causing damage to the photocathode, and release of gas which can overpressure the tube.

To safeguard the detector, checks of the global (over the whole detector) and local (per pixel) illumination rates are automatically performed in flight for all SBC exposures. The *global illumination rate* is monitored continuously; if the global rate approaches the level where the detector can be damaged, the high voltage on the detector is automatically turned off. This event can result in the loss of all observations scheduled to be taken with that detector for the remainder of the calendar (~1 week). The *peak local illumination rate* is measured over the SBC field at the start of each new exposure. If the local rate approaches the damage level, the SBC filter wheel will be used to block the light, since there is no “shutter”. Also, all subsequent SBC exposures in the obset will be lost until a new filter is requested.



Sources that would over-illuminate the SBC detector cannot be observed. It is the responsibility of the observer to avoid specifying observations that exceed the limits described below. Please refer to Section 7.2 for more information.

4.6.2 Observational Limits

To ensure the safety of the SBC detector and the robustness of the observing timeline, we have established observational limits on the

incident count rates. Observations which exceed the allowed limits will not be scheduled. The allowed limits are given in Table 7.3, which includes separate limits for nonvariable and irregularly-variable sources. The limits for irregular variable sources are a factor 2.5 more conservative than for sources with predictable fluxes. Predictable variables are treated as nonvariable for this purpose. Examples of sources whose variability is predictable are Cepheids or eclipsing binaries. Irregularly variable sources are, for instance, cataclysmic variables or AGN.

SBC observations of targets subject to large, unpredictable outbursts must be preceded by groundbased monitoring within the previous 24 hours, or by an HRC NUV observation a couple of orbits in advance. In the latter case, the HRC observation must be included in the Phase I orbit request.

For further information about checking for SBC bright object limits while planning your observations, please refer to Section 7.2.

CHAPTER 5: Imaging

In this chapter . . .

| |
|---|
| 5.1 Imaging Overview / 51 |
| 5.2 Important Considerations for ACS Imaging / 56 |
| 5.3 Wide Field Optical CCD Imaging / 60 |
| 5.4 High-Resolution Optical and UV Imaging / 62 |
| 5.5 Ultraviolet Imaging with the SBC / 64 |
| 5.6 ACS Point Spread Functions / 65 |

5.1 Imaging Overview

ACS can be used to obtain images through a variety of optical and ultraviolet filters. When the selected ACS camera is the WFC or the HRC, the appropriate filter in one of the two filter wheels is rotated into position, and a clear aperture is automatically selected on the other filter wheel. For SBC imaging the single filter wheel is rotated to the required position. A number of apertures are defined for each ACS camera. In general, these refer to different target positions on the detector.

Table 5.1, Table 5.2, and Table 5.3 provide a complete summary of the filters available for imaging with each detector. Figures 5.1 through 5.6 show the filter transmission curves, and Figure 5.7 shows the integrated system throughputs.

The CCD filter wheels contain filters with two different sizes. Some filters (F435W, F475W, F502N, F550M, F555W, F606W, F625W, F658N, F660N, F775W, F814W, F850LP, and, G800L) are full-sized filters that can be used with both WFC and HRC. Others (F220W, F250W, F330W, F344N, F892N, POL0UV, POL60UV, POL120UV, POL0V, POL60V, POL120V, and PR200L) are smaller, giving a full unvignetted field of view when used with the HRC, but a vignetted field of view of only 72×72 arcseconds when used with the WFC. Use of the small UV filters is not supported with the WFC due to the unpredictable behavior of the silver coatings shortward of 4000 \AA .

The ramp filters are designed to allow narrow or medium band imaging centered at an arbitrary wavelength. Each ramp filter is divided into three segments, of which only the middle segment may be used with the HRC. More information is available at Section 7.7.2.

Note that although the CLEAR filters are specified in the filter wheel tables, users do not need to specify these filters in their HST proposals; they are added automatically in conjunction with the desired filter in the complementary wheel. In the SBC filter wheel, every third slot (#1, 4, 7, 10) is blocked off, so that in the case of a bright object limit violation, it is only necessary to rotate the filter wheel to an adjacent slot to block the incoming light.

With either the WFC or HRC, it is possible to select a filterless observation by specifying CLEAR (this is an “available-but-unsupported” filter) as the filter name, although the image will be of degraded quality. Rough wavelengths and widths, when used with the WFC or HRC, are listed in Table 5.1 under CLEAR entries. Use of CLEAR will provide slightly degraded PSFs with the HRC and seriously degraded PSFs for the WFC. More details on PSFs with use of CLEAR are provided in [ACS ISR 2003-03](#). Applications are expected to be rare, but a valid use could be astrometry of extremely faint targets with the HRC when color information is not required.

Table 5.1: ACS WFC/HRC filters in Filter Wheel #1.

| Filter name | Central wavelength (Å) | Width (Å) | Description | Camera |
|-------------|------------------------|-----------|-------------------|-----------|
| CLEAR | 6200 | 5200 | Clear aperture | WFC/HRC |
| F555W | 5346 | 1193 | Johnson V | WFC/HRC |
| F775W | 7764 | 1528 | SDSS i | WFC/HRC |
| F625W | 6318 | 1442 | SDSS r | WFC/HRC |
| F550M | 5580 | 547 | Narrow V | WFC/HRC |
| F850LP | 9445 | 1229 | SDSS z | WFC/HRC |
| POL0UV | 2000 to 6000 | - | 0° UV polarizer | HRC[/WFC] |
| POL60UV | 2000 to 6000 | - | 60° UV polarizer | HRC[/WFC] |
| POL120UV | 2000 to 6000 | - | 120° UV polarizer | HRC[/WFC] |
| F892N | 8917 | 154 | Methane (2%) | HRC[/WFC] |
| F606W | 5907 | 2342 | Broad V | WFC/HRC |
| F502N | 5022 | 57 | [OIII] (1%) | WFC/HRC |
| G800L | 5800 to 11,000 | - | Grism (R~100) | WFC/HRC |
| F658N | 6584 | 78 | H α (1%) | WFC/HRC |
| F475W | 4760 | 1458 | SDSS g | WFC/HRC |

[/WFC] indicates that polarizer filters, designed for the HRC field of view, induces vignetting when used with the WFC, producing a 72 by 72 arcsecond field of view.

Table 5.2: ACS WFC/HRC filters in Filter Wheel #2.

| Filter name | Central wavelength (Å) | Width (Å) | Description | Camera |
|-------------|------------------------|-----------|--------------------------------|-----------|
| CLEAR | 6000 | 5200 | Clear aperture | WFC/HRC |
| F660N | 6602 | 40 | [NII] (1%) | WFC/HRC |
| F814W | 8333 | 2511 | Broad I | WFC/HRC |
| FR388N | 3710 to 4050 | 2% | [OII] Ramp—middle segment | WFC/HRC |
| FR423N | 4050 to 4420 | 2% | [OII] Ramp—inner segment | WFC |
| FR462N | 4420 to 4820 | 2% | [OII] Ramp—outer segment | WFC |
| F435W | 4297 | 1038 | Johnson B | WFC/HRC |
| FR656N | 6270 to 6850 | 2% | H α Ramp—middle segment | WFC/HRC |
| FR716N | 6850 to 7470 | 2% | H α Ramp—inner segment | WFC |
| FR782N | 7470 to 8160 | 2% | H α Ramp—outer segment | WFC |
| POL0V | 4000 to 8000 | - | 0° Visible Polarizer | HRC[/WFC] |
| F330W | 3354 | 588 | HRC U | HRC |
| POL60V | 4000 to 8000 | - | 60° Visible Polarizer | HRC[/WFC] |
| F250W | 2696 | 549 | Near-UV broadband | HRC |
| POL120V | 4000 to 8000 | - | 120° Visible Polarizer | HRC[/WFC] |
| PR200L | 2000 to 4000 | - | NUV Prism (R~100 @ 200 nm) | HRC |
| F344N | 3434 | 60 | Ne V (2%) | HRC |
| F220W | 2228 | 485 | Near-UV broadband | HRC |
| FR914M | 7570 to 10,710 | 9% | Broad Ramp—middle segment | WFC/HRC |
| FR853N | 8160 to 8910 | 2% | IR Ramp—inner segment | WFC |
| FR931N | 8910 to 9720 | 2% | IR Ramp—outer segment | WFC |
| FR459M | 3810 to 5370 | 9% | Broad Ramp—middle segment | WFC/HRC |
| FR647M | 5370 to 7570 | 9% | Broad Ramp—inner segment | WFC |
| FR1016N | 9720 to 10,610 | 2% | IR Ramp—outer segment | WFC |
| FR505N | 4820 to 5270 | 2% | [OIII] Ramp—middle segment | WFC/HRC |
| FR551N | 5270 to 5750 | 2% | [OIII] Ramp—inner segment | WFC |
| FR601N | 5750 to 6270 | 2% | [OIII] Ramp—outer segment | WFC |

[/WFC] indicates that polarizer filters, designed for the HRC field of view, induces vignetting when used with the WFC, producing a 72 by 72 arcsecond field of view.

Table 5.3: ACS SBC filter complement.

| Filter name | Description |
|-------------|--|
| F115LP | MgF ₂ (1150 Å longpass) |
| F125LP | CaF ₂ (1250 Å longpass) |
| F140LP | BaF ₂ (1400 Å longpass) |
| F150LP | Crystal quartz (1500 Å longpass) |
| F165LP | Fused Silica (1650 Å longpass) |
| F122M | Ly- α ($\lambda = 1200$ Å, $\Delta\lambda = 60$ Å) |
| PR110L | LiF Prism (R~100) |
| PR130L | CaF ₂ Prism (R~100) |

Figure 5.1: ACS broad-band filters.

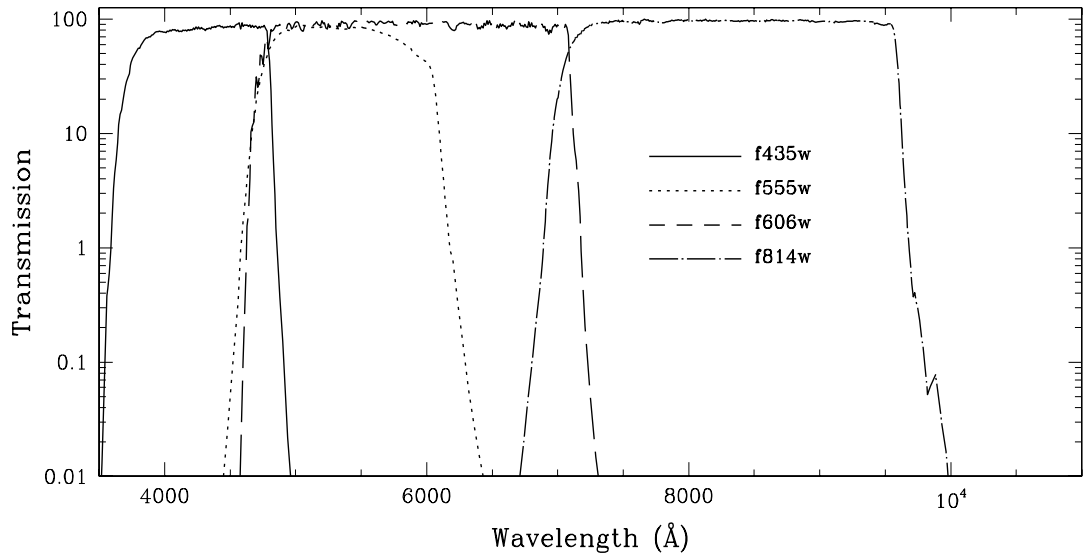


Figure 5.2: ACS SDSS filters.

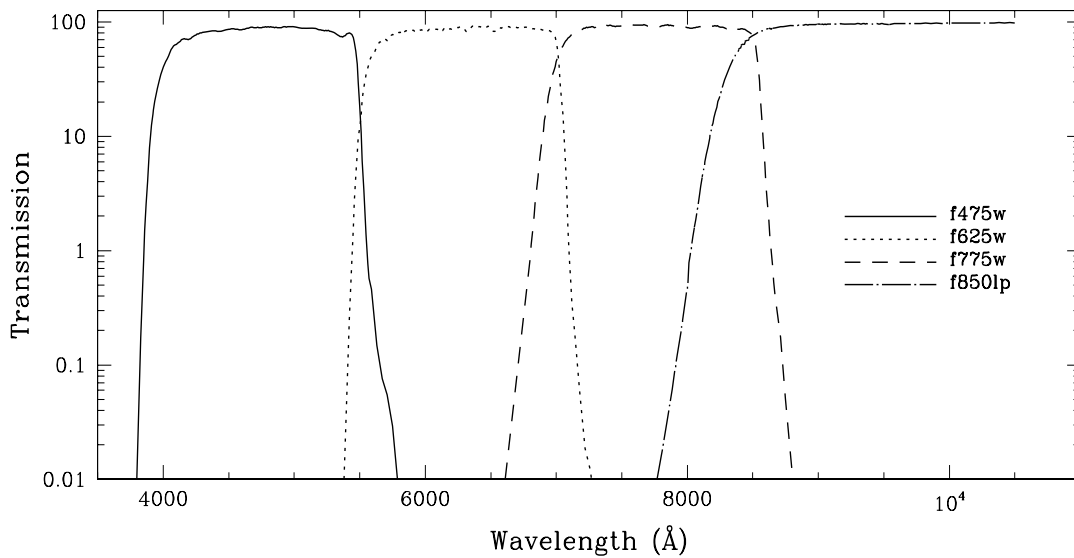


Figure 5.3: ACS UV and medium-band filters.

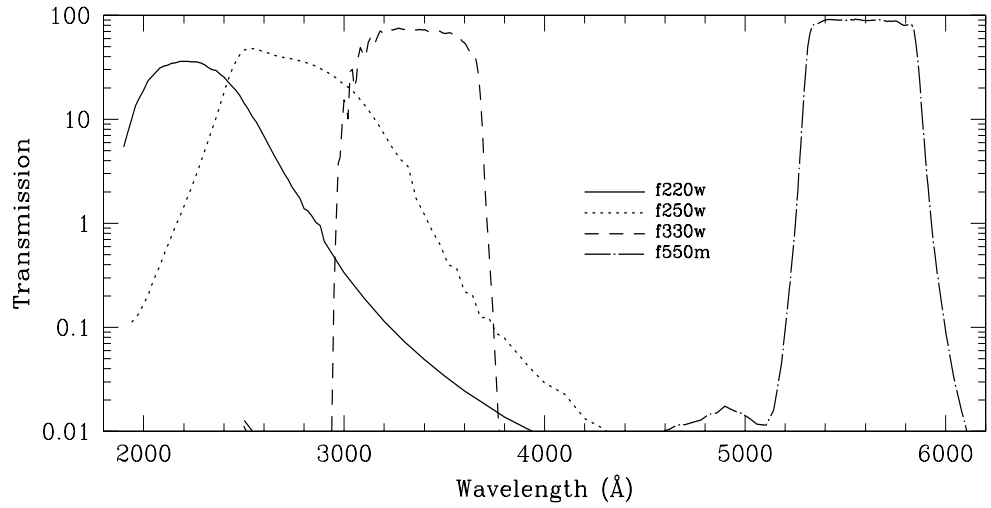


Figure 5.4: ACS narrow-band filters.

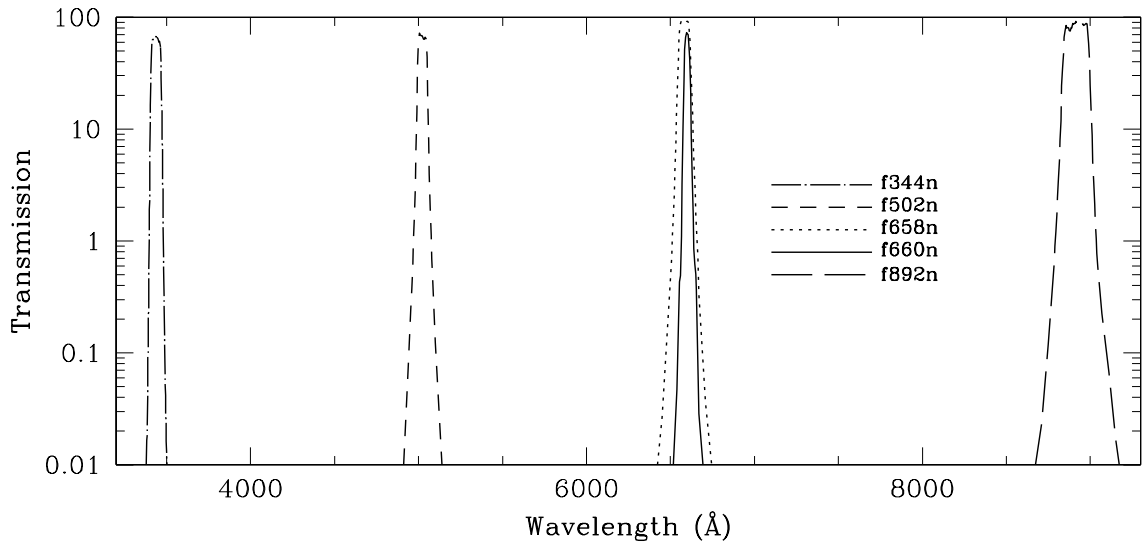


Figure 5.5: ACS SBC filters.

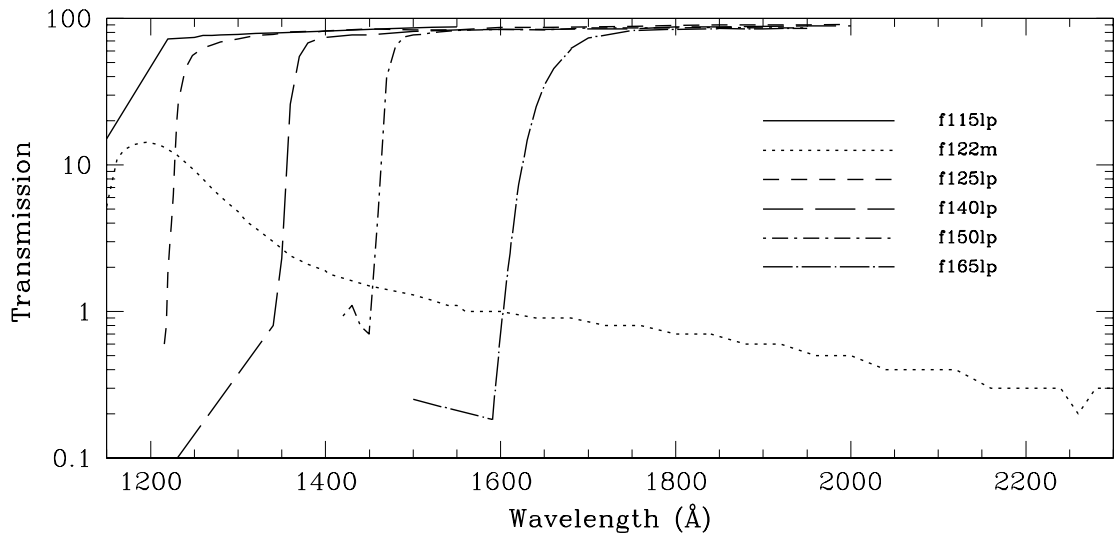
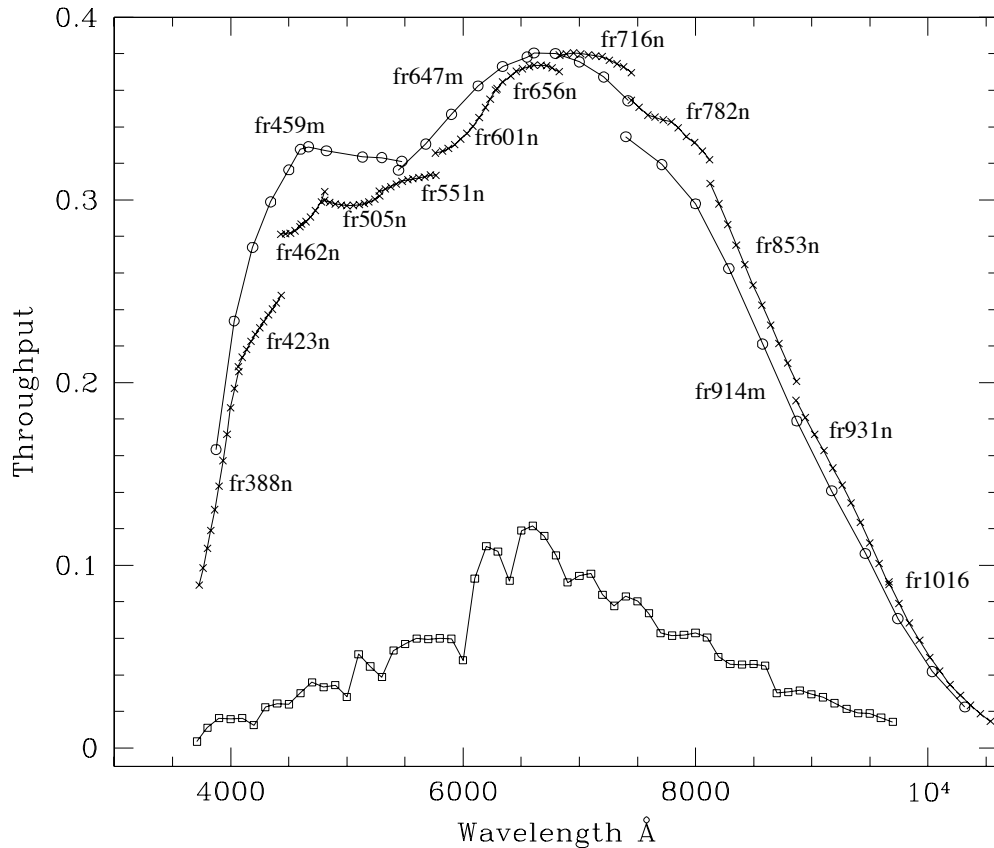


Figure 5.6: Comparison between the ACS and WFPC2 ramp filters.



The crosses and open circles are for the ACS narrow and medium band ramps. The open squares are for the 4 WFPC2 ramps. For each of the ACS ramps the peak throughput that was calculated for eleven central wavelength values is plotted. For the WFPC2 ramps, the peak throughput calculated every 100 Å within the field of view of any of the 4 chips, and a 0° filter rotation angle (as mapped in Figures 3.4 and 3.5 of the WFPC2 Instrument Handbook, version 3.0), are plotted.

5.2 Important Considerations for ACS Imaging

There are a few characteristics of ACS that should be taken into account when imaging with ACS:

- The HRC and WFC filters are housed in two filter wheels shared by both cameras. As a consequence, when a filter is chosen for the primary camera, the filter used in the parallel camera is not independently selectable.
- The ACS cameras are designed to be used with a single filter, and for this reason unfiltered imaging or imaging through two filters leads to significantly degraded imaging quality (particularly in the WFC) and is not normally used except for polarization observations, or bright

target acquisitions with the HRC. The polarizer filters were designed with a zero optical thickness so that they can and should be used with another filter.

- The geometric distortion of the WFC is significant and causes the projected pixel area to vary by $\pm 9\%$ over the field of view. This distortion affects both the photometric accuracy and the astrometric precision, and must be accounted for when the required accuracy is better than 10%.
- The ratio of in-band vs. out-of-band transmission for the ACS CCD UV filters is similar to that of WFPC2, once the two detector QE curves are taken into account (the red leak on ACS F330W is very small). This implies that the effect of filter red leaks needs to be calibrated for UV imaging of intrinsically red objects.
- The cosmic ray fluxes for HRC and WFC are comparable, respectively, to those of the STIS CCD and WFPC2. As with these instruments, typical imaging observations will need to be split or dithered for cosmic ray rejection.
- Section 4.3.5 provides further details and a recommendation that separate exposures with small dithers be considered as a means of helping to remove residual hot pixels.
- The large format of the WFC requires significantly more shifts to read out data compared to STIS or WFPC2. Therefore, the impact of decreasing charge transfer efficiency will be encountered earlier. Section 4.3.7 details current expectations.
- The default GAIN setting for WFC primary observations is GAIN=2. This allows for good sampling of the readout noise and allows one to reach the full well counts of WFC. For the HRC primary observations, the default gain is GAIN=2. To sample the detector full well depth, GAIN=4 is needed, but this results in modest undersampling of the readout noise. For HRC ACQ data, the default setting is GAIN=4. Users may select the GAIN they wish to use for their ACS observations by using the GAIN optional parameter in their Phase II proposal. However, not all GAIN settings are supported (see Section 7.6).
- At wavelengths longward of $\sim 8000 \text{ \AA}$, internal scattering in the HRC CCD produces an extended PSF halo. This should affect only a small number of observations since the WFC camera is normally preferred at these wavelengths. The WFC CCDs include a front-side metallization that eliminates the large angle, long wavelength halo problem for $\lambda < 9000 \text{ \AA}$. (For observations of red targets with the F850LP refer to Section 9.3.2).

- The ACS filter complement is not as rich as that in WFPC2. In particular, the Strömgren filter set and several narrow band filters available in WFPC2 (F375N, F390N, F437N, F469N, F487N, F588N, F631N, F656N, F673N, F953N) are not available on ACS. In general, these filters were not heavily used by the GO community. For most applications they can be replaced with the ACS medium and narrow ramps.

5.2.1 Optical Performance

Testing of the WFC and HRC cameras, following fine alignment activities on-orbit, has shown that the optical quality objectives of the cameras are met. The encircled energy values obtained from observations made in SMOV are given in Table 5.4.

Table 5.4: Encircled energy measurements for the ACS channels.

| Channel | Encircled energy | |
|---|------------------|---------------|
| | Center of field | Edge of field |
| WFC at 632.8 nm in 0.25 arcseconds diameter | 80.0% | 79.4% |
| HRC at 632.8 nm in 0.25 arcseconds diameter | 81.8% | 81.6% |
| SBC at 121.6 nm in 0.10 arcseconds diameter | 28% | --- |

5.2.2 Throughputs and Limiting Magnitudes

Figure 5.7 shows the throughput of the two unfiltered ACS CCD cameras: WFC and HRC. Superposed on this plot are unfiltered WFPC2 (WF4) and the clear STIS throughputs.

5.2.3 Limiting Magnitudes

Table 5.5 contains Johnson-Cousins V magnitudes for unreddened O5 V, A0 V, and G2 V stars, generated using the Exposure Time Calculator. WFC and HRC values used the parameters CR-SPLIT=2, GAIN=2, and a 0.2 arcsecond circular aperture. For the SBC, a 0.5 arcsecond circular aperture was used. An average sky background was used in these examples. However, limiting magnitudes are sensitive to the background levels; for instance, the magnitude of an A0 V in the WFC using the F606W filter changes by ± 0.4 magnitudes at the background extremes.

Figure 5.7: ACS CCD system throughputs + OTA versus those of STIS and WFPC2.

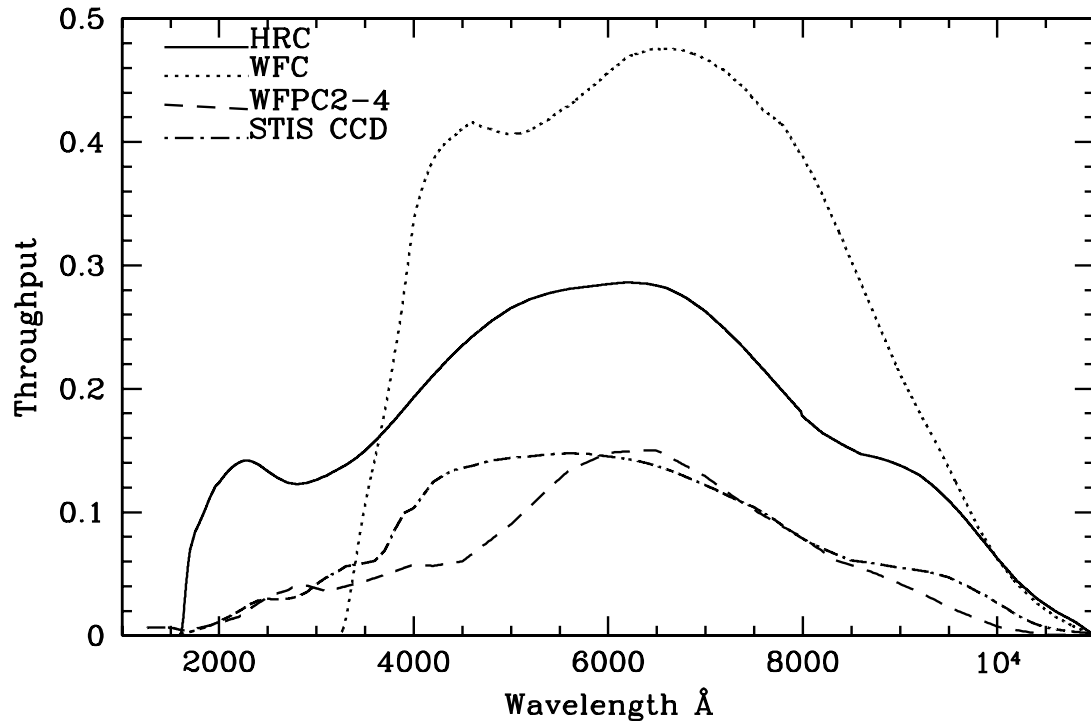


Table 5.5: V detection limits for ACS, HRC, and SBC direct imaging.

| Camera | Filter | V limit (S/N = 5, exposure time = 1 hour) | | |
|--------|--------|---|-------------|------------|
| | | O5 V (Kurucz model) | A0 V (Vega) | G2 V (Sun) |
| WFC | F606W | 27.8 | 27.8 | 28.0 |
| WFC | F814W | 26.7 | 27.0 | 27.7 |
| HRC | F330W | 26.8 | 24.8 | 24.1 |
| HRC | F606W | 27.3 | 27.3 | 27.5 |
| SBC | F125LP | 27.8 | 23.2 | 13.5 |

5.2.4 Signal-To-Noise Ratios

In Chapter 10, we present, for each imaging mode, plots of exposure time versus magnitude to achieve a desired signal-to-noise ratio. These plots, which are referenced in the individual imaging-mode sections below, are useful for getting an idea of the exposure time you need to accomplish your scientific objectives. More accurate estimates require the use of the ACS Exposure Time Calculator (<http://www.stsci.edu/hst/acs/software>).

5.2.5 Saturation

Both CCD and SBC imaging observations are subject to saturation at high total accumulated counts per pixel. For the CCDs, this is due either to the depth of the full well or to the 16 bit data format. For the SBC, this is due to the 16 bit format of the buffer memory (see Section 4.3.1 and Section 4.5.2).

5.3 Wide Field Optical CCD Imaging

The Wide Field Channel of ACS was designed primarily for high throughput observations at visible wavelengths. The use of protected silver mirror coatings, the small number of reflections, and the use of a red sensitive CCD have provided the high throughput required for this camera at the expense of a 3700 Å blue cutoff. The WFC detectors are two butted 2K by 4K thinned, backside-illuminated, SiTe CCDs with a red optimized coating and long- λ halo fix. The plate scale is 0.050 arcseconds per pixel, which provides a good compromise between adequately sampling the PSF and a wide field of view. The WFC PSF is critically sampled at 11,600 Å and undersampled by a factor 3 at the blue end of the WFC sensitivity range (3700 Å). We expect that it will be possible to achieve a final reconstructed FWHM of 0.100 to 0.140 arcseconds for well-dithered observations. Because the WFC PSF FWHM is largely dependent on the blurring caused by CCD charge diffusion, dithering will not be able to recover the full resolution of the optical system. See Section 7.4 for more discussion of how to use dithered observations to optimally sample the PSF.

The optical design of the camera introduces a two-component geometric distortion. The detectors themselves are at an angle with respect to the optical axis. This produces an 8% stretching of one pixel diagonal compared to the other. As a result, WFC pixels project on the sky as rhombuses rather than squares. These effects are purely geometrical and are routinely corrected in the ACS data reduction pipeline. The second component of geometric distortion is more complex. This distortion causes up to $\pm 9\%$ variation in effective pixel area and needs to be taken into account when doing accurate photometry or astrometry as the effective area of the detector pixels varies nonlinearly with field position.

5.3.1 Filter Set

WFPC2 and Johnson-Cousins filters

All of the most commonly used WFPC2 filters are included in the ACS filter set. In addition to a medium and a broad V band filter (F550M and F606W), there is a complete Johnson-Cousins *BVI* set (F435W, F555W, F814W).

Sloan Digital Sky Survey filters

The Sloan Digital Sky Survey (SDSS) *griz* filter set (F475W, F625W, F775W, F850LP) is designed to provide high throughput for the wavelengths of interest and excellent rejection of out-of-band wavelengths. The filters were designed to provide wide, non-overlapping filter bands that cover the entire range of CCD sensitivity from blue to near-IR wavelengths.

Narrow Band filters

The H α (F658N), [OIII] (F502N), and [NII] (F660N) narrow band filters are full-size, and can be used with both the WFC and HRC.

Ramp filters

ACS includes a complete set of ramp filters that provide full coverage of the WFC wavelength range at 2% and 9% bandwidth. Each ramp filter consists of three segments. The inner and outer filter segments can be used with the WFC only, while the central segments can be used by both WFC and HRC. Unlike the WFPC2, where the desired wavelength is achieved by offsetting the telescope, the wavelength of ACS ramps is selected by rotating the filter while the target is positioned in one of the pre-defined apertures. The monochromatic field of view of the ramp filters is approximately 40 by 80 arcseconds. Details of how to use the ramp filters are given in Section 7.7.2.

Polarizer filters

The WFC/HRC filter wheels contain polarizers with pass directions spaced by 60°, optimized for both the UV (POL0UV, POL60UV, and POL120UV) and the visible (POL0V, POL60V, and POL120V). All the polarizer filters are sized for the HRC field of view. They induce vignetting when used with the WFC, for which the FOV will be about 72 by 72 arcseconds. More information on the use of the polarizers is given in Chapter 6.

Grism and Prism

The CCD channels also have a grism (G800L) for use with both WFC and HRC from 5500 Å to 11,000 Å, and a prism (PR200L) for use with the HRC from 1600 Å to 3500 Å. These are described more fully in Chapter 6.

5.4 High-Resolution Optical and UV Imaging

The High Resolution Channel of ACS is the prime ACS camera for near-UV imaging. HRC provides high throughput in the blue and a better sampling of the PSF than either the WFC or other CCD cameras on HST. The HRC pixel size critically samples the PSF at 6300 \AA and is undersampled by a factor 3.0 at the blue end of its sensitivity range (2000 \AA). With this capability, the HRC functionally replaces the Faint Object Camera as the instrument able to critically sample the PSF in the V band. For this reason, most of the usage of HRC will be for UV and blue imaging. HRC can also be convenient for imaging in the red when the PSF sampling is important. As an example, better PSF sampling is probably important for accurate stellar photometry in crowded fields. We expect that the photometric accuracy achievable by the HRC will be higher than that achievable with the WFC. Well-dithered observations with the HRC should lead to a reconstructed PSF FWHM of 0.03 arcsec at $\sim 4000 \text{ \AA}$, increasing towards longer wavelengths. HRC also includes a coronagraph that is discussed in Chapter 6. The HRC CCD presents a long wavelength halo problem similar to the STIS CCD since the front-side metallization correcting the halo problem for the WFC CCDs was implemented only after the HRC CCD had been procured. Although most of the HRC imaging is likely to occur in the UV, users should be cautioned to take into account the effects of the long wavelength halo when using the HRC in combination with near-IR filters (See Section 5.6.5).

5.4.1 Filter Set

The HRC-specific filters are mostly UV and blue. The set includes UV and visible polarizers (discussed in Chapter 6), a prism (PR200L, discussed in Chapter 6), three medium-broad UV filters (F330W, F250W, and F220W) and two narrow band filters (F344N and F892N). Use of the UV filters with the WFC is not supported because of the uncertainty of the WFC silver coating transmission below 4000 \AA .

All broad, medium and narrow band WFC filters can be used with the HRC whenever a better PSF sampling is required. In general, the throughput of WFC is higher than that of HRC where their sensitivity overlaps. Only some of the WFC ramp filters can be used with the HRC since only the middle ramp segment overlaps with the HRC FOV. In particular, HRC can use the FR459M and FR914M broad ramps, and the FR505N [OIII], FR388N [OII], and FR656N ($H\alpha$) narrow ramps.

5.4.2 Multiple Electron Events

Like the STIS CCD but unlike WFPC2, the HRC CCD is directly sensitive to UV photons and for this reason is much more effective in detecting them. However, whenever a detector has non-negligible sensitivity over more than a factor two in wavelength, it becomes energetically possible for a UV photon to generate more than one electron and be counted more than once. This effect has been seen for STIS and also during the ground testing of the HRC detector. The effect is only important shortward of 3200 Å, and reaches a magnitude of approximately 1.7 e⁻/photon at 2000 Å. Multiple counting of photons has to be taken into account when estimating the detector QE and the noise level of a UV observation since multiple photons cause a distortion in the Poisson distribution of electrons.

5.4.3 Red Leaks

When designing a UV filter, a high suppression of off-band transmission, particularly in the red, has to be traded with overall in-band transmission. The very high blue quantum efficiency of the HRC compared to WFPC2 makes it possible to obtain an overall red leak suppression comparable to that of the WFPC2 while using much higher transmission filters. The ratio of in-band versus total flux is given in Table 5.6 for a few UV and blue HRC filters, where the cutoff point between in-band and out-of-band flux is defined as the filter's 1% transmission point. The same ratio is also listed for the equivalent filters in WFPC2. Clearly, red leaks are not a problem for F330W, F435W, and F475W. Red leaks are more important for F250W and F220W. In particular, accurate UV photometry of objects with the spectrum of an M star will require correction for the redleak in F250W and will be essentially impossible in F220W. For the latter filter a redleak correction will also be necessary for K and G stars.

Table 5.6: In-band flux as a percentage of the total flux.

| Stellar type | WFPC2 F218W | HRC F220W | WFPC2 F255W | HRC F250W | WFPC2 F300W | HRC F330W | WFPC2 F439W | HRC F435W | WFPC2 F450W | HRC F475W |
|--------------|-------------|-----------|-------------|-----------|-------------|-----------|-------------|-----------|-------------|-----------|
| O5 V | 99.8 | 99.8 | 99.6 | 99.7 | 99.9 | 99.9 | 99.9 | 99.9 | 99.9 | 99.9 |
| B1 V | 99.7 | 99.7 | 99.6 | 99.7 | 99.9 | 99.9 | 99.9 | 99.9 | 99.9 | 99.9 |
| A1 V | 99.4 | 99.1 | 99.2 | 99.3 | 99.2 | 99.9 | 99.9 | 99.9 | 99.9 | 99.9 |
| F0 V | 98.5 | 97.8 | 98.8 | 99.0 | 98.8 | 99.9 | 99.9 | 99.9 | 99.9 | 99.9 |
| G2 V | 92.5 | 90.2 | 97.4 | 98.4 | 97.4 | 99.9 | 99.9 | 99.9 | 99.8 | 99.9 |
| K0 V | 71.7 | 69.6 | 95.0 | 97.3 | 95.0 | 99.9 | 99.9 | 99.9 | 99.8 | 99.9 |
| M2 V | 0.03 | 2.5 | 45.5 | 71.9 | 45.4 | 99.9 | 99.9 | 99.9 | 99.6 | 99.9 |

5.5 Ultraviolet Imaging with the SBC

The Solar Blind Channel is the ACS camera optimized for UV imaging. The SBC uses the same optical train as the HRC and is comparable in performance to the FUV MAMA of STIS. The use of the repeller wire increases the quantum efficiency of the detector by $\sim 30\%$, but adds a halo to the PSF. Bright object limits are discussed in detail in Section 7.2.

5.5.1 Filter Set

Several filters are available for use with the SBC, including a Lyman α narrow band filter (F122M), a long pass quartz filter (F150LP), MgF₂ filter (F115LP), and a CaF₂ filter (F125LP). The SBC also includes two additional long pass filters (F140LP and F165LP) as well as prisms (discussed in Chapter 6). A list of filters is given in Table 5.3

5.5.2 Red Leaks

The visible light rejection of the SBC is excellent, but users should be aware that stars of solar type or later will have a significant fraction of the detected flux coming from outside the nominal wavelength range of the detector. Details are given below, in Table 5.7.

Table 5.7: Visible-light rejection of the SBC F115LP imaging mode.

| Stellar type | Percentage of all detected photons which have $\lambda < 1800 \text{ \AA}$ | Percentage of all detected photons which have $\lambda < 3000 \text{ \AA}$ |
|--------------|--|--|
| O5 | 99.5 | 100 |
| B1 V | 99.4 | 100 |
| A0 V | 98.1 | 100 |
| G0 V | 72.7 | 99.8 |
| K0 V | 35.1 | 94.4 |

5.5.3 SBC Imaging Filter Shifts

The SBC focal surface, like that of the HRC, is tilted significantly with respect to the chief ray. Because the MAMA detector is a STIS spare, its window is approximately parallel to the MCP surface and the whole detector must tilt to achieve good focus over the field. Because the window is therefore tilted, "lateral color" is introduced, which would result in dispersion-induced degradation of the PSF, so the filters are canted in the

opposite direction to that of the window to ameliorate the color. The filter thickness is matched to the mean index of refraction over its bandpass to maintain focus. These result in unavoidable image location offsets between filters. In contrast, the WFC and HRC filters and windows are normal to the chief ray and the detector surfaces are tilted within their housings to match the focal surface tilt. In Table 5.8, we list the shifts for each SBC imaging filter with respect to the F115LP filter.

Table 5.8: Shifts between SBC imaging filters.

| Spectral Element | Offset (pixels) in the x,y directions |
|------------------|---------------------------------------|
| F115LP | 0,0 |
| F122M | 0,0 |
| F125LP | -5,15 |
| F140LP | -7,21 |
| F150LP | -3,11 |
| F165LP | -4,12 |

5.6 ACS Point Spread Functions

The ACS point spread function has been studied in ground test measurements, and by using on-orbit data and models generated by the **Tiny TIM** software (<http://www.stsci.edu/software/tinytim/tinytim.html>) developed by J. Krist and R. Hook. As with other HST instruments, the ACS point spread function is affected by both optical aberrations and geometric distortions. Point sources imaged with WFC and HRC experience blurring due to charge diffusion into adjacent pixels because of CCD subpixel variations, which reduces the limiting magnitudes that can be reached by WFC/HRC. The SBC PSF and the long-wavelength HRC PSF are also affected by a halo produced by the detectors themselves.

5.6.1 CCD Pixel Response Function

The sharpness of the CCD PSF is somewhat degraded by charge diffusion into adjacent pixels. The effect is usually described in terms of the pixel response function (PRF), which gives the distribution of flux from within the pixel into adjacent pixels. Charge diffusion results in ~ 0.5 magnitude loss in the WFC limiting magnitude at short wavelengths (the worst case). At longer wavelengths and at all wavelengths for the HRC

the reduction in the limiting magnitude is ~ 0.2 magnitudes or less. Due to variations in the CCD thickness, charge diffusion is not constant over the field of view. At different wavelengths, the CCD pixel response functions can be represented by the following kernels (for the center of the field):

Figure 5.8: Kernels representing CCD pixel functions for HRC and WFC.

$$K_{HRC} = \begin{bmatrix} 0.02 & 0.07 & 0.02 \\ 0.07 & 0.64 & 0.07 \\ 0.02 & 0.07 & 0.02 \end{bmatrix}, \quad K_{WFC} = \begin{bmatrix} 0.04 & 0.11 & 0.04 \\ 0.11 & 0.40 & 0.11 \\ 0.04 & 0.11 & 0.04 \end{bmatrix}$$

at $\lambda = 4000 \text{ \AA}$,

$$K_{HRC} = \begin{bmatrix} 0.02 & 0.06 & 0.02 \\ 0.06 & 0.68 & 0.06 \\ 0.02 & 0.06 & 0.02 \end{bmatrix}, \quad K_{WFC} = \begin{bmatrix} 0.03 & 0.10 & 0.03 \\ 0.10 & 0.48 & 0.10 \\ 0.03 & 0.10 & 0.03 \end{bmatrix}$$

at $\lambda = 5500 \text{ \AA}$, and

$$K_{HRC} = \begin{bmatrix} 0.02 & 0.04 & 0.02 \\ 0.04 & 0.76 & 0.04 \\ 0.02 & 0.04 & 0.02 \end{bmatrix}, \quad K_{WFC} = \begin{bmatrix} 0.02 & 0.07 & 0.02 \\ 0.07 & 0.64 & 0.07 \\ 0.02 & 0.07 & 0.02 \end{bmatrix}$$

at $\lambda = 8000 \text{ \AA}$.

More details on ACS CCD charge diffusion are given in [ACS ISR 2003-06](#).

5.6.2 Model PSFs

Table 5.9 and Table 5.10 give ACS model PSFs in the central 5×5 pixel region in two wavelength bands (filters). Numbers listed are the fraction of the total energy received in each pixel. The models have been generated using **Tiny TIM**, taking into account the HST optical aberrations and obscurations as well as the CCD pixel response function. Field dependent geometrical distortions are included. The real PSF will also differ from the model because of the jitter in the HST pointing, HST focus variation (focus breathing), and other instrumental effects, some of which are briefly discussed below. The SBC PSF is shown Figure 5.10.

Table 5.9: Model ACS CCD PSFs.

| WFC model PSF, filter F435W | | | | | WFC model PSF, filter F814W | | | | |
|-----------------------------|------|------|------|------|-----------------------------|------|------|------|------|
| 0.00 | 0.01 | 0.01 | 0.01 | 0.00 | 0.01 | 0.01 | 0.02 | 0.01 | 0.01 |
| 0.01 | 0.04 | 0.07 | 0.05 | 0.02 | 0.01 | 0.03 | 0.07 | 0.03 | 0.02 |
| 0.02 | 0.08 | 0.17 | 0.08 | 0.02 | 0.02 | 0.07 | 0.18 | 0.07 | 0.02 |
| 0.01 | 0.04 | 0.08 | 0.04 | 0.01 | 0.01 | 0.03 | 0.07 | 0.03 | 0.01 |
| 0.00 | 0.01 | 0.02 | 0.01 | 0.00 | 0.01 | 0.02 | 0.02 | 0.01 | 0.00 |
| HRC model PSF, filter F435W | | | | | HRC model PSF, filter F814W | | | | |
| 0.01 | 0.01 | 0.01 | 0.01 | 0.01 | 0.00 | 0.01 | 0.02 | 0.01 | 0.00 |
| 0.02 | 0.03 | 0.06 | 0.03 | 0.01 | 0.01 | 0.04 | 0.05 | 0.04 | 0.01 |
| 0.01 | 0.06 | 0.16 | 0.06 | 0.01 | 0.02 | 0.05 | 0.08 | 0.05 | 0.02 |
| 0.01 | 0.03 | 0.07 | 0.03 | 0.01 | 0.01 | 0.04 | 0.05 | 0.04 | 0.01 |
| 0.01 | 0.02 | 0.01 | 0.01 | 0.01 | 0.00 | 0.01 | 0.02 | 0.01 | 0.00 |

Table 5.10: Model ACS SBC PSFs.

| SBC PSF at 120 nm | | | | | SBC PSF at 160 nm | | | | |
|-------------------|------|------|------|-------|-------------------|-------|-------|-------|-------|
| <0.01 | 0.01 | 0.01 | 0.01 | <0.01 | <0.01 | <0.01 | <0.01 | <0.01 | <0.01 |
| 0.01 | 0.02 | 0.03 | 0.02 | 0.01 | <0.01 | 0.02 | 0.04 | 0.02 | <0.01 |
| 0.01 | 0.03 | 0.15 | 0.03 | 0.01 | <0.01 | 0.04 | 0.20 | 0.04 | <0.01 |
| 0.01 | 0.02 | 0.03 | 0.02 | 0.01 | <0.01 | 0.02 | 0.04 | 0.02 | <0.01 |
| <0.01 | 0.01 | 0.01 | 0.01 | <0.01 | <0.01 | <0.01 | <0.01 | <0.01 | <0.01 |

5.6.3 Encircled Energy

In general, the ACS channels encircled energy distribution has been found to be within the original instrument specifications. Figure 5.9 and Figure 5.10 show the ACS encircled energy curves derived from on-orbit images. Tabulated values of the encircled energy for most filters are available in Sirianni et al. (2005, *astroph/0507614*) (<http://adcam.pha.jhu.edu/instrument/photometry/sirianni.pdf>).

5.6.4 Geometric Distortions

Geometric distortions produce a significant impact on the shape of the PSF in all three of the ACS channels, as can readily be seen in Figure 5.11 and Figure 5.12, which display WFC and HRC PSF images. The log stretch enhances the spider diffraction patterns, which the distortion renders non-perpendicular, and the outer Airy rings, which appear elliptical. The distortion owes primarily to the tilt of the focal surface to the chief ray at the large OTA field angles of the ACS apertures. The linear, field-independent approximation for the WFC produces a difference in plate scale of about 8% between the two diagonals of the field and, in the HRC and SBC, about a 16.5% difference in scale between orthogonal directions rotated about 20° from the aperture edges. Field-dependent distortions, measured as actual vs. predicted distances from field center, amount to about 2% peak in the WFC and about 1% in the HRC and SBC.

The distortions render the pixels, as projected on the sky, trapezoidal in shape and their area varies over the field by about 19% and 3.5% in the WFC and HRC/SBC, respectively. These variations have significant ramifications concerning appropriate techniques for flat-fielding and photometric calibration, especially when complicated by resampling in order to combine dithered image sets. Related issues are the manner in which the halation effects of the HRC and SBC detectors are removed and the treatment of spectra from the prisms and grism, which are not subject to the same distortion effects.

More details concerning geometric distortions in ACS can be found in [ACS ISR 2002-02](#) and [ACS ISR 2004-15](#). An introduction to *calacs*, and to *multidrizzle* which applies corrections for geometric distortion, is available on-line at <http://www.stsci.edu/hst/acs/analysis/multidrizzle>.

Figure 5.9: Encircled energy for the CCD channels.

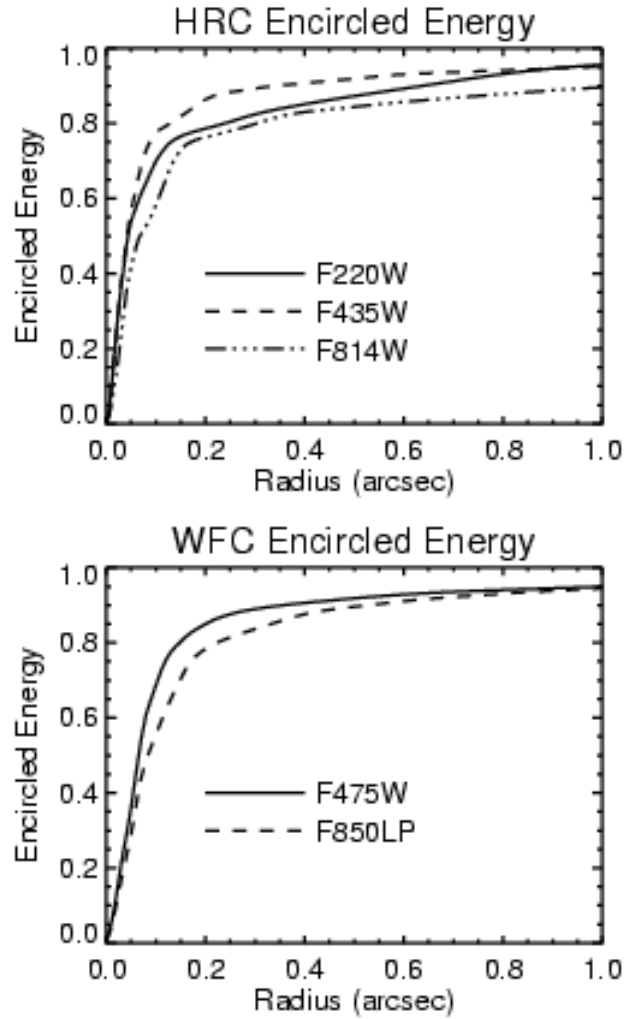


Figure 5.10: Encircled energy for the SBC.

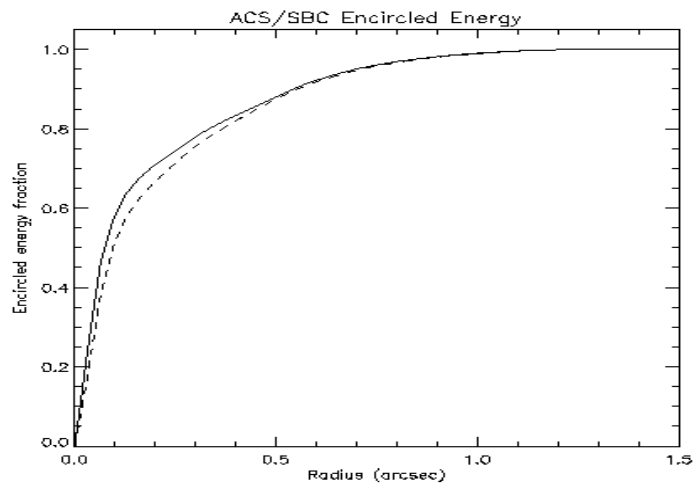


Figure 5.11: ACS WFC PSF - F625W.

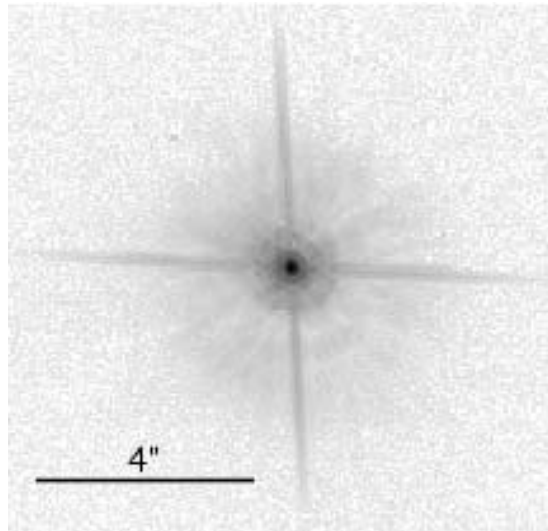
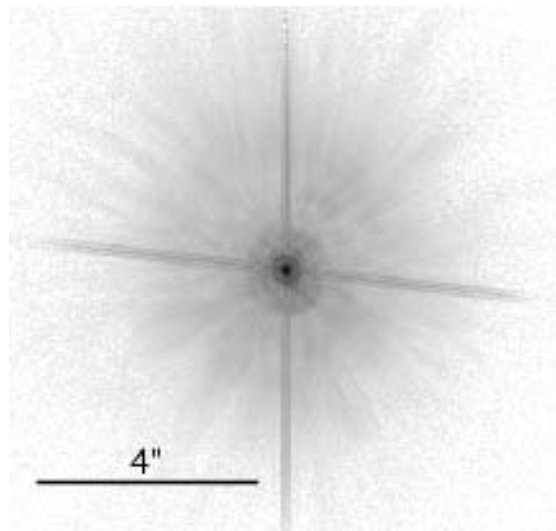


Figure 5.12: ACS HRC PSF - F625W.



5.6.5 PSFs at Red Wavelengths and the UV

The CCDs used in the HRC and WFC suffer from a halo that is caused by very red photons passing through the device and being scattered back into the detector by the mounting substrate. This creates a large halo in HRC images beyond 7000 Å and WFC images past 9000 Å. At 8000 Å in the HRC, the halo contains about 10% of the light. At 10,000 Å, it contains about 30% and increases the surface brightness of the PSF wings by over an order of magnitude, overwhelming the PSF diffraction rings and spikes. A discussion of this may be found in Gilliland & Riess, (2002) *HST Calibration Workshop* at:

http://www.stsci.edu/hst/HST_overview/documents/calworkshop/workshop2002/CW2002_Papers/CW02_gilliland.

In the F850LP filter, in particular, extremely red stars show a progressive loss of flux in small to moderate sized apertures as a function of color. A paper by Sirianni et al. (2005, *astroph/0507614*, available at:

<http://adcam.pha.jhu.edu/instrument/photometry/sirianni.pdf>

The paper provides a detailed recipe to correct for this effect. This halo effect is only partially treated by the [Exposure Time Calculator](#). Observers can use *synphot* (see Section 9.3.2) to accurately calculate the photometry of red sources in the SDSS z-filter.

Long wavelength photons that pass through the CCD can also be scattered by the electrode structure on the back side of the device. This creates two spikes that extend roughly parallel to the x-axis. These spikes are seen at wavelengths longer than 9500 Å in both the HRC and WFC (see Figure 5.13 and Figure 5.14).

Figure 5.13: ACS WFC PSFs (10" x10"). FR914M images are saturated.

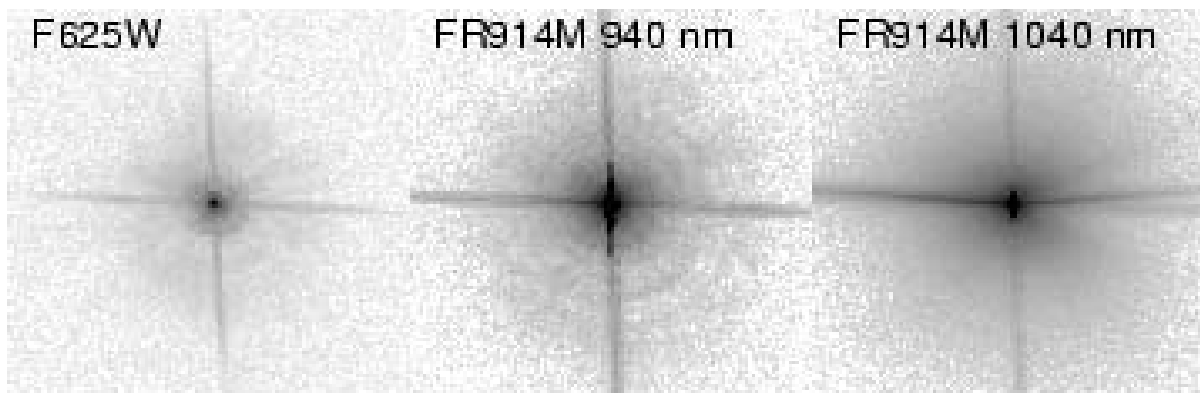
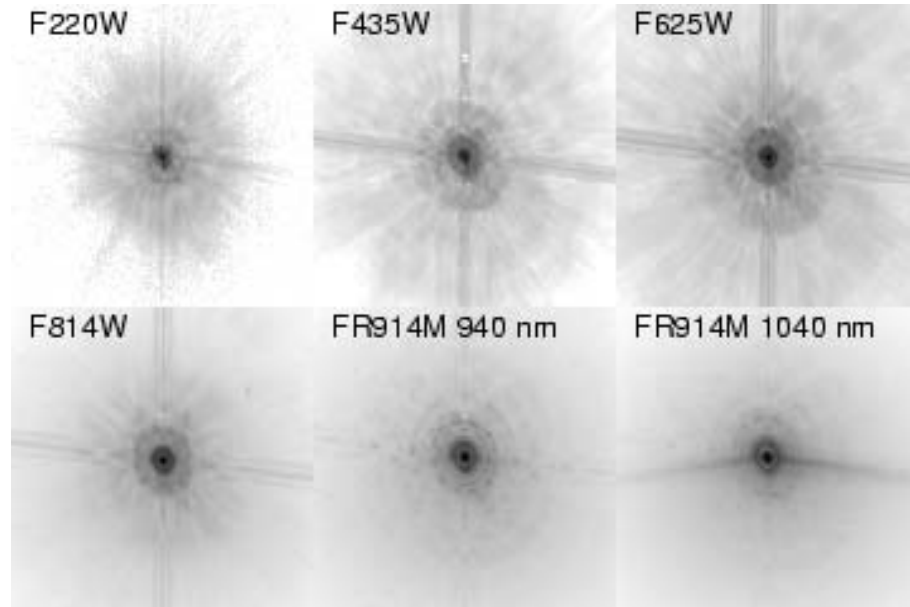


Figure 5.14: ACS HRC PSFs (3.25" x3.25").



In the UV the core of the PSF becomes rather asymmetrical due to midfrequency optical surface errors. In the SBC, a halo is created by charge migration at the microchannel plate surface. This effect, seen previously in STIS MAMA images, broadens the PSF core and redistributes a small portion of flux into a broad halo that can be approximated by a Gaussian with FWHM ~ 20 pixels. The peak flux for a point source centered on a pixel is reduced by 30% to 40% depending on wavelength.

The encircled energy curves presented in this handbook and incorporated into the ETC include all of the scattering effects discussed here.

5.6.6 Residual Aberrations

Residual aberration levels at the center of the field in each camera are $1/30$ wave (HRC) and $1/20$ wave (WFC) rms at 5500\AA (excluding defocus). Coma and astigmatism are minimized at the field center of each camera. The ACS PSF varies far less over the field of view than those of WFPC2 and STIS. WFPC2 especially suffers from a variable obscuration pattern that significantly alters the PSF structure depending on field position. Lacking the additional obscurations present in WFPC2, ACS PSF variations are instead due to changes in aberrations and charge diffusion.

At the extreme corners of the WFC field, increased astigmatism slightly elongates the PSF core. The axis of elongation rotates by 90° if the system passes through focus due to breathing. This may affect ellipticity measurements of small galaxies with bright cores at the field edges. Focus

variations in the WFC, which alter the amount of light in the peak, are largely due to detector surface height irregularities and amount to the equivalent of 5 microns of breathing (1/18 wave rms). The largest focus offset is along the gap between the two CCDs. Variations in the width of the PSF core are dominated by changes in CCD charge diffusion, which is dependent on the thickness of the detector (12 to 17 microns for the WFC). The PSF FWHM in F550M, for example, can vary by 20% (0.10 to 0.13 arcseconds) over the field.

The PSFs in the HRC and SBC are reasonably constant over their fields. The HRC FWHM is 0.060 to 0.073 arcseconds in F550M. More details on ACS PSF field variations are provided in [ACS ISR 2003-06](#). The [Tiny Tim](#) PSF simulator includes field dependent aberrations and charge diffusion and may be used to estimate the impact of these variations.



CHAPTER 6:

Polarimetry, Coronagraphy and Prism/Grism Spectroscopy

In this chapter. . .

| |
|------------------------------------|
| 6.1 Polarimetry / 75 |
| 6.2 Coronagraphy / 81 |
| 6.3 Grism/Prism Spectroscopy / 101 |

6.1 Polarimetry

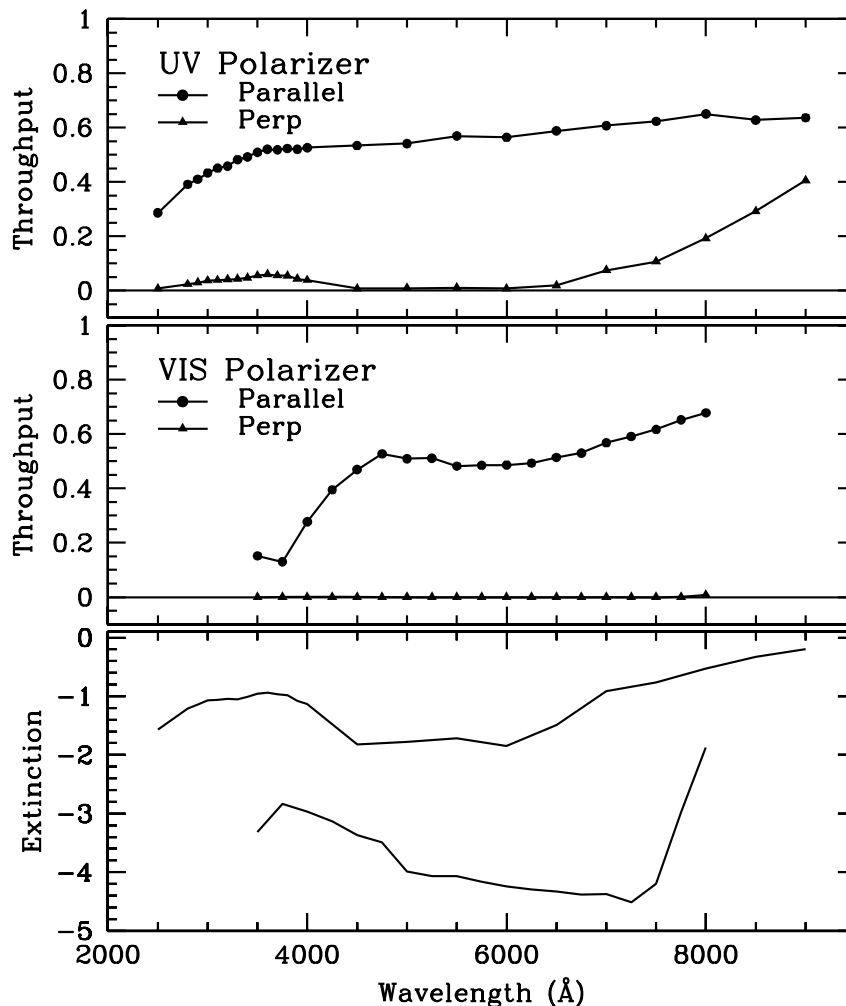
The ACS has an imaging polarimetric capability. Polarization observations require a minimum of three images taken using polarizing optics with different polarization characteristics in order to solve for the source polarization unknowns (polarization degree, position angle, and total intensity). To do this, ACS offers two sets of polarizers, one optimized for the blue (POLUV) and the other for the red (POLV). These polarizers can be used in combination with most of the ACS filters (see Table 6.2) allowing polarization data to be obtained in both the continuum and in line emission; and to perform rudimentary spectropolarimetry by using the polarizers in conjunction with the dispersing elements. (Due to the large number of possibilities in combination with ramp and dispersing elements, and heavy calibration overheads, observers wishing to use those modes should request additional calibration observations). For normal imaging polarization observations, the target remains essentially at rest on the

detector with a suitable filter in beam, and an image is obtained with each of the appropriate polarizing elements in turn. The intensity changes between the resulting images provide the polarization information.

Each set of polarizers comprises three individual polarizing filters with relative position angles 0° , 60° , and 120° . The polarizers are designed as aplanatic optical elements and are coated with “Polacoat 105UV” for the blue optimized set, and HN32 polaroid for the red set. The blue/near-UV optimized set is also effective all through the visible region, giving a useful operational range from approximately 2000 \AA to 8500 \AA . The second set is optimized for the visible region of the spectrum and is fully effective from 4500 \AA to about 7500 \AA .

The relative performance of the UV-optimized versus the visible optimized polarizers is shown in Figure 6.1.

Figure 6.1: Throughput and rejection of the ACS polarizers.



In the top two boxes, the upper curve is the parallel transmission, while the lower curve is the perpendicular transmission. The bottom panel shows the logarithm of the ratio of perpendicular to parallel transmission.

The visible polarizers clearly provide superior rejection for science in the 4500 Å to 7500 Å bandpass, while the UV optimized polarizers deliver lower overall rejection across a wider range from 2000 Å to 7500 Å. While performance of the polarizers begins to degrade at wavelengths longer than about 7500 Å, useful observations should still be achievable to approximately 8500 Å in the red. In this case, allowance for imperfect rejection of orthogonally polarized light should be made at the analysis stage.

Imperfections in the flat fields of the POLVIS polarizer set have been found which may limit the optimal field of view somewhat. Potential users are encouraged to check [ACS ISR 2005-10](#) the STScI [ACS Web site](#) for the latest information.

To first approximation, the ACS polarizers can be treated as three essentially perfect polarizers. The Stokes parameters (I, Q, U) in the most straightforward case of three images obtained with three perfect polarizers at 60° relative orientation, can be computed using simple arithmetic. Using *im1*, *im2*, and *im3* to represent the images taken through the polarizers POL0, POL60, and POL120 respectively, the Stokes parameters are as follows:

$$Q = \frac{2}{3}(2im1 - im2 - im3)$$

$$U = \frac{2}{\sqrt{3}}(im3 - im2)$$

$$I = \frac{2}{3}(im1 + im2 + im3)$$

These values can be converted to the degree of polarization P and the polarization angle θ , measured counterclockwise from the x axis as follows:

$$P = \frac{\sqrt{Q^2 + U^2}}{I}$$

$$\theta = \frac{1}{2}\tan^{-1}(U/Q)$$

A more detailed analysis, including allowance for imperfections in the polarizers may be found in Sparks & Axon, 1999 *PASP*, **111**, 1298. They find that the important parameter in experiment design is the product of expected polarization degree and signal-to-noise. A good approximation for the case of three perfect polarizers oriented at the optimal 60° relative

position angles (as in ACS) is that the error on the polarization degree P (which lies in the range 0 for unpolarized to 1 for fully polarized) is just the inverse of the signal-to-noise per image. Specifically, they found

$$\log\left(\frac{\sigma_P}{P}\right) = -0.102 - 0.9898 \log(P \langle S/N \rangle_i)$$

where $\langle S/N \rangle_i$ is the signal to noise of the i^{th} image; and

$$\log \sigma_\theta = 1.514 - 1.068 \log(P \langle S/N \rangle_i)$$

The above discussion is for ideal polarizers with no instrumental polarization. Of course, the reality is that the polarizer filters, especially the UV polarizer, has significant leakage of cross-polarized light. The instrumental polarization of the HRC ranges from a minimum of 4% in the red to 14% in the far-UV, while that of the WFC is $\sim 2\%$ (see [ACS ISR 2004-09](#)). Other effects, such as phase retardance in the mirrors, may be significant as well. Please consult the *ACS Data Handbook* (http://www.stsci.edu/hst/acs/documents/handbooks/DataHandbookv4/ACS_longdhbcover.html), STSci Web pages, and ISRs (<http://www.stsci.edu/hst/acs/documents/isrs>) for more detailed information.

The implementation of the ACS polarizers is designed for ease of use. The observer merely selects the camera (either HRC or WFC) and the spectral filter, and then takes images stepping through the three filters of either the VIS set (POL0V, POL60V, POL120V) or the UV set (POL0UV, POL60UV, POL120UV). Once the camera and polarizer are specified, the scheduling system automatically generates slews to place the target in the optimal region of the field of view.

Since the ACS near-UV and visible filter complement is split between two filter wheels, there are restrictions on which filters the polarizer sets can be combined with. The choices available were determined by the relative performance of the polarizers and the near-UV limitations of the WFC resulting from the silver mirror coatings.

The near-UV optimized polarizers are mounted on Filter Wheel 1 and may be crossed with the near-UV filter complement, which are mounted on Filter Wheel 2. The visible optimized polarizers are mounted on Filter Wheel 2 and can be crossed with filters on Filter Wheel 1, namely the primary broadband filters, and discrete narrowband filters $H\alpha$, [OII], and their continuum filters. Due to the calibration overhead required, we do not plan to support the use of ramp filters with either polarizer set. GOs are required to include calibration observations if they plan to use the ramp filters with the polarizers.

The polarizer sets are designed for use on the HRC where they offer a full unvignetted field of view, 29×26 arcseconds with any of the allowable filter and coronagraph combinations including those ramps and

spectroscopic elements that may also be used on the HRC (although see above re. additional calibrations).

The same allowable combinations, either UV or visible optimized, may also be used on the WFC where an unvignetted field of view of diameter 70 arcseconds is obtained. This does not fill the field of view of the WFC due to the small size of the polarizing filters. However, it does offer an area approximately five times larger than that obtained on the HRC. In order to avoid the gap between the WFC CCDs, and to optimize the readout noise and CTE effects, the scheduling system will automatically slew the target to roughly pixel (3096,1024) on the WFC1 CCD whenever the WFC aperture is selected in conjunction with one of the polarizers. Also, to reduce camera overhead times, only a 2048 x 2048 subimage centered on the target location will be readout from WFC1 (see Table 6.1).

Occasionally observers will ask to obtain non-polarized images at the same physical location on the detector as their polarized images. This is straightforward for the HRC; one merely takes the exposure without the polarizer filter. However, for the WFC it is more complicated because specifying WFC together with a polarizer automatically invokes a large slew, whereas no slew is performed when the polarizer filter is omitted. To obtain a non-polarizer image at the same physical detector location as the polarizer image in the WFC, one needs to specify the aperture as WFC1-2K instead of WFC (see Table 6.1).

Table 6.1: Examples of polarizer and non-polarizer exposures in a Phase II proposal.

| Aperture | Filters | Comment |
|----------|----------------|---|
| HRC | F606W, POL0V | 1024 x 1024 image centered at usual HRC aperture. |
| HRC | F606W, POL60V | Same but with POL60V. |
| HRC | F606W, POL120V | Same but with POL120V. |
| HRC | F606W | Non-polarizer image centered at same detector location as polarizer exposure. |
| WFC | F606W, POL0V | Target automatically placed at WFC1 pixel (3096,1024); 2048 x 2048 image. |
| WFC | F606W, POL60V | Same but with POL60V. |
| WFC | F606W, POL120V | Same but with POL120V. |
| WFC1-2K | F606W | Non-polarizer image at same detector location. Target at WFC1 pixel (3096,1024); 2048 x 2048 image. |

Table 6.2: Filters that can be used in conjunction with the ACS polarizers.

| Polarizer set | Filters | Filter comments |
|---------------|---------|-----------------|
| POL0UV | F220W | HRC NUV short |
| POL60UV | F250W | HRC NUV long |
| POL120UV | F330W | HRC U |
| | F435W | Johnson B |
| | F814W | Broad I |
| POL0V | F475W | SDSS g |
| POL60V | F606W | Johnson V |
| POL120V | F625W | SDSS r |
| | F658N | H α |
| | F775W | SDSS i |

The filters specified in Table 6.2 are those that we expect users to choose for their polarization observations. We will calibrate the most popular of these filters. Filter combinations not on this list will most probably not be calibrated, so potential users who have a strong need for such a polarizer/filter combination should include any necessary calibrations in their proposals.

We anticipate that the most accurate polarization observations will be obtained in the visible band (i.e., F606W) with the HRC and the visible polarizers. This mode has the advantages of a very high rejection of perpendicular polarization, and known mirror coatings with readily modeled properties. The WFC may be capable of similar accuracy to the HRC; however, its proprietary mirror coatings will make modeling of the polarization properties, and hence calibration, much more difficult (e.g., unknown phase retardance effects in the WFC IM3 mirror are a concern).

Polarimetry in the UV will be more challenging for a number of reasons. The UV polarizer has relatively poor rejection in the UV, and the instrumental polarization of the HRC, which is 4% to 7% in the visible, rises to 8% to 9% in the UV, and reaches 14% at 2200 Å (see [ACS ISR 2004-09](#)). Far-UV polarimetry will be especially challenging since the polarizer properties were not well-characterized shortwards of 2800 Å, and appear to change rapidly with wavelength. Moreover, the low UV transmission of the UV polarizer, and the poor polarization rejection in the far-red, work together to exacerbate red leaks which are normally seen in the far-UV spectral filters.

The polarizer filters contribute a weak geometric distortion which rises to about 0.3 pixels near the edges of the HRC field-of-view. This is caused by a weak positive lens in the polarizers, which is needed to maintain proper focus when multiple filters are in the beam. In addition, the visible polarizer has a weak ripple structure which is related to manufacture of its polaroid material; this contributes an additional ± 0.3 pixel distortion with a very complex structure (see [ACS ISR 2004-10](#) and [ACS ISR 2004-11](#)). All these geometric effects are correctable with the drizzle software. However,

astrometry will likely be less accurate in the polarizers due to residual errors and imperfect corrections.

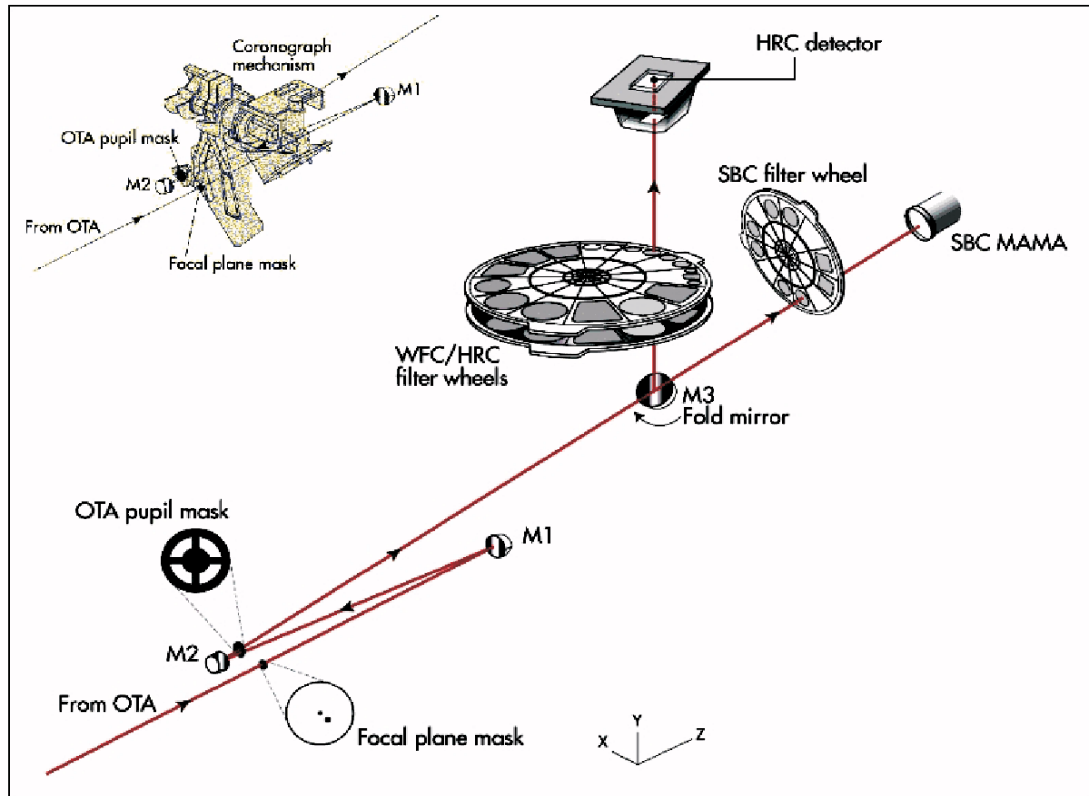
Bubbles in the Visible Polarizers

The POL0V and POL60V filters contain bubbles which impact the PSF and flat fields. These bubbles are far out of focus, and hence appear as large patterns (400 pixels diameter in WFC, 370 pixels in HRC) of concentric bright and dark rings, and streaks in the flats. The worst case is the HRC in the POL60V filter, where the amplitude reaches $\pm 4\%$ in the flats; the affected region for this case is roughly centered at pixel (835,430). Other combinations involving the POL0V filter or the WFC show more minor effects, with amplitudes typically $\pm 1\%$. Observers requiring precision polarimetry would do well to avoid these regions of the field of view. While the polarizer flats attempt to correct these features (see [ACS ISR 2005-10](#)), the corrections are likely to be imperfect and depend somewhat on the illumination provided by the target (i.e., stellar vs. extended target, etc.). The locations of these features and their effects can be discerned more accurately by examining the "pfl" flats for the respective spectral filter crossed with the visual polarizers.

6.2 Coronagraphy

The ACS High Resolution Camera has a user-selectable coronagraphic mode for the imaging of faint objects (circumstellar disks, substellar companions) near bright point sources (stars or luminous quasar nuclei). The coronagraph suppresses the diffraction spikes and rings of the central source to below the level of the scattered light, most of which is caused by surface errors in the HST optics. The coronagraph was added after ACS construction began, at which point it was impossible to insert it into the aberration-corrected beam. Instead, the system is used in the aberrated beam, which is corrected after the coronagraph. While not as efficient as a corrected-beam coronagraph, especially for imaging close to the central source, it does provide a significant improvement to the high-contrast imaging capabilities of HST. Care must be taken, however, to design an observation plan that properly optimizes the coronagraph's capabilities and accounts for its limitations.

Figure 6.2: Schematic layout of the ACS HRC coronagraph.



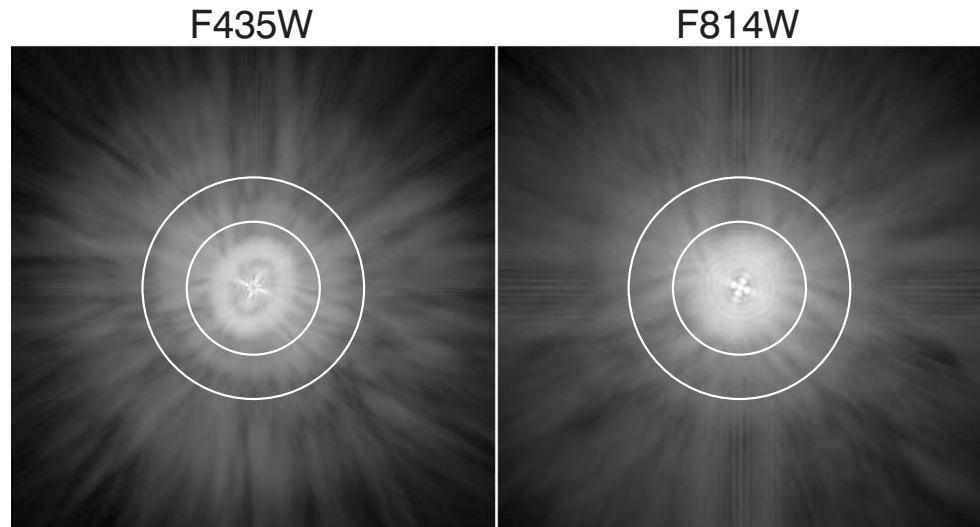
The upper left inset shows a schematic of the coronagraph mechanism that can be flipped in-and-out of the HRC optical path.

6.2.1 Coronagraph Design

A schematic layout of the ACS coronagraph is shown in Figure 6.2. The aberrated beam from the telescope first encounters one of two occulting spots. The beam continues to the M1 mirror, which forms an image of the HST entrance pupil on the M2 mirror, which corrects for the spherical aberration in the HST primary mirror. The coronagraph's Lyot stop is placed in front of M2. A fold mirror directs the beam onto the CCD detector. The field is 29×26 arcseconds with a mean scale of 0.026 arcseconds/pixel (geometric distortion results in effectively non-square pixels). The coronagraph can be used over the entire HRC wavelength range of $\lambda = 2000 \text{ \AA}$ to $10,000 \text{ \AA}$ using a variety of broad-to-narrowband filters.

The occulting spots are placed in the plane of the circle of least confusion, near where the unaberrated HST focal plane would be. At this location the balance of defocus and spherical aberration provides a good compromise between maximal occulted flux and minimal spot radius. The angular extent of the PSF in this plane necessitates larger spots than would be used in an unaberrated system (Figure 6.3).

Figure 6.3: Computed point spread functions at the plane of the occulting spots through filters F435W and F814W.



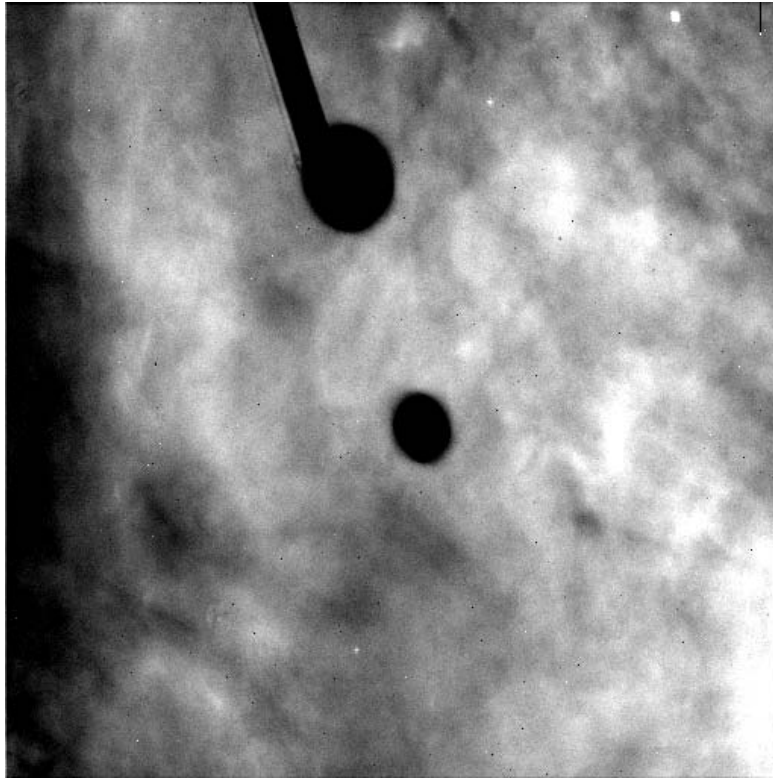
The elliptical, cross-shaped patterns in the cores are due to astigmatism at the off-axis location of the ACS aperture. It is corrected later by the ACS optics. The sizes of the two occulting spots ($D=1.8$ arcseconds and 3.0 arcseconds) are indicated. Logarithmic intensity scaled.

The ACS spots are solid (unapodized) metallic coatings deposited on a glass substrate (which reduces throughput by 4.5%). The smaller spot is 1.8 arcseconds in diameter and is at the center of the field. Its aperture name is CORON-1.8. The second spot, 3.0 arcseconds in diameter, is near a corner (Figure 6.4) and is designated as aperture CORON-3.0. The smaller spot is used for the majority of the coronagraphic observations, as it allows imaging closer to the central source. The larger one may be used for very deep imaging of bright targets with less saturation around the spot edge than would occur with the smaller spot. Its position at the edge of the field also allows imaging of material out to 20 arcseconds from the central source. The Lyot stop is located just in front of the M2 aberration correction mirror, where an image of the HST primary is formed. The stop is a thin metal mask that covers all of the diffracting edges in the HST system at the reimaged pupil (outer aperture, secondary mirror baffle, secondary mirror support vanes, and primary mirror support pads). The sizes of the stop and occulting spots were chosen to reduce the diffracted light below the level of the scattered light, which is unaltered by the coronagraph. The stop reduces the throughput by 52%, and it broadens the field PSF due to the smaller aperture and larger central obscuration relative to the beam diameter. The spots and Lyot stop are located on a panel attached to the ACS calibration door mechanism, which allows them to be flipped out of the beam when not in use. The inside surface of this door can be illuminated by a lamp to provide flat field calibration images for

direct-mode imaging. However, the arrangement prevents the acquisition of internal flat fields in coronagraphic mode.

In addition to the combination of the occulting spots and Lyot stop that comprise the coronagraph, there is a 0.8 arcseconds wide, 5 arcseconds long occulting finger (OCCULT-0.8) permanently located at the window of the CCD dewar. It does not provide any suppression of diffracted light because it occurs after the Lyot stop. It was to be used to image closer to stars than is possible with the occulting spots while preventing saturation of the detector. However, because the finger is located some distance from the image plane, there is significant vignetting around its edges, reducing its effectiveness. Originally aligned to cover the central portion of the 3.0 arcsecond spot, shifting of the spot relative to the beam during launch now places the finger along that spot's edge. Because of vignetting and the sensitivity of the PSF wings to the centering of the star, unocculted saturated observations of sources will likely be more effective than using the occulting finger.

Figure 6.4: Region of the Orion Nebula observed with the coronagraph in filter F606W.



The silhouettes of the occulters can be seen superposed against the background nebulosity. The 1.8 arcsecond spot is located at the center and the 3.0 arcsecond spot towards the top. The finger is aligned along one edge of the larger spot. This image has not been geometrically corrected, so the spots appear elliptical.

6.2.2 Acquisition Procedure and Pointing Accuracy

The central source must be placed precisely behind the occulting spot to ensure the proper suppression of the diffracted light. The absolute pointing accuracy of HST is about 1 arcsecond, too crude to ensure accurate positioning. An on-board acquisition procedure is used to provide better alignment. The observer must request an acquisition image immediately before using the coronagraph, and must specify a combination of filter and exposure time that provides an unsaturated image of the source. An acquisition image is taken by specifying HRC-ACQ as the aperture and ACQ as the opmode in [APT](#).

Acquisition images are taken with the coronagraphic masks inserted. The star is imaged within a predefined 200 x 200 pixel (5 x 5 arcseconds) subarray near the small occulting spot. Two identical exposures are taken, each of the length specified by the observer (rather than each being half the length specified, as they would be for a conventional CR-SPLIT). From these two images, the on-board computer selects the minimum value for each pixel as a crude way of rejecting cosmic rays. The result is then smoothed with a 3 x 3 pixel box and the maximum pixel in the subarray is identified. The center-of-mass centroid is then computed for the unsmoothed image within a 5 x 5 pixel box centered on this pixel. Based on this position, the telescope is then slewed to place the star behind the occulting spot.

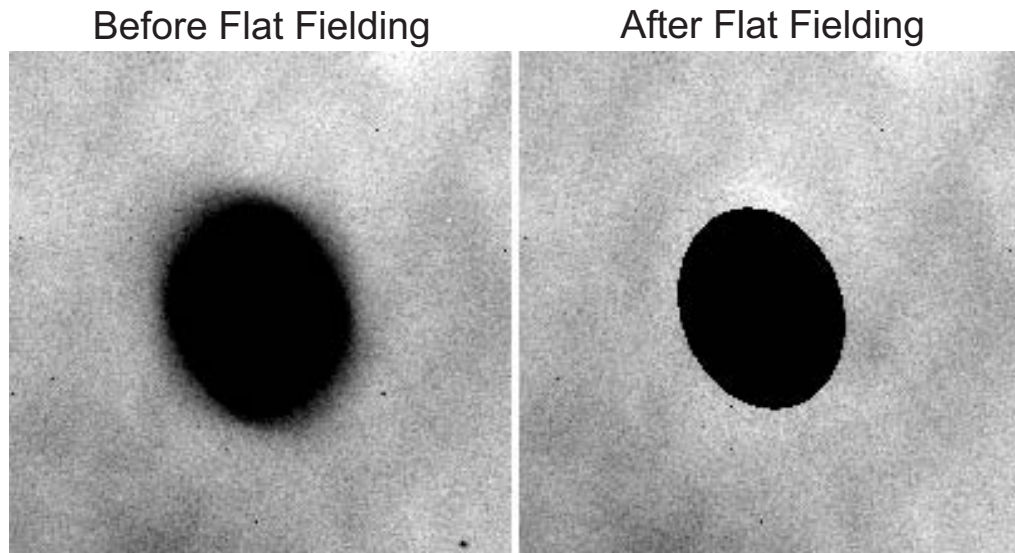
Because the coronagraphic masks are in place during acquisition, throughput is decreased by 52% relative to a non-coronagraphic observation. Also, the PSF is broader than in the normal imaging mode due to the larger obscurations in the Lyot stop, resulting in a lower relative peak pixel value (see Section 6.2.6). Care must be taken to select a combination of exposure time and filter that will prevent saturation of the star while providing enough flux to provide a good centroid measurement. A peak pixel flux of 2000 e⁻ should be considered the minimum while 50,000 e⁻ is a safe maximum (the HRC saturation limit is ~140,000 e⁻). Narrowband filters can be used, but for the brightest targets crossed filters are required. Allowable filter combinations for acquisitions are F220W+F606W, F220W+F550M, and F220W+F502N, in order of decreasing throughput. Be warned that the calibration of these filter combinations is poor, so estimated count rates from *synphot* or the APT ETC should be considered to be a factor of two off (either high or low).

Initial results from multiple on-orbit observations indicate that the combined acquisition and slew errors are on the order of ±0.25 pixels (±6 milliarcseconds). While small, these shifts necessitate the use of subpixel registration techniques to subtract one coronagraphic PSF from another (Section 6.2.5). The position of the spots relative to the detector also varies over time. This further alters the PSF, resulting in subtraction residuals.

6.2.3 Vignetting and Flat Fields

ACS coronagraphic flat fields are different from the standard flats due to the presence of the occulting spots and alteration of the field vignetting caused by the Lyot stop. The large angular extent of the aberrated PSF results in vignetting beyond one arcsecond of the spot edge (Figure 6.4), which can be corrected by dividing the image by the spot pattern (Figure 6.5). To facilitate this correction, separate flat fields have been derived that contain just the spot patterns (spot flats) and the remaining features (P-flats). For a full discussion see [ACS ISR 2004-16](#).

Figure 6.5: Region of the Orion Nebula around the $D = 1.8$ arcseconds spot.



(Left) The spot edge appears blurred due to vignetting. The image has not been geometrically corrected. (Right) The same region after the image has been corrected by dividing the flat field. The interior of the spot has been masked.

The ACS pipeline will divide images by the P-flat. P-flats specific to the coronagraph have been derived from either ground-based or on-orbit data for filters F330W, F435W, F475W, F606W, and F814W. Other filters use the normal flats, which may cause some small-scale errors around dust diffraction patterns. The pipeline then divides images by the spot flat, using a table of spot positions versus date to determine the proper shift for the spot flat. However, there is a lag in determining the spot position, so it may be a month after the observation before the archive knows where the spot was on that date. So, coronagraph users should note that their data may be calibrated with an incorrect spot flat if they extract their data from the archive soon after they were taken. (Spot flats for the filters listed above are available for download from the [ACS reference files web page](#). For other filters, the available spot flat closest in wavelength should be used. The spot flat must be shifted by an amount listed on the reference files page to account for motions of the occulting spots.)

Because coronagraphic P-flats and spot flats exist only for the few filters listed above, observers are encouraged to use those filters. It is unlikely that flat fields for other filters will be available in the future.

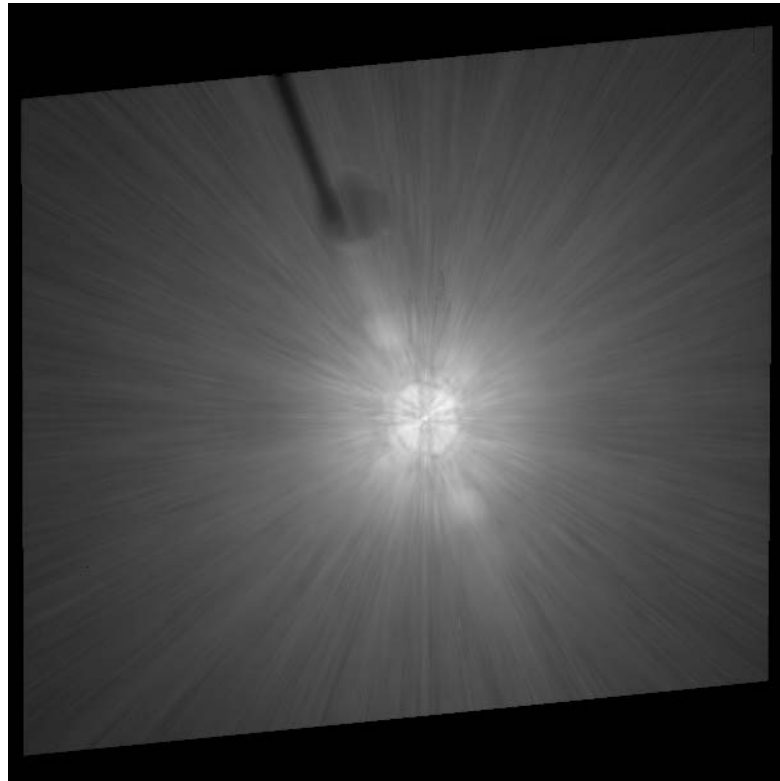
6.2.4 Coronagraphic Performance

Early in Cycle 11, coronagraphic performance verification images were taken of the $V = 0$ star Arcturus (Figure 6.6 and Figure 6.7). This star has an angular diameter of 25 milliarcseconds and is thus unresolved by the coronagraph. The coronagraphic image of a star is quite unusual. Rather than appearing as a dark hole surrounded by residual light, as would be the case in an aberration-free coronagraph, the interior of the spot is filled with a diminished and somewhat distorted image of the central source. This is due to the M2 mirror correction of aberrated light from the star that is not blocked by the spot. The small spot is filled with light, while the large one is relatively dark. Broad, ring-like structures surround the spots, extending their apparent radii by about 0.5 arcseconds. These are due to diffraction in the wings of the aberrated PSF by the occulting spot itself. A consequence of these features is that stars may saturate the interior and edges of the spot within a short time. Within the small spot, the brightest pixels can become saturated in less than one second for a $V = 0.0$ star, while pixels at edge of the larger spot will saturate in about 14 seconds.

The measured radial surface brightness profiles (Figure 6.8) show that the coronagraph is well aligned and operating as expected. The light diffracted by the HST obscurations is suppressed below the level of the scattered light – there are no prominent diffraction spikes, rings, or ghosts beyond the immediate proximity of the spots. At longer wavelengths ($\lambda > 6000 \text{ \AA}$) the diffraction spikes appear about as bright as the residual scattered light (at longer wavelengths, the diffraction pattern is larger and therefore not as well suppressed by the coronagraph). The spikes are more prominent in images with the large spot than the small one. This can be explained by the fact that the Lyot stop is not located exactly in the pupil plane but is instead slightly ahead of it, so the beam can “walk” around the stop depending on the field angle of the object. Because the large spot is at the edge of the field, the beam is slightly shifted, allowing more diffracted light to pass around the mask edges.

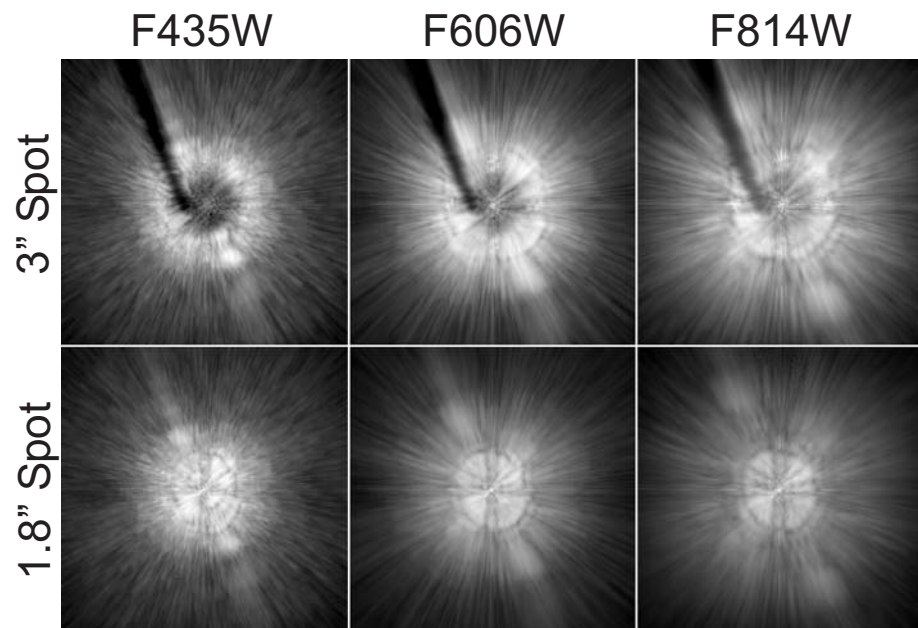
The residual background is dominated by radial streaks that are caused primarily by scattering from zonal surface errors in the HST mirrors. This halo increases in brightness and decreases in size towards shorter wavelengths. One unexpected feature is a diagonal streak or “bar” seen in both direct and occulted star images. It is about 5 times brighter than the mean azimuthal surface brightness in the coronagraphic images. This structure was not seen in the ground-test images and is likely due to scattering introduced by the HST optics. There appears to be a corresponding feature in STIS as well.

Figure 6.6: Geometrically corrected (29 arcseconds across) image of Arcturus observed in F814W behind the 1.8 arcseconds spot.



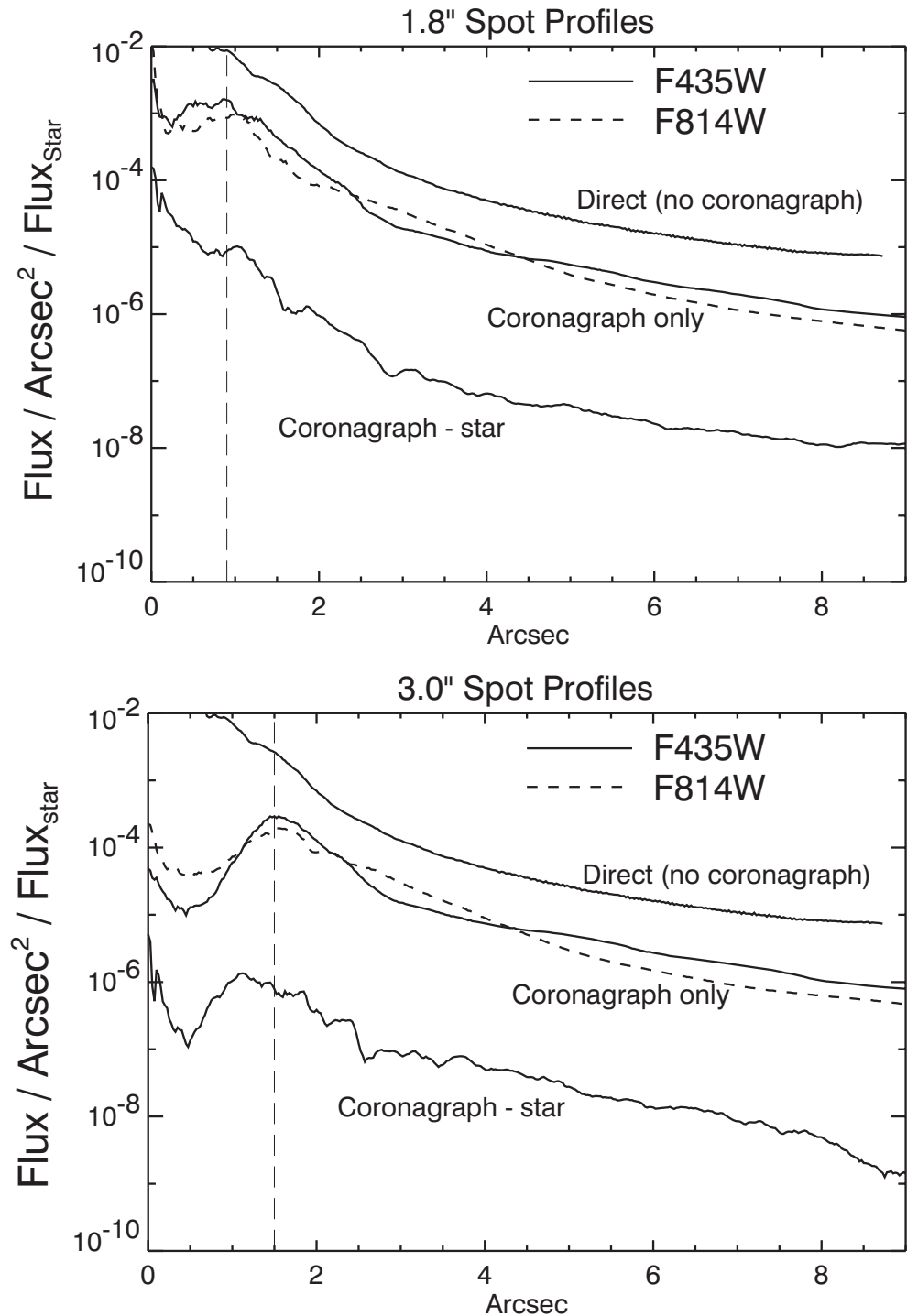
This is a composite of short, medium, and long (280 seconds) exposures. The “bar” can be seen extending from the upper left to lower right. The shadows of the occulting finger and large spot can be seen against the scattered light background. Logarithmic intensity scale.

Figure 6.7: Regions around the occulting spots in different filters.



The occulting finger can be seen in the 3 arcseconds spot images. Logarithmic intensity scaled.

Figure 6.8: Surface brightness plots derived by computing the median value at each radius.



The brightness units are relative to the total flux of the star. The direct profile is predicted; the coronagraphic profiles are measured from on-orbit images of Arcturus. "Coronagraph-star" shows the absolute median residual level from the subtraction of images of the same star observed in separate visits.

6.2.5 Residual Light Subtraction

While the coronagraph suppresses the diffracted light from the central star, the scattered light still overwhelms faint, nearby sources. It is possible to subtract most of the remaining halo using an image of another occulted star. PSF subtraction has been successfully used with images taken by other HST cameras, with and without a coronagraph. The quality of the subtraction depends critically on how well the target and reference PSFs match.

As mentioned above, for any pair of target and reference PSF observations, there is likely to be a difference of 5 to 20 milliarcseconds between the positions of the stars. Because the scattered light background is largely insensitive to small errors in star-to-spot alignment (it is produced before the coronagraph), most of it can be subtracted if the two stars are precisely registered and normalized. Due to the numerous sharp, thin streaks that form the scattered light background, subtraction quality is visually sensitive to registration errors as small as 0.03 pixels (0.75 milliarcseconds). To achieve this level of accuracy, the reference PSF may be iteratively shifted and subtracted from the target until an offset is found where the streaks are minimized. This method relies on the judgment of the observer, as any circumstellar material could unexpectedly bias a registration optimization algorithm. A higher-order sampling method, such as cubic convolution interpolation, should be used to shift the reference PSF by subpixel amounts; simpler schemes such as bilinear interpolation degrade the fine PSF structure too much to provide good subtractions.

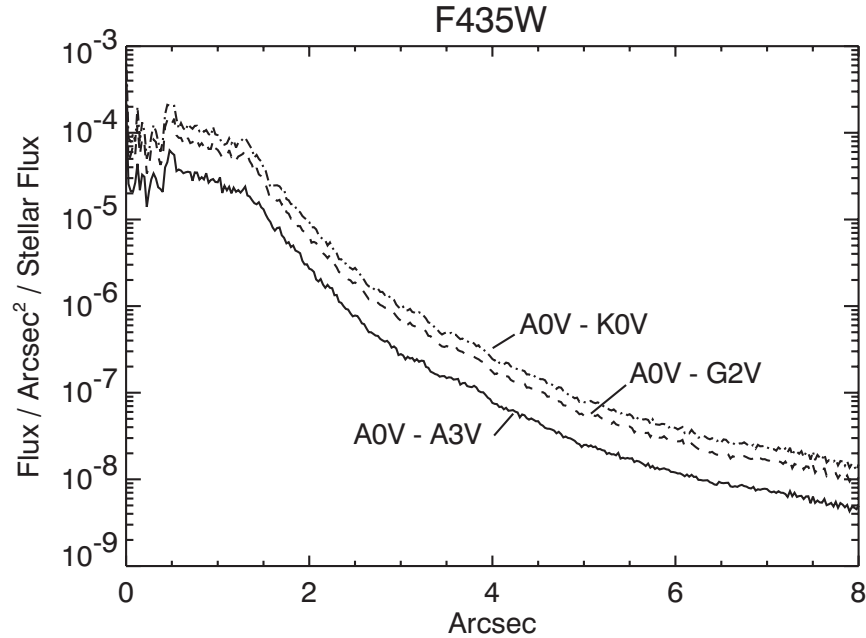
Normalization errors as small as 1% to 4% between the target and reference stars may also create significant residuals. However, derivation of the normalization factors from direct photometry is often not possible. Bright, unocculted stars will be saturated in medium or broadband filters at the shortest exposure time (0.1 seconds). An indirect method uses the ratio of saturated pixels in unocculted images (the accuracy will improve with greater numbers of saturated pixels). A last-ditch effort would rely on the judgment of the observer to iteratively subtract the PSFs while varying the normalization factor.

In addition to registration offsets, positional differences can alter the diffraction patterns near the spots' edges. The shape and intensity of these rings are very sensitive to the location of the star relative to the spot. They cannot be subtracted by simply adjusting the registration or normalization. These errors are especially frustrating because they increase the diameter of the central region where the data are unreliable. The only solution to this problem is to observe the target and reference PSF star in adjacent orbits without flipping the masks out of the beam between objects.

Color differences between the target and reference PSF can be controlled by choosing an appropriate reference star. As wavelength increases, the speckles that make up the streaks in the halo move away from the center while their intensity decreases (Figure 6.7). The diffraction

rings near the spot edges will expand as well. These effects can be seen in images through wideband filters – a red star will appear to have a slightly larger PSF than a blue one. Thus, an M-type star should be subtracted using a similarly red star – an A-type would result in significant residuals. Even the small color difference between A0 V and B8 V stars, for example, may be enough to introduce bothersome errors (Figure 6.9).

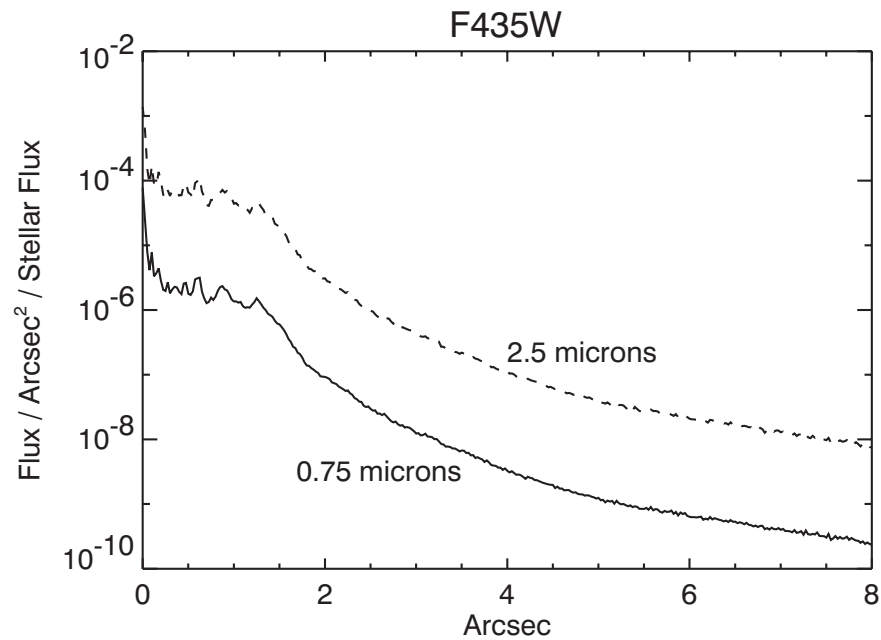
Figure 6.9: Predicted absolute mean subtraction residual levels for cases where the target and reference stars have color mismatches.



The brightness units are relative to the total flux of the target star.

A focus change can also alter the distribution of light in the PSF. The telescope focus changes over time scales of minutes to months. Within an orbit, the separation between the primary and secondary mirrors varies on average by $3 \mu\text{m}$ (resulting in $1/28$ wave rms of defocus @ $\lambda = 5000 \text{ \AA}$) – an effect called *breathing*. This is caused by the occultation of the telescope's field of view by the warm Earth, which typically occurs during half of each 96-minute orbit. This heats HST's interior structure, which expands. After occultation the telescope gradually shrinks. Changes relative to the sun (mostly anti-sun pointings) cause contraction (not expansion) of the telescope, which gradually expands to "normal" size after a few orbits. The main result of these small focus changes is the redistribution of light in the wings (Figure 6.10).

Figure 6.10: Predicted absolute mean subtraction residual levels for cases where the target and reference stars are imaged at different breathing-induced focus positions.



The offset (0.75 or 2.5 μm) from perfect focus (0 μm) is indicated with respect to the change in primary-secondary mirror separation (the typical breathing amplitude is 3 to 4 μm within an orbit). The brightness units are relative to the total flux of the target star.

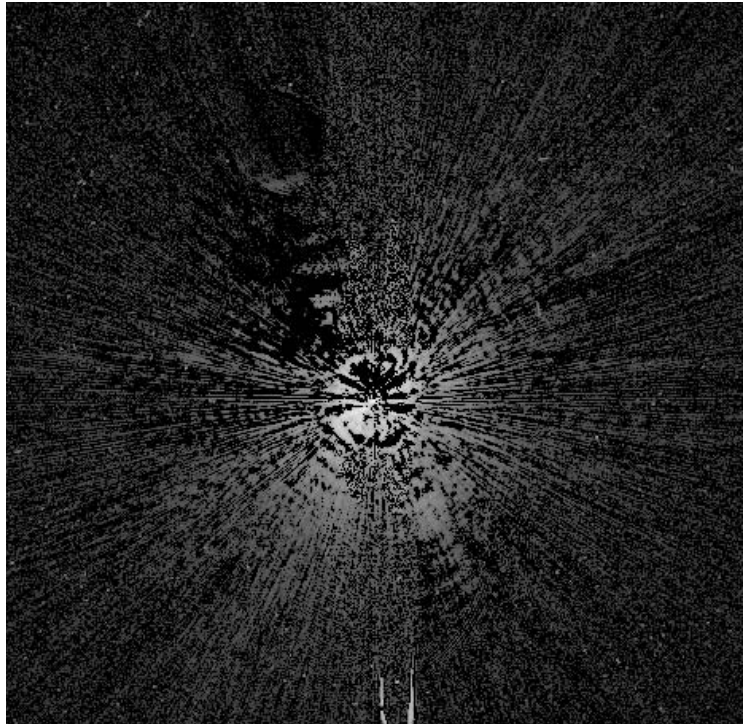
Plots of the azimuthal median radial profiles after PSF subtraction are shown in Figure 6.8. In these cases, images of Arcturus were subtracted from others of itself taken a day later. The images were registered as previously described. Combined with PSF subtraction, the coronagraph reduces the median background level by 250x to 2500x, depending on the radius and filter. An example of a PSF subtraction is shown in Figure 6.11. The mean of the residuals is not zero. Because of PSF mismatches, one image will typically be slightly brighter than the other over a portion of the field (such as shown in Figure 6.12). The pixel-to-pixel residuals can be more than 10x greater than the median level (Figure 6.13). Note that these profiles would be worse if there were color differences between the target and reference PSFs.

One way to get around both the color and normalization problems is to take images of the central source at different orientations, and subtract one from the other (*roll subtraction*). This can be done by either requesting a roll of the telescope about the optical axis (up to 30° total) between orbits or by revisiting the object at a later date when the default orientation of the telescope is different. This technique only works when the nearby object of interest is not azimuthally extended. It is the best method for detecting point source companions or imaging strictly edge-on disks (e.g. Beta Pictoris). This method can also be used to reduce the

pixel-to-pixel variations in the subtraction residuals by rotating and co-adding the images taken at different orientations (this works for extended sources if another PSF star is used). Ideally, the subtraction errors will decrease as the square root of the number of orientations.

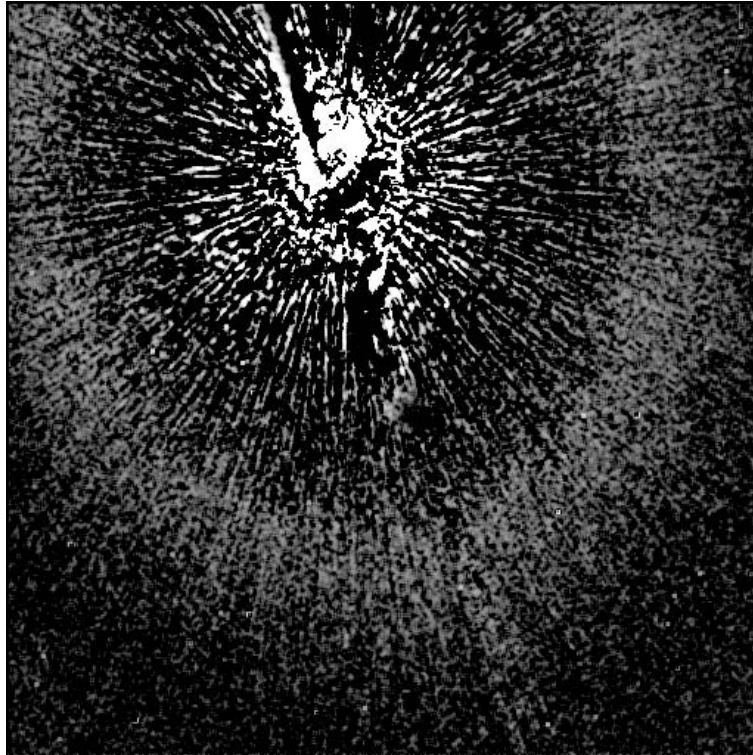
The large sizes of the occulting spots severely limit how close to the central source one can image. It may be useful to combine coronagraphic imaging with direct observations of the target, allowing the central columns to saturate (additional observations at other rolls would help). PSF subtraction can then be used to remove the diffracted and scattered light.

Figure 6.11: Residual errors from the subtraction of one image of Arcturus from another taken in a different visit (filter = F435W, $D = 1.8$ arcseconds spot).



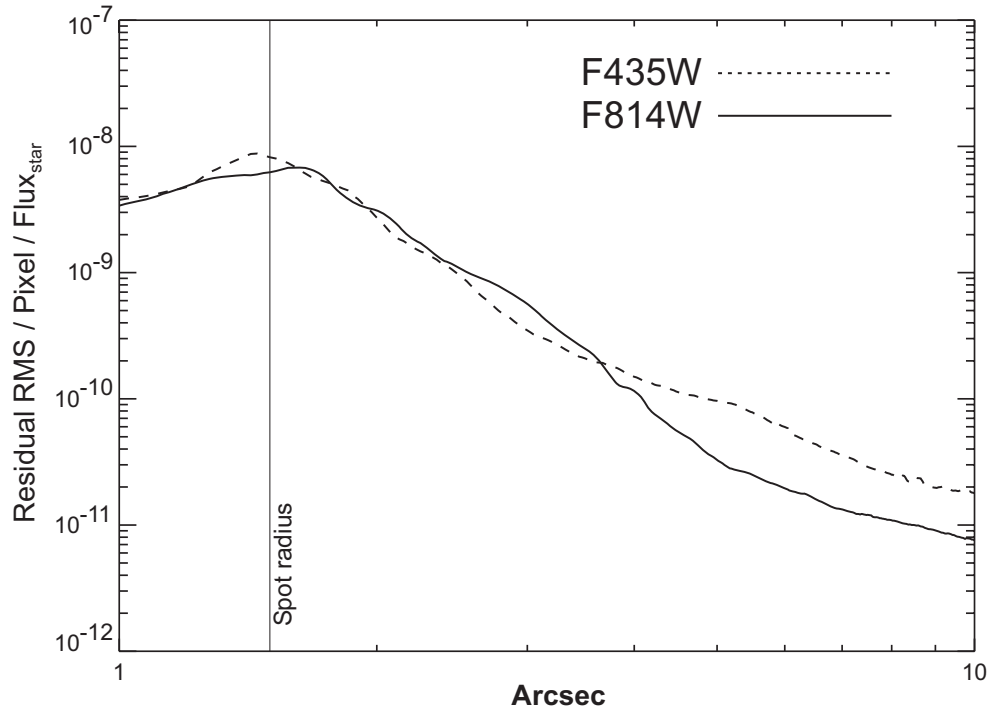
The image is 29 arcseconds across and has not been geometrically corrected. Logarithmic intensity scaled.

Figure 6.12: Subtraction of Arcturus from another image of itself taken during another visit using the large ($D = 3.0$ arcseconds) spot and F435W filter.



The image has been rebinned, smoothed, and stretched to reveal very low level residuals. The broad ring at about 13 arcseconds from the star is a residual from some unknown source – perhaps it represents a zonal redistribution of light due to focus differences (breathing) between the two images. The surface brightness of this ring is 20.5 magnitudes/arcseconds² fainter than the star. The diameter, brightness, and thickness of this ring may vary with breathing and filter. The image has not been geometrically corrected.

Figure 6.13: Plots of the azimuthal RMS subtraction residual levels at each radius for the large (3 arcseconds) spot.

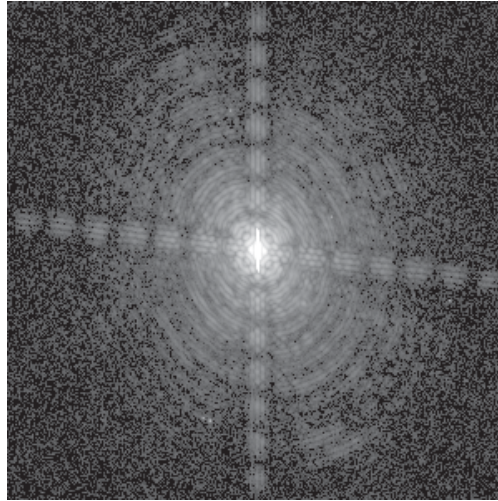


The flux units are counts per pixel relative to the total unocculted flux from the central source. These plots were derived from Arcturus-Arcturus subtractions represent the best results one is likely to achieve. The undistorted HRC scale assumed here is 25 milliarcseconds/pixel.

6.2.6 The Off-Spot PSF

Objects that are observed in the coronagraphic mode but that are not placed behind an occulting mask have a PSF that is defined by the Lyot stop. Because the stop effectively reduces the diameter of the telescope and introduces larger obscurations, this PSF is wider than normal, with more power in the wings and diffraction spikes (Figure 6.14). In addition, the stop and spot substrate reduce the throughput by 52.5%. In F814W, this PSF has a peak pixel containing 4.3% of the total (reduced) flux and a sharpness (including CCD charge diffusion effects) of 0.010 (compare these to 7.7% and 0.026, respectively, for the normal HRC PSF). In F435W the peak is 11% and the sharpness is 0.025 (compared to 17% and 0.051 for the normal F435W PSF). Observers need to take the reduced throughput and sharpness into account when determining detection limits for planned observations. [Tiny Tim](#) can be used to compute off-spot PSFs.

Figure 6.14: Image of Arcturus taken in coronagraphic mode with the star placed outside of the spot.



The coronagraphic field PSF has more pronounced diffraction features (rings and spikes) than the normal HRC PSF due to the effectively larger obscurations introduced by the Lyot stop. The central portion of this image is saturated. It was taken through a narrowband filter (F660N) and is not geometrically corrected.

6.2.7 Occulting Spot Motions

Monitoring of the occulting spot positions using earth flats shows that they move over weekly, and even daily time scales in an unpredictable manner. The cause of this motion is unknown. Their locations typically vary by ~ 0.3 pixels (8 milliarcseconds) over the span of one week, but on occasion they have shifted by 1 to 5 pixels over 1 to 3 weeks. While inserted in the beam, however, they remain stable to better than ± 0.1 pixel, and when cycled within an orbit they return to the same position within ± 0.25 pixel.

The uncertainties in the locations lead to star-to-spot registration errors. After the acquisition exposure the star is moved to the predefined aperture position of the spot, which is measured on the ground from on-orbit flats and may be out of date. Due to the layout of ACS, it is not possible to determine the spot location automatically before a coronagraphic observation, as can be done for NICMOS. Also, unlike STIS, the star cannot be dithered around until the stellar flux within the occulter is minimized.

Star-to-spot registration errors affect coronagraphic imaging. If the star is significantly offset from the spot center (> 3 pixels), then one side of the spot interior and edge will be brighter than expected, and may possibly saturate much earlier than predicted. A large offset will also slightly degrade the coronagraphic suppression of the diffraction pattern. Most importantly, even slight changes in the spot position will alter the residual diffraction pattern, introducing mismatches between the target and

reference PSFs that may result in large subtraction residuals. This means that an observer cannot rely on reference PSFs taken in other programs or at different times.

To reduce the impact of spot motion, observers using the ACS coronagraph are required to obtain a reference PSF in an orbit immediately before or after their science observation. A single reference PSF can be used for two science targets if all three objects can be observed in adjacent orbits and are of similar color (note that it is difficult to schedule more than five consecutive orbits). Otherwise, if multiple science targets are observed, each one will require a reference PSF. The additional reference PSF orbit(s) must be included in the Phase 1 proposal.

STScI is using a revised procedure to update the coronagraphic spot positions shortly before a proposal executes to provide better registration. In this procedure, the last measured offset of the spot from its defined aperture location is uploaded to HST a few orbits before a coronagraphic observation executes. By including a `USE_OFFSET` special requirement for each coronagraphic exposure after an acquisition, the target is shifted by the appropriate amount. The spots are measured weekly from earth flats, so this method provides up-to-date positions than relying on the aperture location. This procedure adds approximately 40 seconds to each visit. This procedure is required for all coronagraphic observations. More details will be provided on the STScI [ACS Web](#) site and in *Phase II Proposal Instructions*.

6.2.8 Planning ACS Coronagraphic Observations

Exposure Time Estimation

The estimation of exposure time for coronagraphic observations is similar to direct-mode time calculations, except that the additional background contribution from the central source's PSF has to be accounted for. Generally, most coronagraphic observations are limited by the central source's PSF wings. The [APT Exposure Time Calculator](#) includes a coronagraphic mode for estimating exposure times. We will now demonstrate how exposure times for coronagraphic observations can be determined using the Web-based version of the [ACS Exposure Time Calculator](#). The following steps are required:

- Determine which occulting mask to use
- Calculate the count rate for the target
- Calculate the count rate for the central source
- Calculate the background contribution from the surface brightness of the central source's PSF wings at the location of the target.
- Verify that background+target does not saturate at this location in exposure time t_{exp} (or use exposure times of increasing length)

- Calculate the signal-to-noise ratio Σ , given by:

$$\Sigma = \frac{Ct}{\sqrt{Ct + N_{pix}(B_{sky} + B_{det} + B_{PSF})t + N_{pix}N_{read}R^2}}$$

Where:

- C = the signal from the astronomical target in electrons/sec from the CCD.
- N_{pix} = the total number of detector pixels integrated over to achieve C .
- B_{sky} = the sky background in counts/sec/pixel.
- B_{det} = the detector dark current in counts/sec/pixel.
- B_{PSF} = the background in counts/sec/pixel from the wings of the central source's PSF at the same distance from the central source as the target.
- N_{read} = the number of CCD readouts.
- t = the integration time in seconds.
- R is the readout noise of the HRC CCD = $4.7e^-$.

In order to illustrate a calculation we shall consider the case where we are trying to determine the S/N achieved in detecting a M6 V star with a V magnitude of 20.5 at a distance of 4.25 arcseconds from a F0 V star with a V magnitude of 6, for an exposure time of 1000 seconds with the F435W filter. Using the [ACS Exposure Time Calculator](#) and considering the case for the 3.0 arcseconds occulting mask:

- Target count rate = $5.9 e^-/\text{second}$ for a 5×5 aperture (including 47.5% throughput of coronagraph)
Sky count rate = $0.003 e^-/\text{second/pixel}$
Detector dark rate = $0.0036 e^-/\text{second/pixel}$
- Central star count rate = $3.3 \times 10^7 e^-/\text{second}$ for a 101×101 aperture (101×101 aperture used to estimate total integrated flux)
- At a distance 4.25 arcseconds from the central star, from Figure 6.8, the fraction of flux per 0.026×0.026 arcseconds pixel in the PSF wings is 5×10^{-9} .
 $B_{PSF} = 3.3 \times 10^7 * 5 \times 10^{-9} = 0.165 e^-/\text{second/pixel}$
- Using the equation above we find the signal to noise for a 1000 seconds exposure is 57. Note that a M6 V star with a V magnitude of 20.5 observed with the HRC in isolation would yield a S/N of 129.

Observing sequence for point source companions

The best way to detect faint stellar or substellar companions is to use roll subtraction to avoid color differences between the target and reference PSFs. This also provides duplicate observations that make it easier to verify

true companions from noise. It is best to roll the telescope between visits and repeat the image sequence in a new orbit. This way, you can better match the breathing cycle of the telescope than if you rolled the telescope in the middle of an orbital visibility window. You can force this to happen by selecting both orientation and time-sequencing constraints in the visit special requirements. Remember that the coronagraphic field PSF is somewhat broader than the normal HRC PSF, which may influence your assumed signal-to-noise ratio. Off-spot PSF models can be generated with the [Tiny Tim](#) PSF software. You can estimate the residual background noise level using Figure 6.13.

Suggested point-source companion observing sequence:

1. Obtain an acquisition image
2. Execute image sequence.
3. Request telescope roll offset (use **ORIENT q₁ TO q₂ FROM n** special requirement in visit).
4. Obtain another acquisition.
5. Repeat image sequence.
6. Repeat 3 to 5 as necessary.

Observing sequence for extended sources (e.g. circumstellar disks and AGN host galaxies)

When imaging extended objects, the remaining scattered light must be subtracted using a reference star image, which should match the color of your target as closely as possible. To reduce the impact of noise in the subtracted images, it helps if the reference PSF is bright enough to provide higher signal-to-noise ratios in the wings, than that of the target source. If possible, select a reference star that is nearby ($< 20^\circ$) and request that it be observed immediately before or after the target source. This reduces the chance that there will be large focus differences between the two visits. In order to better discriminate between subtraction artifacts and real structure, it may also help to obtain images of the target at two or more orientations of the telescope (there is no need to get reference PSF images at different rolls). You can estimate the residual background noise level using Figure 6.13.

Suggested extended source observing sequence:

1. Obtain direct images of the science target in each filter to derive normalization factors
2. Obtain an acquisition image of the science target.
3. Take image sequence of science target.
4. Request a new telescope orientation.
5. Repeat steps 2 to 3.

6. In a new visit immediately after the science observation, point at the reference star.
7. Obtain an acquisition image of reference star.
8. Take image sequence of reference star.
9. Obtain direct images of the reference star in each filter to derive normalization factors.

Note that the order of the observations places direct imaging before or after coronagraphic imaging. This reduces cycling of the coronagraphic mechanism. Because the occulting spots are large, you may wish to image closer to the source using additional direct observations without the coronagraph. Multiple roll angles are necessary in this case because portions of the inner region will be affected by saturated columns and diffraction spikes. Direct observations of the reference star will be required as well to subtract both the diffracted and scattered light. Color and focus mismatches between the target and reference PSFs will be even more important in the direct imaging mode than with the coronagraph because the diffracted light is not suppressed. However, there are no mismatches caused by star-spot alignment to worry about.

6.2.9 Choice of Filters for Coronagraphic Observations

All of the HRC filters are available for coronagraphic observations. However, there are only a few that have been used in the past in this mode, and can be considered well-characterized. These are F435W, F475W, F606W, and F814W. The first three have produced good results and can be considered “safe” choices.

Filter F814W has been problematic, however. Because the PSF is larger at red wavelengths than blue, less of the light from the central star is blocked by the occulting spot. This makes the residual PSF more sensitive to spot shifts and misalignments of the star behind the spot. Mismatches between target and reference PSF star-to-spot alignments may cause significant subtraction residuals. Also, F814W images suffer from the red halo, which still affects coronagraphic observations because the central spot is filled with light that will be scattered to large radii. Color differences between the target and reference PSF stars will thus cause differences in the halo pattern, altering the local background level in unpredictable ways. If multicolor images are needed, it may be safer to choose F435W and F606W rather than F606W and F814W, for instance. Of course, for red objects it may not be feasible to choose a blue filter due to low flux levels, in which case F814W must be used.

6.3 Grism/Prism Spectroscopy

The ACS filter wheels include four dispersing elements for low resolution slitless spectrometry over the field of view of the three ACS channels. One grism (G800L) provides low resolution spectra over the 5500 Å to 10,500 Å range for both the WFC and HRC. A prism (PR200L) in the HRC covers the range 1700 Å to beyond 3900 Å (although reliable wavelength and flux calibration is only guaranteed to 3500 Å). In the SBC a LiF prism covers the wavelength range 1150 Å to ~1800 Å (PR110L) and a CaF₂ prism is useful over the 1250 Å to ~1800 Å range (PR130L). Table 6.3 summarizes the essential features of the four ACS dispersers in the five available modes. The grism provides first order spectra with almost constant dispersion (about 40 Å/pixel) as a function of wavelength but with second order overlap beyond about 10,000 Å; the prisms however have non-linear dispersion with maximum resolution at shorter wavelengths but much lower resolving power at longer wavelengths. The two-pixel resolution is listed for each grism or prism at a selected wavelength in Table 6.3. The pixel scale for the prism spectra is given at the selected wavelength. The tilt of the spectra to the detector X axis (close to the spacecraft V2 axis) is also listed.

Table 6.3: Optical parameters of ACS dispersers.

| Disperser | Channel | Wavelength range (Å) | Resolving power | Å/pixel | Tilt ¹ (deg) |
|-----------|---------|-----------------------------|-----------------|-------------------|-------------------------|
| G800L | WFC | 1st order: 5500 to 10500 | 100 @ 8000 Å | 39.8 ² | -2 |
| G800L | WFC | 2nd order: 5000 to 8500 | 200 @ 8000 Å | 20.7 ² | -2 |
| G800L | HRC | 1st order: 5500 to 10500 | 140 @ 8000 Å | 23.9 ³ | -38 |
| G800L | HRC | 2nd order: 5500 to 8500 | 280 @ 8000 Å | 12.0 ³ | -38 |
| PR200L | HRC | 1700 to 3900 | 59 @ 2500 Å | 21.3 | -1 |
| PR110L | SBC | 1150 to 1800 | 79 @ 1500 Å | 9.5 | 0 |
| PR130L | SBC | 1250 to 1800 | 96 @ 1500 Å | 7.8 | 0 |

1. Tilt with respect to the positive X-axis of the data frame.
2. The dispersion varies over the field by $\pm 11\%$; the tabulated value refers to the field center.
3. The dispersion varies over the field by $\pm 2\%$; the tabulated value refers to the field center.

6.3.1 WFC G800L

The G800L grism and the WFC provide two-pixel resolving power from 69 (at 5500 Å) to 131 (at 10,500 Å) for first order spectra over the whole accessible field of 202 x 202 arcseconds. Table 6.3 lists the linear dispersion, but a second order dispersion solution provides a better fit. Figure 6.15 shows the wavelength extent and sensitivity for the zeroth, first, and second order spectra when used with the WFC. Figure 6.16 shows the same plot in pixel extent. The 0 position refers to the position of the direct image and the pixel size is 0.05 arcseconds. Note that there is contamination of the 1st order spectrum above 10,000 Å by the second order. The total power in the zeroth order is 2.5% of that in the first order, so locating the zeroth order may not be an effective method of measuring the wavelengths of weak spectra. The default method will be to obtain a matched direct image-grism pair. There is also sensitivity of about a percent of first order in the third and fourth orders, and about half a percent in the negative orders. The full extent of the spectrum of a bright source (orders -2, -1, 0, 1, 2, 3) is 1200 pixels (60 arcseconds). The higher orders are not in focus and the spectral resolution of these orders is therefore less than what would be predicted from the nominally higher dispersion.

Figure 6.15: Sensitivity versus wavelength for WFC G800L.

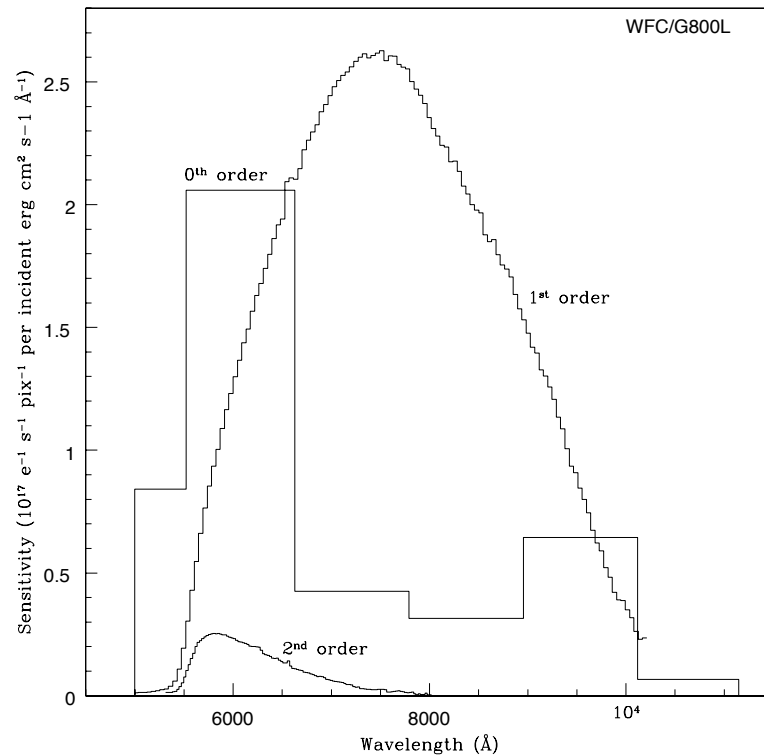


Figure 6.16: Sensitivity versus pixel position for WFC G800L.

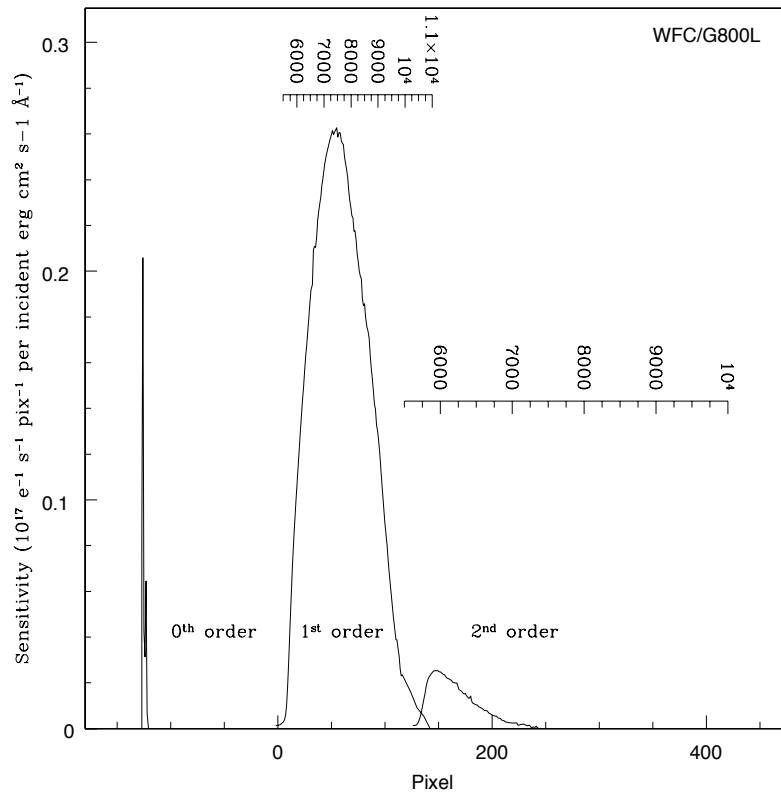


Figure 6.17 shows the full spectrum extent for a 60 second exposure of the white dwarf GD153 ($V = 13.35$) with the individual orders indicated. When bright objects are observed, the signal in fainter orders may be mistaken for separate spectra of faint sources and in crowded fields, many orders from different objects can overlap. The wavelength solution is field dependent on account of the tilt of the grism to the optical axis, and the linear dispersion varies by $\pm 11\%$ from center to corner. This field dependence has been calibrated to allow wavelength determination to better than 0.5 pixels over the whole field.

Figure 6.17: Full dispersed spectrum for white dwarf GD153 with WFC/G800L.



The numbers indicate the different grism orders.

6.3.2 HRC G800L

When used with the HRC, the G800L grism provides higher spatial resolution (0.028 arcseconds) pixels than the WFC and also higher spectral resolution. However, the spectra are tilted at -38° to the detector X axis. Figure 6.18 shows the wavelength extent and sensitivity in the zero, first and second orders, with the pixel extent shown in Figure 6.19. Figure 6.20 shows the observed spectrum of the standard star GD153. Again there is contamination of the first order spectrum by the second order beyond 9500 Å. The total extent of the spectrum (orders -1 and +2) in Figure 6.20 covers about 70% of the 1024 detector pixels. In addition, a much greater number of spectra will be formed by objects situated outside the HRC direct image, or will have their spectra truncated by the chip edges, than for the WFC. The variation of the grism dispersion over the HRC field is about $\pm 2\%$ from center to corner and has been calibrated.

Figure 6.18: Sensitivity versus wavelength for HRC G800L.

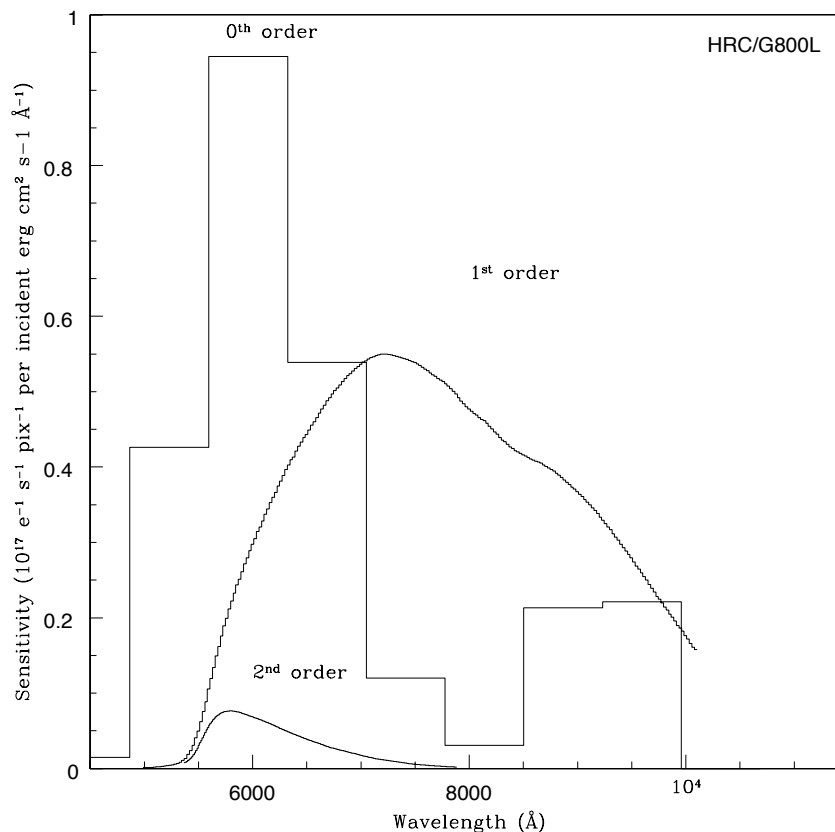


Figure 6.19: Sensitivity versus pixel position for HRC G800L.

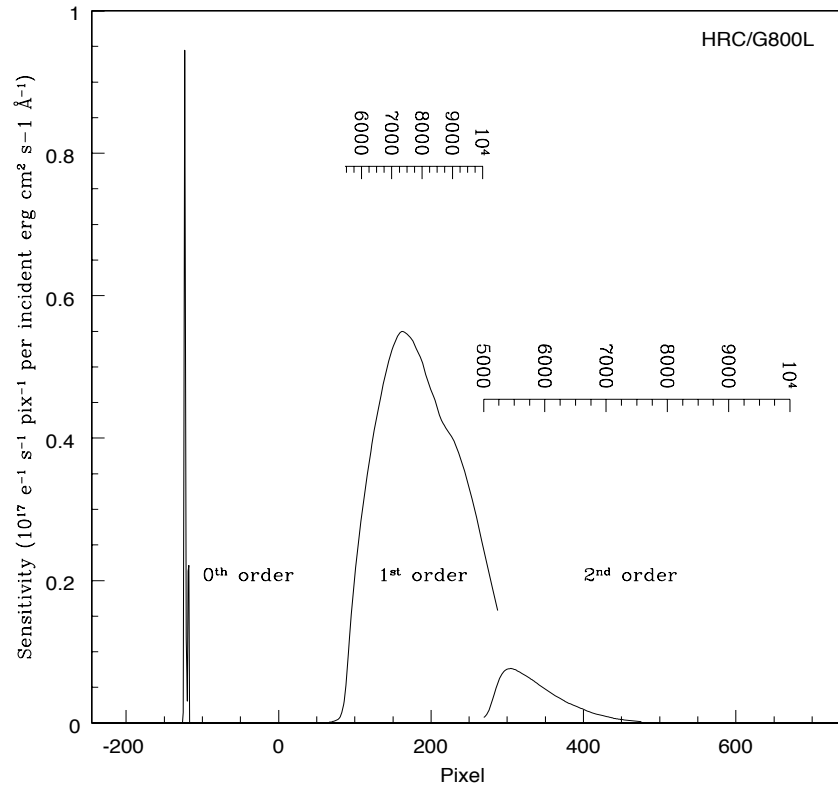
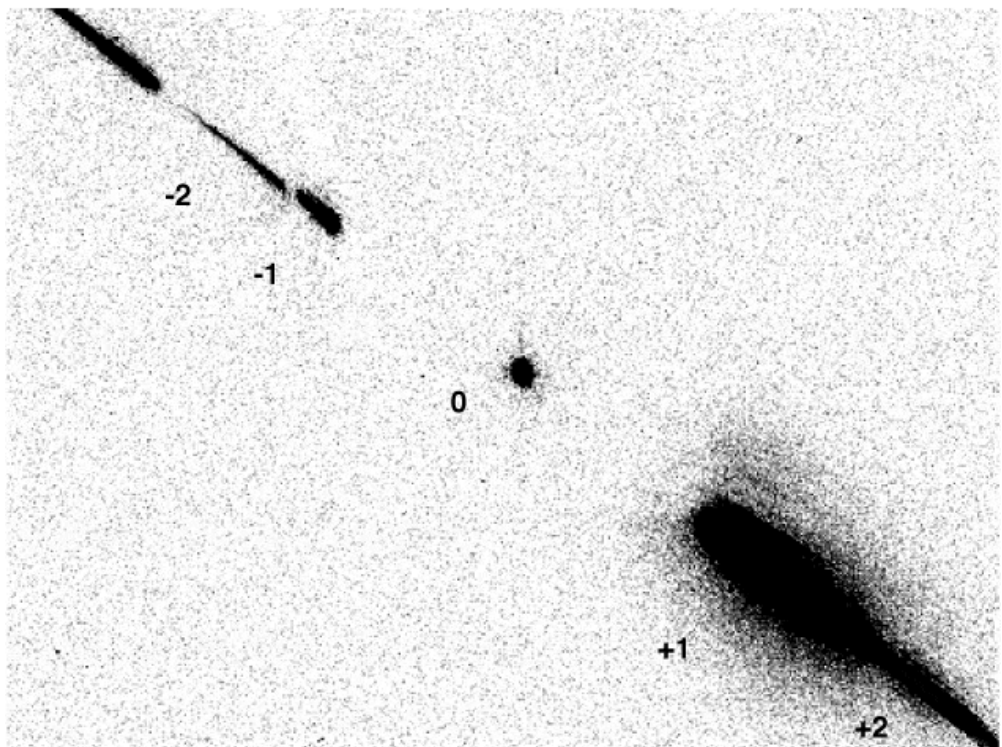


Figure 6.20: Full dispersed spectrum of white dwarf GD153 with HRC/G800L.

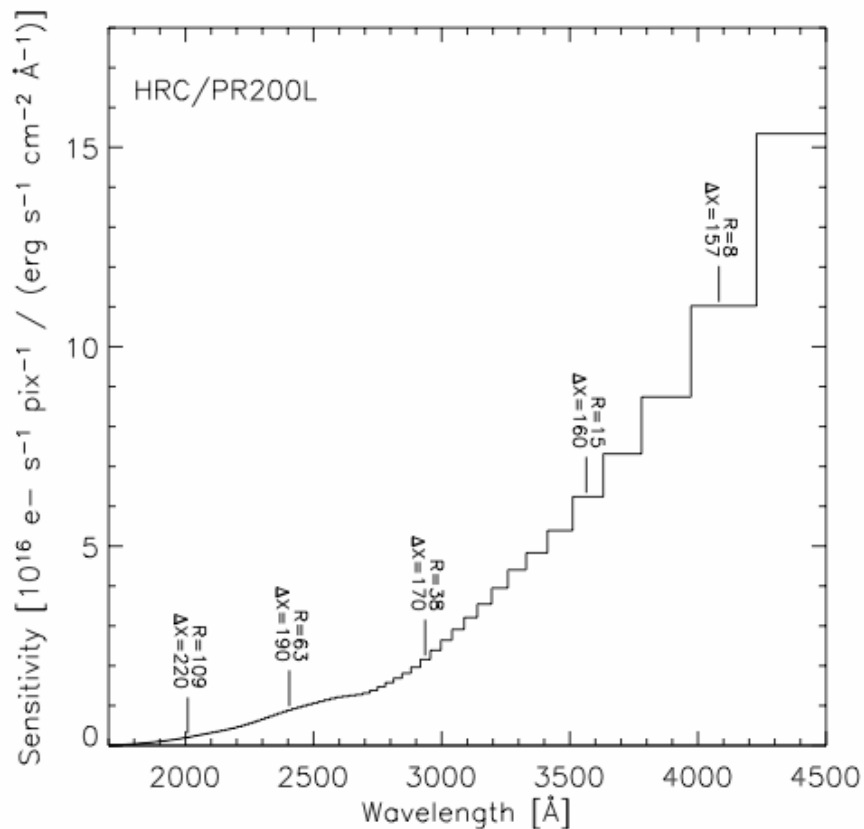


The numbers indicate the different grism orders.

6.3.3 HRC PR200L

The maximum pixel resolution of the prism is 5.3 \AA at 1800 \AA . At 3500 \AA , the dispersion drops to 105 \AA/pix and is 563 \AA/pix at 5000 \AA . The result is a bunching up of the spectrum to long wavelengths with about 8 pixels spanning 1500 \AA . For bright objects, this effect can lead to blooming of the HRC CCD from filled wells; the overfilled pixels bleed in the detector Y direction, and would thus affect other spectra. Figure 6.21 shows the sensitivity versus wavelength for PR200L and the wavelength extent of the pixels is indicated. The variation of the dispersion across the detector for PR200L amounts to about $\pm 4\%$ (corner to corner) at 2000 \AA . The angle of the prism causes a large deviation between the position of the direct object and the region of the dispersed spectrum. The numbers in Figure 6.21 indicate the resolving power (R) and the offset from the direct image in pixels (Δx) as functions of wavelength. On account of the size of this offset, special apertures have been defined in the observation scheduling system so that the spectrum of the target centered on the direct image occurs near the center of the field in the prism image, and a small angle maneuver occurs between the direct and prism images.

Figure 6.21: Sensitivity versus wavelength for HRC/PR200L.

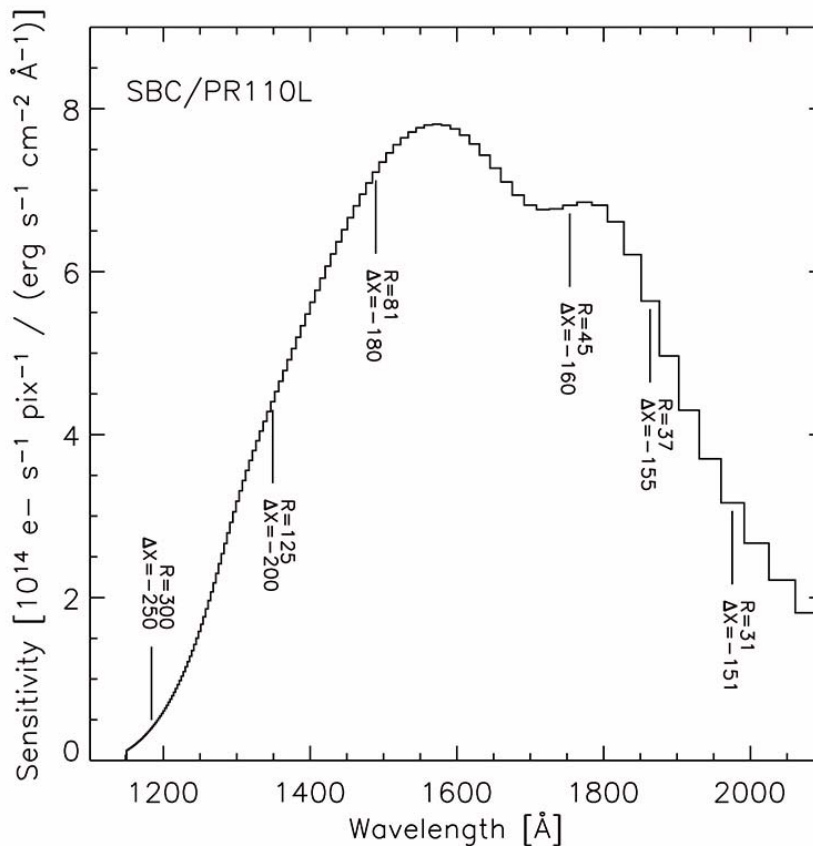


The numbers indicate the resolving power (R) and the offset from the direct image in pixels (Δx) as functions of wavelength.

6.3.4 SBC PR110L

The PR110L prism is sensitive to below 1200 Å and includes the geo-coronal Lyman-alpha line, so it is subject to high background. The dispersion at Lyman-alpha is 2.6 Å per pixel. Figure 6.22 shows the sensitivity with wavelength and the wavelength width of the pixels. The long wavelength cut-off of the CsI MAMA detector at ~1800 Å occurs before the long wavelength build-up of flux; the dispersion at 1800 Å is 21.6 Å/pixel. However the detected counts at the long wavelength edge must be within the MAMA Bright Object Protection Limits (BOP) (see Section 4.6). These limits must include the contribution of the geo-coronal Lyman-alpha flux per SBC pixel. The numbers in Figure 6.22 indicate the resolving power (R) and the offset from the direct image in pixels (Δx) as functions of wavelength. The direct and prism images use distinct apertures with a small angle maneuver between them.

Figure 6.22: Sensitivity versus wavelength for SBC PR110L.

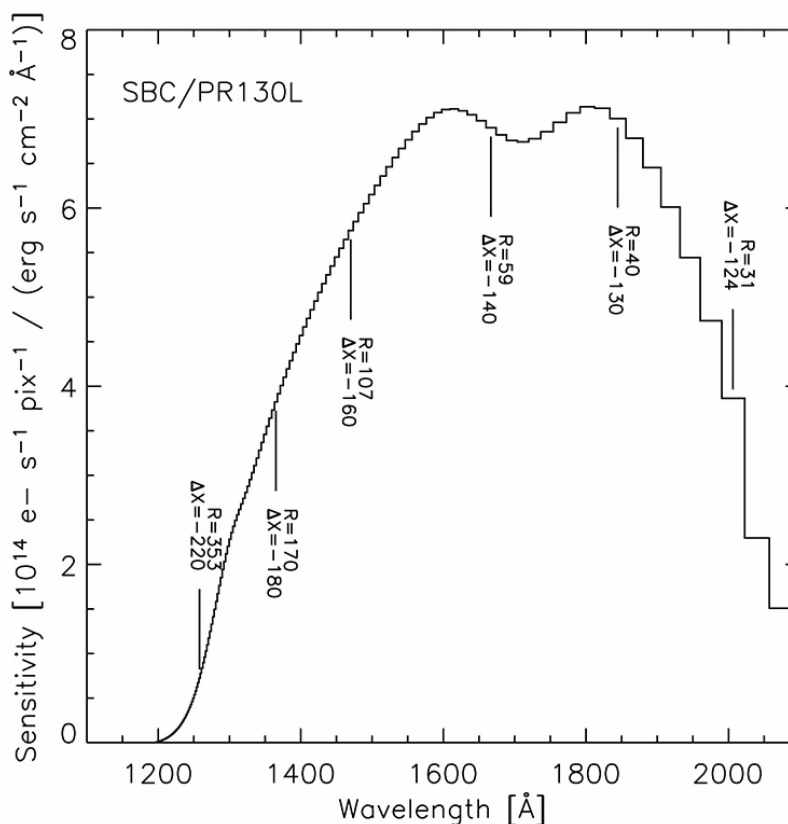


The numbers indicate the resolving power (R) and the offset from the direct image in pixels (Δx) as functions of wavelength.

6.3.5 SBC PR130L

The short wavelength cut-off of the PR130L prism at 1250 Å excludes the geocoronal Lyman-alpha line, making it the disperser of choice for faint object detection in the 1250 Å to 1800 Å window. The dispersion varies from 1.65 Å/pixel at 1250 Å to 20.2 Å/pixel at 1800 Å. Figure 6.23 shows the sensitivity versus wavelength, with the resolving power (R) and the offset from the direct image in pixels (Δx) as functions of wavelength. Bright Object Protection considerations similar to the case of PR110L also apply to the use of this prism, except that the background count rate is lower (see Section 4.6). As for the other prisms, the direct and dispersed images use different apertures with a small angle maneuver between them.

Figure 6.23: Sensitivity versus wavelength for SBC/PR130L.



The numbers indicate the resolving power (R) and the offset from the direct image in pixels (Δx) as functions of wavelength.

6.3.6 Observation Strategy

The normal observing technique for all ACS spectroscopy is to obtain a direct image of the field followed by the dispersed grism/prism image. This combination allows the wavelength calibration of individual target spectra

by reference to the corresponding direct images. For WFC and HRC, the scheduling system automatically inserts a default direct image for each specified spectroscopic exposure, which for G800L consists of a 3 minute F606W exposure, and for PR200L, a 6 minute F330W exposure. If the observer wishes to eliminate the default image, the supported Optional Parameter AUTOIMAGE=NO can be specified. Then a direct image with a different filter and/or exposure time can be specified manually, or no direct image at all in the case of repeated spectroscopic exposures within an orbit, or if no wavelength calibration is required. For the SBC prisms, there is no default direct image because of the Bright Object Protection requirements (Section 7.2); the direct image must always be specified manually, and it must satisfy the BOP limits, which will be more stringent than for the dispersed image.

Because of the offset between the direct imaging and prism aperture definitions, the SAME POS AS option will generally not have the desired effect for prism spectroscopy (PR110L, PR130L, and PR200L). Users who wish to specify offsets from the field center by means of the POS-TARG option should do so by explicitly specifying the same POS-TARG for the direct imaging and prism exposures.

Table 6.4 lists the V detection limits for the ACS grism/prism modes for unreddened O5 V, A0 V, and G2 V stars, generated using the [Exposure Time Calculator](#). WFC and HRC values used the parameters CR-SPLIT=2 and GAIN=2. An average sky background was used in these examples. However, limiting magnitudes are sensitive to the background levels; for instance, the limit magnitude of an A0 V in the WFC using the F606W filter changes by ± 0.4 magnitudes at the background extremes.

Table 6.4: V detection limits for the ACS grism/prism modes.

| Mode | V limit (S/N = 5, exposure time = 1 hour) | | | Wavelength of reference (Å) |
|------------|--|-------------|------------|--------------------------------|
| | O5 V (Kurucz model) | A0 V (Vega) | G2 V (Sun) | |
| WFC/G800L | 24.2 | 24.4 | 24.9 | 7000 |
| HRC/G800L | 23.4 | 23.6 | 24.2 | 7000 |
| HRC/PR200L | 25.6 | 22.7 | 18.8 | 2500 |
| SBC/PR110L | 24.9 | 20.9 | 9.3 | 1500 |
| SBC/PR130L | 25.6 | 21.5 | 9.9 | 1500 |

Chapter 9 provides details of the calculations. Depending on the wavelength region, the background must also be taken into account in computing the signal-to-noise ratio. The background at each pixel consists of the sum of all the dispersed light in all the orders from the background source. For complex fields, the background consists of the dispersed

spectrum of the unresolved sources; for crowded fields, overlap in the spectral direction and confusion in the direction perpendicular to the dispersion may limit the utility of the spectra.

The [ACS Exposure Time Calculator](#) supports all the available spectroscopic modes of the ACS and is available for more extensive calculations at http://apt.stsci.edu/webetc/acs/acs_spec_etc.jsp. The current version employs the on-orbit determinations of the dispersion solution and sensitivity determination where available.

For more detailed simulations of ACS spectra, an image-spectral simulator, called **SLIM**, is available. This tool allows synthetic target fields to be constructed and dispersed images from spectrum templates to be formed. **SLIM** can simulate spectra for all the ACS spectral modes. The simulator runs under Python and an executable version is available at: <http://www.stecf.org/software/SLIM/SLIM10/index.html>. Version 1.0 uses a Gaussian PSF but this has been found to be an adequate representation to the **Tiny Tim** model of the ACS PSF. A detailed description of the tool and examples of its use are given by Pirzkal et. al. ([ACS ISR 01-03](#)).

6.3.7 Extraction and Calibration of Spectra

Since there is no slit in the ACS, the Point Spread Function of the target modulates the spectral resolution. In the case of extended sources it is the extension of the target in the direction of dispersion which sets the achievable resolution. Simulations show that for elliptical sources, the spectral resolution depends on the orientation of the long axis of the target to the dispersion direction and is described in more detail in [ACS ISR 2001-02](#). The dispersion of the grisms and prisms is well characterized, but for the wavelength zero point it is important to know the position of the target in the direct image. For the grisms, the zeroth order will generally be too weak to reliably set the wavelength zero point. Given the typical spacecraft jitter, wavelength zero points to ± 0.4 pixels should be routinely achievable using the direct image taken just before or after the slitless spectrum image.

The jitter information can be used to obtain more accurate coordinates for the center of the FOV. These in turn allow one to determine better relative offsets between the direct and the spectroscopic images.

The wavelength extent of each pixel for the WFC and HRC G800L modes in the red is small enough that fringing modulates the spectra. For the HRC, the peak-to-peak fringe amplitude is about 30% at 9500 Å, and is about 25% for the WFC chips. In practice, for observations of point sources, and even more so for extended objects, the amount of detectable fringing is significantly reduced by the smoothing effect that the PSF, together with the intrinsic object size, have on the spectrum in the dispersion direction. Moreover, application of an optical model for the

CCD fringing can allow the fringe amplitude per pixel to be reduced to below 4% peak-to-peak.

Because the STSCI pipeline does not provide an extracted spectral count rate vs. wavelength, an extraction software package, **aXe**, is available to extract, wavelength calibrate, flat field, and flux calibrate ACS grism and prism spectra. Full details can be found at:

<http://www.stecf.org/software/aXe/>.

The package is also available in **STSDAS**.

Observing Techniques

In this chapter . . .

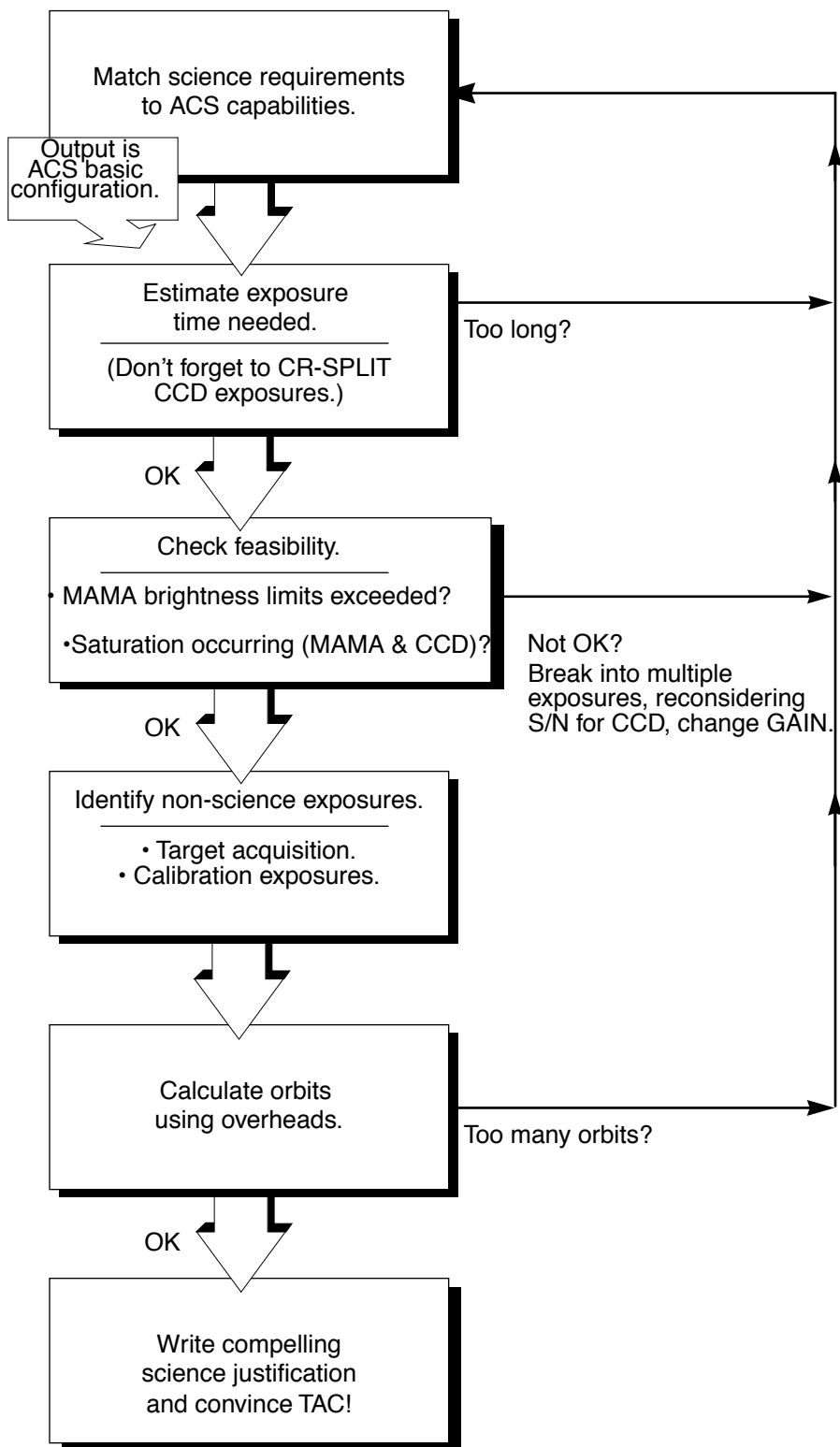
| |
|--|
| 7.1 Designing an ACS Observing Proposal / 113 |
| 7.2 SBC Bright Object Protection / 120 |
| 7.3 Operating Modes / 126 |
| 7.4 Patterns and Dithering / 131 |
| 7.5 A Road Map for Optimizing Observations / 132 |
| 7.6 CCD Gain Selection / 134 |
| 7.7 ACS Apertures / 136 |
| 7.8 Specifying Orientation on the Sky / 144 |
| 7.9 Parallel Observations / 148 |
| 7.10 Pointing Stability for Moving Targets / 154 |

7.1 Designing an ACS Observing Proposal

In this section, we describe the sequence of steps you will need to take when designing your ACS observing proposal. The process is an iterative one, as trade-offs are made between signal-to-noise ratio and the limitations of the instrument itself. The basic sequence of steps in defining an ACS observation are:

- Identify science requirements and select the basic ACS configuration to support those requirements.
- Estimate exposure time to achieve the required signal-to-noise ratio, determine GAIN selection, CR-SPLIT, dithering, and mosaic strategy, and check feasibility, including saturation and bright-object limits.
- Identify any additional target acquisition (coronagraph) and calibration exposures needed.
- Calculate the total number of orbits required, taking into account the overheads.

Figure 7.1: Defining an ACS observation.



7.1.1 Identify Science Requirements and Define ACS Configuration

First and foremost, of course, you must identify the science you wish to achieve with ACS. Basic decisions you will need to make are:

- Nature of target
- Filter selection

As you choose your science requirements and work to match them to the instrument's capabilities, keep in mind that those capabilities differ greatly depending on whether you are observing in the optical or near-UV with the CCD, or in the far-UV using the MAMA detector. Trade-offs are described in Table 7.1.

Table 7.1: Science decision guide.

| Decision | Choices | Tradeoffs |
|--------------------|---|--|
| Field of view | Camera Filter selection | WFC: 202 x 202 arcseconds HRC: 29 x 26 arcseconds SBC: 35 x 31 arcseconds |
| Spectral response | Camera Filter selection | WFC: 3700-11,000 Å HRC: 2000-11,000 Å SBC: 1150-1700 Å |
| Spatial resolution | Camera | WFC: ~50 milliarcsecond pixels HRC: ~27 milliarcsecond pixels SBC: ~32 milliarcsecond pixels |
| Filter selection | Camera | WFC: broad, medium & narrow band, ramps HRC: Visible, UV, ramp middle sections |
| Spectroscopy | Camera Spatial resolution Field of view Wavelength range | Grism (G800L): WFC and HRC Prism (PR200L): HRC Prism (PR110L, PR130L): SBC |
| Polarimetry | Filters | UV polarizers combine with Wheel 2 filters VIS polarizers combine with Wheel 1 filters |
| Coronagraphy | Filter selection | Coronagraphic imaging available with HRC only |

Imaging

For imaging observations, the base configuration is detector (Configuration), operating mode (MODE=ACCUM), and filter. Chapter 5 presents detailed information about each ACS imaging mode.

Special Uses

We refer you to Chapter 6 if you are interested in any of the following special uses of ACS: slitless spectroscopy, polarimetry, and coronagraphy.

7.1.2 Use of Available-but-Unsupported Capabilities

A set of core ACS capabilities to support scientific observations has been established. In addition there are a few capabilities with ACS, some of which are mentioned in this Handbook, for which limited access is available. These capabilities are “available-but-unsupported,” but, in consultation with an ACS Instrument Scientist, may be requested. These include a few apertures, limited interest optional parameters, some GAIN options, and filterless (CLEAR) operation. If you find that your science cannot be obtained using fully supported modes, or that it would be much better with use of these special cases, then you may wish to consider use of an unsupported mode.

Use of unsupported modes comes at a price; they should only be used if the technical requirements and scientific justifications are particularly compelling. The following caveats apply:

- Calibrations for available-but-unsupported modes will not be provided by STScI. It is the observer’s responsibility to obtain such calibrations as needed.
- STScI adopts a policy of shared risk with the observer for the use of these modes. Requests to repeat failed observations taken with unsupported capabilities will not be honored if the failure is related to use of this capability.
- User support from STScI will be more limited.

Phase I proposals that include use of unsupported ACS capabilities must include the following:

- Justification of why supported modes don’t suffice;
- A request for any observing time needed for calibration purposes;
- Justification for added risk of use in terms of scientific payback;
- Demonstration that the observers are able to analyze such data.

During the Phase II proposal submission process, use of available-but-unsupported modes requires formal approval from the ACS Team at STScI. To request permission for use of an available-but-unsupported mode, please send a brief e-mail to your Program Coordinator (PC) that addresses the above four points. The PC will relay the request to the contact scientist or relevant ACS instrument scientist, who will decide whether the use will be allowed. This procedure ensures that any potential technical problems have been taken into account. Note also that archival research may be hindered by use of these modes. As a result, requests for use of unsupported modes which do not adequately address the above four points, or which will result in only marginal improvements in the quality of the data obtained, may be denied, even if the request was included in your approved Phase I proposal.

The current list of available-but-unsupported items are:

- Targets: BIAS
- Apertures: WFC2-2K
- Optional parameters: SIZEAXIS1, SIZEAXIS2, CENTERAXIS1, CENTERAXIS2, COMPRESSION, AMP, FLASHEXP, WFC: GAIN=4,8, HRC: GAIN=1,8
- Spectral elements: CLEAR (both WFC and HRC)
- ACQ mode: optional parameter GAIN

7.1.3 Determine Exposure Time and Check Feasibility

Once you've selected your basic ACS configuration, the next steps are:

- Estimate the exposure time needed to achieve your required signal-to-noise ratio, given your source brightness. (You can use the [ACS Exposure Time Calculator](#) for this; see also Chapter 9 and the plots in Chapter 10).
- For observations using the CCD detectors, ensure that for pixels of interest, you do not exceed the per pixel saturation count limit of the CCD full well or the 16 bit word size at the GAIN setting you choose.
- For observations using the MAMA detector, ensure that your observations do not exceed brightness (count rate) limits.
- For observations using the MAMA detector, ensure that for pixels of interest, your observations do not exceed the limit of 65,535 accumulated counts per pixel per exposure imposed by the ACS 16 bit buffer.

To determine your exposure-time requirements, consult Chapter 9 where an explanation of how to calculate a signal-to-noise ratio and a description of the sky backgrounds are provided. To assess whether you are close to the brightness, signal-to-noise, and dynamic-range limitations of the detectors, refer to Chapter 4.

If you find that the exposure time needed to meet your signal-to-noise requirements is too great, or that you are constrained by the detector's brightness or dynamic-range limitations, you will need to adjust your base ACS configuration. Table 7.2 summarizes the options available to you and steps you may wish to take as you iterate to select an ACS configuration which is both suited to your science and is technically feasible.

Table 7.2: Science feasibility guide.

| Action | Outcome | Recourse |
|--|---|---|
| Estimate exposure time. | If too long, re-evaluate instrument configuration. | Consider use of an alternative filter. |
| Check full-well limit for CCD observations. | If full well exceeded and you wish to avoid saturation, reduce time per exposure. | Divide total exposure time into multiple, short exposures. ¹ Consider use of different Gain. |
| Check bright-object limits for MAMA observations. | If source is too bright, re-evaluate instrument configuration. | Consider the use of an alternative filter or change detectors and wavelength regime. |
| Check 65,535 counts-per pixel limit for MAMA observations. | If limit exceeded, reduce time per exposure. | Divide total exposure time into multiple, short exposures |

1. Splitting CCD exposures affects the exposure time needed to achieve a given signal-to-noise ratio because of the read noise.

7.1.4 Identify Need for Additional Exposures

Having identified a sequence of *science* exposures, you need to determine what additional exposures you may require to achieve your scientific goals. Specifically:

- For coronagraphy, determine what filter and target-acquisition exposure will be needed to acquire your target in the target acquisition aperture. This target acquisition zeroes out the position errors inherent in the guide stars.
- If the success of your science program requires calibration to a higher level of precision than is provided by STScI calibration data, and if you are able to justify your ability to reach this level of calibration accuracy yourself, you will need to include the necessary calibration exposures in your program, including the orbits required for calibration in your total orbit request.

7.1.5 Data Volume Constraints

If ACS data are taken at the highest possible rate for more than a few orbits or in the Continuous Viewing Zone (CVZ), it is possible to accumulate data faster than it can be transmitted to the ground. High data volume proposals will be reviewed and, on some occasions, users may be requested to break the proposal into different visits. Consider using sub-arrays, or take other steps to reduce data volume.

7.1.6 Determine Total Orbit Request

In this step, you place all of your exposures (science and non-science, alike) into orbits, including tabulated overheads, and determine the total number of orbits required. Refer to Chapter 8 when performing this step. If you are observing a small target and find your total time request is significantly affected by data-transfer overheads (which will be the case *only* if you are taking many separate exposures under 339 seconds with the WFC), you can consider the use of CCD subarrays to lessen the data volume. Subarrays are described in Section 7.3.1 (WFC), Section 7.3.2 (HRC), and in Section 8.2.1.

At this point, if you are happy with the total number of orbits required, you're done! If you are unhappy with the total number of orbits required, you can adjust your instrument configuration, lessen your acquisition requirements, or change your target signal-to-noise or wavelength requirements, until you find a combination which allows you to achieve your science goals.

7.1.7 Charge Transfer Efficiency

All CCDs operated in a radiative environment are subject to a significant degradation in charge transfer efficiency (CTE). The degradation is due to radiation damage of the silicon, inducing the creation of traps that impede an efficient clocking of the charge on the CCD. Since reading out the ACS WFC requires 2048 parallel transfers and 2048 serial transfers, it is not surprising that CTE effects have begun to manifest themselves in the first years of ACS operation. For this reason, it is likely that some types of science, particularly those in which the source flux in each image is expected to be low (< 0.1 electrons/second) and compact, will be most effectively performed during the first few years of ACS operation.

Initial expectations for growth of CTE for the Wide Field Camera have proven to be conservative. Multiple iterations of special programs designed to track the growth of CTE over time show that after 1 year of operation, there was a loss of approximately 1 to 2% in the counts from a star with between 50 and 150 total electrons, a nominal sky background of 30 electrons, and a placement at row 1024 (center) in one of the WFC chips. Absolute and relative measurements of the CTE show that the degradation proceeds linearly with time. Thus, such a target would experience a loss of approximately 4% to 8% in early 2006. A target placed at the WFC aperture reference point, near the maximum number of parallel shifts during readout, would have approximately twice the loss. Expected absolute errors after calibration of science data, at these low-loss levels, is expected to be of order 25% the relative loss.

The aperture WFC1-CTE is available to mitigate CTE loss. This aperture has the same area as the WFC1 aperture except that the reference

position is 200 pixels from the upper right corner of chip 1, in both the chips x- and y- direction. Therefore, WFC1-CTE is not appropriate for highly extended targets.

As the CTE effects worsen in future cycles, users may want to consider using the post-flash capability (currently an “available-but-unsupported” mode) to add a background level to their images. This causes the Poisson noise from the background level to increase and imposes a non-uniform background, but to-date only marginally improves the CTE performance of the detector. At present, we do not recommend the use of the post-flash capability for any applications, but we will continue to track this carefully.

7.2 SBC Bright Object Protection

7.2.1 How Do You Determine if You Violate a Bright Object Limit for SBC Exposures?

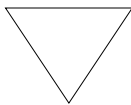
High global and local count rates can cause catastrophic damage to the SBC detector. Therefore, targets should be checked to verify that their fluxes do not exceed the defined SBC safety limits. As a first step, you can check your source V magnitude and peak flux against the bright-object screening magnitudes in Table 7.4 for your chosen observing configuration. In many cases, your source properties will be much fainter than these limits, and you need not worry further.

However, the magnitudes in this table are hard screening limits that correspond to the count rate limits in Table 7.4 and the output of the [ACS Exposure Time Calculator](#). In earlier editions of this Handbook, these magnitudes were made fainter by arbitrary 1 or 2 magnitude pads, depending on the spectral-type range, which have now been removed. If your target is near these limits (within 2 magnitudes or a factor of 6.3 of the flux limits), then you need to carefully consider whether your source will be observable in the chosen configuration. Remember that the limits in these tables assume zero extinction. Thus, you will want to correct the limits appropriately for your source reddening due to interstellar dust.

You can use the information presented in Section 9.2 to calculate peak and global count rates. You can also use the [ACS Exposure-Time Calculator](#) to calculate the expected count rate from your source. The ETC has a host of template stellar spectrograms. If you have a spectrum of your source (e.g., from IUE, FOS, GHRS, or STIS) you can also use it directly in the calculator. As implied by the footnotes to Table 7.4, the model spectra in the [ETC](#) cannot be used for bright-object checking at the solar spectral type and later; the UV spectra of such stars are dominated by emission lines and continua not reproduced by the models. For these types,

more realistic theoretical or observational input spectra (e.g., from the IUE or HST archives) must be used. The calculator will evaluate the global and per pixel count rates, and will warn you if your exposure exceeds the absolute bright-object limits. We recommend you use the [ACS Exposure Time Calculator](#) if you have *any doubt* that your exposure may exceed the bright-object MAMA limits.

7.2.2 Policy and Observers' Responsibility in Phase I and Phase II



It is the responsibility of the observer to ensure that observations do not exceed the bright-object count limits stated in Table 7.3.

It is your responsibility to ensure that you have checked your planned observations against the brightness limits prior to proposing for Phase I. If your proposal is accepted and we, or you, subsequently determine in Phase II that your source violates the absolute limits, then you will either have to change the configuration or target, if allowed, or lose the granted observing time. We encourage you to include a justification in your Phase I proposal if your target is within 1 magnitude of the bright-object limits for your observing configuration. For SBC target-of-opportunity proposals, please include in your Phase I proposal an explanation of how you will ensure your target can be safely observed.

STScI will screen all ACS observations that use the MAMA detector to ensure that they do not exceed the bright-object limits. In Phase II, you will be required to provide sufficient information to allow screening to be performed.

Policy on Observations Which Fail Because they Exceed Bright-Object Limits

If your source passes screening, but causes the automatic flight checking to shutter your exposures or shut down the detector voltage causing the loss of your observing time, *then that lost time will not be returned to you*; it is the observer's responsibility to ensure that observations do not exceed the bright-object limits.

Prism Spectroscopy

To allow screening of your target in Phase II for spectroscopic MAMA observations, you must provide the following information for your target (i.e., for all sources which will illuminate the detector during your observations):

- V magnitude.
- Expected source flux at observing wavelength.
- Spectral type.
- E(B-V).
- B-V color.

If you wish to observe a target which comes within one magnitude (or a factor of 2.5 in flux) of the limits in the magnitude limit table (Table 7.4) after correction for reddening, but which you believe will not exceed the absolute limits in Table 7.3, you must provide auxiliary information to justify your request. Specifically,

- You must provide an existing UV spectrum (e.g., obtained with IUE, FOS, GHRS, STIS or GALEX) of the star which proves that neither the global nor the local absolute limits will be exceeded.

Table 7.3: Absolute SBC count rate screening limits for nonvariable and variable objects.

| Target | Limit type | Screening limit |
|-----------------------------------|------------|------------------------|
| Nonvariable | Global | 200,000 counts/second |
| Nonvariable | Local | 50 counts/second/pixel |
| Irregularly variable ¹ | Global | 80,000 counts/second |
| Irregularly variable ¹ | Local | 20 counts/second/pixel |

1. Applies to the brightest state of the target.

The limits for irregular variable sources are a factor 2.5 more conservative than for sources with predictable fluxes. Predictable variables are treated as nonvariable for this purpose. Examples of sources whose variability is predictable are Cepheids or eclipsing binaries. Irregularly variable sources are, for instance, cataclysmic variables or AGN.

Table 7.4: Bright limit V-band magnitudes for observations with the SBC filters and prisms (no reddening).

| Spectral type | Log T_{eff} | F122M | F115LP | F125LP | F140LP | F150LP | F165LP | PR110L | PR130L |
|---------------------|----------------------|-------|--------|--------|--------|--------|--------|--------|--------|
| O5 V | 4.648 | 16.1 | 19.2 | 19.0 | 18.5 | 18.0 | 16.6 | 15.8 | 15.5 |
| B1 V | 4.405 | 15.2 | 18.4 | 18.2 | 17.7 | 17.1 | 15.7 | 15.0 | 14.7 |
| B3 V | 4.271 | 14.3 | 17.6 | 17.5 | 17.0 | 16.4 | 15.2 | 14.2 | 14.0 |
| B5 V | 4.188 | 13.5 | 17.0 | 16.9 | 16.5 | 15.9 | 14.7 | 13.7 | 13.4 |
| B8 V | 4.077 | 12.0 | 15.9 | 15.9 | 15.5 | 15.0 | 13.8 | 12.7 | 12.5 |
| A1 V | 3.965 | 9.4 | 14.0 | 13.9 | 13.8 | 13.6 | 12.6 | 11.1 | 11.0 |
| A3 V | 3.940 | 8.2 | 13.0 | 13.0 | 12.9 | 12.8 | 12.2 | 10.5 | 10.3 |
| A5 V | 3.914 | 6.8 | 11.9 | 11.9 | 11.9 | 11.9 | 11.6 | 9.9 | 9.8 |
| F0 V | 3.857 | 4.8 | 10.0 | 10.0 | 10.0 | 10.0 | 9.8 | 8.2 | 8.2 |
| F2 V | 3.838 | 4.0 | 9.0 | 9.0 | 9.0 | 9.0 | 9.0 | 7.5 | 7.5 |
| F5 V | 3.809 | 2.1 | 7.4 | 7.4 | 7.4 | 7.4 | 7.3 | 5.9 | 5.8 |
| F8 V | 3.792 | 0.9 | 6.2 | 6.2 | 6.2 | 6.1 | 6.1 | 4.7 | 4.7 |
| G2 V ² | --- | 2.2 | 5.6 | 5.2 | 5.1 | 5.0 | 4.7 | 3.1 | 3.1 |
| G8 V ³ | --- | --- | 5.1 | 5.0 | 4.8 | 4.6 | 3.9 | 2.1 | 2.0 |
| K2 V ⁴ | --- | --- | 5.1 | 5.1 | 4.8 | 4.5 | 3.6 | 3.1 | 3.0 |
| KM III ⁵ | --- | --- | 3.7 | 3.7 | 3.2 | 2.8 | 1.8 | 1.6 | 1.1 |
| Double ⁶ | --- | 13.4 | 16.5 | 16.3 | 15.8 | 15.3 | 13.9 | 13.1 | 12.8 |
| AG Peg ⁷ | --- | 12.9 | 16.0 | 15.8 | 15.4 | 15.0 | 13.3 | 12.4 | 12.1 |

1. O5 V through F8 V values are based on Kurucz models.
2. The magnitudes listed for G2 V are for the Solar template in the [ACS Exposure Time Calculator](#).
3. The magnitudes listed for G8 V are from IUE data for the star Tau Ceti.
4. The magnitudes listed for K2 V are from IUE data for the star Epsilon Eri.
5. The magnitudes listed for KM III are from IUE data for 9 stars of these types.
6. System made of a main sequence late-type star with an O5 V star contributing 20% to the total light in the V band. In the UV, the O5 component dominates and sets the same magnitude limit for companion types A to M.
7. A star with a flux distribution like the symbiotic binary AG Peg.

Imaging

The SBC imaging bright-object screening magnitudes in Table 7.4 are very stringent, ranging from $V = 15.5$ to $V = 19.2$ for an unreddened O5 star in the different imaging apertures, and apply to all sources imaged onto the MAMA detector (i.e., not just the intended target of interest).

STScI has been using the second-generation [Guide-Star Catalog \(GSC II\)](#) to perform imaging screening for objects in the field of view other than the target itself. The [GSC II](#) contains measurements from photometrically calibrated photographic plates with color information for magnitudes down to at least $V = 22$ magnitudes. This information is used to support bright-object checking for fixed and for moving targets. STScI will make a best effort to perform the imaging screening using [GSC II](#). However, observers should be prepared for the possibility that under exceptional circumstances [GSC II](#) may be insufficient. For instance, fields close to the Galactic plane may be too crowded to obtain reliable photometry. If for any reason the screening cannot be done with [GSC II](#), the observer is responsible for providing the required photometry. In the case of moving targets, STScI will identify “safe” fields, and the observations will be scheduled accordingly.

7.2.3 Bright-Object Protection for Solar System Observations

Observations of planets with the SBC require particularly careful planning due to very stringent overlight limits. In principle, Table 7.3 and Table 7.4 can be used to determine if a particular observation of a solar-system target exceeds the safety limit. In practice, the simplest and most straightforward method of checking the bright object limits for a particular observation is to use the [ACS Exposure-Time Calculator](#). With a user-supplied input spectrum, or assumptions about the spectral energy distribution of the target, the [ETC](#) will determine whether a specified observation violates any bright object limits.

Generally speaking, for small ($< \sim 0.5$ to 1 arcseconds) solar-system objects the local count rate limit is the more restrictive constraint, while for large objects ($> \sim 1$ to 2 arcseconds) the global limit is more restrictive.

As a first approximation, small solar system targets can be regarded as point sources with a solar (G2 V) spectrum, and if the V magnitude is known, Table 7.3 and Table 7.4 can be used to estimate whether an observation with a particular ACS prism or filter is near the bright-object limits. V magnitudes for the most common solar-system targets (all planets and satellites, and the principal minor planets) can be found in the *Astronomical Almanac*. This approximation should provide a conservative estimate, particularly for the local limit, because it is equivalent to assuming that all the flux from the target falls on a single pixel, which is an overestimate, and because the albedos of solar-system objects in the UV

are almost always significantly less than their values in the visible part of the spectrum. A very conservative estimate of the global count rate can be obtained by estimating the peak (local) count rate assuming all the flux falls on one pixel, and then multiplying by the number of pixels subtended by the target. If these simple estimates produce numbers near the bright-object limits, more sophisticated estimates may be required to provide assurance that the object is not too bright to observe in a particular configuration.

For large solar-system targets, checking of the bright-object limits is most conveniently done by converting the integrated V magnitude (V_0 , which can be found in the *Astronomical Almanac*) to V magnitude/arcseconds² as follows:

$$V/(\text{arcsec}^2) = V_0 - 2.5\log(1/\text{area})$$

where *area* is the area of the target in arcseconds². This surface brightness and the diameter of the target in arcseconds can then be input into the [ETC](#) (choose the Kurucz model G2 V spectrum for the spectral energy distribution) to test whether the bright-object limits are satisfied.

7.2.4 Prime and Parallel Observing with the SBC

STScI will perform screening of all SBC exposures prior to scheduling. Targets not established as safe for the configuration in which they are being observed will not be scheduled. Observations that pass screening but are lost in orbit due to a bright-object violation will not be rescheduled. Observers are responsible for ensuring that their observations do not violate the SBC count-rate limits.

To ensure that STScI can adequately screen observations, special constraints are imposed on parallel observing with the SBC. In particular:

- No pure parallels are allowed using the SBC.
- Coordinated parallels are allowed with the SBC only if an exact spacecraft orientation (ORIENT) is requested, and the RA and Declination of the parallel field are determined. Note that the specification of an exact ORIENT usually limits the scheduling of observations each year. The observer is responsible for ensuring that observations do not violate the SBC count rate limits both for coordinated parallel SBC observations and for prime observations.
- SNAPSHOT observations with the SBC are not allowed.

Table 7.5: Bright object protection policy for SBC observations.

| Type of observing | Policy |
|----------------------|--|
| Prime | Allowed if target passes screening |
| Snapshots | Not allowed |
| Coordinated parallel | Allowed only if ORIENT is exactly specified and field passes screening |
| Pure parallel | Not allowed |

Targets that are one magnitude or more fainter than the magnitude limits in the screening tables generally automatically pass screening. For a target that is within one magnitude of the screening limits, observers must provide a calibrated spectrum of the source at the intended observing wavelength. If such a spectrum is not available, the prospective GO must request an orbit in Phase I for a pre-qualification exposure, during which the target spectrum must be determined by observation in an allowed configuration.

Please note that if you are proposing SBC target-of-opportunity observations, we ask you to provide an explanation in your Phase I proposal of how you will ensure that your target can be safely observed.

7.3 Operating Modes

ACS supports two types of operating modes:

- **ACCUM** for each of the cameras. This is the standard data taking mode used by observers.
- **ACQ** (acquisition). This is the mode used to acquire a target for coronagraphic observations. ACQ is only available with the HRC.

7.3.1 WFC ACCUM Mode

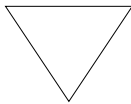
In this mode the WFC CCD accumulates signal during the exposure in response to photons. The charge is read out at the end of the exposure and translated by the A-to-D converter into a 16 bit data number (DN), ranging from 0 to 65,535. The number of electrons per DN can be specified by the user as the **GAIN** value. The full well of the WFC CCD is about 85,000 electrons and consequently, all **GAIN** values larger than 1 will allow the observer to count up to the full well capacity. For **GAIN=1** only 75% of full well capacity is reached when the DN value saturates at 65,535. The read-out noise of the WFC CCD is about 5 electrons rms and thus it is critically sampled even at **GAIN=2**. WFC can make use of a

user-transparent, lossless, on-board compression algorithm, the benefits of which will be discussed in the context of parallel observations. The algorithm is more effective with higher GAIN values (i.e. when the noise is undersampled).

Fifteen supported apertures, (see Table 7.6) are accessible to WFC users. WFC1-FIX and WFC2-FIX select the geometric centers of the two WFC camera chips. WFCENTER corresponds to the geometric center of the combined WFC field, and will be useful for facilitating mosaics and obtaining observations at multiple orientations. WFC, WFC1, and WFC2 are located near the field of view center and the centers of chips 1 and 2, respectively. Their locations were chosen to be free of detector blemishes and hot pixels, and they are the preferred apertures for typical observations. See Section 7.7 for more details about ACS apertures, including subarray apertures.

Usually each CCD is read from two amplifiers to minimize charge transfer efficiency (CTE) problems and read-out time. As a result, the two 2K by 2K portions in a single chip may have slightly different read-out noise. The WFC chips have both physical and virtual overscans that can be used to estimate the bias level and the read-out noise on each single image.

The ACS internal buffer can store only a single full frame WFC image. When this image is compressed, and depending on the compression factor, the buffer can store additional HRC and SBC images. As a consequence of the implementation of the compression strategy, under no circumstance can more than one full frame WFC image be stored in the buffer. Note that the adopted policy is not to compress primary WFC observations. The present flight software does not allow reading an ACS frame directly into the HST on-board recorder. Images have to be first stored in the internal buffer. When more than one WFC image is obtained during an orbit a buffer dump must occur during the visibility period so as to create space in the buffer for a new WFC image.



If each exposure is longer than approximately 339 seconds, buffer dumps can occur during the integration of the following image with no impact on observing efficiency.

Conversely, short, full frame, integrations with the WFC during the same orbit will cause buffer dumps to be interleaved with observations and will negatively affect the observing efficiency. See Chapter 8 for more details about ACS overheads.

WFC CCD Subarrays

It is possible to read-out only a portion of a detector with subarrays, which have a smaller size than the full frame. Subarrays are used to reduce

data volume, to store more frames in the internal buffer (thus avoiding the efficiency loss due to buffer dumps), or to read only the relevant portion of the detector when imaging with ramp filters or with HRC filters (which produce a vignetted field of view on WFC). WFC subarrays have some limitations:

1. They can be specified only on a single WFC chip;
2. They may have physical but no virtual overscan;
3. They cannot include the CCD edge (i.e. the maximum subarray size is 4140 by 2046); and
4. They are read through a single amplifier and may take longer to read-out than a full-frame image, depending on size and location.

Users can use WFC subarrays either by using a supported pre-defined subarray (which is recommended) or by defining their own general subarrays. For supported subarrays, the dark, flat, and bias frames used for calibration will simply be extracted from available full-frame images. Tests have shown that this does not degrade the quality of the dark, flat-field or bias corrections, as compared to full-frame data. However, this is true only for subarrays that fall entirely within a single amplifier quadrant and include a corner section with the overscan (true for all the supported subarrays). Users who define general subarrays that cross amplifier boundaries or do not include a corner (not advised) must request their own subarray bias images, and these will typically be scheduled during the following occultation. In some special cases where a general subarray is cleverly defined so as to include a physical overscan region, no separate bias frames are needed.

Pre-defined subarrays are the appropriate choice for observing a small target when lessening the data volume is desired. These supported subarrays for WFC are invoked by using the named apertures WFC1-1K, WFC1-2K, and WFC1-512. On WFC1, at the amplifier B corner there are square apertures WFC1-512, WFC1-1K, and WFC1-2K with light collecting areas being squares with sides of length 512, 1024, and 2048 pixels. A 2048 pixel aperture is available at the amplifier D corner of WFC2 called WFC2-2K, but is available-but-unsupported. These all incorporate 22 columns of the physical overscan pixels. These have been chosen bearing in mind that as charge transfer efficiency degrades with radiation damage to the detectors, there is an advantage in being close to the readout amplifier. The reference pixel and extent of the subarrays are listed in Table 7.6. More information about pre-defined subarray apertures can be found in Section 7.7

To define a general subarray, the available-but-unsupported parameters SIZEAXIS1, SIZEAXIS2, CENTERAXIS1, and CENTERAXIS2 can be used. More practical information about defining subarrays can be found at <http://www.stsci.edu/hst/acs/faqs/subarrays.html>. When polarizers

or the small HRC filter F892N are used with the WFC, the aperture WFC must be selected and a subarray is forced by the system. If the user chooses to use a polarizer with a ramp filter, then they may select an available-but-unsupported ramp aperture, but a subarray is still read out.

Ramp Filters

Unlike WFPC2, ACS ramp filter observations at different wavelengths are obtained at the same location on the CCD, thus simplifying data processing. In practice the observer specifies a ramp filter and a central wavelength; the filter wheel is automatically rotated to place the central wavelength at the reference point of the relevant aperture. The different ramp apertures and their reference points on the WFC chips are shown in Table 7.6 and Figure 7.4. To select the desired wavelength, the ramp filter is rotated to move the appropriate part of the filter over the specified pointing. Observations with different ramp filters do not generally occur at the same pointing. The precise location where a given observation will be performed can be found from Table 7.6 where for each ramp filter we list the fiducial pointing for the inner IRAMP, middle MRAMP, and outer ORAMP filter segment. The inner segment corresponds to the WFC1 chip, while the outer segment corresponds to the WFC2 chip. The middle segment can be used with either of the WFC chips but is used by default with WFC1. For any ramp filter observation three ramp filters will end up in the FOV even though the target is properly positioned only for the requested one. Or, if desired, the user can define a general subarray to readout only a portion of the chip. Table 5.1 and Table 5.2 can be used to determine the remaining two ramp filters which can be of interest for serendipitous observations. While all fifteen ramp filters can be used with the WFC, only the five middle ramp filters are available with the HRC. Ramps used with the HRC cover the region over the HRC chip defined by the HRC aperture (Table 7.8).

7.3.2 HRC ACCUM Mode

In this mode the HRC CCD accumulates signal during the exposure in response to photons. The charge is read out at the end of the exposure, and translated by the A-to-D converter into a 16 bit data number (DN) ranging from 0 to 65,535. The number of electrons per DN can be specified by the user as the GAIN value. The full well of the HRC CCD is about 155,000 electrons. In order not to overflow the 16 bit pixel word size, one needs to use GAIN=4. In many applications GAIN=2 is adequate since it still allows critical sampling of the read-out noise of HRC (about 4.7 electrons rms) and, for this reason, it is the default GAIN ratio. For typical HRC observations the observer should specify the HRC aperture which is approximately located at the center of the field of view in a location free of detector blemishes and hot pixels. The HRC-FIX aperture

is located at the geometric center of the field-of-view. Additional apertures are used for coronagraphic observations - see Table 7.8 for more details of HRC apertures.

Up to 16 HRC images can be stored in the ACS buffer. Alternatively, HRC images can share the buffer with some SBC images and/or a single compressed WFC image. The number of HRC images will depend in the latter case on the WFC compression factor.

HRC CCD Subarrays

Similarly to the WFC, a subarray is obtained when only a portion of the detector is read-out and transmitted to the ground. Generally the smaller size of the HRC CCD reduces the usefulness of subarrays. However, subarrays are used during on-board coronagraphic target acquisition, which is similar to the STIS target acquisition and cannot be changed. A square subarray of 512 x 512 pixels in the C Amp readout corner and a 512 pixel square aperture centered on the 1.8 arcseconds coronagraphic spot are available. In addition, on an available-but-unsupported basis, nearly arbitrary sizes and locations for subarrays can be specified. When coupling use of subarrays with PATTERNS or POS TARGs, the issue arises of whether to keep the subarray fixed in pixel space, or have it track and stay centered on the target. With PATTERNS, the subarray stays fixed in pixel space. When using POS TARGs, the observer can decide which mode to adopt.

7.3.3 SBC ACCUM Mode

The SBC ACCUM mode accumulates photons into a 1024 by 1024 array, with 16 bits per pixel. The data are sent to the onboard recorder via the internal ACS memory buffer at the end of the exposure. ACCUM is the only mode available for SBC observations; the Time Tag mode of the STIS MAMAs is not available on ACS. The minimum SBC exposure time is 0.1 seconds and the maximum is 1.0 hour. The minimum time between SBC exposures is 40 seconds. Note that the SBC, like the STIS MAMAs, has no read-out noise. As a consequence there is no scientific driver for longer exposure times apart from the small overhead between successive images, described in Section 8.2.

Up to 16 SBC images can be stored in the internal buffer. SBC images can also share the buffer with HRC images and/or a single, compressed WFC image.

7.3.4 HRC ACQ Mode

The HRC target acquisition mode is used to place a target under the occulting finger or the coronagraphic mask. Observations through two

(non-polarizer) filters are allowed in ACQ images to cut down the flux to acceptable levels for very bright targets. Due to the optical design of HRC the simultaneous use of two filters leads to a degraded imaging quality but which is still acceptable for a successful target acquisition. The ACS IDT has identified a number of filter combinations that effectively act as neutral density filters, and allow the observer to acquire a very bright target that would otherwise saturate the CCD. These filter pairs are F220W+F606W, F220W+F550M, and F220W+F502N in order of decreasing transmission. A more complete description of the target acquisition procedure is given in Section 6.2.2.

7.4 Patterns and Dithering

A number of different patterns are available for ACS to support dithered observations, i.e., observations where the pointing is shifted between frames. The size of the offsets can be very different depending on the purpose of offsetting the pointing between exposures. In particular, it is useful to distinguish between *mosaicing* and *dithering*. Mosaicing is done with the aim of increasing the area covered by a particular set of exposures, while providing a seamless joining of contiguous frames. Dithering is done for a variety of reasons, such as

- better removal of detector blemishes
- straightforward removal of hot pixels
- improving the PSF sampling
- improving the photometric accuracy by averaging over flat fielding errors
- obtaining a contiguous field of view for the WFC.

Patterns have been defined to allow ACS users to easily carry out both mosaicing and dithering. Using patterns allows exposures to be automatically associated in *calacs* pipeline processing with the following restrictions: only pattern exposures obtained within a single visit, and those patterns where the cumulative offset is under the ~ 100 arcsecond guide star limitation, can be associated. For the latter, these patterns include the dither patterns for all three cameras, the HRC and SBC mosaic patterns, and the 2-point ACS-WFC-MOSAIC-LINE pattern. All patterns designed with POS TARGs will not be associated. These are described in detail on the ACS Dither Web page: <http://www.stsci.edu/hst/acs/proposing/dither>.

The plate scale for the WFC varies by about $\pm 5\%$, so a one pixel dither near the center will be 0.95 or 1.05 pixels near the corners. For this reason, dither patterns should strike a balance between being large enough to reject detector artifacts, and being as compact as possible to maintain the

integrity of the pattern over the entire field-of-view. Large displacements will have varying sub-pixel properties across the image.

In addition to the plate scale variation associated with the significant ACS geometric distortion, there can also be a temporal variation of overall image alignment. Some CR-SPLIT images taken during SMOV testing, in which the two components were separated by the scheduling system across orbital occultations (about a one hour gap), showed registration differences of about 0.5 pixels corner-to-corner. Thus, to combine multiple images to create oversampled images at the resolution ACS is capable of providing, the user may need to allow for the general problem of combining distorted, misregistered images. A variety of tools are being made available within STSDAS and `pyraf` to assist with these tasks including `pydrizzle` and `multidrizzle`. See the [ACS Drizzle Web](#) page and the *ACS Data Handbook*.

Additional information on dithering, and processing drizzled data using `multidrizzle` can be obtained from the *Dither Handbook*

7.5 A Road Map for Optimizing Observations

Dithering and CR-SPLITting more than the minimum recommended values tends to yield higher quality images with fewer residual detector defects, hot pixels or CR signatures in the final combined image. In cases where hot pixels are of particular concern, dithering may be especially useful for simultaneous removal of hot pixels and cosmic rays. Unfortunately, splitting a given exposure time into several exposures reduces its signal-to-noise when a noise-limited image is read-out. WFC images longer than about 500 seconds are background limited, while shorter exposures and narrow band images are read-out noise limited for all practical exposure times. Thus, the optimal number of CR-SPLITs and dithering positions is a result of a trade-off between completeness of the hot pixel elimination, CR-rejection, final image quality, and optimal S/N. A schematic flow chart of this trade-off is given in Figure 7.2. The main steps in this, possibly iterative, process are the following:

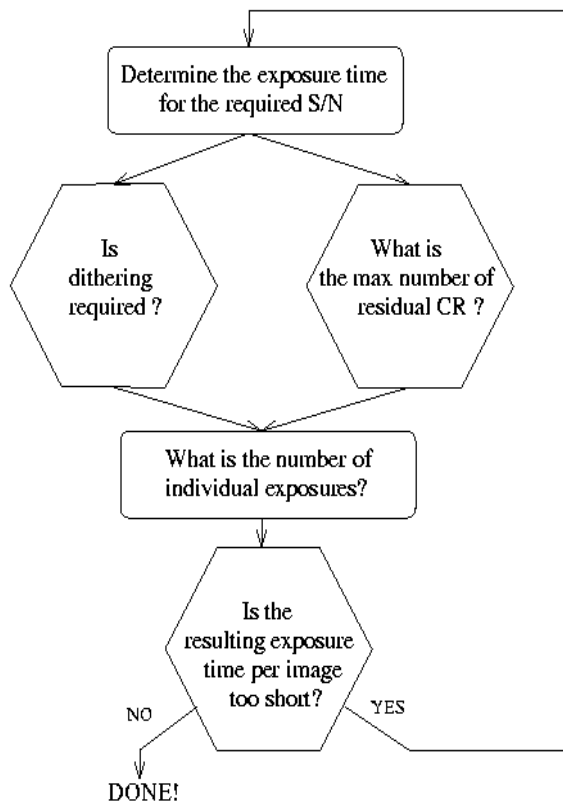
1. Determine the exposure time required to achieve the desired S/N
2. Determine the maximum number of acceptable residual CR in the final combined image. This number depends critically on the scientific objective. For example, for a survey of distant galaxies or a globular cluster color magnitude diagram, a few residual CR will not compromise the scientific output of the observations. In contrast, for a search for an optical counterpart of some radio or gamma ray selected object even one residual CR would not be acceptable over the region of interest. In this latter case, since we expect about ~4% to 7% of the pixels to be affected by CR hits during a one orbit exposure on the WFC, the requirement that no pixel in the final image is

affected by CR hits would force one to use at least 4 CR-SPLITS. For an experiment in which the number of allowed false alarms is zero (e.g., a search for cosmological supernovae), observers may wish to consider using at least twice the number of CR-SPLITS required to formally avoid coincidences. Note also that given the large number of pixels in the WFC even a few thousand residual CR hits would correspond to only a small fraction of the total number of pixels. In general, the number of pixels affected by coincident CR hits for a given total exposure time and number of CR-SPLITS N will be:

$$\left(0.05 \times \frac{ExposureTime}{2400s \times N}\right)^N \times 4096^2$$

3. Determine whether dithering is required. CR-SPLITS have no effect on hot pixels, which result from CCD radiation damage and which persist for about weeks or indefinitely. If such features would critically affect the science, then dithering is required to remove them. For some imaging programs the spatial resolution provided by the WFC and the presence of some detector defects and hot pixels in the final image are acceptable. For such observations, dithering would not be required and one would simply split the exposure time for CR correction. For observations where several orbits worth of data are obtained with each filter, the best strategy is to observe using a sub-pixel dither pattern *without* obtaining multiple images at each position. Since each CR will now influence more than one output pixel the requirement on the number of separate exposures is more stringent than in the simple CR-SPLIT case. If the total exposure time with each filter is short, one will have to compromise between S/N and image quality. In general, dithering with sub-pixel steps increases the number of individual exposures required to eliminate CR hits. Given that the geometric distortion of WFC makes any dithering step non-integer somewhere in the field of view (unless the dither steps are very small, < 2 pixels), the size of the high image quality field of view also comes into play. If the high quality area is small, one may make do with integer pixel dithers. In this case a few CR-SPLITS may be obtained at each dithering position and the combined images may then be combined together using *drizzle* or *multidrizzle*. On the edges of the field the CR-rejection quality will be lower than in the field center. A minimum of 4 images for a two position dither, and 8 for a four position dither are then required.
4. Once the required number of individual exposures has been established on the basis of CR rejection and dithering requirements, the observer will need to verify whether the resulting read-out noise affects the achieved S/N.

Figure 7.2: Schematic flow-chart of the CR-split vs. dithering vs. S/N trade-off.



7.6 CCD Gain Selection

As quantified in Table 4.2 both the WFC and HRC CCDs have selectable gain values near 1, 2, 4, and 8 electrons per digital number. Various factors should influence the gain selected in Phase II for your science program: level of support and calibrations provided, influence of associated readout noise on data quality, dynamic range on the bright end, and data compressibility for WFC in limited applications.

7.6.1 WFC Gain

GAINS 1 and 2 are fully supported for the WFC, since GAIN=1 provides the smallest readout noise, while GAIN=2 (or higher) is needed to sample the available full well depth. It is the goal, now closely achieved, to provide equal calibration support for data taken in these two supported gains, although more calibration data will be taken in the default GAIN=2 setting. Calibration support will not be provided for the

“available-but-unsupported” GAIN=4 and 8 settings; users proposing their use should provide special justification and discussion of calibrations to be used. Note that WFC auto-parallel data is taken with GAIN=2.

While the readout noise is lower at GAIN=1, the advantage over GAIN=2 ($< 0.3 e^-$ extra rms) is modest. GAIN=2 has the offsetting advantage of completely sampling the full well depth of nearly 85,000 e^- , thus providing a > 0.3 magnitudes dynamic range extension before saturation is reached. The latter could be advantageous even for programs in which the prime targets are very faint, if serendipitous objects in the field of view can be used to support image-to-image registration solutions as needed for optimal dithered image combinations. Furthermore, charge is conserved even beyond filling the full well depth; for point sources at GAIN=2 it is possible to obtain valid aperture photometry several magnitudes beyond saturation by summing over all pixels bled into. Both GAINs 1 and 2 provide better than critical sampling of the readout noise supporting robust background sky-level determination even at low values. Recent evidence also suggests that a minor electronic cross-talk feature is relatively less pronounced with GAIN=2 than GAIN=1 (see [ACS ISR 2004-13](#)).

The large pixel count for WFC can create data rate problems if images are acquired as quickly as possible over multiple orbits. The available-but-unsupported mode COMPRESSION is more effective when the noise is undersampled which could result in special circumstances for which the GAIN values of 4 or 8 are preferred.

7.6.2 HRC Gain

GAINs 2 and 4 are fully supported for the HRC, and analogous to the supported WFC values provide a low readout noise case and a GAIN that provides sampling of the physical full well depth.

GAIN=4 on the HRC, which is needed if high dynamic range on the bright end is desired, does not provide critical sampling of the readout noise. Not only is the readout noise penalty in going from GAIN=2 to 4 non-trivial, but background estimation will be less robust without critical noise sampling. As with WFC, when the full well depth is sampled with GAIN=4 the detector response remains accurately linear up to and even well beyond saturation. Compression is not an issue for the small HRC images, therefore use of the unsupported GAIN=8 is not anticipated. GAIN=1 is available-but-unsupported, but the very modest improvement of readout noise in comparison to GAIN=2 ($< 0.2 e^-$ higher rms) seems unlikely to present compelling need for its use.

7.7 ACS Apertures

As discussed in Section 3.3, the ACS consists of three cameras: the WFC, the HRC, and the SBC. The WFC is constructed of two CCDs each nominally 2048 by 4096 pixels, with their long sides adjacent to form a roughly square array, 4096 pixels on a side. The HRC CCD and the SBC MAMA detectors are each 1024 pixels square.

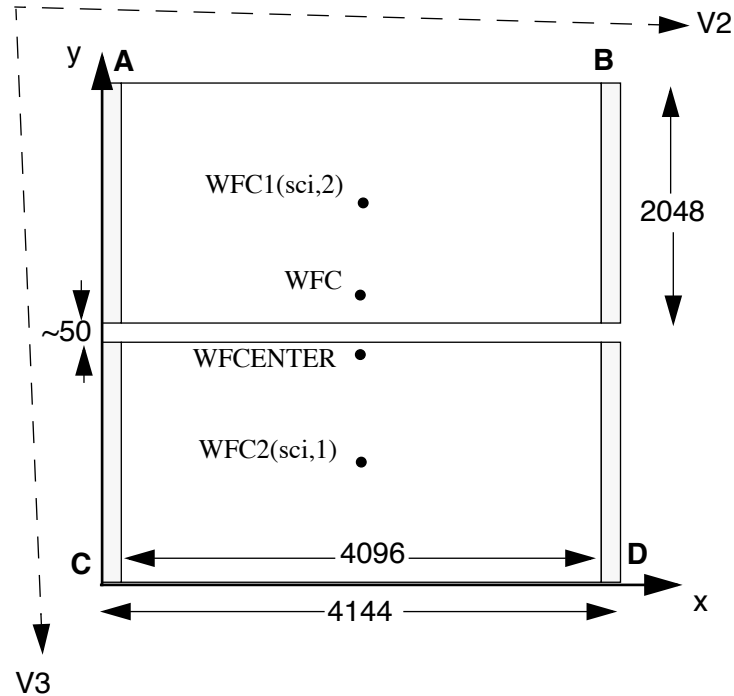
7.7.1 WFC Apertures

The active image area of each WFC detector is 4096 by 2048. The mean scale is 0.049 arcseconds/pixel, and the combined detectors cover an approximately square area of 202 arcseconds on a side. In establishing reference pixel positions we have to consider the overscan pixel areas which extend 24 pixels beyond the edges in the long direction. So each CCD must be regarded as a 4144 by 2048 pixel area. The gap between the two CCDs is equivalent to 50 pixels. In Figure 7.3 the letters A, B, C, and D show the corner locations of the four readout amps.

We define apertures named WFC1 and WFC2 which represent the two CCDs, with their reference points near the geometric center of each chip. The positions have been moved about 50 pixels from the center line to avoid a discontinuity at the amplifier readout boundary. However, we keep two other apertures named WFC1-FIX and WFC2-FIX at the original central locations (2072,1024). For extended sources, choosing new positions may not be of any advantage and it may be more effective to use these fixed positions.

The aperture WFC encompasses both detectors, and has its reference point near the overall center but about 10 arcseconds away from the interchip gap. This has been chosen to be position (2124,200) on the WFC1 CCD. Again, this has been moved away from the center line, but the reference point for WFC-FIX remains at (2073,200). Selection of WFC1, WFC2 or WFC only changes the pixel where the target will be positioned. In all three cases data is normally delivered in a file containing two imsets, one for each detector. See the *ACS Data Handbook* for details of the ACS data format. Reading out a subarray, which consists of part of only one of the chips, is done only if requested.

Figure 7.3: WFC aperture definitions.



WFCENTER is similar to WFC, but is placed at the center of the combined WFC full field. The center is defined as the average of the four corners in the distortion corrected space. Because of the scale variation this does not appear at the center in pixel space, but rather is on WFC2 about 20 pixels from the edge. Selection of WFCENTER can be of use in obtaining observations with maximum overlap at unique orientations and for mosaics.

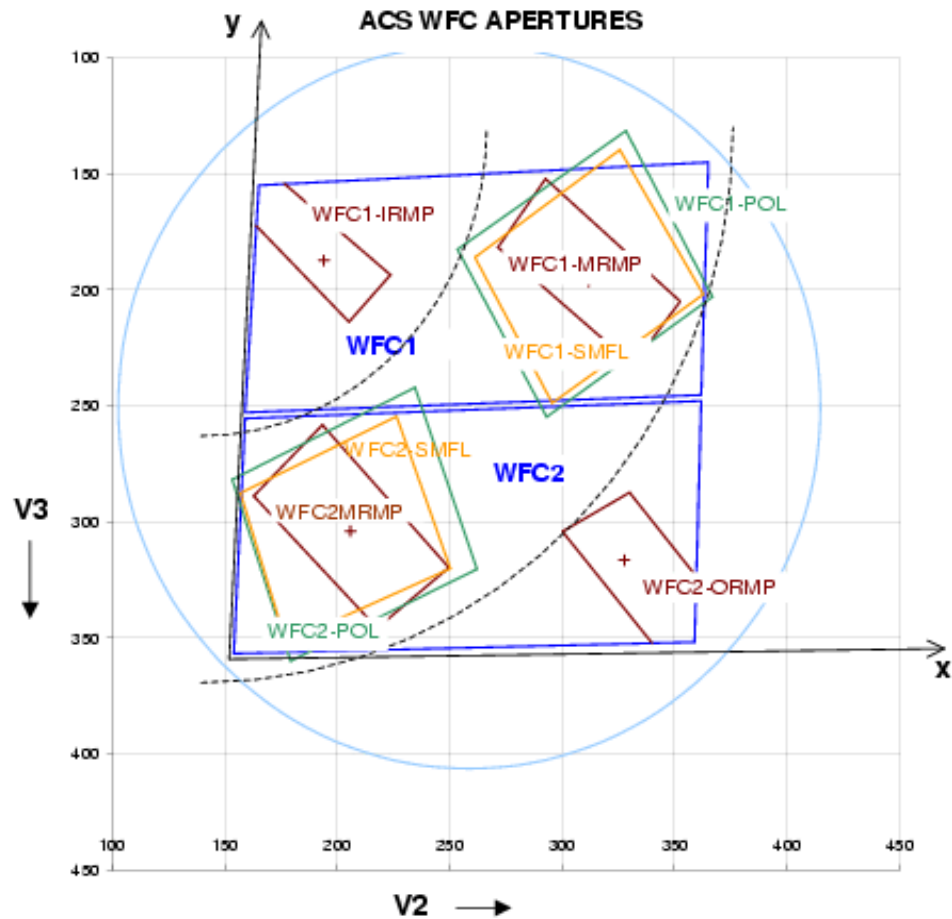
For sets of observations which take place over a substantial part of a year, the telescope roll limitations will require measurements to be taken over most of the angular range. On sky, the WFC aperture is roughly square, and it is natural to design observations in steps of 90° to consistently cover the same area. There will be some region at the edges not covered at all four orientations. However, a square area of side 194.8 arcseconds centered on WFCENTER, and with edges parallel to the V2 and V3 axes, is overlapped at all four positions. In designing a mosaic which combines observations at 90° steps, a translation of about 190 arcseconds between pointings would provide continuous coverage.

7.7.2 Ramp Filter Apertures

Each ramp filter consists of three segments that can be rotated across the WFC field of view as indicated in Figure 7.4. The IRAMP filter can only be placed on WFC1 in a location which will define the aperture WFC1-IRAMP

and the ORAMP only on WFC2 creating the aperture WFC2-ORAMP. The MRAMP filter can lie on WFC1 or WFC2 with corresponding apertures WFC1-MRAMP and WFC2-MRAMP. The approximate aperture locations are indicated in Figure 7.4, while actual data obtained during ground calibrations are overlaid on an image of a ramp filter in Figure 7.5. Operationally, a fixed reference point will be defined for each detector and filter combination. Then the ramp filter will be rotated to place the required wavelength at the reference position.

Figure 7.4: Schematic WFC apertures and ramp filters.

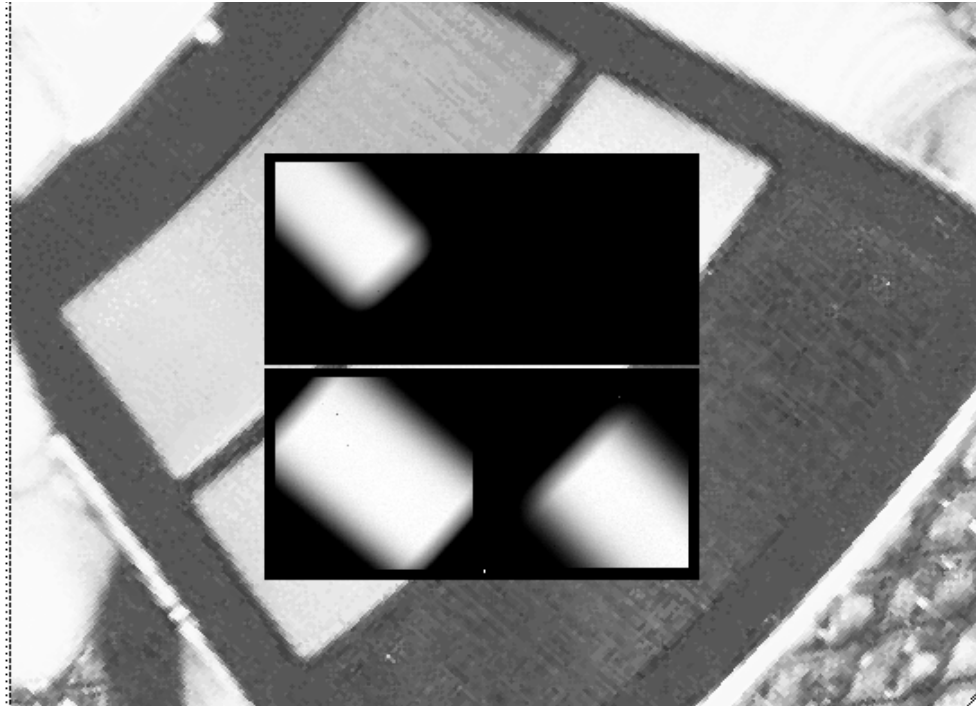


Shown are the approximate active areas defined by the filters. The actual readout areas are the quadrants for the polarizers and small (HRC) filters, and either the quadrant or the full chip for the ramp filters.

The reference positions for all defined apertures are given in Table 7.6 in pixels, and in the telescope V2,V3 reference frame where values are measured in arcseconds. The values given here are based on in-flight calibration results. The x and y axis angles are measured in degrees from the V3 axis towards the V2 axis. This is in the same sense as measuring from North to East on the sky. The “extent” of the ramp filter apertures

given in Table 7.5 are the FWHM of the monochromatic patches (visible in Figure 7.4) measured from a small sample of ground calibration data. To use a ramp filter in a Phase II program, specify the filter name, the wavelength, and the aperture. The scheduling software will then automatically rotate the filter to the appropriate wavelength, and point at the reference point of the aperture chosen. The aperture chosen may either be the full chip or just the quadrant on which the ramp filter lies. This second choice is new as of Cycle 15, and requires that the aperture be specified. The apertures matching each filter are given in Table 7.6 Those with names ending in Q are the quadrants. It will normally be preferable to choose the quadrant aperture to save data volume and buffer dumping time. All listed apertures will be supported and may also be used with non-ramp filters. A target may thereby be put at the same position using a ramp and a non-ramp filter.

Figure 7.5: Monochromatic patches in ground calibration data showing actual aperture sizes through ramp filters (superimposed on photo of ramp filters).



7.7.3 The Small Filter Apertures

When a filter designed for the HRC is used with the WFC, it only covers a small area on either WFC1 or WFC2. The projected filter position may be placed on either chip by selection of the filter wheel setting. Figure 7.4 shows how the filter projection may be placed so as to avoid the borders of the chips. When a WFC observation is proposed using a HRC filter spacecraft commanding software automatically uses internal built-in

apertures designed for these observing scenarios, called WFC1-SMFL and WFC2-SMFL. Reference positions at or near the center of these apertures are defined so that a target may be placed in the region covered by the chosen filter.

The axis angles given in Table 7.6 do not refer to the edges of the apertures as drawn, but rather to the orientation of the x and y axes at the WFC reference pixel. These angles vary slightly with position due to geometric distortion.

For the polarizers and F892N used with WFC, the default will be to read out a subarray. The subarray will be a rectangular area with sides parallel to the detector edges which encompasses the indicated filtered areas. For ramp filters the default will be to readout the entire WFC detector, unless a polarizer is used with the ramp filter, in which case a subarray is readout. Users cannot override the small filter subarrays.

Table 7.6: WFC aperture parameters.

| APT Aperture Name | Readout area | Extent (arcsec) | Reference pixel | Reference V2,V3 (arcsec) | x-axis angle | y-axis angle |
|--------------------------|--------------|-----------------|-------------------------------|--------------------------|------------------------------|--------------|
| | | | | | (degrees from V3 through V2) | |
| WFC | 4096 × 4096 | 202 × 202 | (2124,200) <i>on WFC1</i> | (262,239) | 92.2 | 177.5 |
| WFC-FIX | 4096 × 4096 | 202 × 202 | (2073,200) | (261,198) | 92.5 | 177.3 |
| WFCENTER | 4096 × 4096 | 202 × 202 | (2114,2029) <i>on WFC2</i> | (261,252) | 92.1 | 177.5 |
| WFC1 | 4096 × 4096 | 202 × 202 | (2124, 1024) | (263,198) | 92.5 | 177.4 |
| WFC1-FIX | 4096 × 4096 | 202 × 202 | (2072, 1024) | (261,198) | 92.5 | 177.4 |
| WFC2 | 4096 × 4096 | 202 × 202 | (2124, 1024) | (259,302) | 91.7 | 177.8 |
| WFC2-FIX | 4096 × 4096 | 202 × 202 | (2072, 1024) | (257,302) | 91.7 | 177.8 |
| WFC1-IRAMP | 4096 × 4096 | 25 × 65 | (680,1325) | (194,187) | 93.1 | 176.6 |
| WFC1-MRAMP | 4096 × 4096 | 35 × 80 | (3096,1024) | (312,196) | 92.2 | 177.8 |
| WFC2-MRAMP | 4096 × 4096 | 40 × 80 | (1048,1024) | (206,304) | 91.9 | 177.5 |
| WFC2-ORAMP | 4096 × 4096 | 35 × 65 | (3494,708) | (328,316) | 91.4 | 178.2 |
| WFC1-SMFL ¹ | 2048 × 2048 | 70 × 80 | (3096,1024) | (312,196) | 92.2 | 177.8 |
| WFC2-SMFL ¹ | 2048 × 2048 | 70 × 80 | (1048,1024) | (206,304) | 91.9 | 177.5 |
| WFC1-POL0UV ² | 2048 × 2048 | 90 × 80 | (3096,1024) | (312,196) | 92.1 | 177.8 |
| WFC1-POL0V ² | 2048 × 2048 | 90 × 80 | (3096,1024) | (312,196) | 92.2 | 177.8 |
| WFC2-POL0UV ² | 2048 × 2048 | 90 × 80 | (1048,1024) | (206,304) | 91.9 | 177.5 |
| WFC2-POL0V ² | 2048 × 2048 | 90 × 80 | (1048,1024) | (206,304) | 91.9 | 177.5 |
| WFC1-512 | 512 × 512 | 25 × 25 | (3864,1792) | (352,158) | 92.1 | 178.0 |
| WFC1-1K | 1024 × 1024 | 50 × 50 | (3608,1536) | (338,170) | 92.1 | 177.9 |
| WFC1-2K | 2048 × 2048 | 101 × 101 | (3096,1024) | (312,196) | 92.2 | 177.8 |
| WFC2-2K | 2048 × 2048 | 101 × 101 | (1048,1024) | (206,304) | 91.9 | 177.5 |

Table 7.6: WFC aperture parameters.

| APT Aperture Name | Readout area | Extent (arcsec) | Reference pixel | Reference V2,V3 (arcsec) | x-axis angle | y-axis angle |
|-------------------|--------------|-----------------|-----------------|--------------------------|------------------------------|--------------|
| | | | | | (degrees from V3 through V2) | |
| WFC1-IRAMPQ | 2048 × 2048 | 25 × 65 | (680,1325) | (194,187) | 93.1 | 176.6 |
| WFC1-MRAMPQ | 2048 × 2048 | 35 × 80 | (3096,1024) | (312,196) | 92.2 | 177.8 |
| WFC2-MRAMPQ | 2048 × 2048 | 40 × 80 | (1048,1024) | (206,304) | 91.9 | 177.5 |
| WFC2-ORAMPQ | 2048 × 2048 | 35 × 65 | (3494,708) | (328,316) | 91.4 | 178.2 |
| WFC1-CTE | 4096 × 2048 | 202 × 101 | (3920,1848) | (354,155) | 92.1 | 178 |

1. Apertures are automatically created by commanding software when a HRC filter is used in WFC observations. (Apertures are not listed in the APT aperture pull-down menu.)

2. Apertures are automatically created by commanding software when a polarizer filter is used. Same parameters apply for POL60 and POL120 in V and UV. (Apertures are not listed in the APT aperture pull-down menu.)

Table 7.7: Ramp filter apertures.

| Filter | Ramp Segment | Full-frame apertures | Quadrant aperture |
|--|--------------|--------------------------|----------------------------|
| FR423N FR716N FR853N FR5551N FR647M | Inner | WFC1-IRAMP | WFC1-IRAMPQ |
| FR388N FR656N FR459M FR647M FR505N FR914M | Middle | WFC1-MRAMP WFC2-MRAMP | WFC1-MRAMPQ WFC2-MRAMPQ |
| FR462N FR782N FR931N FR1016N FR601N | Outer | WFC2-ORAMP | WFC2-ORAMPQ |

7.7.4 Polarizer Apertures

Apertures have been provided for use with the polarizer sets similar to the SMFL apertures. These apertures are selected automatically when a polarizing spectral element is used, and a single WFC chip quadrant readout is obtained. The aperture parameters given in Table 7.6 are valid for all three polarizing filters in each polarizer set, UV or visible, to the stated significant figures.

7.7.5 HRC Apertures

The HRC has an area of 1062 by 1024 including 19 physical overscan pixels at each end in the x direction. The active area is 1024 by 1024 pixels. The mean scales along the x and y directions are 0.028 and 0.025 arcseconds/pixel, thus providing a field of view of about 29 by 26 arcseconds in extent. The anisotropy and variation of scales is discussed in a later section of this handbook. The reference point for the aperture labelled HRC-FIX, and initially for HRC, is at the geometric center, (531,512). As with the WFC apertures, there may be reason to move the HRC reference point later.

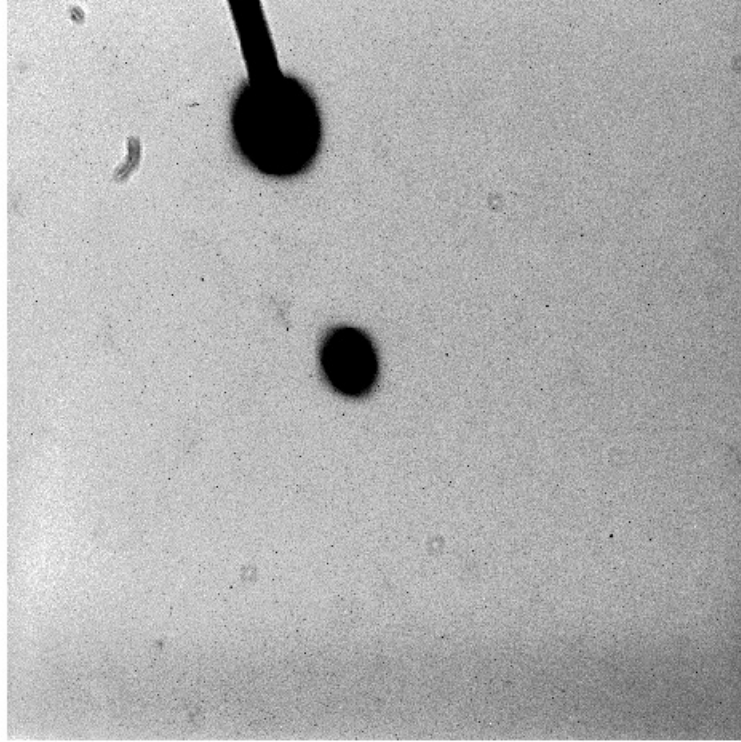
The HRC is equipped with two coronagraphic spots, nominally 1.8 and 3.0 arcseconds in diameter and a coronagraphic finger, 0.8 arcseconds in width. Apertures HRC-CORON1.8, HRC-CORON3.0, and HRC-OCCULT0.8 are defined to correspond to these features. In addition we define a target acquisition aperture, HRC-ACQ designed for acquiring targets which are subsequently automatically placed behind a coronagraphic spot or the occultation finger. The positions of the coronagraphic spots have been found to fluctuate. Observations will need to incorporate a USE OFFSET special requirement to allow current values to be inserted at the time of the observation (see the *Phase II Proposal Instructions*).

A substantial region masked out by the occulting finger can be present in the HRC data (Figure 7.6). The occulting finger is not retractable -- it will be in every HRC exposure. However as with any other detector feature or artifact, the "lost" data can be recovered by combining exposures which were suitably shifted with respect to each other. A dither pattern, ACS-HRC-DITHER-LINE has been defined for this purpose and spans the area flagged for the HRC occulting finger (~1.6 arcseconds or ~56 pixels wide), with an extra ~0.3 arcseconds or ~10 pixels of overlap. More details can be found in the *Phase II Proposal Instructions*.

Use of the prism PR200L requires specifying aperture HRC, but results in a reference point of [671,512] to optimally center the target coordinates within the somewhat vignetted prism field of view. Although the HRC direct imaging and PR200L prism apertures have the same name in APT, they are actually distinct, and HST executes a small angle maneuver

between observations of a given target with them, to compensate for the positional deflection by the prism. One consequence is that the Special Requirement `SAME POS AS` cannot be used among mixed direct and prism exposures, as always with different apertures.

Figure 7.6: HRC coronagraphic finger and spots.



The HRC aperture parameters are summarized in Table 7.8.

Table 7.8: HRC aperture parameters.

| APT Aperture Name | Active area | Extent (arcsec) | Reference pixel | Reference V2,V3 (arcsec) | x-axis angle | y-axis angle |
|------------------------|-------------|-----------------|------------------------|--------------------------|--------------|--------------|
| HRC | 1024 × 1024 | 29 × 26 | (531, 512) | (206,472) | -84.1 | 0.1 |
| HRC-FIX | 1024 × 024 | 29 × 26 | (531, 512) | (206,472) | -84.1 | 0.1 |
| HRC-CORON1.8 | 200 × 200 | 6 × 5 | (564,466) ¹ | (205,471) ¹ | -84.1 | 0.1 |
| HRC-CORON3.0 | 200 × 200 | 6 × 5 | (467,794) ¹ | (208,479) ¹ | -84.2 | 0.1 |
| HRC-OCCULT0.8 | 200 × 200 | 6 × 5 | (443,791) | (209,477) | -84.2 | 0.2 |
| HRC-ACQ | 200 × 200 | 6 × 5 | (735,575) | (200,474) | -84.1 | 0.0 |
| HRC-512 | 512 × 512 | 15 × 13 | (276,256) | (214,465) | -84.1 | 0.2 |
| HRC-SUB1.8 | 512 × 512 | 15 × 13 | (570,468) | (205,471) | -84.1 | 0.1 |
| HRC-PRISM ² | 744 × 1024 | 21 × 26 | (671,512) | (214,471) | -84.2 | 0.2 |

1. These values fluctuate and will be updated at the time of the observation.

2. HRC-PRISM is automatically created by commanding software when spectral element PR200L and aperture HRC are selected in APT.

7.7.6 SBC Apertures

The SBC aperture is 1024 pixels square. There are no overscan pixels to consider. The x and y scales are 0.034 and 0.030 arcseconds/pixel leading to a coverage on the sky of 35 by 31 arcseconds. The reference point has been moved to (512,400) to place targets further from a bad anode which disables several rows of the detector near $y = 600$. As with the CCDs we maintain an SBC-FIX aperture which will always have position (512,512). MAMA detectors slowly lose efficiency with each exposure, therefore the SBC reference point may be shifted again if the chosen position shows this effect to a measurable degree.

The (512,512) reference point falls near to the same position in (V2,V3) as the HRC, namely (205, 470), and the x and y axis angles are -85.4° and -0.9° .

Use of either prism PR110L or PR130L requires use of aperture SBC and results in a reference point of [425,400] to optimally center the target coordinates with respect to vignetting on the right side of the field and to avoid a set of bad rows at 599 to 605.

Although the SBC direct imaging and prism apertures have the same name in APT, they are actually distinct, and HST executes a small angle maneuver between observations of a given target with them, to compensate for the positional deflection by the prisms. One consequence is that the Special Requirement SAME POS AS cannot be used among mixed direct and prism exposures, as always with different apertures.

Table 7.9: SBC aperture parameters

| APT Aperture Name | Active area | Extent (arcsec) | Reference pixel | Reference V2,V3 (arcsec) | x-axis angle | y-axis angle |
|------------------------|-------------|-----------------|-----------------|--------------------------|--------------|--------------|
| SBC | 1024 × 1024 | 34 × 31 | (512, 400) | (205, 467) | -85.4 | -1.0 |
| SBC-FIX | 1024 × 1024 | 34 × 31 | (512, 512) | (205, 470) | -85.4 | -1.0 |
| SBC-PRISM ¹ | 1024 × 1024 | 28 × 31 | (425, 400) | (203, 467) | -85.4 | -1.0 |

1. SBC-PRISM is automatically created by commanding software when spectral elements PR110L and PR130L, and aperture SBC, are selected in APT.

7.8 Specifying Orientation on the Sky

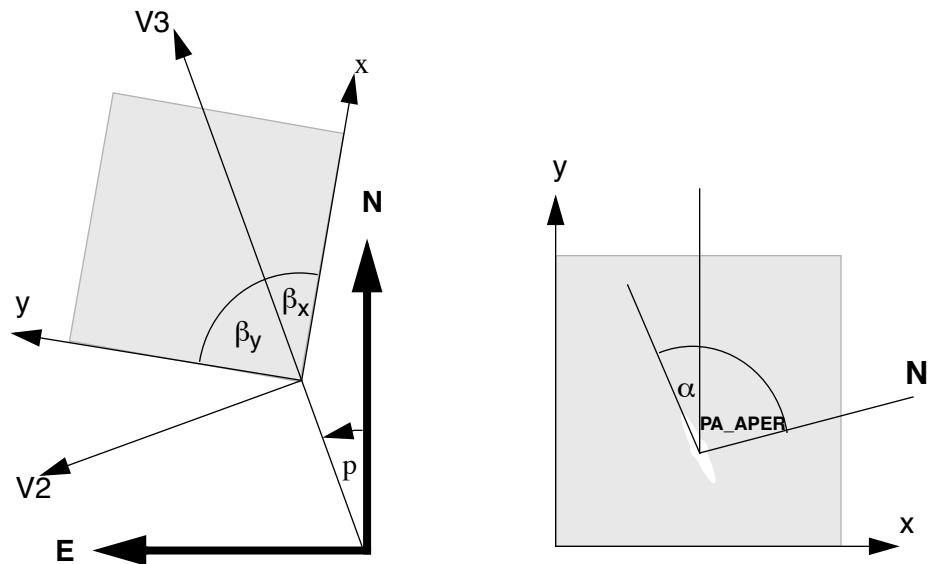
Determining the orientation of an image requires knowledge of the telescope roll and the angle of the aperture relative to the HST coordinate frame. A target may need to be oriented in a preferred direction on a detector, particularly when spectroscopy is to be performed.

To specify an ORIENT in Phase II, note that this parameter is just the usual PA (Position Angle) of the HST U3 axis ($= -V3$, see below); see

Figure 3.1 and Figure 7.8 in this Handbook, as well as the *Phase II Proposal Instructions*. APT/VTT provides a convenient interactive display of the aperture and orientations in your field. The ORIENT parameter is related to the following discussion of ACS geometry.

All HST aperture positions and orientations are defined within an orthogonal coordinate system labeled V1,V2,V3, in which V1 is nominally along the telescope roll axis. Apertures are therefore in the V2,V3 plane. (For more information about HST instrument aperture locations and axes in the HST FOV, please visit the Observatory Support web page section on apertures at: <http://www.stsci.edu/hst/observatory/apertures>.) The V3 position angle p is defined as the angle of the projection of the V3 axis on the sky, measured from North towards East with the aperture denoting the origin. This is almost identical to the telescope roll angle. (There is a small difference between roll angles measured at the V1 axis and those measured at the aperture. This can amount to several tenths of a degree depending on the target declination.) When the position angle is zero, V3 points North and V2 points East. In the V2V3 coordinate system, as shown in Figure 7.8, aperture orientations are defined by β_x and β_y , the angles their x and y axes make with the V3 axis, measured in an anti-clockwise direction. (The value of β_x as illustrated in Figure 7.7, would be considered negative.) Hence, the angles these axes make with North are found by adding the axis angles to the position angle.

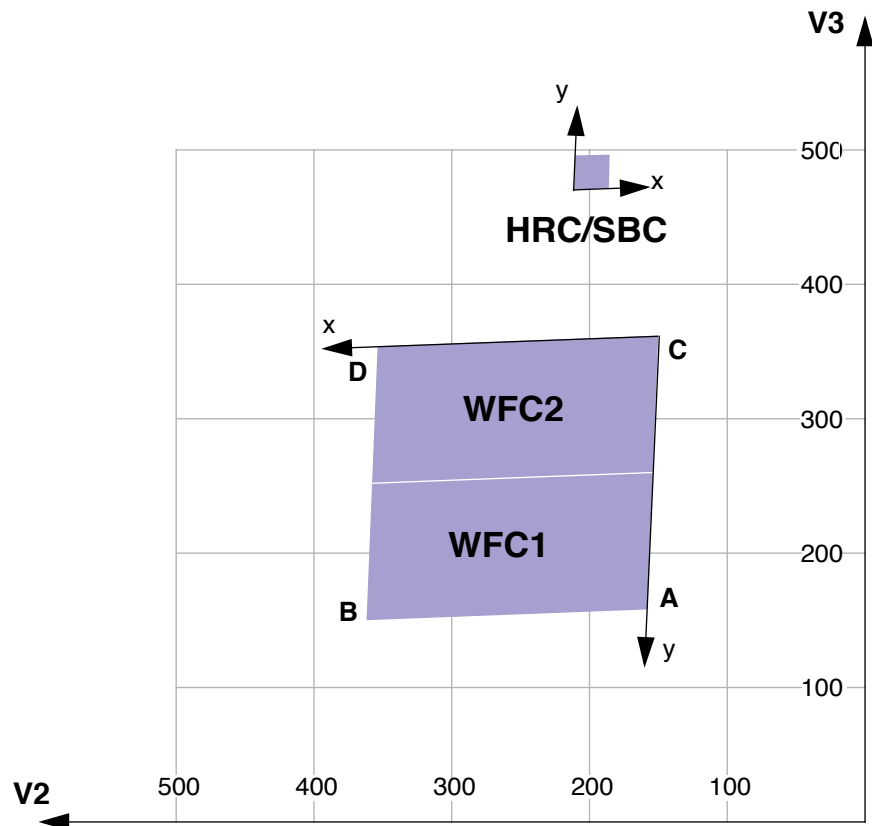
Figure 7.7: Aperture and image feature orientation.



The science image header supplies the value of `ORIENTAT`, the angle the detector y axis makes with North, which is equal to $p + \beta_y$. Another angle keyword supplied is `PA_APER` which is the angle the aperture y axis makes with North. Both angles are defined at the aperture so using them does not involve the displacement difference. Normally the aperture and detector y axes are parallel, and so `PA_APER` = `ORIENTAT`. Several STIS slit apertures were not aligned parallel to the detector axes, so this distinction was meaningful, but ACS has no slit apertures so this difference will probably not arise. In any case, we recommend using `PA_APER`.

Beyond establishing the direction of the aperture axes, it will often be necessary to know the orientation of a feature, such as the plane of a galaxy, within an image. Conversely, we need to know what direction within an image corresponds to North. To this end we define a feature angle α within the aperture as measured on the science image, anti-clockwise from the y -axis so that it is in the same sense as the previously defined angles. For an orthogonal set of aperture axes the direction of this feature would be `PA_APER` + α and the image direction of North would be the value of α which makes this angle zero, namely $-\text{PA_APER}$, still measured in an anti-clockwise direction from the y axis.

Figure 7.8: ACS apertures in the V2/V3 reference frame.



The readout amplifiers (A,B,C,D) are indicated on the figure. The WFC data products from the calibration pipeline will be oriented so that WFC1 (chip 1, which uses amps A and B) is on top. The HRC data products will also be oriented such that amps A and B are on top, but they will be inverted from WFC images with respect to the sky.

The x and y axes projected on the sky are not necessarily orthogonal. For all instruments prior to the ACS the departure from orthogonality has been negligible, but for the ACS the angle between the axes is about 85°. Figure 7.8 realistically represents the alignment of the ACS apertures and shows that the apertures are not square. The x and y axes indicated are those that will be used for the science images. The V2,V3 coordinates can be calculated from the x, y coordinates according to

$$V2 = V2_0 + s_x \sin \beta_x x + s_y \sin \beta_y y$$

$$V3 = V3_0 + s_x \cos \beta_x x + s_y \cos \beta_y y$$

where s_x and s_y are scales in arcseconds per pixel along the image x and y axes. $V2_0$ and $V3_0$ are the coordinates of the aperture origin, but they do not enter into the angle calculations. Figure 7.8 shows that a rotation from x to y is in the opposite sense to a rotation from V2 to V3. This will be the arrangement for ACS apertures. This is significant in defining the sense of the rotation angles. For a direction specified by displacements Δx and Δy in the image, the angle α is $\arctan(-\Delta x/\Delta y)$.

Because of the oblique coordinates, the angle α_s on the sky will not be equal to α . To calculate the sky angle, it is convenient to define another set of orthogonal axes x_s, y_s , similar to the V2V3 but rotated so that y_s lies along y, and x_s is approximately in the x direction. Let $\omega = \beta_y - \beta_x$ be the angle between the projected detector axes and for simplicity let their origins be coincident. Then the transformation is

$$x_s = s_x \sin \omega x$$

$$y_s = s_x \cos \omega x + s_y y$$

By comparing differentials and defining α_s as $\arctan(-\Delta x_s/\Delta y_s)$ we find

$$\tan \alpha_s = \frac{s_x \sin \omega \sin \alpha}{s_y \cos \alpha - s_x \cos \omega \sin \alpha}$$

The equation as written will place the angle in the proper quadrant if the ATAN2 Fortran function or the IDL ATAN function is used. To get the true angle East of North, for a feature seen at angle α in the image, calculate α_s and add to PA_APER.

The inverse relation is

$$\tan \alpha = \frac{s_y \sin \alpha_s}{s_x \sin(\alpha_s + \omega)}$$

To find the value of α corresponding to North we need the value of α_s such that $\text{PA_APER} + \alpha_s = 0$. So substitute $-\text{PA_APER}$ for α_s in the equation to get the angle α in the image which corresponds to North. The values of

the scales and axis angles for all instruments are maintained on an [Observatory Science Group Web page](#).

For the ACS apertures, the values in Table 7.10 have been derived from results of operating the ACS in the Refractive Aberrated Simulator. These should not be considered as true calibrations but they indicate some aperture features, such as the non-orthogonality of the aperture axes, and the x and y scale differences for HRC and SBC.

Table 7.10: Plate scales and axis angles for the 3 ACS channels.

| | s_x | s_y | β_x | β_y | $\beta_y - \beta_x$ |
|-----|--------------|-------|-----------|-----------|---------------------|
| | arcsec/pixel | | degrees | | |
| WFC | .0494 | .0494 | 92.2 | 177.5 | 85.3 |
| HRC | .0284 | .0248 | -84.1 | 0.1 | 84.2 |
| SBC | .0338 | .0301 | -85.4 | -1.0 | 84.4 |

7.8.1 Determining Orientation for Phase II

A particular orientation is specified in an HST Phase II proposal using yet another coordinate system: U2,U3. These axes are opposite to V2 and V3, so, for example, $U3 = -V3$. The angle **ORIENT**, used in a Phase II proposal to specify a particular spacecraft orientation, is the position angle of U3 measured from North towards East. The direction of the V3 axis with respect to North is $PA_APER - \beta_y$ and so

$$ORIENT = PA_APER - \beta_y \pm 180^\circ.$$

The IRAF task *rotate* in the package *images.geom* takes an image and rotates it counter-clockwise by a specified angle. To orient an image so that its y axis becomes North, the angle to specify is PA_APER . The x axis will then point approximately 5° North of East. Orientations can be checked by using the [Visual Target Tuner \(VTT\)](#) in the [APT](#).

7.9 Parallel Observations

7.9.1 Parallel Observing

Parallel observing allows HST to operate several other instruments while the prime instrument is executing its observations. While the primary instrument observes a fixed target at user-specified coordinates, the parallel instrument observes at coordinates 5 to 10 arcminutes away, depending on the parallel instrument. The HST field of view following SM3B (Figure

3.1) shows the general locations of the instrument apertures adjacent to one another on the sky. Accurate relative positions for all instruments can be found on STScI's [Observatory Web page](#) in the [Pointing section](#).

The recommended method of determining the field of view for any instrument is the [Visual Target Tuner \(VTT\)](#). A Digital Sky Survey (or user supplied) image of the primary target area is displayed with an HST field of view overlay. Any desired coordinate and ORIENT combination for the primary target will then display the possible pointings of any instrument operated in parallel. If the primary exposure will execute at a known (absolute) orientation, the [VTT](#) will display the exact field of view for any instrument executed in parallel. If the primary exposure will execute at a random (nominal) orient or range of orient values, the [VTT](#) allows the HST field of view to be rotated interactively about the primary pointing. The [VTT](#) can be an invaluable resource for parallel observing programs, especially those designed for, or restricted to specific pointings for the parallel FOV.

Certain operating limits are in place to restrict use of configurations, modes, parameters, elements, and requirements allowed for each instrument while used in parallel. Details on these limits are documented in the [Call for Proposals](#) and [Primer](#). General information on ACS specific parallel operations are documented in the following sections for each of the three types of ACS parallel observing: coordinated, auto, and pure.

ACS Coordinated Parallels

Coordinated parallel observations are specified in the same Phase II observing program as the primary observations via the prime and parallel group containers in [APT](#). A single ACS channel may be used for a coordinated parallel observation, with, and only with, another instrument. Unlike NICMOS, coordinated parallels cannot be used to operate any of the ACS channels simultaneously. ACS exposures may not be used as both the prime and parallel exposures within the same parallel container. In order to operate ACS channels simultaneously, the use of ACS auto-parallels is described in the following section.

In order to protect the ACS SBC detector from inadvertent over illumination, the ACS/SBC configuration may be used as a coordinated parallel only if an exact spacecraft orientation (ORIENTation) is specified, the coordinates of the parallel field are determined, and the parallel target or field passes the same bright-object screening applied to SBC primary observations. The [Visual Target Tuner](#) will greatly assist in defining this type of ACS parallel program.

Currently ACS and WFPC2, used together in a coordinated parallel program, result in the ACS auto-parallel capability being disabled. This restriction is made to prevent potential conflicts between ACS buffer dumps and WFPC2 readouts. The user may attempt to restore autoparallels via `PAREXP=MULTIPLE`.

ACS Auto-Parallels

The ACS auto-parallel capability is intended to increase the scientific return of the instrument by adding exposures with the parallel detector while interfering as little as possible with the observer's primary program. When either the WFC or HRC is the primary channel, and the exposure in that channel meets the requirements stated below, an auto-parallel observation will be automatically scheduled in the parallel channel during Phase II processing. Parallel detector exposures will be added automatically with the longest possible exposure time that does not interfere with the primary program. In order for an auto-parallel to be scheduled, the *primary* observation must meet the specifications that depend primarily on the exposure time and the filter selection of the primary exposure.

The user has three control options: This is done by selecting the PAREXP optional parameter. A user may either choose to explicitly add the auto-parallels by choosing PAREXP=MULTIPLE; choose to have no auto-parallels added by selecting PAREXP=NONE; or leave the special requirement set to the default, DEF. When DEF is selected, auto-parallels will be added according to the same primary exposure requirements as those for the MULTIPLE option. When MULTIPLE is selected an auto-parallel will be added for each CR-SPLIT part of the primary exposure (see Figure 7.9). There is a simple algorithm that the Phase II software follows in order to determine if an auto-parallel is feasible:

1. The primary exposure must be for an external target, in ACCUM mode, and either in the WFC or HRC channel. It is not possible to observe simultaneously with the HRC and SBC since they share the same optical train up to the flip mirror. Simultaneous operation of the WFC and SBC is not supported.
2. The primary exposure must be taken with a filter from the list of primary/auto-parallel filter combinations (Table 7.11). HRC and WFC share the same filter wheels, so the filter selection for the primary camera predetermines which filter will be used for the simultaneous observation in the other channel. (The HRC primary/WFC parallel filter combination will not always be the inverse of the WFC primary/HRC parallel combination, because the WFC and HRC optical paths are not diametrically opposite each other in the filter wheel).
3. The primary exposure time must be greater than the minimum exposure time, defined in Table 7.12. These values are calculated such that all of the commanding associated with the auto-parallel is scheduled during the exposure time of the primary CR-SPLIT portion.
4. The primary exposure is not allowed to have any EXPAND, MIN DUR, MAX DUR, or RT ANALYSIS special requirements.

Table 7.11: Filter combinations for auto-parallels in the two cases of (i) HRC camera prime and (ii) WFC camera prime.

| HRC primary | WFC auto-parallel | WFC primary | HRC auto-parallel |
|-------------|-------------------|-------------|-------------------|
| CLEAR | CLEAR | CLEAR | CLEAR |
| F892N | F775W | F475W | F850LP |
| F606W | F625W | F658N | F550M |
| F502N | F550M | G800L | F625W |
| G800L | F850LP | F502N | F775W |
| F555W | F606W | F606W | F555W |
| F775W | F502N | F850LP | G800L |
| F625W | G800L | F550M | F502N |
| F550M | F658N | F625W | F606W |
| F850LP | F475W | F775W | F892N |
| F330W | F660N | F660N | F330W |
| F250W | F814W | F814W | F250W |
| F220W | F435W | F435W | F220W |

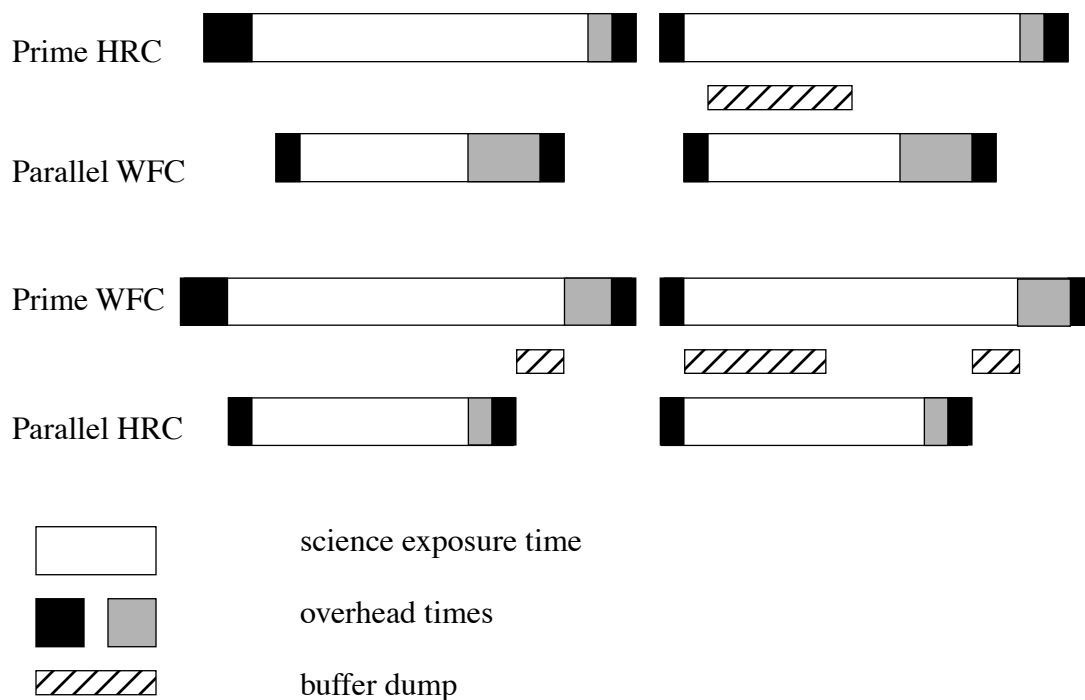
Note that since the WFC and HRC apertures are not opposite each other on the filter wheels, filter pairs in columns 1 and 2 do not map to columns 3 and 4.

Table 7.12: Minimum primary exposure time (seconds) to attach an auto-parallel for CR-SPLIT=n.

| Primary exposure type | Multiple auto-parallel scenario ($n \geq 1$) |
|-----------------------|--|
| HRC | $n \times 495$ |
| WFC compressed | $n \times 406$ |
| WFC uncompressed | $n \times 465$ |

(if CR-SPLIT=NO then $n=1$, if CR-SPLIT not specified $n=2$.)

Figure 7.9: Scheduling of auto-parallels.



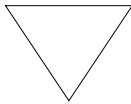
There are a few things to remember about auto-parallels:

- In order to avoid the addition of serial buffer dumps in the primary program, group short HRC exposures and long WFC exposures separately. It takes approximately 349 seconds to dump a WFC image from the buffer. When WFC is the parallel camera, this buffer dump can occur during the following exposure if its exposure time is greater than ~ 339 seconds, otherwise a serial buffer dump must be added. This can be avoided by scheduling long WFC full-frame exposures together.
- auto-parallels will not be assigned when the number of exposure iterations specified for the primary exposure is greater than one. It is assumed that the observer will use exposure iterations to obtain coarse time resolution. These exposures will in most cases be too short for auto-parallel observations.

The following policies will be in effect for Auto-Parallel observations:

- Auto-Parallel observations are the property of the PI of the program using the prime ACS detector.
- Auto-Parallel observations are not available for independent scheduling.

- There are some fairly severe timing constraints under which Auto-Parallel observations may be added. The scheduling system will add parallels only if it can do so without affecting the prime science.
- If WFC data are taken in parallel with prime HRC observations, the GAIN setting will be 2 (see Section 4.3). For HRC parallels added to prime WFC exposures the GAIN will be 2.
- WFC Auto-parallel observations are subject to compression of one quadrant at a level that can occasionally result in some data loss. Such observations will not be repeated.



This data loss will be considered routine and it will be the policy of STScI not to repeat observations scheduled as auto-parallels which exhibit partial data loss due to the data compression.

ACS Pure Parallels

In ACS pure parallel observations, an observation is taken with ACS on an essentially random area of the sky while another instrument is making prime observations. No SBC pure parallels will be allowed due to bright object concerns.

Unlike the previous two types of parallel programs, pure parallels contain only parallel visits. Use of the GO/PAR proposal category will make any visit in the program a pure parallel.

The ACS default (archival) pure parallel program continued to execute for the community until midway through Cycle 13 when all of the "Default" HST archival pure parallel programs were discontinued to prolong the lifetime of transmitters on HST. This non-proprietary data currently comes from programs 9575, 9584, and 9701. A list of all pure parallel datasets in the HST archive is updated regularly at:

<http://www.stsci.edu/instruments/parallels/retrieve.html>.

Pure parallel observations are executed at every possible opportunity, although there are many constraints which can render pure parallels unselectable in any given orbit. Pure parallels will always be given lower priority than primaries, and are thus scheduled only on a non-interference basis.

ACS Auto-Parallels with ACS Coordinated and ACS Pure Parallels

ACS auto-parallels can be added to ACS pure and ACS coordinated parallels by default if scheduling constraints allow. However auto-parallels cannot be added to observations that make use of EXPAND or MAX DUR

special requirements. Therefore ACS pure parallels can either be crafted to expose for the maximum duration allowed in each individual orbit by using EXPAND/MAX DUR or have auto-parallels added, but not both.

7.10 Pointing Stability for Moving Targets

Observations of Solar System targets are subject to some special limitations on the achievable pointing stability during a visit. These limitations apply to both two-gyro and three-gyro operations.

For moving targets, the HST ground system assumes that the position of the target as seen from the center of the earth can be approximated as a linear function of time. This is done using rates of motion calculated from the object's ephemeris for a time near the start of each orbit. If the target's geocentric ephemeris departs significantly from this linear approximation over the course of an orbit, this can lead to small but noticeable pointing offsets. If you think this may adversely affect your science, please consult with your PC about possible strategies for ameliorating this effect.

The correction for the variable parallax to a solar system object due to HST's orbit around the Earth is calculated on-orbit using the best ephemeris for HST's orbit that was available at the time the detailed weekly schedule was created. However, the real position of HST along its orbit often differs by up to 1 to 2 seconds (7 to 15 kilometers) from the predicted ephemeris position. This leads to small errors in the phasing of the calculated parallax correction. For example, when observing a Solar System object at a distance of 0.5 AU from the Earth, this can cause typical pointing offsets over the course of an orbit of order 20 to 40 milliarcseconds. As these offsets depend on unpredictable changes in HST's orbit, such drifts are unavoidable when observing near-Earth objects.

Overheads and Orbit-Time Determination

In this chapter . . .

8.1 Overview / 155

8.2 ACS Exposure Overheads / 156

8.3 Orbit Use Determination Examples / 160

8.1 Overview

After you establish a set of scientific exposures, as well as any additional target acquisition or calibration exposures required for your program, you are ready to determine the total number of orbits to request. Generally, this straightforward exercise involves compiling the overheads for individual exposures, packing exposure plus overhead time into individual orbits, and tallying up the results to determine the total number of orbits needed. It may be an iterative process as you refine your exposures to better use the orbit visibility times.

The Phase I Call for Proposals (http://www.stsci.edu/hst/hst/proposing/documents/cp/cp_cover.html) includes proposal instructions that provide information on the Observatory policies and practices with respect to orbit time requests. The HST Primer (<http://www.stsci.edu/hst/proposing/docs/proposing/documents/cp/primer.pdf>) provides specific advice on orbit determination. Below, we provide a summary of the ACS specific overheads, and give several examples that illustrate how to calculate your orbit requirements for a Phase I Proposals.

8.2 ACS Exposure Overheads

Exposure overheads are summarized in Table 8.1 and Table 8.2. All numbers given are approximate; they do not make detailed differentiations between overheads for different ACS modes and configurations. These overhead times are to be used (in conjunction with the actual exposure times and the instructions in the *HST Primer* to estimate the total number of orbits for your proposal. After your HST proposal is accepted, you will be asked to submit a Phase II proposal to support scheduling of your approved observations. At that time you will be presented with actual, up-to-date overheads by the APT scheduling software. *Allowing sufficient time for overhead in your Phase I proposal is important; additional time to cover unplanned overhead will not be granted later.*

The following list presents important points for each type of overhead:

- **Generic (Observatory Level) Overheads:**
 - The first time you acquire an object you must include overhead for the guide-star acquisition (6 minutes).
 - In subsequent contiguous orbits you must include the overhead for the guide-star reacquisition (6 minutes); if you are observing in the Continuous Viewing Zone (see the *Phase I Proposal Instructions*), no guide-star *reacquisitions* are required.
 - Allocate some time for each deliberate movement of the telescope; e.g., if you are performing a target acquisition exposure on a nearby star and then offsetting to your target, or if you are taking a series of exposures in which you move the target on the detector, you must allow time for the moves (20 seconds to 60 seconds, depending on the size of the slew (see Table 8.1 and Table 8.2).

Table 8.1: Science exposure overheads: general.

| Action | Overhead |
|------------------------------------|---|
| Generic (observatory level) | |
| Guide-star acquisition | Initial acquisition overhead = 6 minutes. Reacquisitions on subsequent orbits = 6 minutes per orbit. |
| Spacecraft moves | For offsets less than 1.5 arcminutes and more than 10 arcseconds = 1 minute. For offsets between 10 arcseconds and 1 arcseconds = 0.5 minutes. For offsets less than 1 arcseconds in size = 20 seconds. |

Table 8.2: ACS science exposure overhead times (minutes).

| Exposure type | WFC | HRC | SBC |
|---|-----|-------------------------|-----|
| <i>Mode: ACCUM</i> | | | |
| Single exposure or the first exposure in a series of identical exposures. | 4.0 | 2.5 | 1.7 |
| Subsequent identical exposures in series (within an orbit). | 2.5 | 1.0 | 0.7 |
| Additional overhead for each serial buffer dump (added when WFC exposures are less than 339 seconds long, or the buffer fills with short HRC or SBC exposures). | 5.8 | 5.8 | 5.8 |
| Predefined imaging exposure for prism spectroscopy. | N/A | 8.5 | N/A |
| Predefined imaging exposure for grism spectroscopy. | 7 | 5.5 | N/A |
| <i>Mode: ACQ</i> | | | |
| For the specified acquisition exposure time, $tacq$, the total acquisition time is: | N/A | $3.5 + (2 \times tacq)$ | N/A |
| <i>Additional overheads</i> | | | |
| Additional overhead if switching over from HRC to SBC within an orbit. | | 11.0 | |
| Additional overhead if switching over from SBC to HRC within an orbit. | | 8.0 | |

- ***Onboard Target-Acquisition Overheads:***

- On board target acquisitions only need to be done to place the target under one of the coronagraphic spots.
- An on board target acquisition needs to be done only once for a series of observations in contiguous orbits (i.e., once per visit).
- The drift rate induced by the Observatory is less than 10 milliarcseconds per hour. Thermal drifts internal to ACS are even less.

- ***Scientific Exposures:***

- The overhead times are dominated by the time to move the filter wheel, the CCD readout time, and any necessary serial buffer dumps. Again, it should be stressed that in Phase II, the overheads will frequently be less, but it is important to plan Phase I using the conservative overheads given in Table 8.2 to ensure adequate time for the proposal's scientific goals.

- *Spectroscopy:*

- Each CCD spectroscopic observation is preceded by an imaging exposure used for calibration, with exposure times of 3 and 6 minutes, respectively, for grism and prism observations. SBC prism exposures are not preceded by an automatic calibration exposure. Technically this is an individual single exposure requiring all regular science exposure overheads. For the observer, however, it represents an additional overhead in the observation time budget, so it has been included in the table of instrument overhead times for science exposures. However, if the observing program is already taking an appropriate broadband image, the automatic imaging and associated overheads preceding the spectroscopic grism or prism observations can be avoided by invoking the Optional Parameter `AUTOIMAGE=NO` during the Phase II preparations. More details can be found in the *Phase II Proposal Instructions*.

Note that identical exposures are generated automatically if the observer specifies the proposal optional parameters `CR-SPLIT` (for $n > 1$), or `PATTERN`, or if `Number_of_Iterations > 1`. If it is not specified, `CR-SPLIT` defaults to $n = 2$. In general, identical exposures are defined here as exposures of the same target, with the same detector and filter(s). For identical exposures in `PATTERNS`, this also involves slews and therefore slew overheads.

For `ACQ` mode, the overhead includes double the specified exposure time. The reason for having two acquisition images is to eliminate possible image defects which can interfere with target acquisition. The flight software ensures that two images are taken, so the user does not need to specify that in the proposal.

The overhead time for serial buffer dumps arises in certain cases from the overheads associated with the onboard data management and switching over the cameras. The on-board buffer memory can hold no more than one WFC image. The next WFC image can be placed into the buffer only after the buffer has dumped the previous image, which takes 349 seconds.



If the next exposure time is longer than 339 seconds (for WFC) or 346 seconds (for HRC; 16 HRC images may be taken before a buffer dump is triggered), the buffer dump will occur during that exposure, and no overhead is imposed. However, if the next exposure time is shorter than 339 seconds (WFC) or 346 seconds (HRC), then the dump must occur between the two exposures.

Sequences of many short HRC or SBC exposures can also lead to serial dumps when the buffer becomes full. In this case the buffer dump time becomes an overhead to be included into the orbit time budget. This overhead can severely constrain the number of short exposures one can squeeze into an orbit. Subarrays can be used to lower the data volume for some applications.

A serious penalty is incurred by toggling between SBC and HRC within an orbit. The time to switch over from SBC to HRC is 480 seconds. The opposite switch takes 650 seconds. In both cases, if the buffer has been filled, there will be an additional overhead of 6 minutes for the dump; but if the buffer is not filled during the orbit, the dump will occur at the end of visibility and can be pushed into occultation. Thus, whenever possible, one should plan to use HRC and SBC in different orbits.

8.2.1 Subarrays

At the end of each exposure, data are read out into ACS's internal buffer memory where they are stored until they are dumped into HST's solid state data recorder. The ACS internal buffer memory holds 34 MB or the equivalent of 1 full WFC frame, or 16 HRC or SBC frames. Thus, after observing a full WFC frame, the internal buffer memory must be dumped before the next exposure can be taken. The buffer dump takes 349 seconds and may not occur while ACS is being actively commanded. Of this time, 339 seconds (for one WFC image) or 346 seconds (for 16 HRC images) is spent dumping the image. The buffer dump cannot be done during the next exposure if the latter is shorter than 339 seconds. If, however, the next exposure is less than 339 seconds the buffer dump will create an extra 5.8 minutes of overhead.

If your science program is such that a smaller FOV can be used, then one way of possibly reducing the frequency and hence overheads associated with buffer dumps is to use WFC subarrays. With subarrays, only the selected region of the detector is read out at a normal speed and stored in the buffer, and a larger number of frames can be stored before requiring a dump. Using subarrays not only reduces the amount of time spent dumping the buffer but in some cases may reduce the readout time. See Chapter 7 for a discussion of some of the limitations of subarrays. If the user elects to define a subarray of arbitrary size and location, allowed on an available-but-unsupported basis, then matching bias frames will not be automatically provided by STScI. Any bias frames specified by the user will typically be scheduled during the following occultation (i.e., they do not add to the overheads during visibility time). Dark frames and flat fields will be extracted from full frame images. In some special cases where a general subarray is cleverly defined so as to include a physical overscan region, no separate bias frames are needed.

8.3 Orbit Use Determination Examples

The easiest way to learn to compute total orbit time requests is to work through a few examples. Below we provide five different examples:

- Example 1 is a simple WFC image in one filter.
- Example 2 is a set of short WFC exposures that may require large overheads associated with buffer dumps.
- Example 3 is a one-orbit coronagraphic observation in two filters.
- Example 4 is a two-orbit observation using dithering.
- Example 5 is a one orbit WFC grism spectroscopic observation.

These examples represent fairly typical uses of ACS.

8.3.1 Sample Orbit Calculation 1:

Consider a target to be imaged with WFC in a given filter in one orbit. Using the [Exposure Time Calculator \(ETC\)](#), we find that we need 2400 seconds of exposure time to reach the desired level of signal-to-noise ratio. Given that the observation must be split into a series of two exposures by CR-SPLIT (CR-SPLIT=2), we map the overheads and the science exposure times onto the orbit as follows:

Table 8.3: Orbit calculation for example 1.

| Action | Time (minutes) | Explanation |
|--|----------------|--|
| <i>Orbit 1</i> | | |
| Initial guide-star acquisition | 6 | Needed at start of observation of a new target |
| WFC overhead for the first exposure | 4.0 | Includes filter change, camera set-up, and readout |
| First science exposure | 20.0 | |
| WFC overhead for the subsequent science exposure in the series | 2.5 | Includes readout |
| The next science exposure in the series | 20.0 | |
| Total time for science exposures | 40.0 | |
| Total used time in the orbit | 52.6 | |

Thus, the two WFC exposures totaling 2400 seconds make full use of the typically available time in one orbit. The exposure times can be adjusted if the actual target visibility time differs from the derived total used time.

8.3.2 Sample Orbit Calculation 2:

This example illustrates the impact of short WFC exposures on the useful time in the orbit. We have one orbit to observe a target with WFC in two filters, so the observation consists of two series, each with two identical CR-SPLIT exposures. The ETC has shown that at the minimally accepted signal-to-noise ratio the exposure time must be 540 seconds for each of the filters, so each of the CR-SPLITS must be at least 270 seconds long. For the target declination, we find that the visibility time is 55 minutes. The time budget for the orbit is then as follows:

Table 8.4: Orbit calculation for example 2.

| Action | Time (minutes) | Explanation |
|---|--------------------------|---|
| <i>Orbit 1</i> | | |
| Initial guide-star acquisition | 6 | Needed at start of observation of a new target |
| WFC overhead for the first exposures in two series | $2 \times 4 = 8$ | Includes filter change, camera set-up, and readout |
| WFC overhead for subsequent exposures in each of the two series | $2 \times 2.5 = 5$ | Includes readout |
| Additional overhead for all but the last exposures in the orbit | $5.8 \times 3 = \sim 17$ | Needed to dump the buffer because the next exposure is too short (> 339 seconds) to accommodate the dump time. |
| Science exposures | $4 \times 4.5 = 18$ | |
| Total time for science exposures | 18 | |
| Total used time in the orbit | 54 | |

Comparing with the previous example, we see that although with the adopted minimum exposure times we can squeeze the observation into one orbit, the efficiency of the orbit use is very low because of the large overheads associated with buffer dumps. However, if we increase each of the four exposure times so that they are larger than 339 seconds, we avoid these additional overheads. This would free ~ 17 minutes of the orbit time for science, which allows us to almost double the science exposure time (35 minutes instead of 18 minutes) and thus significantly improve signal-to-noise.

Similarly, a subarray can be used to readout only a fraction of the detector, allowing more frames to be stored in the buffer before requiring a dump. In this example, using four WFC1-1K subarrays for 4 short ($t < 339$ seconds) exposures would save 176 seconds in readout time and 1047 seconds in dump time. This frees up ~ 20 minutes of orbit time to be used for science.

8.3.3 Sample Orbit Calculation 3:

This example demonstrates the orbit calculation for a coronagraphic observation. We want to obtain coronagraphic images of a star in two filters, F250W and F606W. The ETC has shown that the exposure times adequate for our scientific goals are 5 minutes in F606W and 30 minutes in F250W. From the orbit visibility table (see the [HST Primer](#)) we find that at the target declination of 15° the target visibility time is 52 minutes. With CR-SPLIT=2, we thus have to accommodate in that period 35 minutes of four science exposures grouped in two series. The orbit calculation goes like this:

Table 8.5: Orbit calculation for example 3.

| Action | Time (minutes) | Explanation |
|---|------------------------------|--|
| <i>Orbit 1</i> | | |
| Initial guide-star acquisition | 6 | Needed at start of observation of a new target |
| Target acquisition | $3.5 + (2 \times 0.1) = 3.7$ | Point-source acquisition on target |
| HRC overhead for the first exposures in the series | $2 \times 2.5 = 5$ | Includes filter change, camera set-up, and readout |
| HRC overhead for the subsequent exposures in the series | $2 \times 1 = 2$ | Includes readout |
| Science exposures in F606W | $2 \times 2.5 = 5$ | |
| Science exposures in F250W | $2 \times 15 = 30$ | |
| Total time for science exposures | 35 | |
| Total used time in the orbit | ~52 | |

The derived total used time in the orbit shows that our target can indeed be imaged in the selected filters in one orbit. Since there remains 3 minutes of unused time, we can adjust our exposure times to make full use of the available time.

8.3.4 Sample Orbit Calculation 4:

This example illustrates the orbit calculation for a WFC observation with the ACS box pattern, which implements imaging at four offset pointings. The goal of the observation is to obtain a dithered image of a field in such a way that would allow us to bridge the 50 pixel interchip gap between the WFC CCDs in the combined image. Given the WFC plate scale of 0.05 arcseconds/pixel, this requires that the offsets in the dithering pattern are larger than 2.5 arcseconds. Each offset will then take 0.5 minutes to move the spacecraft from one pointing in the pattern to another. We have determined that the exposure time necessary to reach the desired signal-to-noise ratio is 80 minutes. The visibility time at our target

declination is 58 minutes. In this observation we do not want to rely on cosmic ray removal provided by the dithering data reduction package, and set `CR-SPLIT=2` to be able to remove cosmic rays from the four individual images separately. As a result, the orbit calculation will involve a series of 8 exposures (two exposures at each of the four pointings in the dithering pattern) split across two orbits:

Table 8.6: Orbit calculation for example 4.

| Action | Time (minutes) | Explanation |
|---|----------------------|---|
| <i>Orbit 1</i> | | |
| Initial guide-star acquisition | 6 | Needed at start of observation of a new target |
| WFC overhead for the first exposures in the series | 4 | Includes filter change, camera set-up, and readout |
| WFC overhead for the subsequent 3 exposures in the series | $3 \times 2.5 = 7.5$ | Includes readout |
| Spacecraft slew | 0.5 | To offset from the first to the second pointing |
| Four science exposures | $4 \times 10 = 40$ | Exposures at the first two pointings in the dither pattern |
| Total time for science exposures | 40 | |
| Total used time in the orbit | 58 | |
| <i>Orbit 2</i> | | |
| Guide-star re-acquisition | ~6 | Needed at start of a new orbit to observe the same target |
| WFC overhead for the remaining exposures in the series | $4 \times 2.5 = 10$ | Includes readout |
| Spacecraft slews | $2 \times 0.5 = 1$ | To offset to the third and fourth pointings |
| Four science exposures | $4 \times 10 = 40$ | Exposures at the second two pointings in the dither pattern |
| Total time for science exposures | 40 | |
| Total used time in the orbit | 57 | |

The total used time in the first orbit comes out a little bit larger than the visibility time. However, given the conservative nature of the adopted overhead times as well as a bit of flexibility in the adopted signal-to-noise ratio, the difference is not significant. It should be remembered that the purpose of the above exercises is to estimate how many orbits to request for our science program rather than to exactly design the observation.

8.3.5 Sample Orbit Calculation 5:

This example illustrates the orbit calculation for a simple 30 minutes WFC grism spectroscopic observation broken down by CR-SPLIT=2 into a series of two exposures.

Table 8.7: Orbit calculation for example 5.

| Action | Time (minutes) | Explanation |
|--|----------------------|--|
| <i>Orbit 1</i> | | |
| Initial guide-star acquisition | 6 | Needed at start of observation of a new target |
| Predefined imaging exposure for grism spectroscopy | 7 | Needed to co-locate the targets and their spectra in the FOV |
| WFC overhead for the first science exposure in the series | 4.0 | Includes filter change, camera set-up, and readout |
| WFC overhead for the subsequent science exposure in the series | 2.5 | Includes readout |
| Two science exposures | $2 \times 15.0 = 30$ | |
| Total science exposure time | 30.0 | |
| Total used time in the orbit | 49.5 | |

Unlike similar imaging exposures, here we have to take into account an additional imaging exposure before the sequence of spectroscopic exposures, which takes 10 minutes off the available orbit time.

Exposure-Time Calculations

In this chapter. . .

| |
|--|
| 9.1 Overview / 165 |
| 9.2 Determining Count Rates from Sensitivities / 166 |
| 9.3 Computing Exposure Times / 172 |
| 9.4 Detector and Sky Backgrounds / 175 |
| 9.5 Extinction Correction / 180 |
| 9.6 Exposure-Time Examples / 181 |
| 9.7 Tabular Sky Backgrounds / 185 |

9.1 Overview

The *Phase I Call for Proposals* includes proposal instructions that provide information on the Observatory policies and practices with respect to orbit-time requests. The *HST Primer* provides specific advice on orbit determination. Below, we provide a summary of the ACS specific overheads and give several examples that illustrate how to calculate your orbit requirements for Phase I Proposals. Examples are provided at the end of the chapter.

9.1.1 The ACS Exposure Time Calculator

The ACS Exposure-Time Calculator (ETC) is available to help with proposal preparation at:

http://www.stsci.edu/hst/acs/software/etcs/ETC_page.html.

This [ETC](#) calculates count rates for given source and background parameters, signal-to-noise ratios for a given exposure time, or count rates and exposure time for a given signal-to-noise ratio for imaging, spectroscopic, and coronagraphic observations. A variety of apertures are now available, both circular and square, allowing the user to either select a radius in arcseconds or a size in pixels. The current default are a 0.2 arcseconds radius for both the WFC and the HRC, and a 0.5 arcseconds radius for SBC observations, which enclose approximately 80% of the PSF flux. Square and circular apertures are available between 0.1 and 2.0 arcseconds. For extended sources the S/N calculation is based on counts summed over one resolution element of 2 x 2 pixels, as the source size is assumed to be larger than the ACS resolution. A calibrated spectrum of your source can be provided directly to the [Exposure Time Calculator](#). The [ETC](#) also determines peak per-pixel count rates and total count rates to aid in feasibility assessment. Warnings appear if the source exceeds the local or global brightness limits for SBC observations (see Section 7.2). The [ETC](#) has online help for its execution and interpretation of results. Alternatively, users can use *synphot* in [STSDAS](#) to calculate count rates and the wavelength distribution of detected counts.

9.2 Determining Count Rates from Sensitivities

In this Chapter, specific formulae appropriate for imaging and spectroscopic modes are provided to calculate the expected count rates and the signal-to-noise ratio from the flux distribution of a source. The formulae are given in terms of sensitivities, but we also provide transformation equations between the throughput (QT) and sensitivity (S) for imaging and spectroscopic modes.

Throughputs are presented in graphical form as a function of wavelength for the prisms and for the imaging modes in Chapter 10. Given your source characteristics and the sensitivity of the ACS configuration, calculating the expected count rate over a given number of pixels is straightforward, since the ACS PSF is well characterized. The additional required information is the encircled energy fraction (ϵ_f) in the peak pixel, the plate scale, and the dispersions of the grisms and prisms. This information is summarized in Table 9.1, Table 9.2, and Table 9.3.

Table 9.1: Useful quantities for the ACS WFC.

| Filter | Pivot λ (Å) | $\int Q_{\lambda} T_{\lambda} d\lambda/\lambda$ | AB mag zero point | $\int S_{\lambda} d\lambda$ | encircled energy | Flux in central pixel | Background sky rate |
|--------|---------------------|---|-------------------|-----------------------------|------------------|-----------------------|---------------------|
| F435W | 4317.4 | 0.0744 | 25.67 | 3.18E18 | 0.85 | 0.22 | 0.0284 |
| F475W | 4744.3 | 0.1070 | 26.07 | 5.53E18 | 0.86 | 0.21 | 0.0609 |
| F502N | 5023.0 | 0.0032 | 22.27 | 1.88E17 | 0.86 | 0.21 | 0.0020 |
| F550M | 5581.2 | 0.0362 | 24.89 | 2.59E18 | 0.85 | 0.22 | 0.0280 |
| F555W | 5359.6 | 0.0775 | 25.72 | 5.11E18 | 0.86 | 0.21 | 0.0545 |
| F606W | 5917.7 | 0.1573 | 26.49 | 1.26E19 | 0.85 | 0.22 | 0.1358 |
| F625W | 6310.5 | 0.0915 | 25.90 | 8.37E18 | 0.85 | 0.22 | 0.0825 |
| F658N | 6583.9 | 0.0050 | 22.75 | 5.00E17 | 0.85 | 0.22 | 0.0045 |
| F660N | 6599.4 | 0.0019 | 21.67 | 1.87E17 | 0.85 | 0.22 | 0.0017 |
| F775W | 7693.0 | 0.0731 | 25.65 | 9.93E18 | 0.85 | 0.20 | 0.0780 |
| F814W | 8059.8 | 0.0948 | 25.94 | 1.41E19 | 0.83 | 0.19 | 0.1044 |
| F850LP | 9054.8 | 0.0352 | 24.86 | 6.63E18 | 0.73 | 0.14 | 0.0415 |
| F892N | 8914.9 | 0.0036 | 22.37 | 6.48E17 | 0.77 | 0.15 | 0.0039 |
| G800L | 7480.7 | 0.1591 | 26.50 | 2.04E19 | 0.86 | 0.17 | 0.1526 |
| CLEAR | 6269.8 | 0.3833 | 27.45 | 3.46E19 | ---- | 0.10 | 0.3580 |

Table 9.2: Useful quantities for the ACS HRC.

| Filter | Pivot λ (Å) | $\int Q_{\lambda} T_{\lambda} d\lambda/\lambda$ | AB mag zero point | $\int S_{\lambda} d\lambda$ | encircled energy | Flux in central pixel | Background sky rate |
|--------|---------------------|---|-------------------|-----------------------------|------------------|-----------------------|---------------------|
| F220W | 2255.3 | 0.0106 | 23.55 | 1.23E17 | 0.79 | 0.17 | 0.0001 |
| F250W | 2715.8 | 0.0123 | 23.72 | 2.09E17 | 0.82 | 0.16 | 0.0003 |
| F330W | 3362.7 | 0.0172 | 24.08 | 4.47E17 | 0.84 | 0.16 | 0.0006 |
| F344N | 3433.7 | 0.0017 | 21.59 | 4.67E16 | 0.84 | 0.16 | 0.0001 |
| F435W | 4311.0 | 0.0436 | 25.09 | 1.86E18 | 0.86 | 0.17 | 0.0043 |
| F475W | 4775.7 | 0.0650 | 25.53 | 3.40E18 | 0.85 | 0.17 | 0.0120 |
| F502N | 5022.9 | 0.0021 | 21.82 | 1.24E17 | 0.85 | 0.17 | 0.0003 |
| F550M | 5579.8 | 0.0234 | 24.42 | 1.67E18 | 0.85 | 0.15 | 0.0048 |
| F555W | 5356.0 | 0.0503 | 25.25 | 3.31E18 | 0.85 | 0.16 | 0.0099 |
| F606W | 5888.0 | 0.0983 | 25.98 | 7.82E18 | 0.85 | 0.14 | 0.0238 |
| F625W | 6295.5 | 0.0557 | 25.36 | 5.07E18 | 0.84 | 0.13 | 0.0148 |
| F658N | 6583.7 | 0.0030 | 22.18 | 2.98E17 | 0.83 | 0.13 | 0.0008 |
| F660N | 6599.1 | 0.0011 | 21.11 | 1.11E17 | 0.83 | 0.13 | 0.0003 |
| F775W | 7665.1 | 0.0380 | 24.94 | 5.13E18 | 0.78 | 0.11 | 0.0111 |
| F814W | 8115.3 | 0.0521 | 25.29 | 7.88E18 | 0.76 | 0.10 | 0.0161 |
| F850LP | 9145.2 | 0.0228 | 24.39 | 4.37E18 | 0.68 | 0.08 | 0.0075 |
| F892N | 8916.1 | 0.0022 | 21.87 | 4.09E17 | 0.73 | 0.09 | 0.0007 |
| G800L | 7506.4 | 0.0924 | 25.91 | 1.20E19 | 0.81 | 0.07 | 0.0250 |
| PR200L | 5650.2 | 0.2756 | 27.10 | 2.02E19 | 0.80 | 0.16 | 0.0624 |
| CLEAR | 5472.0 | 0.3205 | 27.26 | 2.20E19 | ---- | 0.12 | 0.0683 |

Table 9.3: Useful quantities for the ACS SBC.

| Filter | Pivot λ (Å) | $\int Q_{\lambda} T_{\lambda} d\lambda/\lambda$ | AB mag zero point | $\int S_{\lambda} d\lambda$ | encircled energy | Flux in central pixel | Background sky rate |
|--------|---------------------|---|-------------------|-----------------------------|------------------|-----------------------|---------------------|
| F115LP | 1406.1 | 0.0147 | 23.92 | 6.70E16 | 0.83 | 0.11 | 0.0238 |
| F122M | 1273.8 | 0.0010 | 20.95 | 3.56E15 | 0.82 | 0.09 | 0.0042 |
| F125LP | 1437.5 | 0.0122 | 23.71 | 5.80E16 | 0.83 | 0.12 | 0.0027 |
| F140LP | 1527.0 | 0.0069 | 23.09 | 3.68E16 | 0.84 | 0.13 | 0.0000 |
| F150LP | 1610.7 | 0.0038 | 22.45 | 2.27E16 | 0.84 | 0.14 | 0.0000 |
| F165LP | 1757.9 | 0.0010 | 21.02 | 7.29E15 | 0.85 | 0.16 | 0.0000 |
| PR110L | 1429.4 | 0.0120 | 23.69 | 5.62E16 | 0.86 | 0.26 | 0.0129 |
| PR130L | 1438.8 | 0.0120 | 23.68 | 5.66E16 | 0.87 | 0.28 | 0.0027 |

In each Table, the following quantities are listed:

- The pivot wavelength, a source-independent measure of the characteristic wavelength of the bandpass, defined such that it is the same if the input spectrum is in units of F_{λ} or F_{ν} :

$$\lambda_p = \sqrt{\frac{\int Q(\lambda)T(\lambda)d\lambda}{\int Q(\lambda)T(\lambda)((d\lambda)/\lambda)}}$$

- The integral $\int Q_{\lambda} T_{\lambda} d\lambda/\lambda$, used to determine the count rate when given the astronomical magnitude of the source.
- The ABmag zero point, defined as the AB magnitude of a source with a constant F_{ν} that gives 1 count/second with the specified configuration.
- The sensitivity integral, defined as the count rate that would be observed from a constant F_{λ} source with flux 1 erg/cm/second/Å.
- The encircled energy, defined as the fraction of PSF flux enclosed in the default photometry aperture 0.2 arcseconds for the WFC and HRC, and 0.5 arcseconds for the SBC. These correspond approximately to 5×5 , 9×9 , and 15×15 box-sizes respectively.
- The fraction of PSF flux in the central pixel, useful for determining the peak count rate to check for overflow or bright object protection possibilities.
- The sky background count rate, which is the count rate that would be measured with average zodiacal background, and average earthshine. It does not include the contribution from the detectors, tabulated separately in Table 9.5.

Here, we describe how to determine two quantities:

1. The counts/second (C) from your source over some selected area of N_{pix} pixels, where a signal of an electron on a CCD is equivalent to one count.
2. The peak counts/second/pixel (P_{cr}) from your source, which is useful for avoiding saturated CCD exposures, and for assuring that SBC observations do not exceed the bright-object limits.

We consider the cases of point sources and diffuse sources separately in each of the imaging and spectroscopy sections following.

9.2.1 Imaging

Point Source

For a point source, the count rate, C , can be expressed as the integral over the bandpass of the filter:

$$C = A \int F_{\lambda} \frac{\lambda}{hc} Q_{\lambda} T_{\lambda} \varepsilon_f d\lambda = \int F_{\lambda} S_{\lambda} \varepsilon_f d\lambda$$

Where:

- A is the area of the unobstructed 2.4 meter telescope (i.e., 45,239 cm²)
- F_{λ} is the flux from the astronomical source in erg/second/cm²/Å
- h is Planck's constant
- c is the speed of light
- The factor λ/hc converts ergs to photons.
- $Q_{\lambda} T_{\lambda}$ is the system fractional throughput, i.e. the probability of detecting a count per incident photon, including losses due to obstructions of the full 2.4 meter OTA aperture. It is specified this way to separate out the instrument sensitivity Q_{λ} and the filter transmission T_{λ} .
- ε_f = the fraction of the point source energy encircled within N_{pix} pixels.
- S_{λ} is the total imaging point source sensitivity with units of counts/second/Å per incident erg/second/cm²/Å.

The peak counts/second/pixel/ from the point source, is given by:

$$C_{peak} = \int F_{\lambda} S_{\lambda} \varepsilon_f(1) d\lambda$$

Where:

- F_λ , and S_λ are as above.
- $\varepsilon_f(1)$ is the fraction of energy encircled within the peak pixel.

Again, the integral is over the bandpass.

If the flux from your source can be approximated by a flat continuum ($F_\lambda = \text{constant}$) and ε_f is roughly constant over the bandpass, then:

$$C = F_\lambda \varepsilon_f \int S_\lambda d\lambda$$

We can now define an equivalent bandpass of the filter (B_λ) such that:

$$\int S_\lambda d\lambda = S_{peak} B_\lambda$$

Where:

- S_{peak} is the peak sensitivity.
- B_λ is the effective bandpass of the filter.

The count rate from the source can now be written as:

$$C = F_\lambda \varepsilon_f S_{peak} B_\lambda$$

In Tables 9.1 to 9.3, we give the value of $\int S_\lambda d\lambda$ for each of the filters. Alternatively, we can write the equation in terms of V magnitudes:

$$C = 2.5 \times 10^{11} \varepsilon_f \left(\int QT d\lambda / \lambda \right) \times 10^{-0.4(V + AB_v)}$$

where V is the visual magnitude of the source, the quantity under the integral sign is the mean sensitivity of the detector+filter combination, and is tabulated in Tables 9.1 to 9.3, and AB_v is the filter-dependent correction for the deviation of the source spectrum from a constant F_v spectrum. This latter quantity is tabulated for several different astronomical spectra in Tables 10.1 to 10.3 in Chapter 10.

Diffuse Source

For a diffuse source, the count rate, C , per pixel, due to the astronomical source can be expressed as:

$$C = \int I_\lambda S_\lambda m_x m_y d\lambda$$

Where:

- I_λ = the surface brightness of the astronomical source, in $\text{erg/second/cm}^2/\text{\AA}/\text{arcseconds}^2$.
- S_λ as above.
- m_x and m_y are the plate scales along orthogonal axes.

Emission Line Source

For a source where the flux is dominated by a single emission line, the count rate can be calculated from the equation

$$C = 2.23 \times 10^{12} \cdot (QT)_\lambda \cdot F(\lambda) \cdot \lambda$$

where C is the observed count rate in counts/second, (QT) is the system throughput at the wavelength of the emission line, $F(\lambda)$ is the emission line flux in units of erg/cm²/second, and λ is the wavelength of the emission line in Angstroms. $(QT)_\lambda$ can be determined by inspection of the plots in Chapter 10. See Section 9.6.4 for an example of emission-line imaging using ACS.

9.2.2 Spectroscopy

Point Source

For a point source spectrum with a **continuum flux distribution**, the count rate, C , is per pixel in the dispersion direction, and is integrated over a fixed extraction height N_{spix} in the spatial direction perpendicular to the dispersion:

$$C = F_\lambda S'_\lambda \epsilon'_{Nspix} = F_\lambda A \frac{\lambda}{hc} T_\lambda \epsilon'_{Nspix} d$$

Where:

- S'_λ is the total point source sensitivity in units of counts/second per incident erg/second/cm²/Å; and $S_\lambda = S'_\lambda \cdot d$
- d is the dispersion in Å/pixel.
- ϵ'_{Nspix} is the fraction of the point source energy within N_{spix} in the spatial direction.
- the other quantities are defined above.

For an **unresolved emission line** at $\lambda = L$ with a flux of F_L in erg/second/cm² the total counts recorded over the N_{spix} extraction height is:

$$C = F_\lambda S'_\lambda / d$$

These counts will be distributed over pixels in the wavelength direction according to the instrumental line spread function.

In contrast to the case of imaging, sensitivity S_λ , the spectroscopic point source sensitivity calibration ($S_\lambda \times \epsilon_{Nspix}$) for a default extraction height of N_{spix} is measured directly from observations of stellar flux standards after insertion of ACS into HST. Therefore, the accuracy in laboratory

determinations of T_λ for the ACS prisms and grisms is NOT crucial to the final accuracy of their sensitivity calibrations.

The peak counts/second/pixel from the point source, is given by:

$$P_{cr} = \varepsilon'_f(1)F_\lambda S'_\lambda$$

Where:

- $\varepsilon'_f(1)$ is the fraction of energy contained within the peak pixel.
- the other quantities are as above.

9.3 Computing Exposure Times

To derive the exposure time to achieve a given signal-to-noise ratio, or to derive the signal-to-noise ratio in a given exposure time, there are four principal ingredients:

- Expected counts C from your source over some area.
- The area (in pixels) over which those counts are received (N_{pix}).
- Sky background (B_{sky}) in counts/pixel/second.
- The detector background, or dark, (B_{det}) in counts/second/pixel and the read noise (R) in counts of the CCD.
- Section 9.4 provides the information for determining the sky-plus-detector background.

9.3.1 Calculating Exposure Times for a Given Signal-to-Noise

The signal-to-noise ratio, Σ is given by:

$$\Sigma = \frac{Ct}{\sqrt{Ct + N_{pix}(B_{sky} + B_{det})t + N_{pix}N_{read}R^2}}$$

Where:

- C = the signal from the astronomical source in counts/second, or electrons/second from the CCD. The actual output signal from a CCD is C/G where G is the gain. You must remember to multiply by G to compute photon events in the raw CCD images.
- G = the gain is always 1 for the SBC, and $\sim 1, 2, 4, \text{ or } 8$ for the CCDs, depending on GAIN.

- N_{pix} = the total number of detector pixels integrated over to achieve C .
- B_{sky} = the sky background in counts/second/pixel.
- B_{det} = the detector dark current in counts/second/pixel.
- R = the read noise in electrons; = 0 for SBC observations, 5.0 and 4.7 for WFC and HRC respectively
- N_{read} = the number of CCD readouts.
- t = the integration time in seconds.

This equation assumes the optimistic (and often realistic) condition that the background zero point level under the object is sufficiently well known (and subtracted) to not significantly contribute; in crowded fields this may not be true.

Observers using the CCD normally take sufficiently long integrations that the CCD read noise is not important. This condition is met when:

$$Ct + N_{pix}(B_{sky} + B_{det})t > 2N_{pix}N_{read}R^2$$

For the CCD in the regime where read noise is not important and for all SBC observations, the integration time to reach a signal-to-noise ratio Σ , is given by:

$$t = \frac{\Sigma^2[C + N_{pix}(B_{sky} + B_{det})]}{C^2}$$

If your source count rate is much brighter than the sky plus detector backgrounds, then this expression reduces further to:

$$t = \frac{\Sigma^2}{C}$$

i.e. the usual result for Poisson statistics of $\Sigma = \sqrt{totalcounts}$.

More generally, the required integration time to reach a signal to noise ratio Σ is given by:

$$t = \frac{\Sigma^2[C + N_{pix}(B_{sky} + B_{det})] + \sqrt{\Sigma^4[C + N_{pix}(B_{sky} + B_{det})]^2 + 4\Sigma^2C^2[N_{pix}N_{read}R^2]}}{2C^2}$$

9.3.2 Exposure Time Estimates for Red Targets in F850LP

At wavelengths greater than 7500 Å (HRC) and about 9000 Å (WFC) ACS CCD observations are affected by a red halo due to light scattered off

the CCD substrate. An increasing fraction of the light as a function of wavelength is scattered from the center of the PSF into the wings. This problem affects particularly the very broad z-band F850LP filter, for which the encircled energy depends on the underlying spectral energy distribution the most. In the currently available *ETC*, the treatment of such an effect has been ameliorated but not solved. The encircled energy fraction is calculated at the effective wavelength which takes into account the source spectral distribution. This fraction is then multiplied by the source counts. (The effective wavelength is the weighted average of the system throughput AND source flux distribution integrated over wavelength). However, this does not account for the variation in enclosed energy with wavelength.

As a consequence, in order to obtain correct estimated count rates for red targets, observers are advised to use the *synphot* package in IRAF/STSDAS for which the proper integration of encircled energy over wavelength has now been incorporated. To quantify this new *synphot* capability, we compare *ETC* results with *synphot* for a set of different spectral energy distributions and the observation mode WFC/F850LP. In Table 9.4, the spectral type is listed in the first column. The fraction of light with respect to the total integrated to infinity is listed in the other two columns, for the *ETC* and *synphot* calculations respectively. These values are derived for a 0.2 arcseconds aperture for the *ETC* calculations and *synphot*.

Table 9.4: Encircled energy comparison for WFC/F850LP.

| Spectral type | APT ETC | Synphot |
|---------------|---------|---------|
| O | 0.76 | 0.74 |
| M | 0.71 | 0.7 |
| L | 0.69 | 0.68 |
| T | 0.61 | 0.6 |

The *ETC* results are off by 3% (O star), 2% (M star), 2% (L star), and 1% (T star). If this small effect is relevant to particular observations, then the *synphot* software package can be used. To learn how to use the *synphot* tool, we refer to the instructions provided in the April 2003 STAN, <http://www.stsci.edu/hst/acs/documents/newsletters/stan0302.html>, and in ACS ISR 2003-08.

9.4 Detector and Sky Backgrounds

When calculating expected signal-to-noise ratios or exposure times, the background from the sky, and the background from the detector must be taken into account.

9.4.1 Detector Backgrounds

See Tables 4.1 and 4.2 for read-noise and dark-current characteristics of the detectors, including variations by amplifier and GAIN for the CCDs.

9.4.2 Sky Background

The sources of sky background which will affect ACS observations include:

- Earth shine (ES).
- Zodiacal light (ZL).
- Geocoronal emission (GC).

The background in counts/second/pixel for **imaging observations** can be computed as:

$$B_{sky} = \int I_{\lambda} S_{\lambda} m_x m_y d\lambda$$

Where:

- I_{λ} is the surface brightness of the sky background, in erg/second/cm²/Å/arcseconds².
- S_{λ} is the point source sensitivity for the imaging mode.
- m_x and m_y are the plate scales along orthogonal axes.

The image of the sky through a disperser is not uniform, since some wavelengths fall off the detector for regions of sky near the edge of the field of view (FOV). Since the ACS grism spectra are of order 200 pixels long, the regions of lower sky will be strips at the long and short wavelength edges of the FOV. The maximum width of the strips from where the signal starts to decline to the edge, where the signal is down by roughly 2x, is about half the total length of a spectrum of a point source, i.e. roughly 100 pixels in the case of a sky background with a **continuum** of wavelengths. In the case of the HRC, the sky for the dispersed mode will not have the low background strips, since the FOV is not masked to the detector size. These small strips of lower sky background in the SBC and the WFC are ignored in the following formulae. Furthermore in the SBC

and the WFC, since the spectra do not lie along the direction of the anamorphic distortion, the plate scales of m_x and m_y above must be replaced by the plate scales m_s and m_λ in the orthogonal spatial and dispersion directions, respectively. Interior to the strips, a point on the detector sees a region of sky over the full wavelength coverage of the disperser. Thus, for **spectroscopic observations**:

$$B_{sky}^\lambda = \int I_\lambda S'_\lambda m_s m_\lambda d\lambda$$

For a **monochromatic** sky emission line at $\lambda = L$ like Lyman- α , which will dominate the background through the LiF prism:

$$B_{sky}^L = I_L S'_\lambda m_s m_\lambda / d$$

where

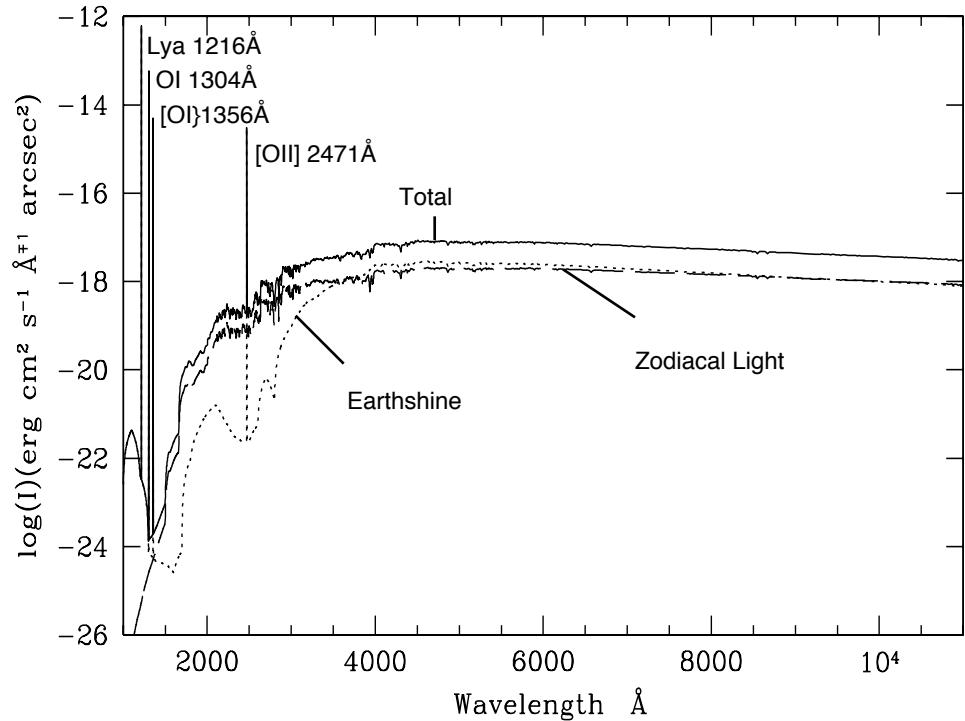
- I_L is the monochromatic intensity of a line at wavelength L in erg/second/cm²/ arcseconds².

The total sky background is:

$$B_{sky} = B_{sky}^\lambda + B_{sky}^L$$

Figure 9.1 and Table 9.7 show “high” sky background intensity as a function of wavelength, identifying the separate components which contribute to the background. The “shadow” and “average” values of the Earthshine contribution in the [ACS Exposure Time Calculator](#) correspond, respectively, to 0 and 50% of the “high” values in Figure 9.1 and Table 9.7. For the zodiacal sky background, the values in Figure 9.1 and Table 9.7 correspond to the high value of $m_V = 22.1$ from Table 9.5, while the “low” and “average” zodiacal light is scaled to $m_V = 23.3$ and 22.7, respectively.

Figure 9.1: High sky background intensity as a function of wavelength.



The zodiacal contribution (ZL) is at ecliptic latitude and longitude of $30^\circ, 180^\circ$, and corresponds to $m_v = 22.7$ per square arcseconds. The Earthshine (ES) is for a target which is 24° from the limb of the sunlit Earth. Use Figure 9.2 to estimate background contributions at other angles. The daytime geocoronal line intensities are in $\text{erg}/\text{cm}^2/\text{second}/\text{arcseconds}^2$ (see Table 9.6).

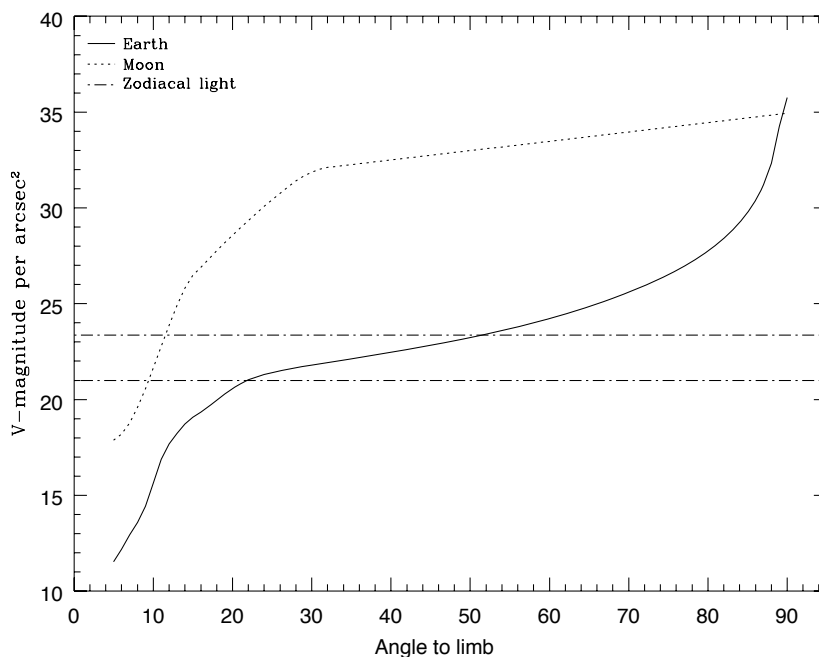
Background Variations and LOW-SKY

In the ultraviolet, the background contains bright airglow lines, which vary from day to night and as a function of HST orbital position. The airglow lines may be the dominant sky contributions in the UV both for imaging-mode and spectroscopic observations. Away from the airglow lines, at wavelengths shortward of $\sim 3000 \text{ \AA}$, the background is dominated by zodiacal light, where the small area of sky that corresponds to a pixel of the high resolution HST instrumentation usually produces a signal that is much lower than the intrinsic detector background. The contribution of zodiacal light does not vary dramatically with time, and varies by only a factor of about three throughout most of the sky. Table 9.5 gives the variation of the zodiacal background as a function of ecliptic latitude and longitude. For a target near ecliptic coordinates of $(50,0)$ or $(-50,0)$, the zodiacal light is relatively bright at $m_v = 20.9$, i.e. about 9 times the faintest values of $m_v = 23.3$. Deep imaging applications must carefully consider expected sky values!

On the other hand, Earthshine varies strongly depending on the angle between the target and the bright Earth limb. The variation of the Earthshine as a function of limb angle from the sunlit Earth is shown in

Figure 9.2. The Figure also shows the contribution of the moon, which is typically much smaller than the zodiacal contribution, for which the upper and lower limits are shown. For reference, the limb angle is approximately 24° when the HST is aligned toward its orbit pole (i.e., the center of the CVZ). The Earthshine contribution shown in Figure 9.1 and Table 9.7 corresponds to this position.

Figure 9.2: Background contributions in V magnitude per arcseconds² due to the zodiacal light, Moon, and the sunlit Earth, as a function of angle between the target and the limb of the Earth or Moon.



The two zodiacal light lines show the extremes of possible values.

For observations taken longward of 3500 \AA , the Earthshine dominates the background at small ($< 22^\circ$) limb angles. In fact, the background increases exponentially for limb angles $< 22^\circ$. The background near the bright limb can also vary by a factor of ~ 2 on timescales as short as two minutes, which suggests that the background from Earthshine also depends upon the reflectivity of the terrain over which HST passes during the course of an exposure. Details of the sky background as it affects ACS, as well as STIS, are discussed by Shaw, et al. (STIS ISR 98-21). The impact of Earthshine on ACS observations is discussed by Biretta, et al., (ACS ISR 03-05).

Table 9.5: Approximate zodiacal sky background as a function of ecliptic latitude and ecliptic longitude (in V magnitudes per square arcseconds).

| Ecliptic longitude (degrees) | Ecliptic latitude (degrees) | | | |
|------------------------------|-----------------------------|------|------|------|
| | 0 | 30 | 60 | 90 |
| 180 | 22.1 | 22.7 | 23.2 | 23.3 |
| 145 | 22.4 | 22.9 | 23.3 | 23.3 |
| 110 | 22.3 | 22.9 | 23.3 | 23.3 |
| 50 | 20.9 | 22.2 | 22.9 | 23.3 |

Observations of the faintest objects may need the special requirement **LOW-SKY** in the Phase II observing program. **LOW-SKY** observations are scheduled during the part of the year when the zodiacal background light is no more than 30% greater than the minimum possible zodiacal light for the given sky position. **LOW-SKY** in the Phase II scheduling also invokes the restriction that exposures will be taken only at angles greater than 40° from the bright Earth limb to minimize Earthshine and the UV airglow lines. The **LOW-SKY** special requirement limits the times at which targets within 60° of the ecliptic plane will schedule, and limits visibility to about 48 minutes per orbit. The use of **LOW-SKY** must be requested and justified in the Phase I Proposal.

The **ETC** provides the user with the flexibility to separately adjust both the zodiacal (low, average, high) and Earthshine (shadow, average, high) sky background components in order to determine if planning for use of **LOW-SKY** is advisable for a given program. However, the absolute sky levels that can be specified in the **ETC** may not be achievable for a given target; e.g., as shown in Table 9.5 the zodiacal background minimum for an ecliptic target is $m_v = 22.4$ which is still brighter than both the low and average options with the **ETC**. By contrast, a target near the ecliptic pole would always have a zodiacal = low background in the **ETC**. The user is cautioned to carefully consider sky levels as the backgrounds obtained in HST observations can cover significant ranges.

Geocoronal Emission and Shadow

Background due to geocoronal emission originates mainly from hydrogen and oxygen atoms in the exosphere of the Earth. The emission is concentrated in the four lines listed in Table 9.6. The brightest line is Lyman- α at 1216 Å. The strength of the Lyman- α line varies between about 2 and ~30 kilo-Rayleighs (i.e., between 6.1×10^{-14} and 6.1×10^{-13} erg /second/cm²/arcseconds² where 1 Rayleigh = 10^6 photons/second/cm per 4π steradian) depending on the position of HST with respect to the day-night terminator and the position of the target relative to the Earth limb. The next strongest line is the OI line at 1304 Å, which rarely exceeds

10% of Lyman- α . The typical strength of the OI 1304 Å line is about 1 kilo-Rayleighs (which corresponds to about 2.85×10^{-14} erg/second/cm²/arcseconds²) on the daylight side and about 75 times fainter on the night side of the HST orbit. OI 1356 Å and OI 2471 Å lines may appear in observations on the daylight side of the orbit, but these lines are ~10 times weaker than the OI 1304 Å line. The width of the lines also vary with temperature, the line widths given in Table 9.6 are representative values assuming a temperature of 2000 °K.

Except for the brightest objects (e.g. planets), a filter or prism mode which does not transmit at Lyman- α should be employed. To minimize geocoronal emission the special requirement SHADOW can be requested. Exposures using this special requirement are limited to roughly 25 minutes per orbit, exclusive of the guide-star acquisition (or reacquisition), and can be scheduled only during a small percentage of the year. SHADOW reduces the contribution from the geocoronal emission lines by roughly a factor of ten while the continuum Earthshine is set to zero. SHADOW requirements must be included and justified in your Phase I proposal (see the *Call for Proposals*).

Table 9.6: Geocoronal emission lines.

| Wavelength (Å) | ID | Line width (Å) | Intensity | | | |
|-------------------|--------------|----------------------|--------------------|--|--------------------|--|
| | | | Day | | Night | |
| | | | kilo- Rayleighs | erg/s/cm ² /arcsec ² | kilo- Rayleighs | erg/s/cm ² /arcsec ² |
| 1216 | Ly- α | 0.04 | ~20 | 6.1×10^{-13} | 2 | 6.1×10^{-14} |
| 1304 | OI | 0.013 | ~2 | 5.7×10^{-14} | 0.013 | 3.8×10^{-16} |
| 1356 | OI | 0.013 | ~0.2 | $\sim 5 \times 10^{-15}$ | ~0.001 | $\sim 3 \times 10^{-17}$ |
| 2471 | OI | 0.023 | <0.2 | $< 3 \times 10^{-15}$ | <0.001 | $< 1.5 \times 10^{-17}$ |

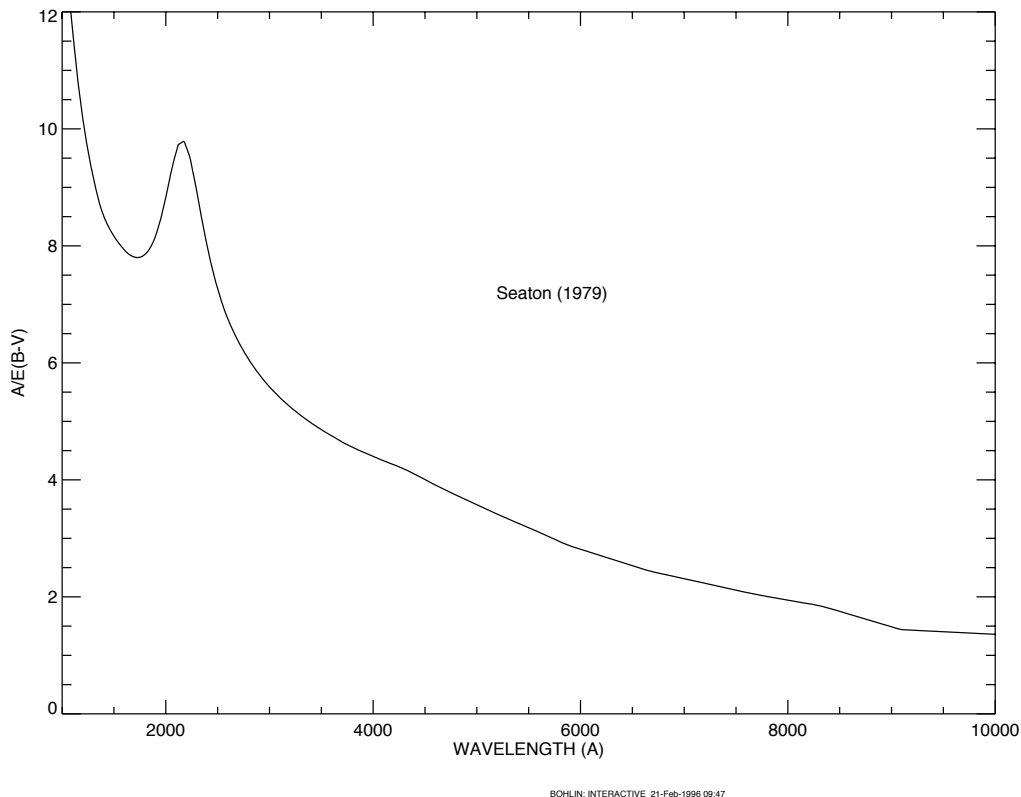
9.5 Extinction Correction

Extinction can dramatically reduce the counts expected from your source, particularly in the ultraviolet. Figure 9.3 shows the average $A_v / E(B-V)$ values for our galaxy, taken from (Seaton, *MNRAS*, **187**, 73P, 1979). Large variations about the average are observed (Witt, Bohlin, Stecher, *ApJ*, **279**, 698, 1984).

Extinction curves have a strong metallicity dependence, particularly in the UV wavelengths. Sample extinction curves can be seen in Koornneef and Code, *ApJ*, **247**, 860 1981 (LMC); Bouchet et al., *A&A*, **149**, 330 1985 (SMC); and Calzetti, Kinney and Storchi-Bergmann, *ApJ*, **429**, 582, 1994,

and references therein. At lower metallicities, the 2200 Å bump which is so prominent in the galactic extinction curve disappears; and $A_V/E(B-V)$ may increase monotonically at UV wavelengths.

Figure 9.3: Extinction versus wavelength.



9.6 Exposure-Time Examples

In the following you will find a set of examples for the three different channels and for different types of sources. The examples were chosen in order to present typical objects for the three channels and also to present interesting cases as they may arise with the use of ACS.

9.6.1 Example 1: WFC Imaging a Faint Point Source

What is the exposure time needed to obtain a signal to noise of 10 for a point source of spectral type F2 V, normalized to $V = 26.5$, when using the WFC, F555W filter? Assume a GAIN of 1 and a photometry box size of 11 x 11 pixels, and average sky values.

The [ACS Exposure Time Calculator \(ETC\)](#) gives a total exposure time of 4410 seconds to obtain this S/N in a single exposure. Since such an

exposure would be riddled with cosmic rays and essentially useless, it is necessary to specify how many exposures to split the observation into. ACS WFC observations generally should be split if the exposure time is larger than about 5 minutes, but for multi-orbit observations, splitting into 2 exposures per orbit is generally sufficient.

For a typical object visibility of 53 minutes, after applying the requisite overheads, there is time for two 1200 seconds exposures per orbit. The required exposure time can thus be reached in 4 exposures, but re-running the ETC using CR-SPLIT=4 raises the required exposure time to 5303 seconds (because of the extra noise introduced by the four extra readouts). To achieve the required exposure time would require CR-SPLIT=5, or three orbits.

Using the pencil and paper method, Table 9.1 gives the integral $QTd\lambda/\lambda$ as 0.0775, and the AB_{ν} correction term can be retrieved from Table 10.1 as 0.040. According to Figure 5.9, a circular aperture of radius 0.3 arcseconds (which has an area of 116 pixels, close to the 121 pixel box specified) encloses about 90% of the light from a star. The count rate is then $2.5 \times 10^{11} * 0.0775 * 0.9 * 10^{-0.4(26.5+0.040)} = 0.423$ counts/second, which agrees with the ETC-returned value of 0.42. The exposure time can then be found by using the equation

$$t = \frac{\Sigma^2 [C + N_{pix}(B_{sky} + B_{det})]}{C^2}$$

to give $t = 4172$ seconds, which is close to the ETC-derived value of 4410 seconds. We have inserted the background rate from Table 9.1 ($B_{sky} = 0.055$) and Table 9.5 ($B_{det} = 0.0032$), and assumed that the noise on the background is much greater than the readout noise.

Note that this can be greatly shortened by specifying a smaller analysis box (for example, 5 x 5) and using LOW-SKY. Dropping the aperture size to 5 x 5 at average sky which still encloses 81% of the light requires 1532 seconds. Including both the smaller 5 x 5 box and LOW-SKY (Zodiacal = LOW, Earthshine = AVERAGE), using the ETC gives the required exposure time as only 1306 seconds (using CR-SPLIT=1), or 1540 seconds with CR-SPLIT=2. The LOW-SKY visibility per orbit is 47 minutes, which allows a total on-target exposure time of 2000 seconds in one orbit with CR-SPLIT=2.

Note also that the count rate from WFPC2 would be 0.167 electrons/second, a factor of 2.5 lower.

9.6.2 Example 2: SBC Objective Prism Spectrum of a UV Spectrophotometric Standard Star

What is the peak count rate using the PR110L prism in the SBC for the HST standard star HS2027+0651 ($V = 16.9$) that was used for the STIS

prism calibration (this spectrum is not in the ETC list, therefore we quote below the flux which could be found by dearchiving the STIS spectrum)?

The sensitivity peaks in the 1500 Å to 1600 Å region. To find the count rate at 1537 Å, inspection of Figure 6.22 gives the sensitivity of 9.9×10^{14} counts/second per $\text{erg}/\text{cm}^2/\text{s}/\text{Å}$. Multiplying by the stellar flux of 5.3587×10^{-14} gives 53.0 counts/second, summed in the cross dispersion direction. For the fraction of light in the central pixel $\epsilon = 0.31$, the brightest pixel at 1437.6 Å is 17.6 counts/second/pixel, well below the bright object limit.

The SBC has no readout noise, and the dark current rate is negligible, while the main sky contribution for PR110L is from Lyman- α . For daytime Ly- α intensity of $20\text{kR} = 6.1 \times 10^{-13}$ $\text{ergs}/\text{cm}^2/\text{second}/\text{arcseconds}^2$, $S' = 1.7 \times 10^{14}$, and d , the dispersion in Å/pixel, is 2.58. Therefore, the background count rate is $6.1 \times 10^{-13} * 1.7 \times 10^{14} * 0.032^2 / 2.58 = 0.041$ counts/second/pixel. This value varies somewhat over the field, as the plate scale varies from the nominal 0.032 arcseconds/pixel. For faint source spectroscopy, it is better to use PR130L, which is on a CaF_2 substrate to block Ly- α .

9.6.3 Example 3: WFC VIS Polarimetry of the Jet of M87

What signal to noise ratio is reached in three one orbit exposures (~2400 seconds each) for M87, when using the WFC, F555W for one orbit each in the three VIS polarizers? Gain is 2, box size is 5 x 5 pixels, CR-SPLIT=2, and average sky.

If the M87 jet region has $\mu_V = 17$ magnitudes/arcseconds², using the ETC with a flat continuum spectral distribution and an exposure time of 2400 seconds (CR-SPLIT=2), gives $S/N = 131.6$ for an observation with each VIS polarizer filter (which is an average of the polarizer at the 3 available position angles 0°, 60°, and 120°). If the polarization P is 20%, then $P*S/N = 26.3$, so using

$$\log\left(\frac{\sigma_P}{P}\right) = -0.102 - 0.9898 \log(P \langle S/N \rangle_i)$$

from Chapter 6, $\sigma_P/P = 0.031$, or $\sigma_P = 6.2 \times 10^{-3}$, which is the error on the fractional polarization. The error on the position angle should be $\sim 1.0^\circ$ using the formula, again from Chapter 6, of

$$\log \sigma_\theta = 1.514 - 1.068 \log(P \langle S/N \rangle_i)$$

9.6.4 Example 4: SBC imaging of Jupiter’s Aurora at Lyman-alpha

What signal to noise ratio is reached in a one orbit exposure (2000 seconds) observing Jupiter’s aurora in Ly- α using the SBC and F122M filter?

The equation from the Section , “Emission Line Source,” on page 171 can be used to calculate the expected count rate. The aurora is variable, up to $\sim 100\text{kR}$. The value of (QT) for the SBC+F122M filter at 1216 \AA is 0.0009, from inspection of Figure 10.106 on page 226. For a surface brightness of $40\text{kR} = 1.22 \times 10^{-12} \text{ erg/cm}^2/\text{second}/\text{arcseconds}^2$ (See “Geocoronal Emission and Shadow” on page 179 for conversion), the total counts per pixel are given by the following calculation:

$$2.23 \times 10^{12} * 0.009 * 1.22 \times 10^{-12} * 1216 * (0.032)^2 * 2000 = 61.0.$$

The background contributions are the detector dark of $1.2 \times 10^{-5} \text{ counts/pixel/second}$ (which can be ignored in this case) and a sky background which is dominated by geocoronal Lyman- α . During the daytime, the geocoronal background is 20kR , or 30.5 counts, while at night the background drops to one tenth of this, or 3.05 counts.

Finally, we calculate the signal to noise ratio Σ for a 2×2 pixel resolution element: in the daytime, $\Sigma = 61.0 \cdot 4 / \sqrt{(61.0 + 30.5) \cdot 4} = 12.7$, while at night, $\Sigma = 61.0 \cdot 4 / \sqrt{(61.0 + 3.05) \cdot 4} = 15.2$

9.6.5 Example 5: Coronagraphic imaging of the Beta-Pictoris Disk

In the final example we shall consider the case where we are trying to determine the S/N achieved on the Beta Pictoris disk, assuming a disk surface brightness of R magnitude of 16 arcseconds² at a distance of 6 arcseconds from the central star with a V magnitude of 3.9, for an exposure time of 1000 seconds with an F435W filter. Assume that the star and disk have an A5 V-type spectrum. Using the [ACS Exposure Time Calculator](#) and considering the case for the 3.0 arcseconds occulting mask:

- Disk count rate = $4.98 \text{ e}^-/\text{second}$ for a 2×2 aperture (including 47.5% throughput of coronagraph)
Sky count rate = $0.010 \text{ e}^-/\text{second}/\text{pixel}$,
Detector dark rate = $0.015 \text{ e}^-/\text{second}/\text{pixel}$
- In 1000 seconds, this gives $4,980 \text{ e}^-/2 \times 2$ aperture in the disk region.
- Central star count rate = $3.63 \times 10^8 \text{ e}^-/\text{second}$ for a 101×101 aperture (101×101 aperture used to estimate total integrated flux)

- At a distance 6 arcseconds from the central star, the fraction of flux per square arcsecond in the PSF wings is 2.6×10^{-6} .
 $B_{\text{PSF}} = 3.63 \times 10^{11} * 2.6 \times 10^{-6} = 943.8 \text{ e}^-$ per square arcsecond. The counts collected in 4 pixels are $4 \times 0.027^2 \times (943.8) = 2.752$.
- The S/N in a 2×2 box is then $4980 / \sqrt{4980 + 2.8} \cong 70.5$.

9.7 Tabular Sky Backgrounds

We provide Table 9.7 of the “high” sky background numbers as plotted in Figure 9.1. See the text and the caption in Figure 9.1 for more details. These high sky values are defined as the earthshine at 38° from the limb and the high zodiacal light of $m_v = 22.1$ magnitude/arcseconds².

Table 9.7: High sky backgrounds.

| Wavelength | Earthshine | Zodiacal light | Total background |
|------------|--|--|--|
| Å | erg/sec/cm ² /Å/arcsec ² | erg/sec/cm ² /Å/arcsec ² | erg/sec/cm ² /Å/arcsec ² |
| 1000. | 2.41E-23 | 1.26E-28 | 2.41E-23 |
| 1100. | 4.38E-22 | 1.02E-26 | 4.38E-22 |
| 1200. | 4.01E-23 | 1.05E-25 | 4.02E-23 |
| 1400. | 4.29E-25 | 2.50E-24 | 2.93E-24 |
| 1500. | 4.16E-25 | 9.12E-24 | 9.54E-24 |
| 1600. | 2.55E-25 | 2.30E-22 | 2.30E-22 |
| 1700. | 7.89E-23 | 7.06E-21 | 7.14E-21 |
| 1800. | 9.33E-23 | 1.50E-20 | 1.51E-20 |
| 1900. | 4.39E-22 | 2.20E-20 | 2.24E-20 |
| 2000. | 1.01E-21 | 3.49E-20 | 3.59E-20 |
| 2100. | 1.60E-21 | 1.21E-19 | 1.23E-19 |
| 2200. | 7.49E-22 | 2.16E-19 | 2.17E-19 |
| 2300. | 3.32E-22 | 1.75E-19 | 1.75E-19 |
| 2400. | 2.50E-22 | 1.79E-19 | 1.79E-19 |
| 2500. | 2.39E-22 | 2.47E-19 | 2.47E-19 |
| 2600. | 5.62E-22 | 2.93E-19 | 2.94E-19 |
| 2700. | 6.77E-21 | 9.95E-19 | 1.00E-18 |
| 2800. | 2.03E-21 | 2.82E-19 | 2.91E-19 |
| 2900. | 4.32E-20 | 2.04E-18 | 2.08E-18 |

Table 9.7: High sky backgrounds.

| Wavelength | Earthshine | Zodiacal light | Total background |
|-------------------|--|--|--|
| Å | erg/sec/cm ² /Å/arcsec ² | erg/sec/cm ² /Å/arcsec ² | erg/sec/cm ² /Å/arcsec ² |
| 3000. | 9.34E-20 | 1.20E-18 | 1.29E-18 |
| 3100. | 2.07E-19 | 1.46E-18 | 1.67E-18 |
| 3200. | 3.60E-19 | 2.25E-18 | 2.61E-18 |
| 3400. | 6.40E-19 | 2.81E-18 | 3.45E-18 |
| 3500. | 8.20E-19 | 2.73E-18 | 3.55E-18 |
| 3600. | 1.06E-18 | 2.68E-18 | 3.74E-18 |
| 3700. | 1.22E-18 | 3.25E-18 | 4.47E-18 |
| 3800. | 1.23E-18 | 3.05E-18 | 4.28E-18 |
| 3900. | 1.52E-18 | 3.27E-18 | 4.79E-18 |
| 4000. | 2.38E-18 | 4.54E-18 | 6.92E-18 |
| 4250. | 2.33E-18 | 4.48E-18 | 6.81E-18 |
| 4500. | 2.78E-18 | 5.32E-18 | 8.10E-18 |
| 5000. | 2.55E-18 | 4.92E-18 | 7.47E-18 |
| 5250. | 2.69E-18 | 5.28E-18 | 7.97E-18 |
| 5500. | 2.56E-18 | 5.20E-18 | 7.76E-18 |
| 5750. | 2.56E-18 | 5.33E-18 | 7.89E-18 |
| 6000. | 2.40E-18 | 5.11E-18 | 7.51E-18 |
| 6250. | 2.27E-18 | 4.94E-18 | 7.21E-18 |
| 6500. | 2.20E-18 | 4.88E-18 | 7.08E-18 |
| 6750. | 2.07E-18 | 4.69E-18 | 6.76E-18 |
| 7000. | 1.90E-18 | 4.40E-18 | 6.30E-18 |
| 7250. | 1.85E-18 | 4.34E-18 | 6.19E-18 |
| 7500. | 1.73E-18 | 4.13E-18 | 5.86E-18 |
| 7750. | 1.63E-18 | 3.95E-18 | 5.58E-18 |
| 8000. | 1.57E-18 | 3.85E-18 | 5.42E-18 |
| 8250. | 1.48E-18 | 3.68E-18 | 5.16E-18 |
| 8500. | 1.37E-18 | 3.46E-18 | 4.83E-18 |
| 8750. | 1.31E-18 | 3.36E-18 | 4.67E-18 |

CHAPTER 10:

Imaging Reference Material

In this chapter . . .

| | |
|---|-------------------------------------|
| 10.1 Introduction / 188 | HRC/F550M / 212 |
| 10.2 Using the Information in this Chapter / 188 | HRC/F555W / 213 |
| WFC/F435W / 191 | HRC/F606W / 214 |
| WFC/F475W / 192 | HRC/F625W / 215 |
| WFC/F502N / 193 | HRC/F658N / 216 |
| WFC/F550M / 194 | HRC/F660N / 217 |
| WFC/F555W / 195 | HRC/F775W / 218 |
| WFC/F606W / 196 | HRC/F814W / 219 |
| WFC/F625W / 197 | HRC/F850LP / 220 |
| WFC/F658N / 198 | HRC/F892N / 221 |
| WFC/F660N / 199 | HRC/G800L / 222 |
| WFC/F775W / 200 | HRC/PR200L / 223 |
| WFC/F814W / 201 | HRC/CLEAR / 224 |
| WFC/F850LP / 202 | SBC/F115LP / 225 |
| WFC/G800L / 203 | SBC/F122M / 226 |
| WFC/CLEAR / 204 | SBC/F125LP / 227 |
| HRC/F220W / 205 | SBC/F140LP / 228 |
| HRC/F250W / 206 | SBC/F150LP / 229 |
| HRC/F330W / 207 | SBC/F165LP / 230 |
| HRC/F344N / 208 | SBC/PR110L / 231 |
| HRC/F435W / 209 | SBC/PR130L / 232 |
| HRC/F475W / 210 | 10.3 Distortion in the ACS / 236 |
| HRC/F502N / 211 | |

In this Chapter, we provide imaging reference material, in support of the information presented in Chapter 9.

10.1 Introduction

This chapter provides reference material to help you select your filter and detector configuration, and determine your observing plan (e.g., total required exposure time, and number of exposures). This chapter is, for the most part, organized by *filter* and *detector*. For each imaging mode the following are provided:

- Plots of integrated system throughput as a function of wavelength.
- Plots of the time needed to achieve a desired signal-to-noise ratio vs. magnitude for all filters for a point source and a one arcseconds² extended source.
- Tables of color corrections AB_v to go from Johnson V magnitude to AB magnitude.

10.2 Using the Information in this Chapter

10.2.1 Sensitivity Units and Conversions

This chapter contains plots of throughputs for each imaging mode. "Determining Count Rates from Sensitivities" in Section 9.2 explains how to use these throughputs to calculate expected count rates from your source.

The first figure for each imaging mode gives the integrated system throughput. This is the combination of the efficiencies of the detector and of the optical elements in the light path. The throughputs in this handbook are based in part on ground test data. Although, at the time of writing the overall detector efficiency curve and most filter throughputs have been adjusted based on in-flight data. The throughput is defined as the number of detected counts/second/cm² of telescope area relative to the incident flux in photons/cm²/second. For the CCD, "counts" is the number of electrons detected. For the MAMA, "counts" is the number of valid events processed by the detector electronics after passing through the various pulse-shape and anti-coincidence filters. In both cases the detected counts obey Poisson statistics. The throughput includes all obscuration effects in the optical train (e.g., due to the HST secondary).

To recalculate the throughput with the most recent CCD QE tables in *synphot*, you can create total-system-throughput tables (instrument plus OTA) using the *synphot calcband* task. *calcband* takes any valid obsmode command string as input and produces an *STSDAS* table with two columns of data called "wavelength" and "throughput" as its output. For example, to

evaluate the throughput for the F475W filter and the WFC detector, chip 1, you would use the command *calcband acs,wfcl,f475w sdssg_thpt*. The resulting throughput table is stored in *sdssg_thpt*.

10.2.2 Signal-To-Noise

For each imaging mode, plots are provided to estimate the signal-to-noise ratio (S/N) for a representative source. The first figure shows S/N for point sources (*GAIN=1*). The second figure shows S/N for uniform extended sources of area 1 arcseconds².

The different line styles in the S/N figures delineate regions where different sources of noise dominate. A particular source of noise (readnoise for example) is presumed to dominate if it contributes more than half the total noise in the observations.

The point- and extended-source S/N figures are shown for average and low sky levels. For point sources, an aperture size of 5 x 5 pixels has been used for the WFC, 9 x 9 pixels for HRC, and 15 x 15 pixels for the SBC S/N evaluation. For extended sources, a 1 arcseconds² aperture was used. For the CCD the read noise has been computed assuming a number of readouts *NREAD*= integer (*t* / 1000 seconds), where *t* is the exposure time, with a minimum *NREAD*=2. That is, each exposure has a minimum *CR-SPLIT*=2. Different line styles in the figures are used to indicate which source of noise dominates.

To the left of the vertical line in the SBC S/N plots, the count rate from the source exceeds the 150 counts/second/pixel local count rate limit. This is computed from the model PSF, which gives 14% to 22% of the flux in the central pixel.

In situations requiring more detailed calculations (non-stellar spectra, extended sources, other sky background levels, unknown target *V* magnitude, etc.), the ACS [Exposure-Time Calculator](#) should be used.

Follow these steps to use the signal-to-noise plots:

1. Determine the AB magnitude of your source at the wavelength of interest. There are several ways to do this.
 - Examine Table 10.1, 10.2, or 10.3 and find AB_V for the desired spectral type and filter. Sum the *V* magnitude of the target and AB_V derived from the table.
 - Alternatively, compute $ABMAG (=V+AB_V)$ from the source flux, using the relation $ABMAG = -2.5 \log f_V - 48.60$, or $ABMAG = -2.5 \log f_\lambda - 5 \log \lambda - 2.406$.
2. Find the appropriate plot for the filter in question, and locate $V+AB_V$ on the horizontal axis. Then read off the signal-to-noise ratio for the desired exposure time, or vice-versa.

The “x” characters at the top of each plot indicate the onset of saturation, in the case of the CCD. The “x” shows where the total number of counts exceeds the 16 bit buffer size of 65,535.

Note that the plots show the S/N as a function of source magnitude for exposure times as short as 0.1 seconds, although the minimum exposure time for the WFC CCD channel is 0.5 seconds.

10.2.3 Point Spread Functions

All information about the PSF are based on the modeled encircled energy data presented in ACS Point Spread Functions in Section 5.6

WFC/F435W

Description

Johnson B filter.

Figure 10.1: Integrated system throughput for WFC/F435W.

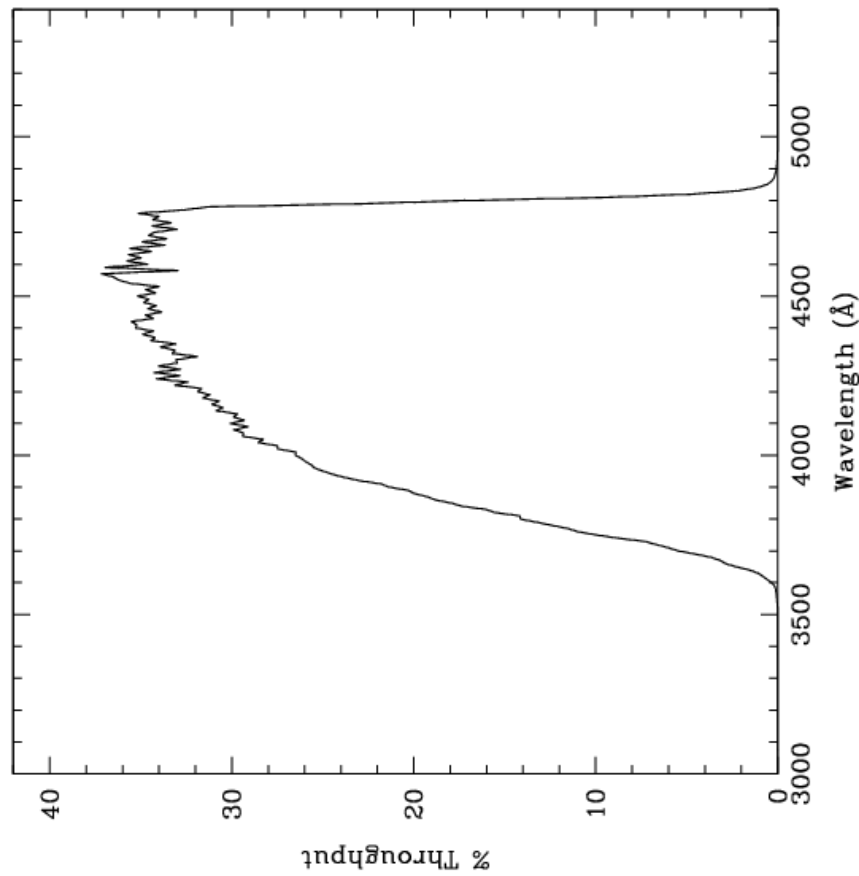


Figure 10.2: Point source S/N vs. $V+AB_V$ for the WFC/F435W filter. Top curves are for low sky; bottom curves are for average sky.

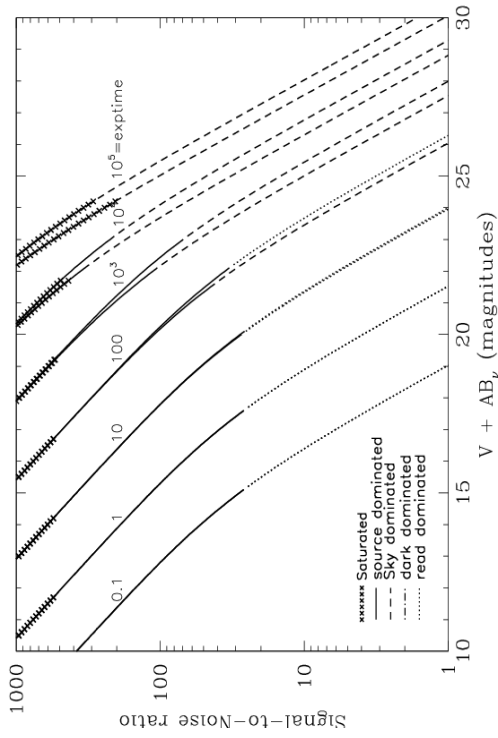
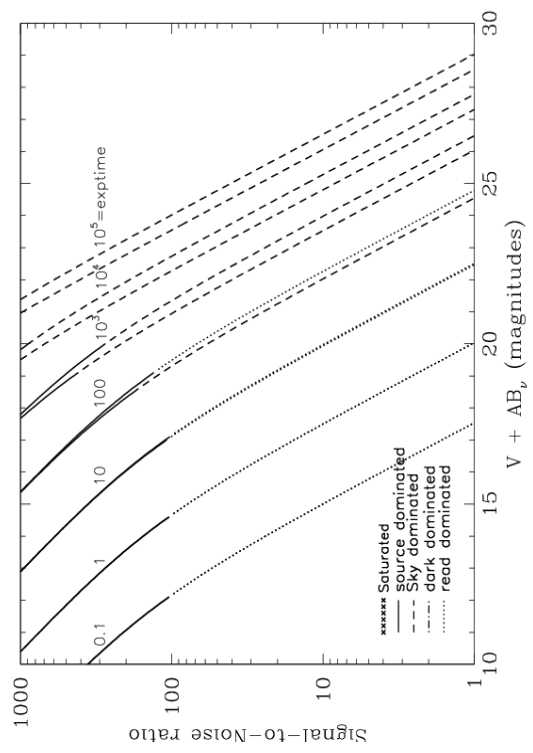


Figure 10.3: Extended source S/N vs. $V+AB_V$ for the WFC/F435W filter. Top curves are for low sky and bottom curves are for average sky for a 1 arcsec² area.



WFC/F475W

Description

Sloan Digital Sky Survey g filter.

Figure 10.4: Integrated system throughput for WFC/F475W.

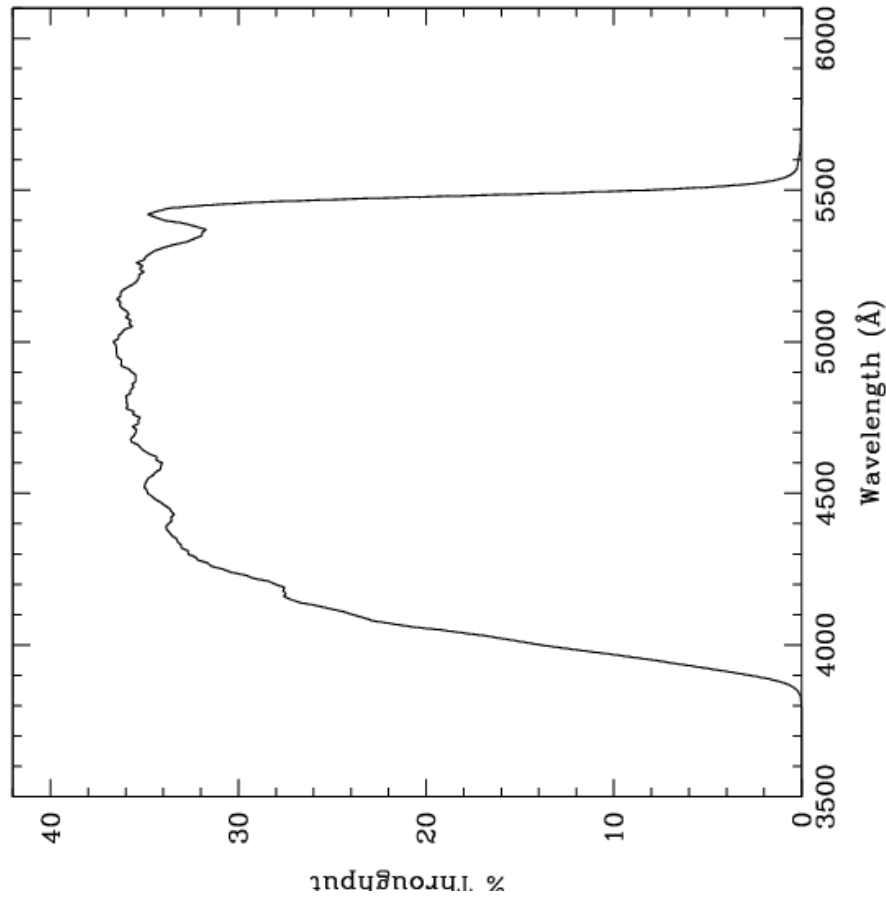


Figure 10.5: Point source S/N vs. $V+AB_V$ for the WFC/F475W filter. Top curves are for low sky; bottom curves are for average sky.

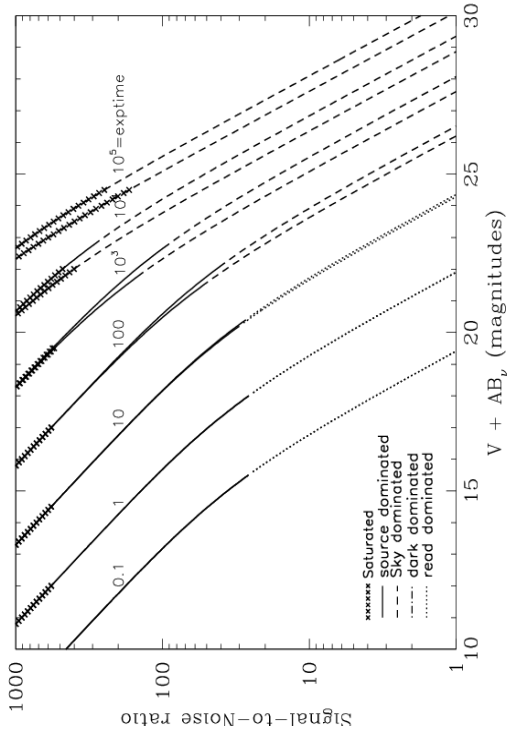
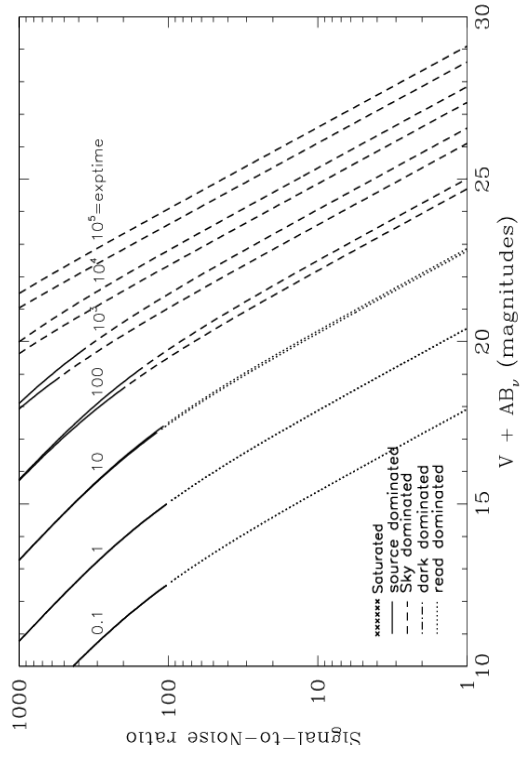


Figure 10.6: Extended source S/N vs. $V+AB_V$ for the WFC/F475W filter. Top curves are for low sky and bottom curves are for average sky for a 1 arcsec² area.



WFC/F502N

Description

OIII filter.

Figure 10.7: Integrated system throughput for WFC/F502N.

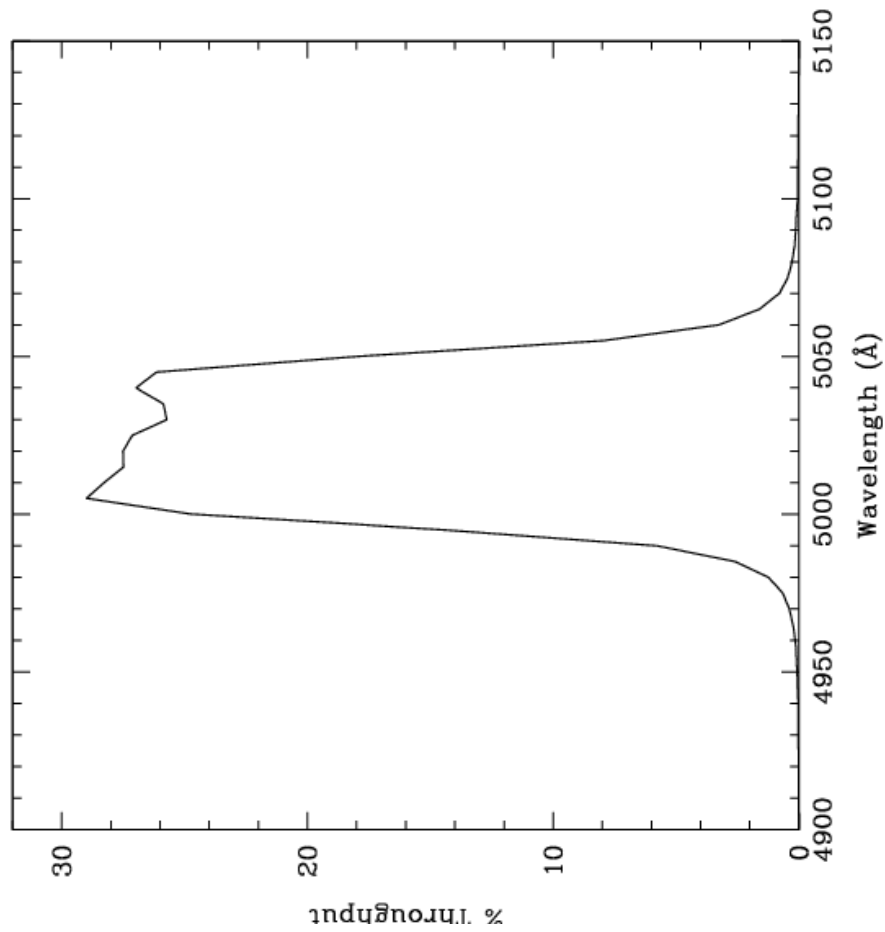


Figure 10.8: Point source S/N vs. $V+AB_V$ for the WFC/F502N filter. Top curves are for low sky; bottom curves are for average sky.

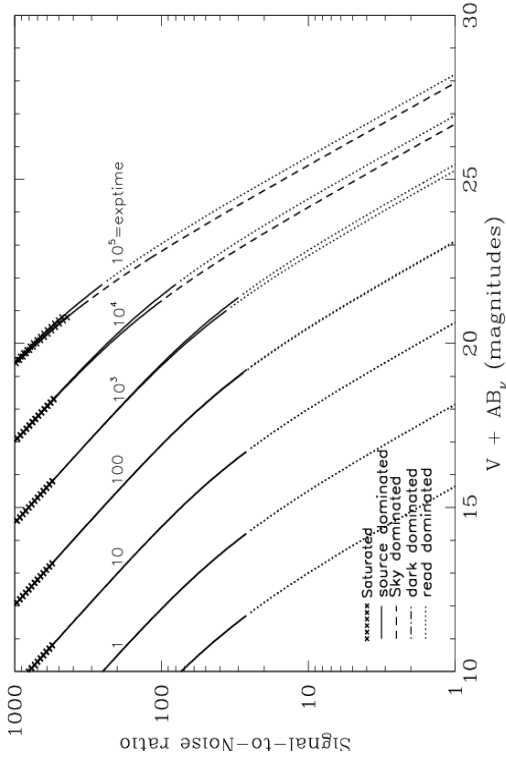
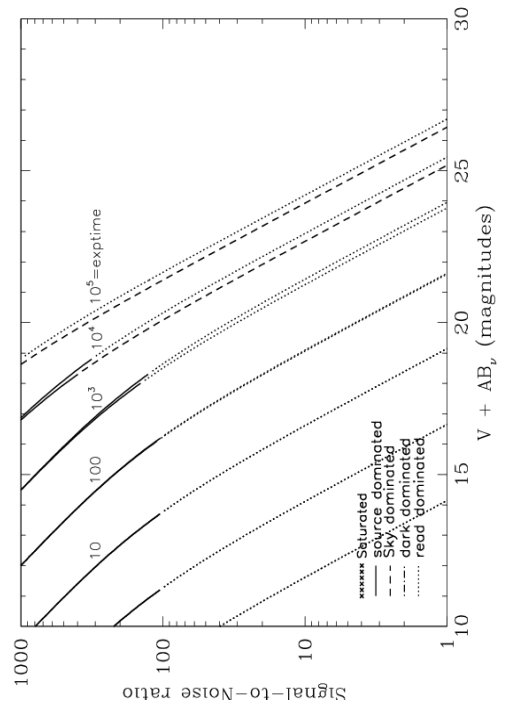


Figure 10.9: Extended source S/N vs. $V+AB_V$ for the WFC/F502N filter. Top curves are for low sky and bottom curves are for average sky for a 1 arcsec² area.



WFC/F550M

Description

Narrow V filter.

Figure 10.10: Integrated system throughput for WFC/F550M.

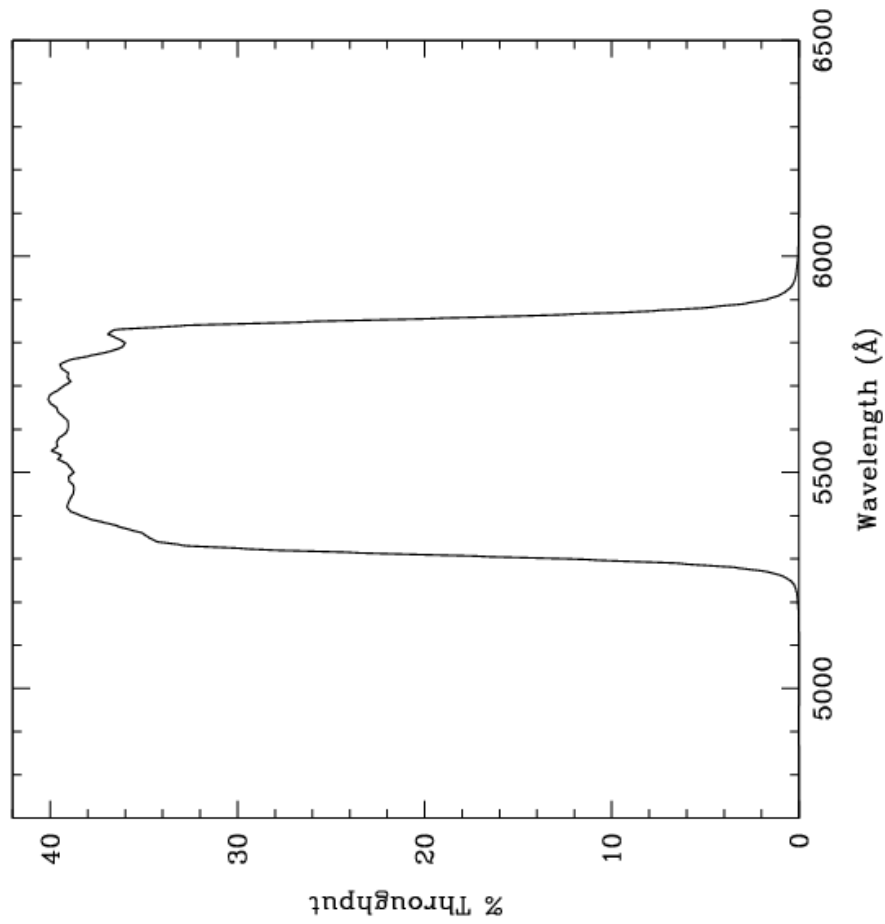


Figure 10.11: Point source S/N vs. $V + AB_V$ for the WFC/F550M filter. Top curves are for low sky; bottom curves are for average sky.

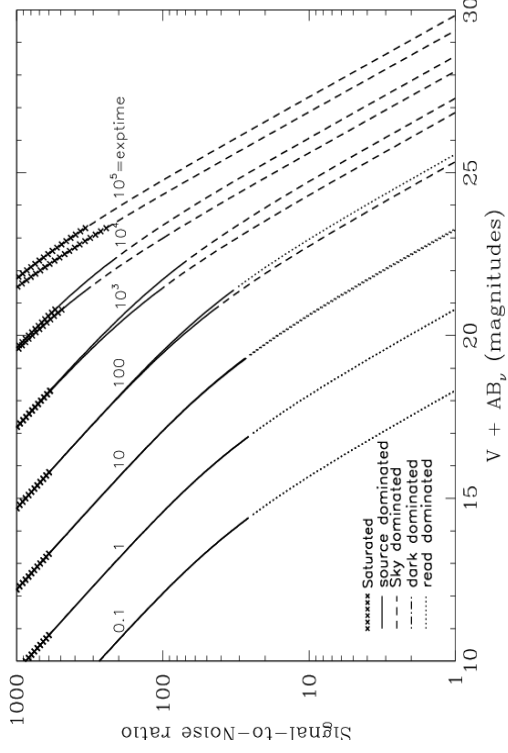
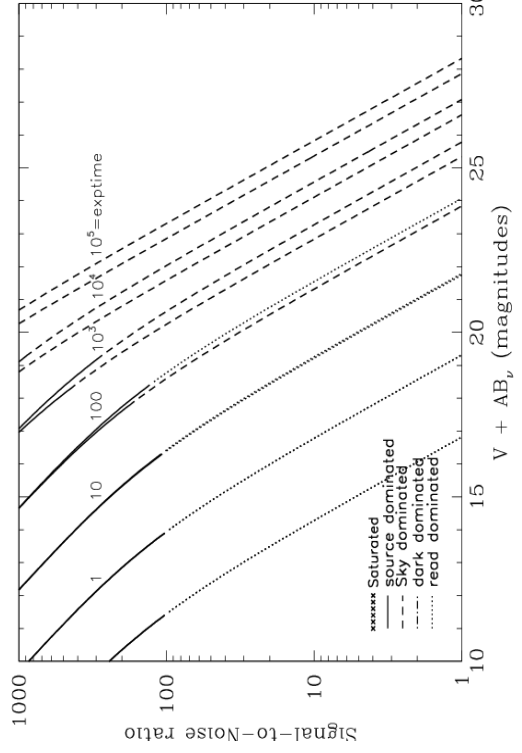


Figure 10.12: Extended source S/N vs. $V + AB_V$ for the WFC/F550M filter. Top curves are for low sky and bottom curves are for average sky for a 1 arcsec^2 area.



WFC/F555W

Description

Johnson V filter.

Figure 10.13: Integrated system throughput for WFC/F555W.

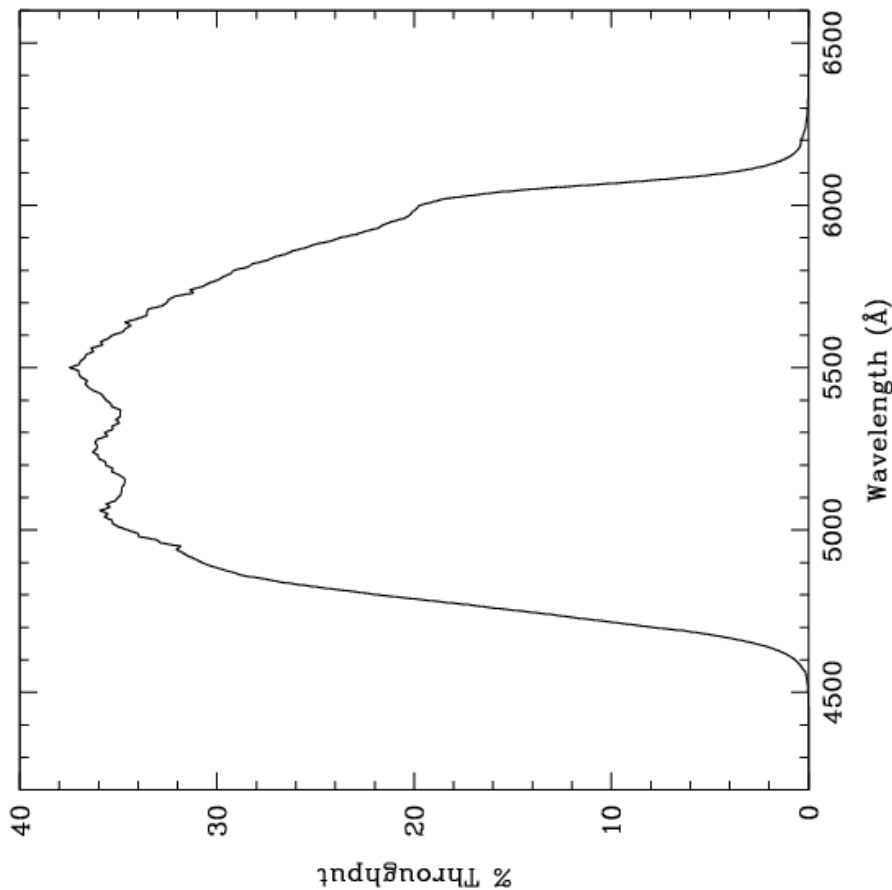


Figure 10.14: Point source S/N vs. $V + AB_V$ for the WFC/F555W filter. Top curves are for low sky; bottom curves are for average sky.

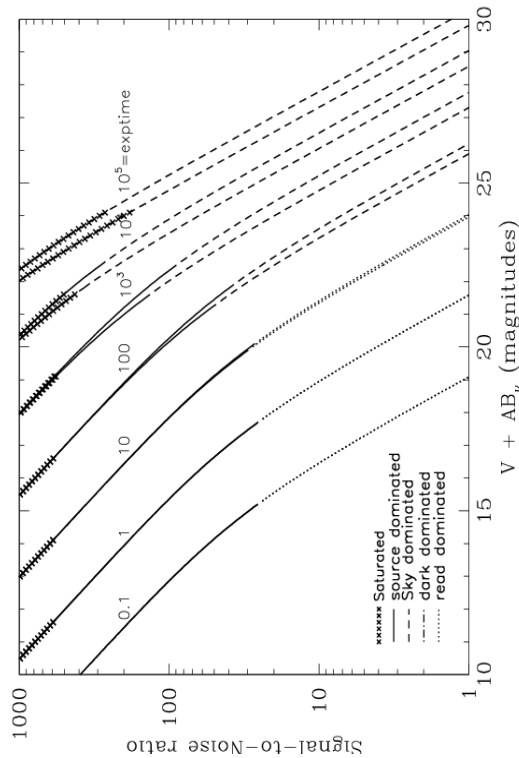
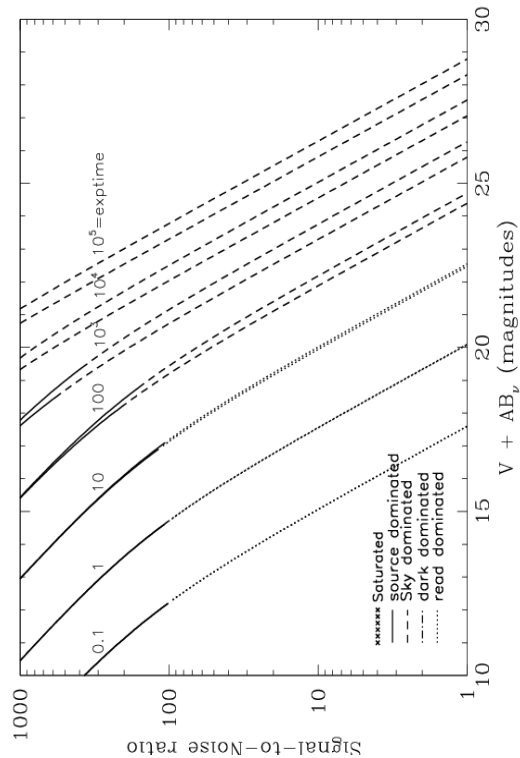


Figure 10.15: Extended source S/N vs. $V + AB_V$ for the WFC/F555W filter. Top curves are for low sky and bottom curves are for average sky for a 1 arcsec^2 area.



WFC/F606W

Description

Broad V filter.

Figure 10.16: Integrated system throughput for WFC/F606W.

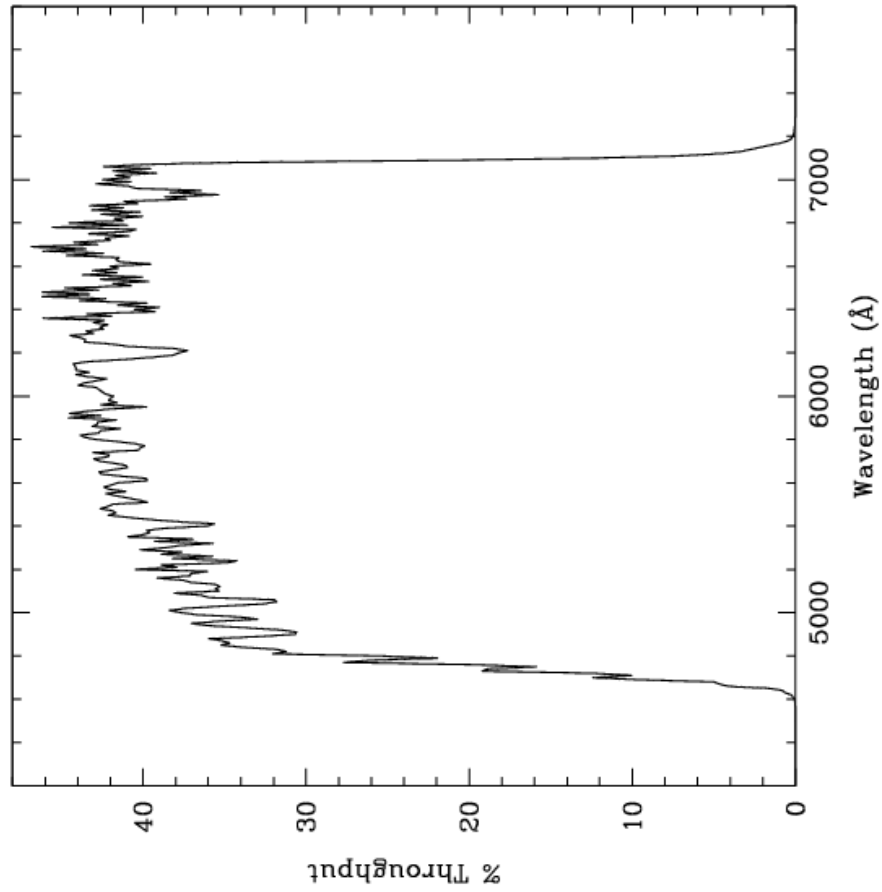


Figure 10.17: Point source S/N vs. $V + AB_V$ for the WFC/F606W filter. Top curves are for low sky; bottom curves are for average sky.

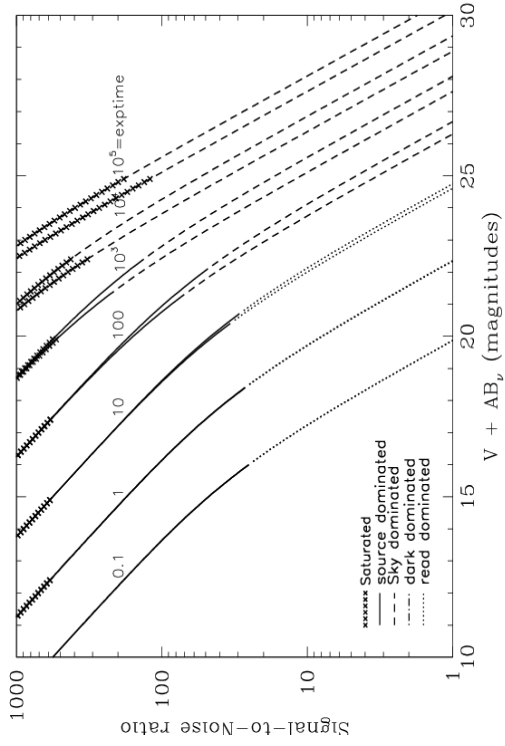
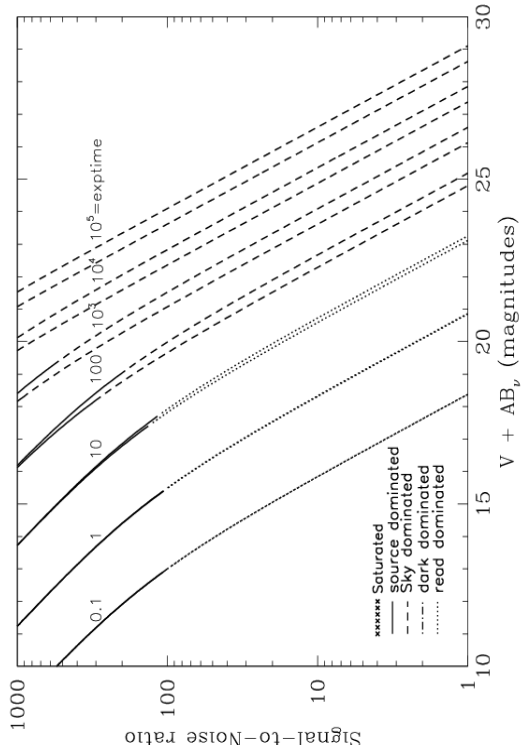


Figure 10.18: Extended source S/N vs. $V + AB_V$ for the WFC/F606W. Top curves are for low sky and bottom curves are for average sky for a 1 arcsec^2 area.



WFC/F625W

Description

Sloan Digital Sky Survey r filter.

Figure 10.19: Integrated system throughput for WFC/F625W.

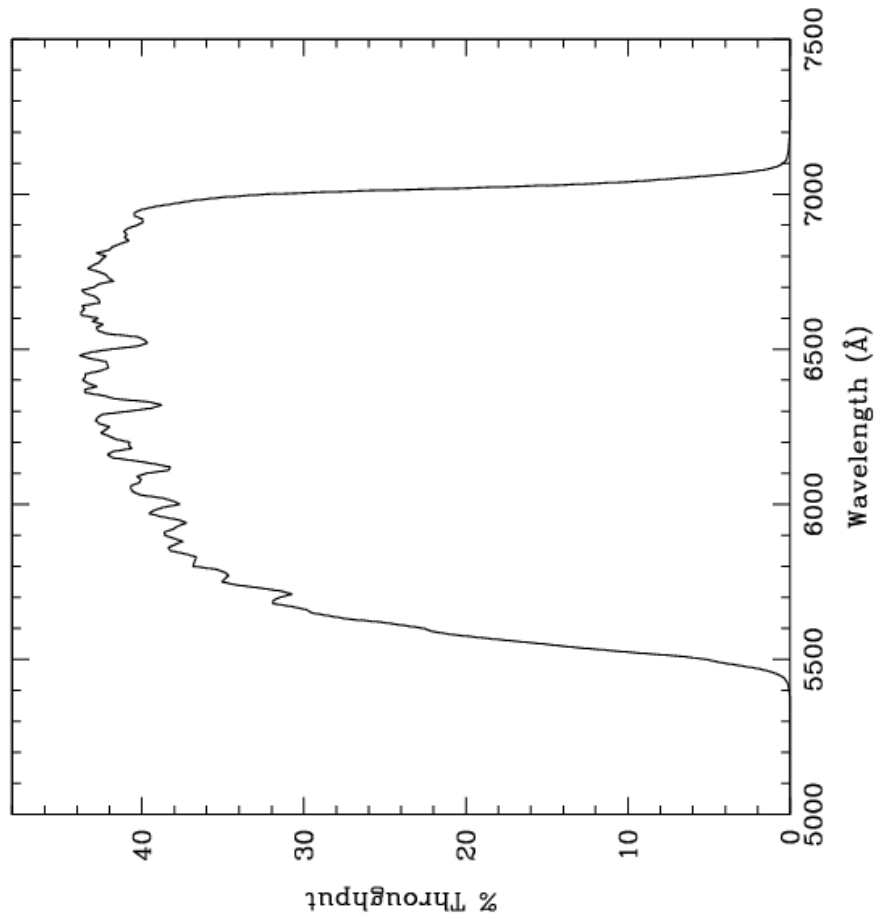


Figure 10.20: Point source S/N vs. $V+AB_V$ for the WFC/F625W filter. Top curves are for low sky; bottom curves are for average sky.

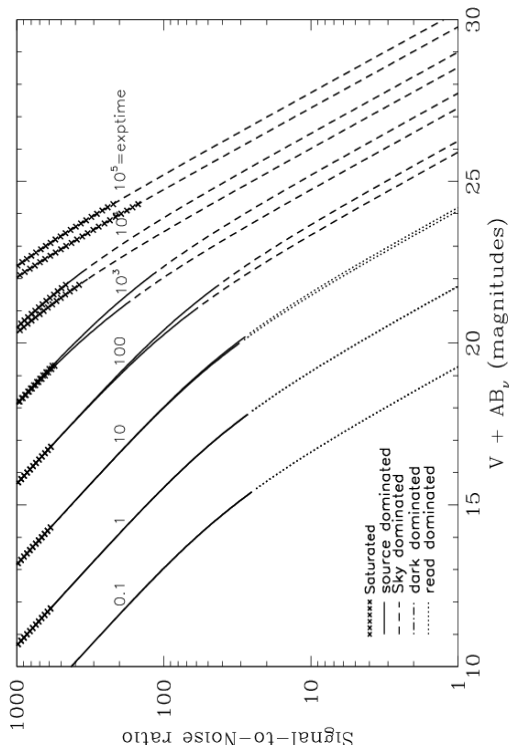
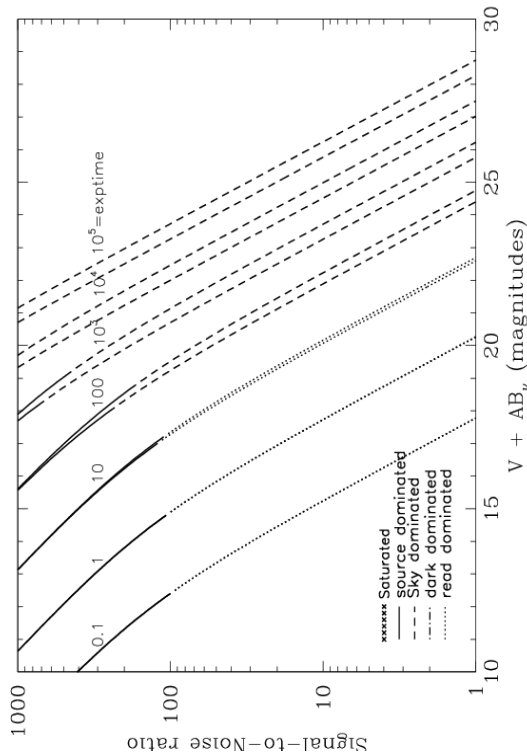


Figure 10.21: Extended source S/N vs. $V+AB_V$ for the WFC/F625W filter. Top curves are for low sky and bottom curves are for average sky for a 1 arcsec² area.



WFC/F658N

Description

H α filter.

Figure 10.22: Integrated system throughput for WFC/F658N.

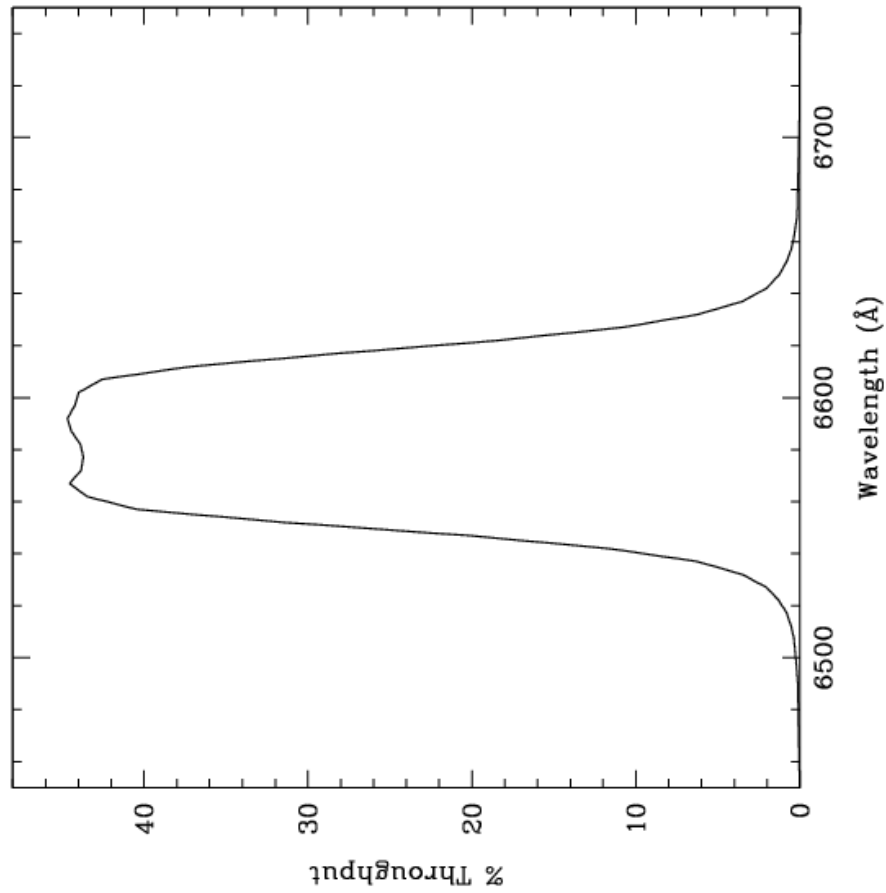


Figure 10.23: Point source S/N vs. $V+AB_V$ for the WFC/F658N filter. Top curves are for low sky; bottom curves are for average sky.

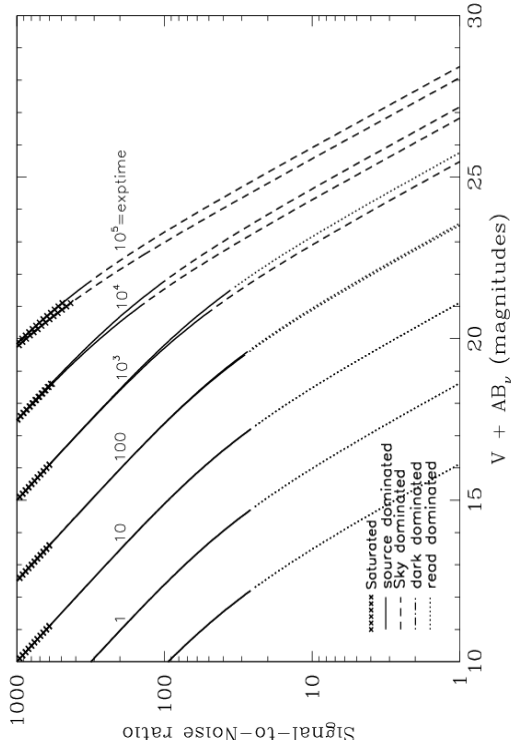
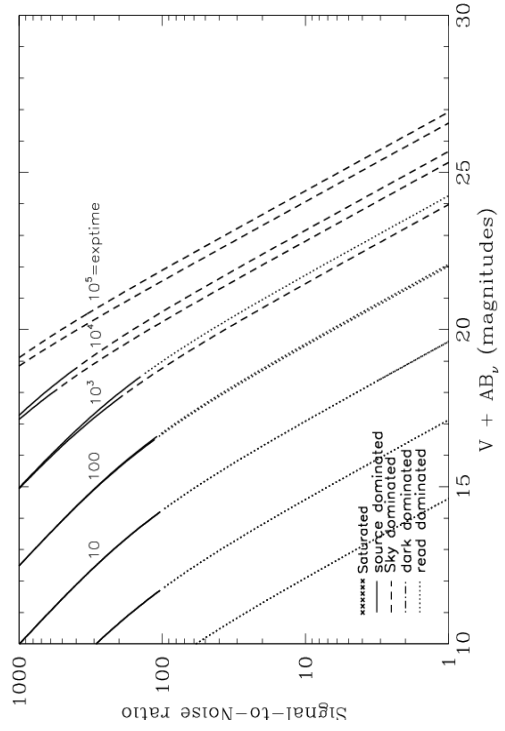


Figure 10.24: Extended source S/N vs. $V+AB_V$ for the WFC/F658N filter. Top curves are for low sky and bottom curves are for average sky for 1 arcsec² area.



WFC/F660N

Description

NII filter.

Figure 10.25: Integrated system throughput for WFC/F660N.

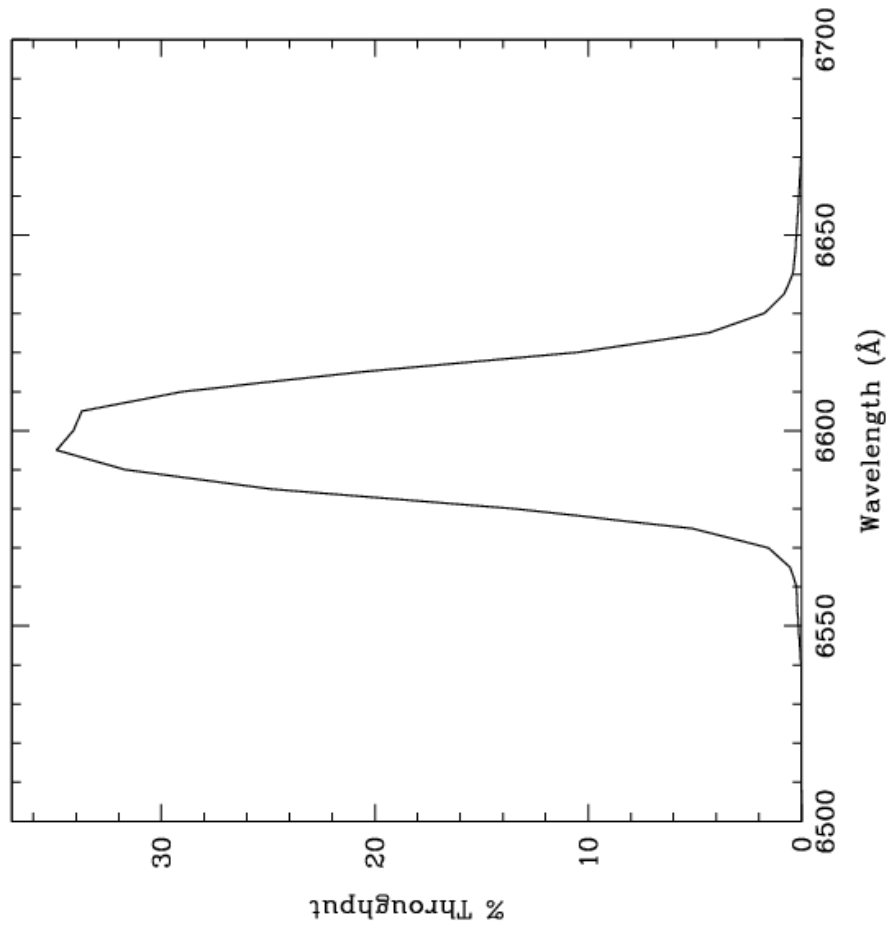


Figure 10.26: Point source S/N vs. $V+AB_V$ for the WFC/F660N filter. Top curves are for low sky; bottom curves are for average sky.

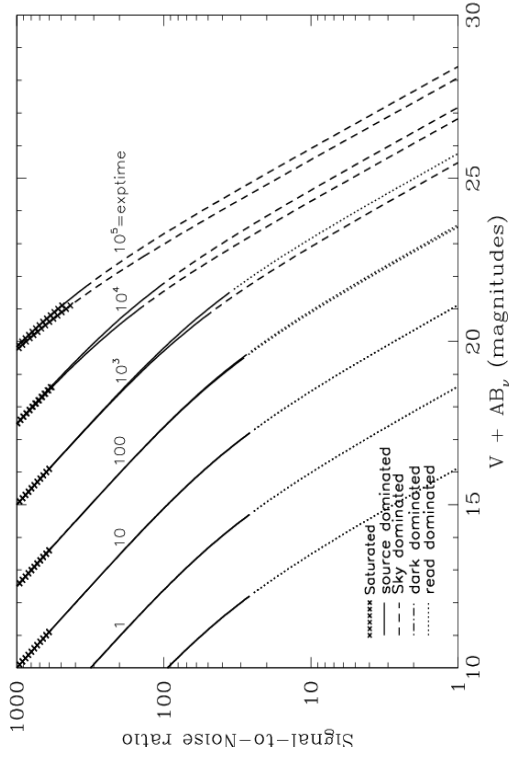
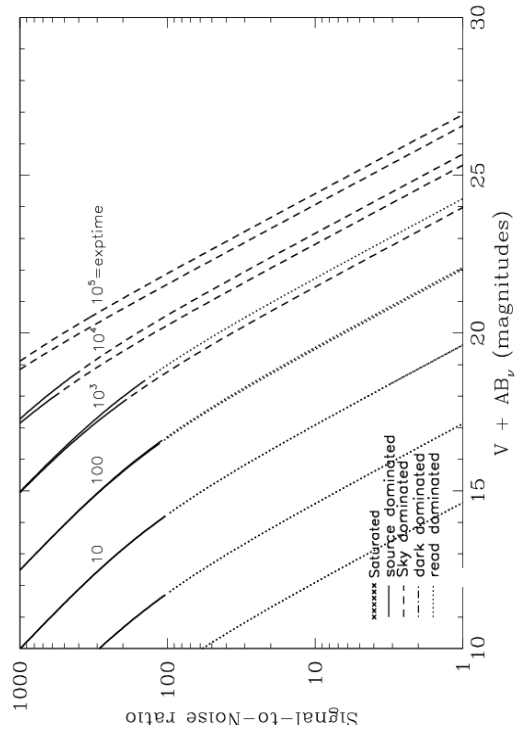


Figure 10.27: Extended source S/N vs. $V+AB_V$ for the WFC/F660N filter. Top curves are for low sky and bottom curves are for average sky for a 1 arcsec^2 area.



WFC/F775W

Description

Sloan Digital Sky Survey i filter

Figure 10.28: Integrated system throughput for WFC/F775W.

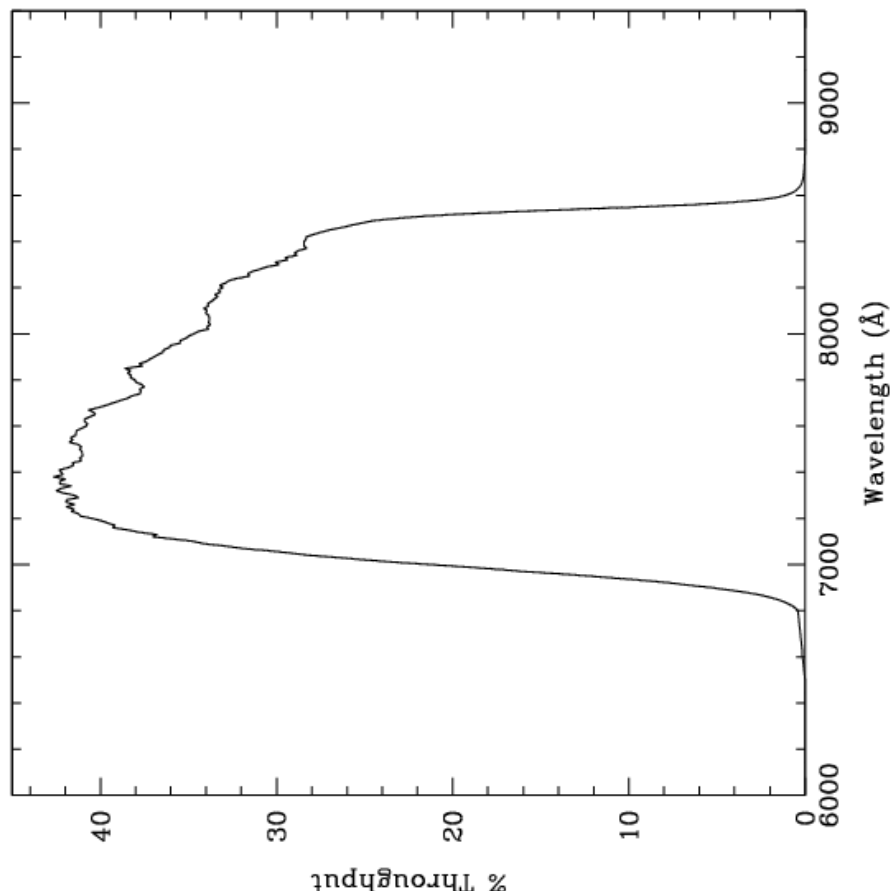


Figure 10.29: Point source S/N vs. $V+AB_V$ for the WFC/F775W filter. Top curves are for low sky; bottom curves are for average sky.

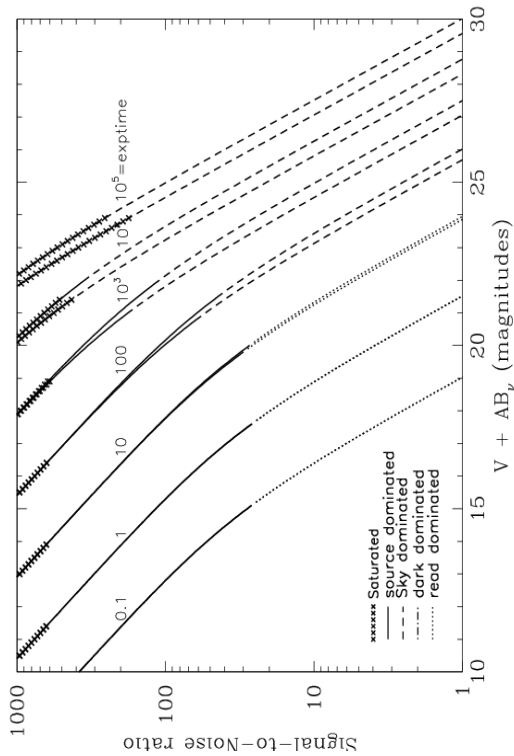
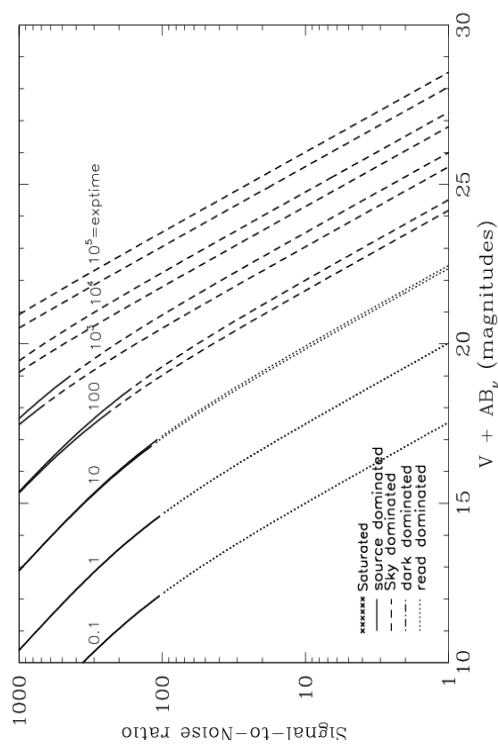


Figure 10.30: Extended source S/N vs. $V+AB_V$ for the WFC/F775W filter. Top curves are for low sky and bottom curves are for average sky for a 1 arcsec^2 area.



WFC/F814W

Description

Broad I filter.

Figure 10.31: Integrated system throughput for WFC/F814W.

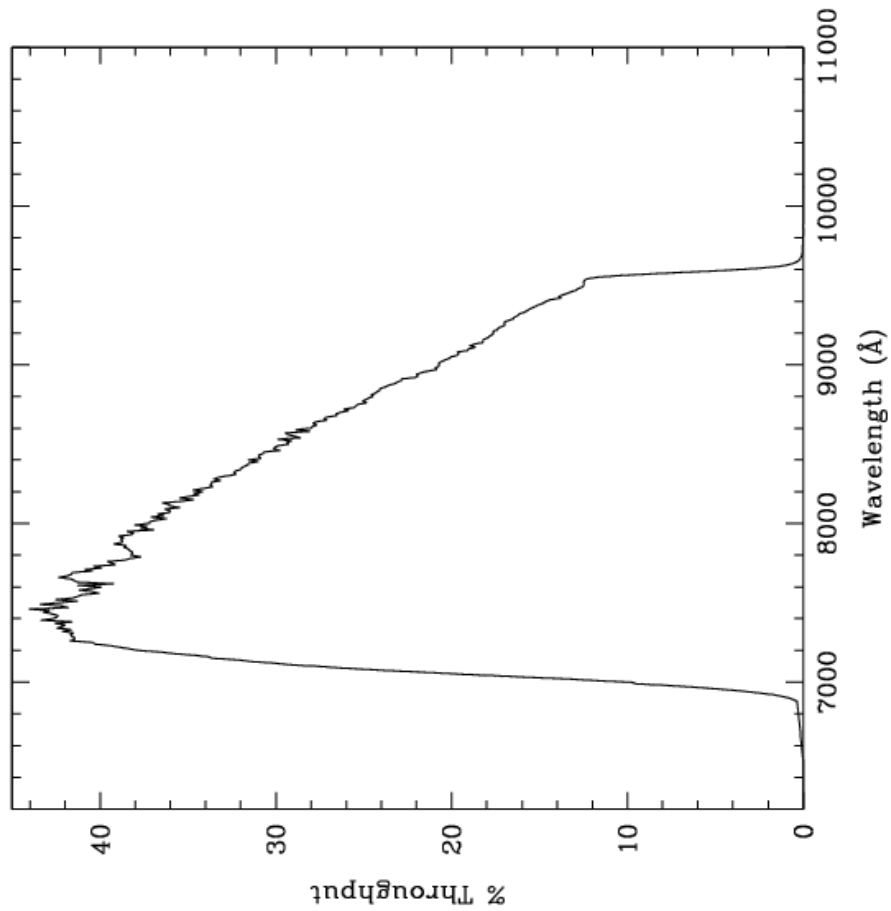


Figure 10.32: Point source S/N vs. $V+AB_V$ for the WFC/F814W filter. Top curves are for low sky; bottom curves are for average sky.

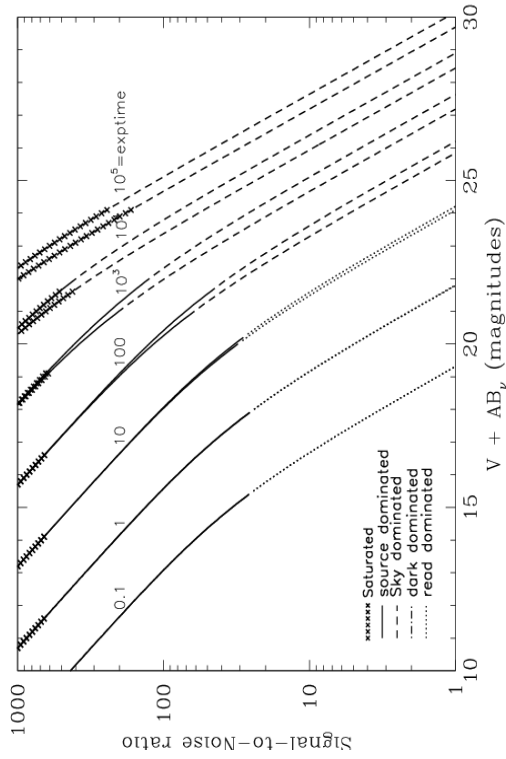
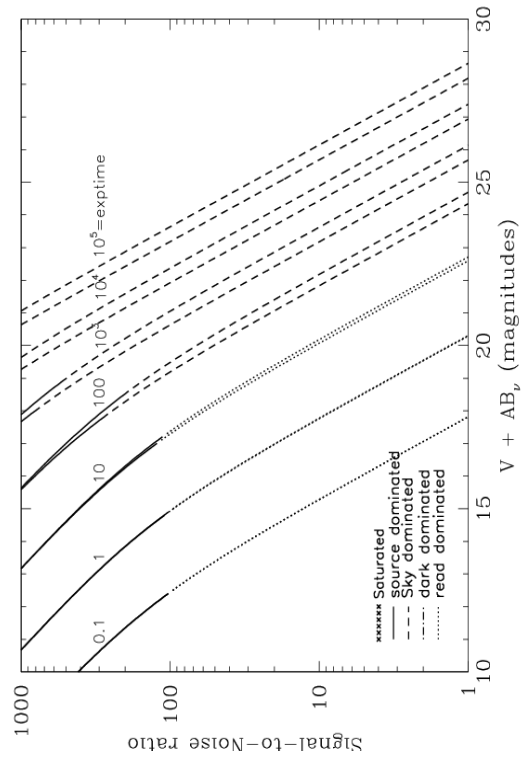


Figure 10.33: Extended source S/N vs. $V+AB_V$ for the WFC/F814W filter. Top curves are for low sky and bottom curves are for average sky for a 1 arcsec^2 area.



WFC/F850LP

Description

Sloan Digital Sky Survey z filter.

Figure 10.34: Integrated system throughput for WFC/F850LP.

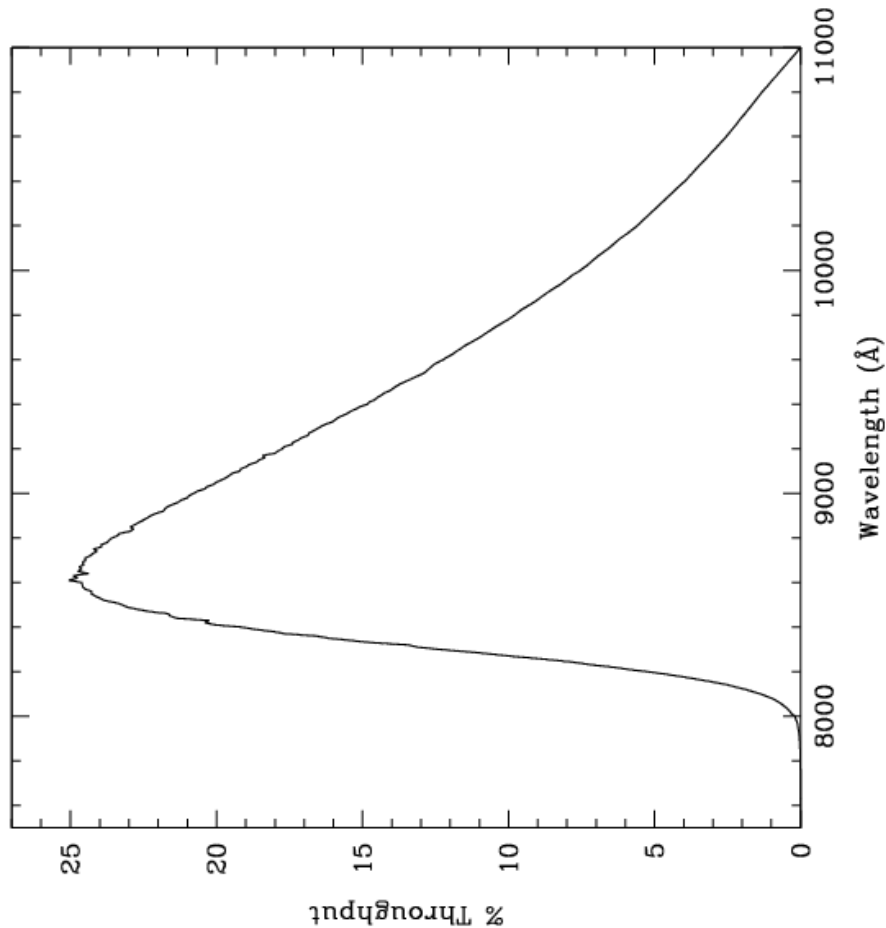


Figure 10.35: Point source S/N vs. $V+AB_V$ for the WFC/F850LP filter. Top curves are for low sky; bottom curves are for average sky.

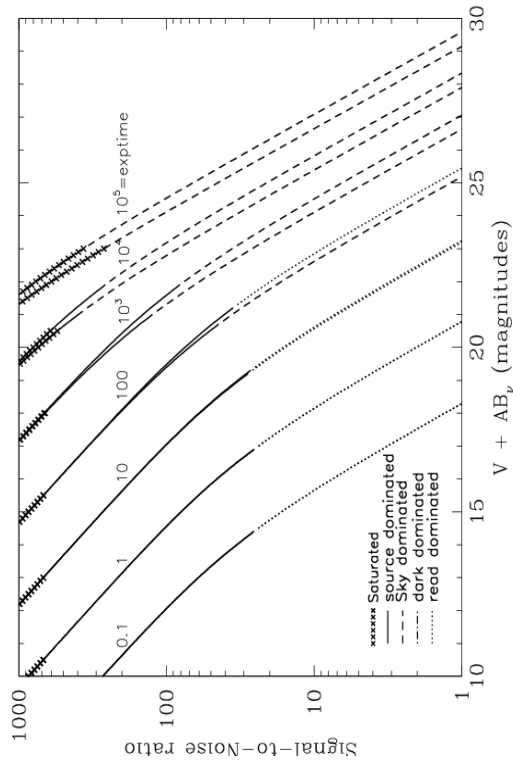
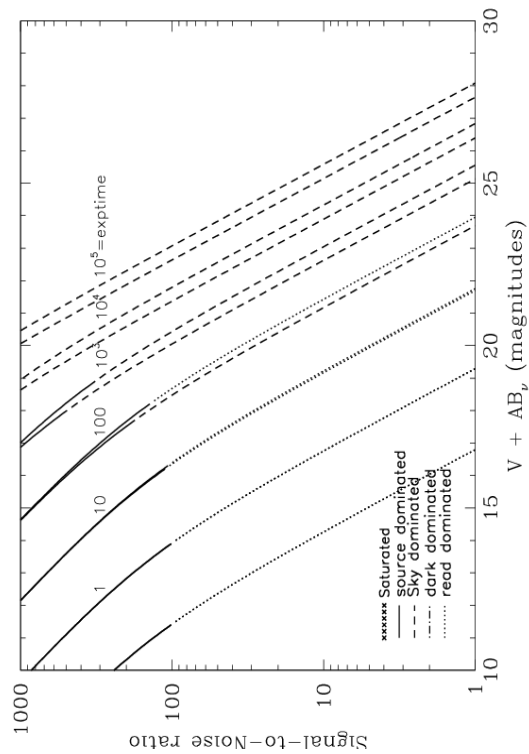


Figure 10.36: Extended source S/N vs. $V+AB_V$ for the WFC/F850LP filter. Top curves are for low sky and bottom curves are for average sky for a 1 arcsec^2 area.



WFC/G800L

Description

Grism.

Figure 10.37: Integrated system throughput for WFC/G800L.

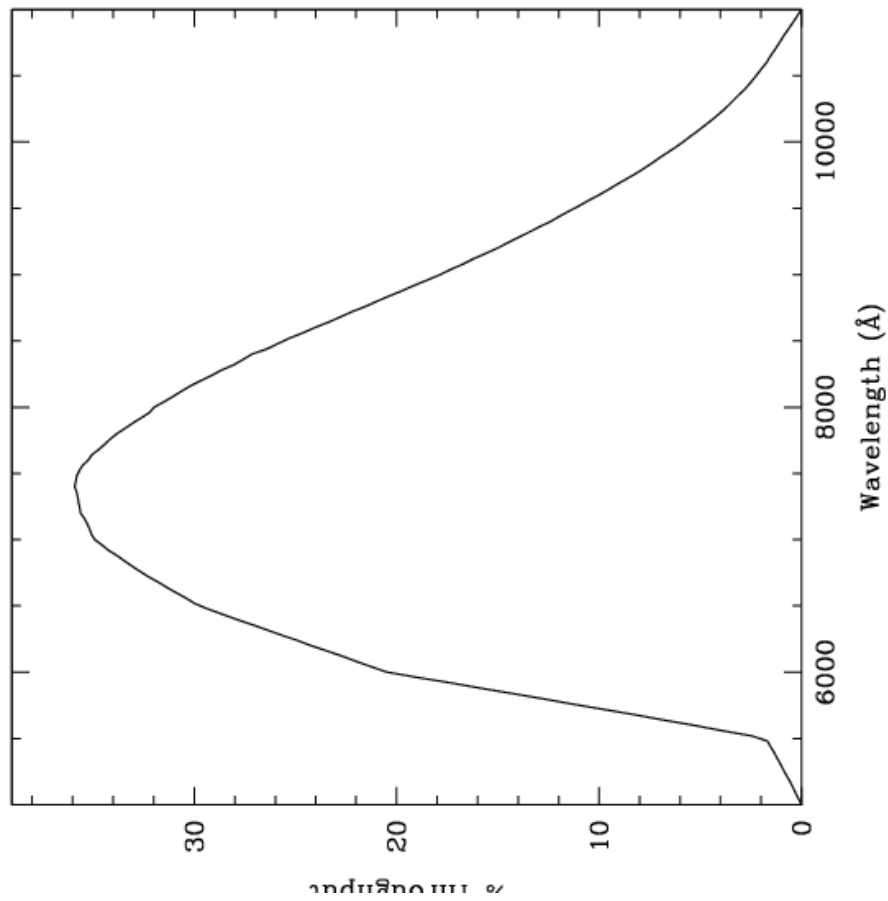


Figure 10.38: Point source S/N vs. $V+AB_V$ for the WFC/G800L filter. Top curves are for low sky; bottom curves are for average sky.

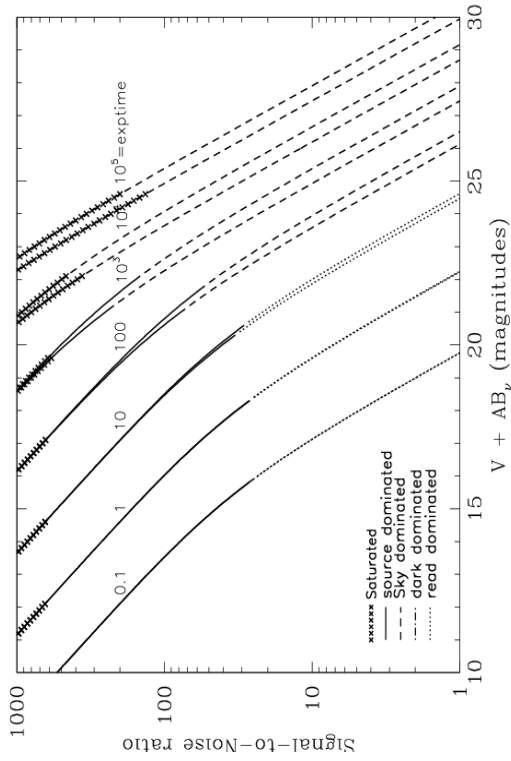
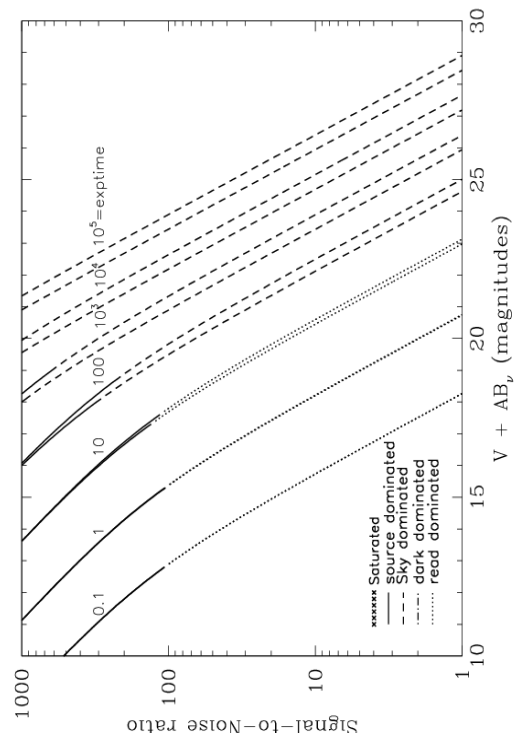


Figure 10.39: Extended source S/N vs. $V+AB_V$ for the WFC/G800L filter. Top curves are for low sky and bottom curves are for average sky for a 1 arcsec^2 area.



WFC/CLEAR

Description

Clear filter.

Figure 10.40: Integrated system throughput for WFC/Clear.

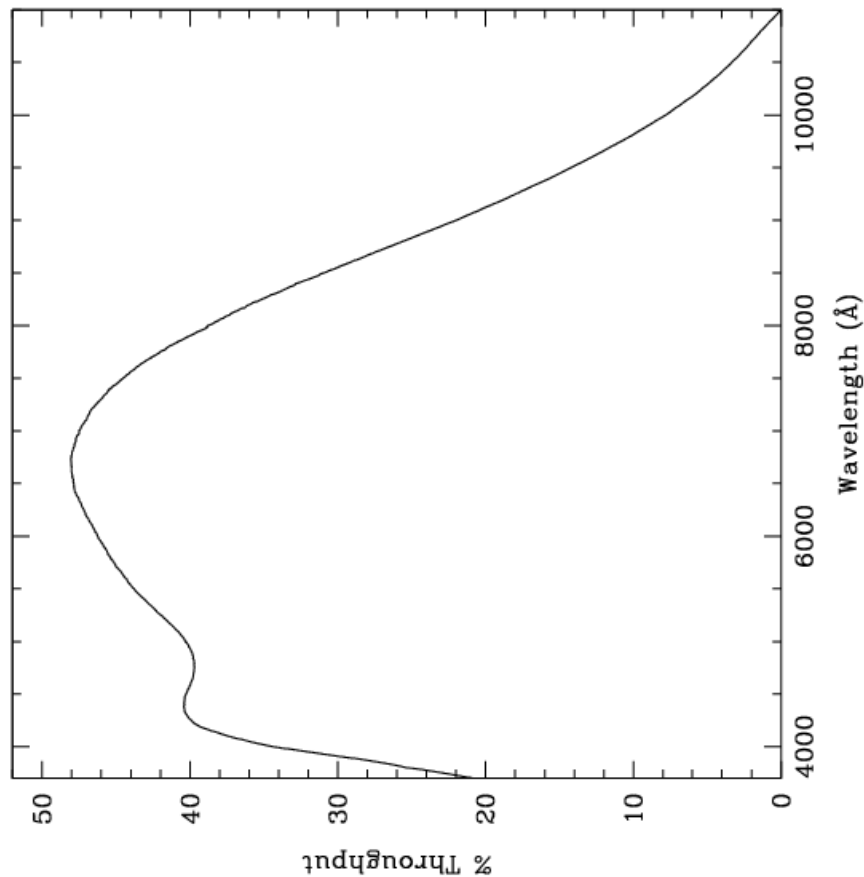


Figure 10.41: Point source S/N vs. $V+AB_V$ for the WFC/Clear filter. Top curves are for low sky; bottom curves are for average sky.

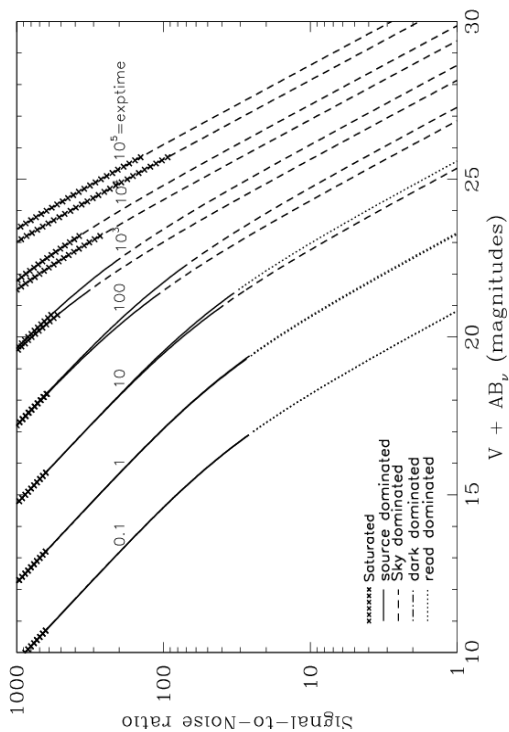
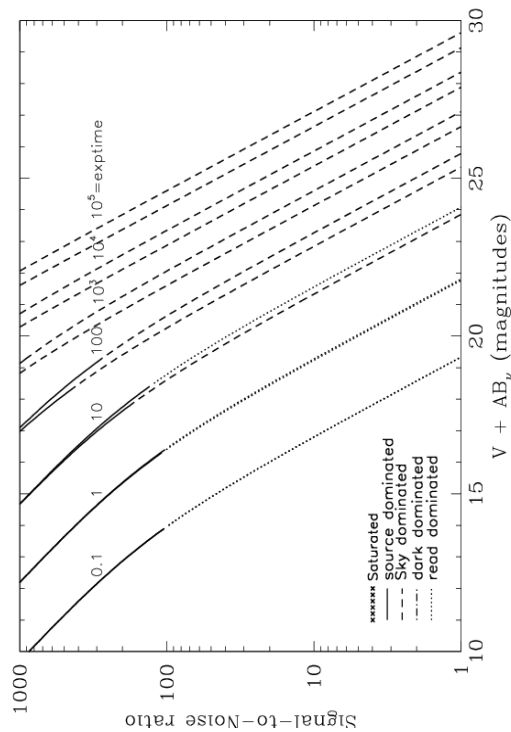


Figure 10.42: Extended source S/N vs. $V+AB_V$ for the WFC/Clear filter. Top curves are for low sky and bottom curves are for average sky for a 1 arcsec² area.



HRC/F220W

Description

Near-UV filter.

Figure 10.43: Integrated system throughput for HRC/F220W.

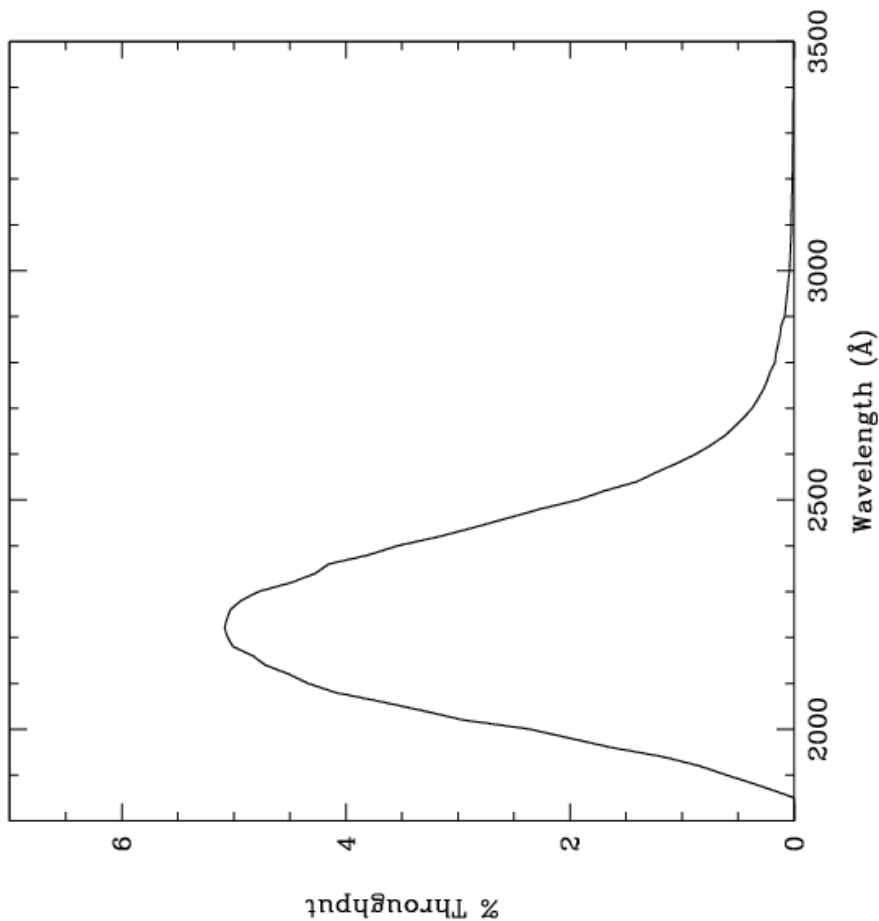


Figure 10.44: Point source S/N vs. $V+AB_V$ for the HRC/F220W filter. Top curves are for low sky; bottom curves are for average sky.

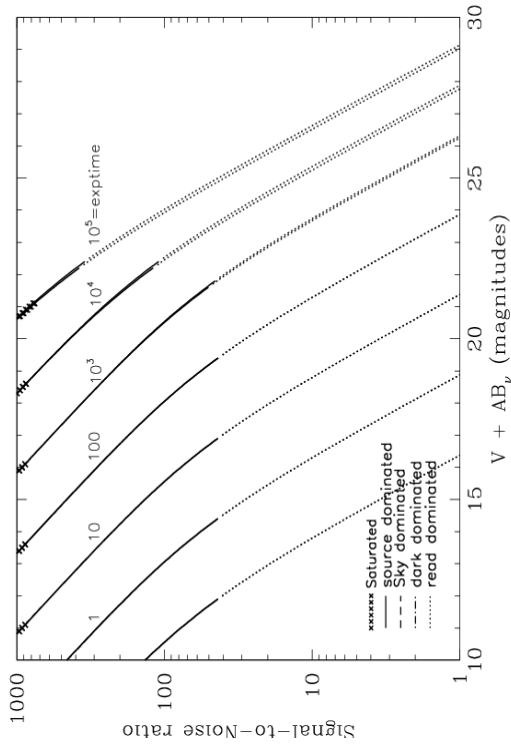
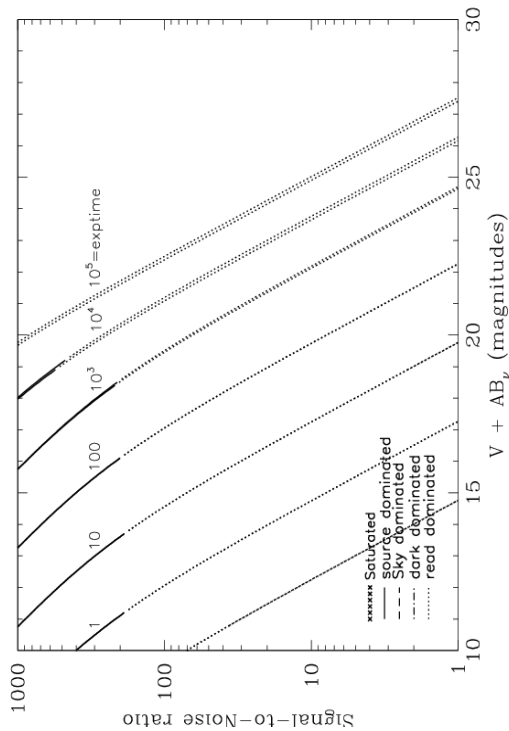


Figure 10.45: Extended source S/N vs. $V+AB_V$ for the HRC/F220W filter. Top curves are for low sky and bottom curves are for average sky for a 1 arcsec² area.



HRC/F250W

Description

Near-UV filter.

Figure 10.46: Integrated system throughput for HRC/F250W.

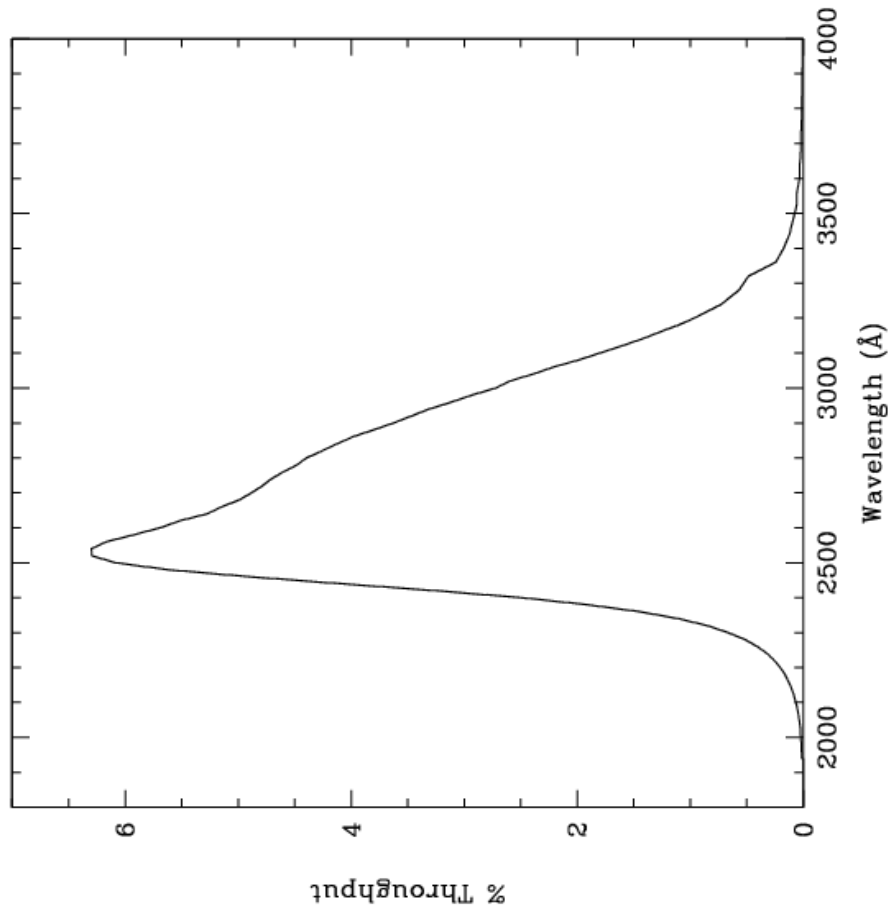


Figure 10.47: Point Source S/N vs. $V+AB_V$ for the HRC/F250W filter. Top curves are for low sky; bottom curves are for average sky.

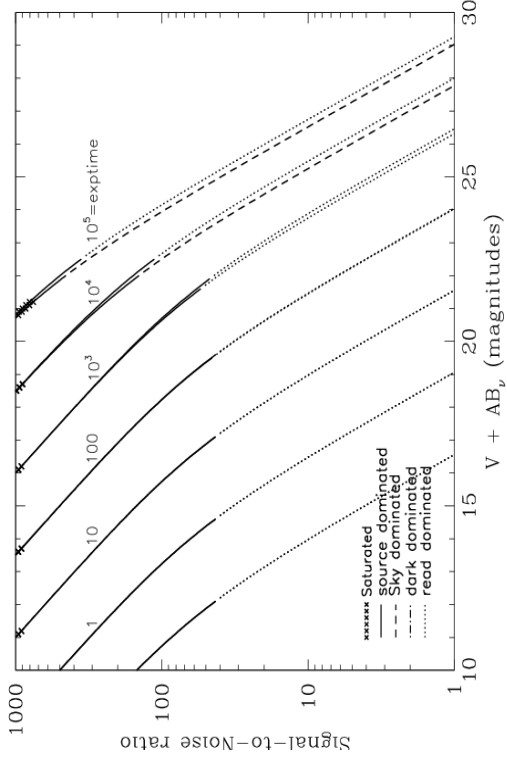
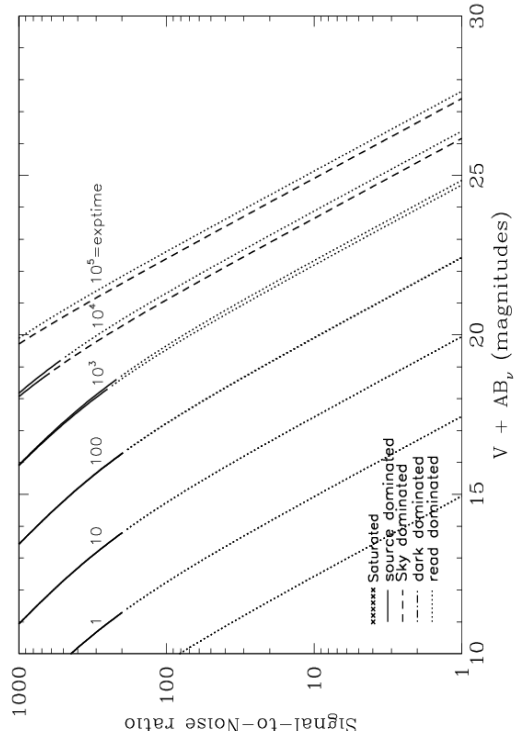


Figure 10.48: Extended Source S/N vs. $V+AB_V$ for the HRC/F250W filter. Top curves are for low sky and bottom curves are for average sky for a 1 arcsec^2 area.



HRC/F330W

Description

HRC u filter.

Figure 10.49: Integrated system throughput for HRC/F330W.

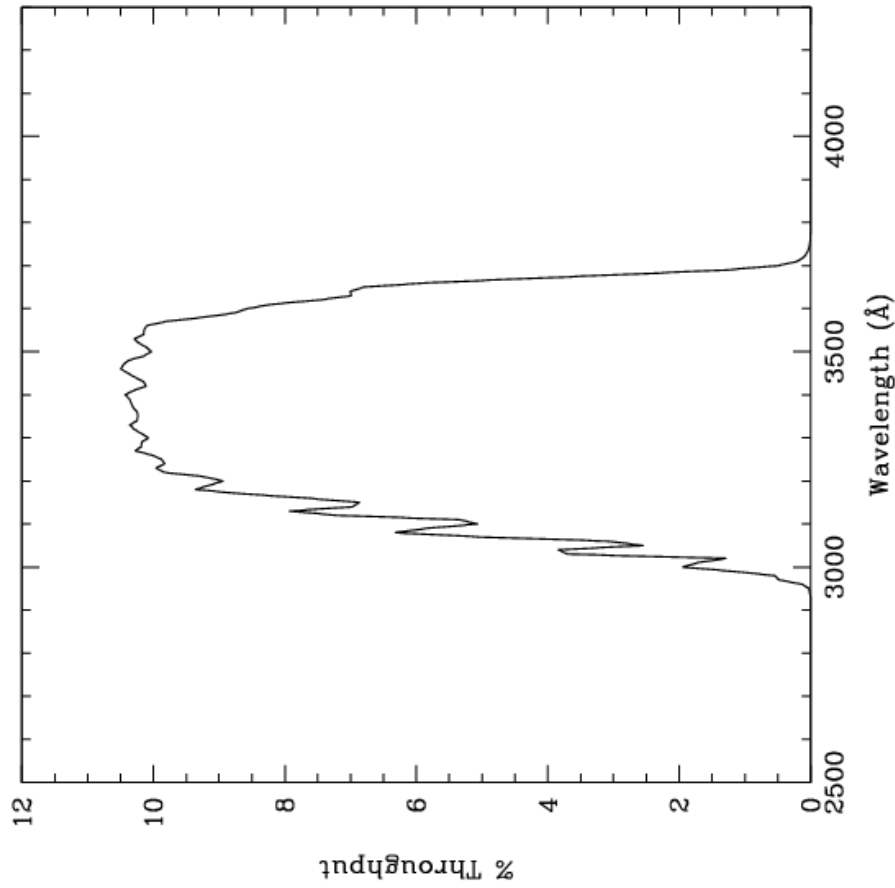


Figure 10.50: Point source S/N vs. $V+AB_V$ for the HRC/F330W filter. Top curves are for low sky; bottom curves are for average sky.

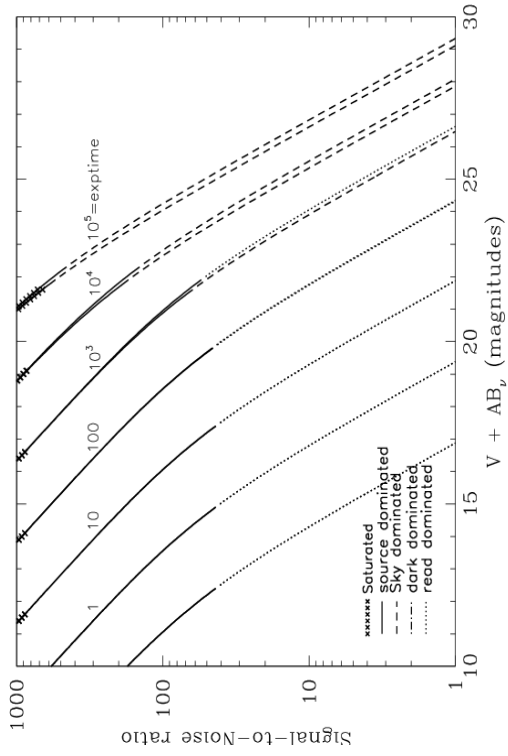
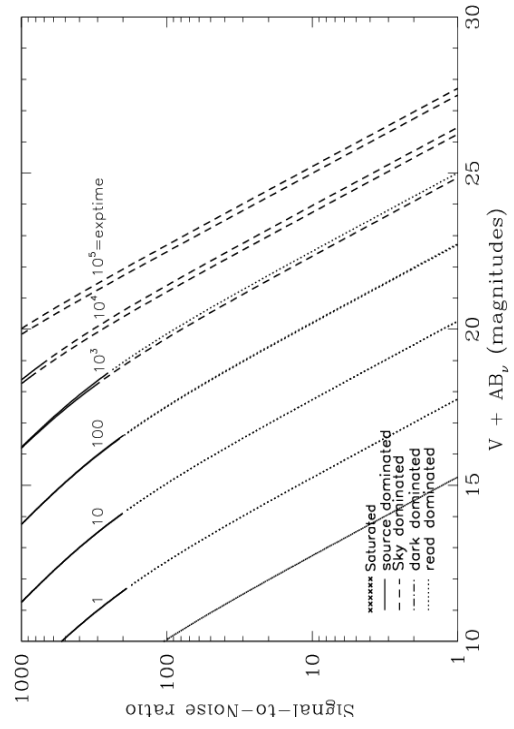


Figure 10.51: Extended source S/N vs. $V+AB_V$ for the HRC/F330W filter. Top curves are for low sky and bottom curves are for average sky for a 1 arcsec^2 area.



HRC/F344N

Description

NeV filter.

Figure 10.52: Integrated system throughput for HRC/F344N.

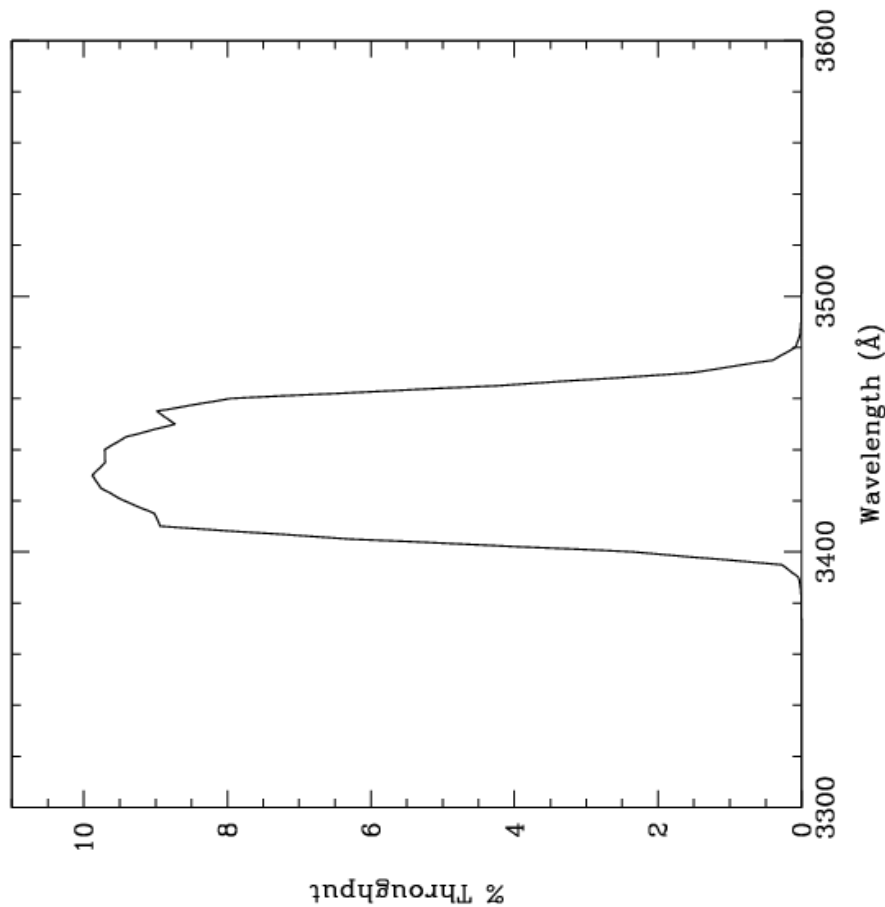


Figure 10.53: Point source S/N vs. $V + AB_V$ for the HRC/F344N filter. Top curves are for low sky; bottom curves are for average sky.

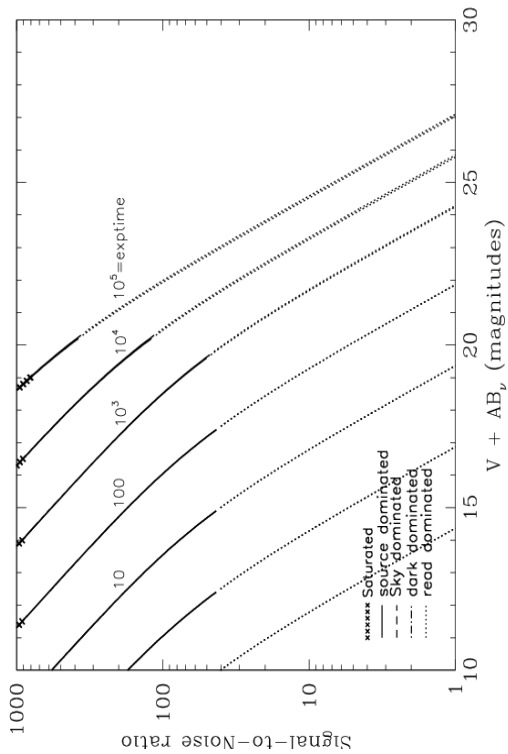
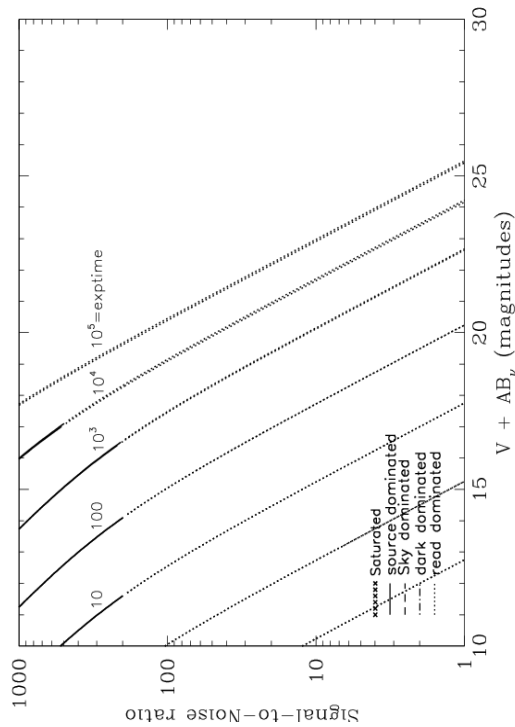


Figure 10.54: Extended source S/N vs. $V + AB_V$ for the HRC/F344N filter. Top curves are for low sky and bottom curves are for average sky for a 1 arcsec^2 area.



HRC/F435W

Description

Johnson B filter.

Figure 10.55: Integrated system throughput for HRC/F435W.

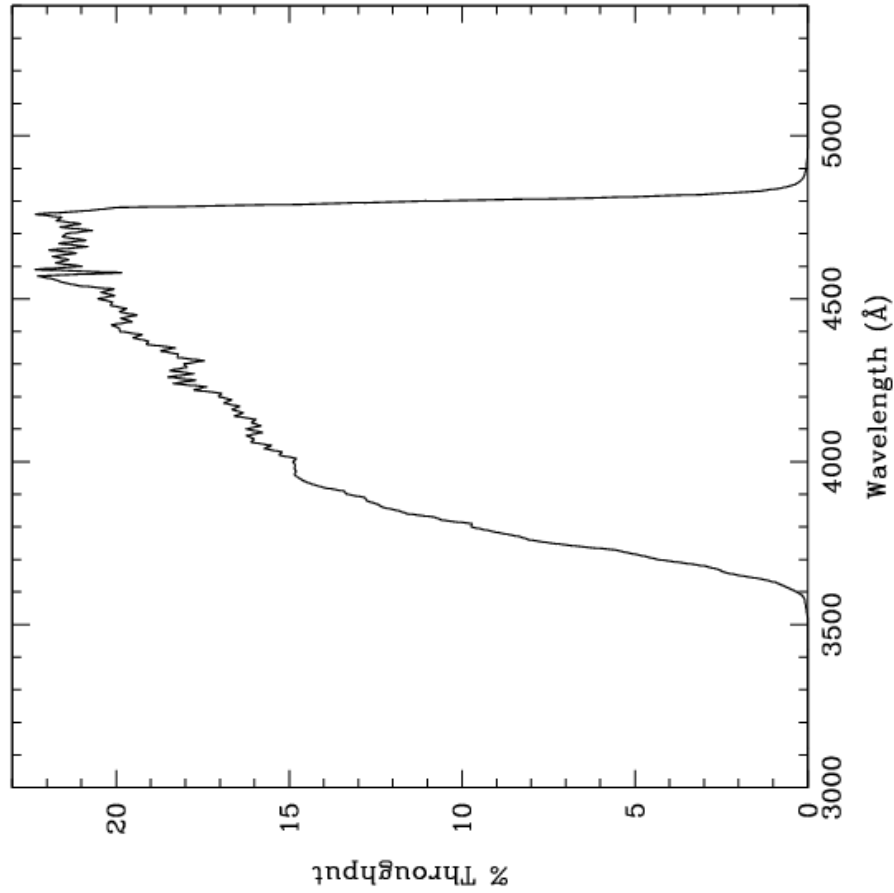


Figure 10.56: Point source S/N vs. $V+AB_V$ for the HRC/F435W filter. Top curves are for low sky; bottom curves are for average sky.

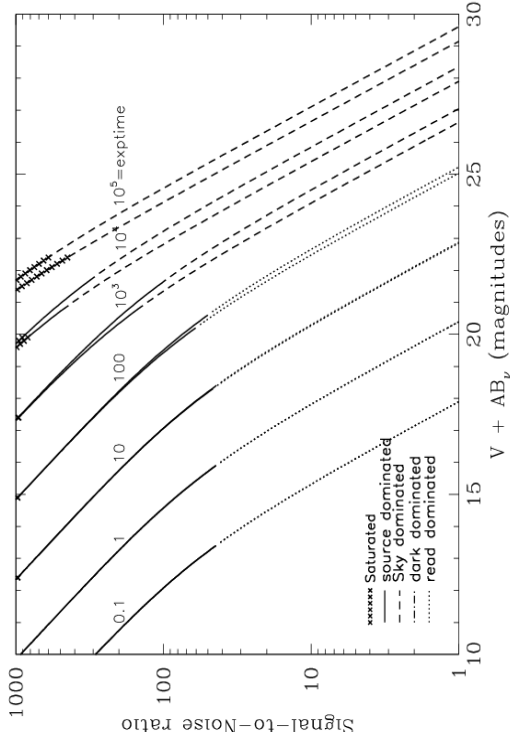
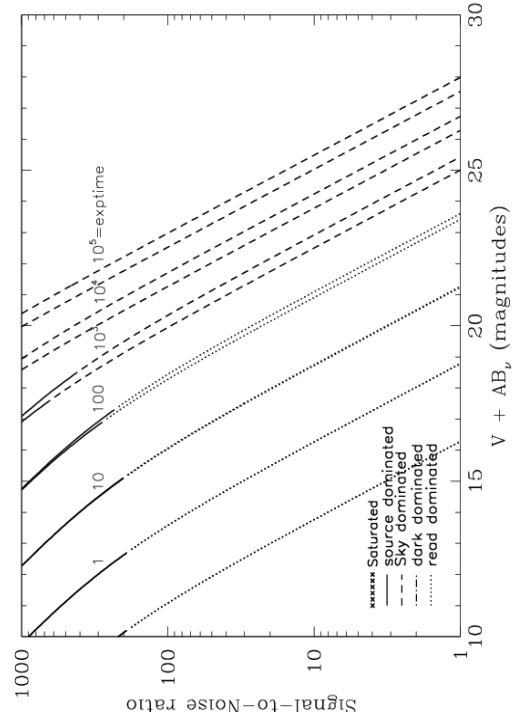


Figure 10.57: Extended source S/N vs. $V+AB_V$ for the HRC/F435W filter. Top curves are for low sky and bottom curves are for average sky for a 1 arcsec^2 area.



HRC/F475W

Description

Sloan Digital Sky Survey g filter.

Figure 10.58: Integrated system throughput for HRC/F475W.

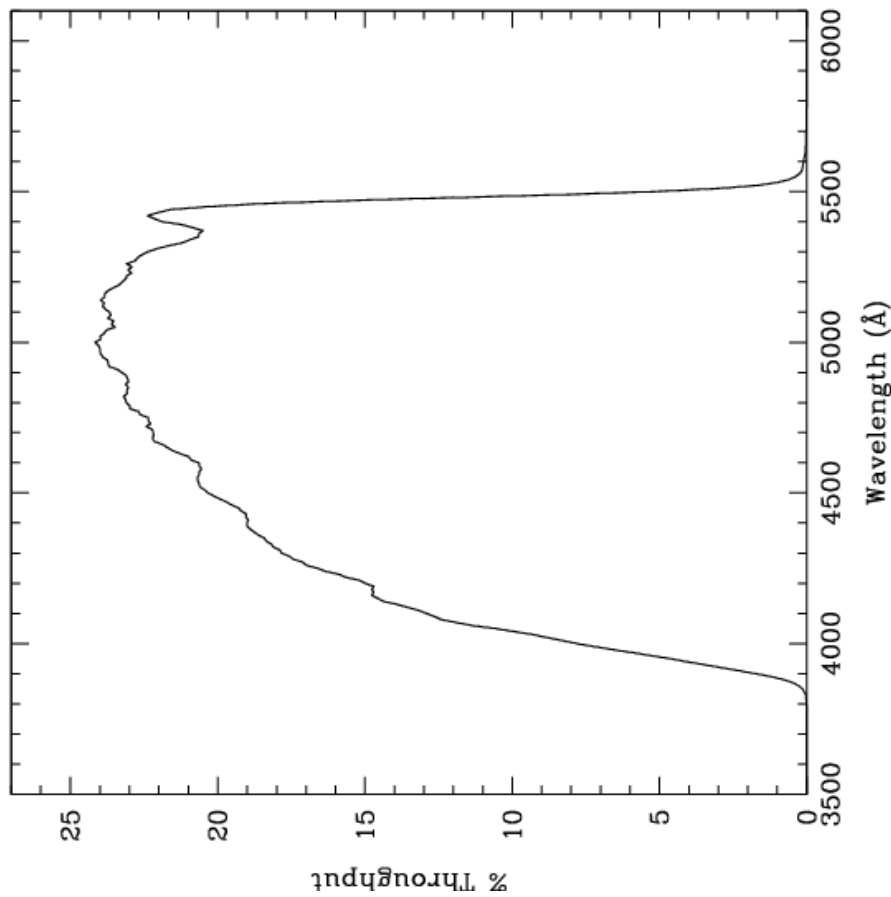


Figure 10.59: Point source S/N vs. $V+AB_V$ for the HRC/F475W filter. Top curves are for low sky; bottom curves are for average sky.

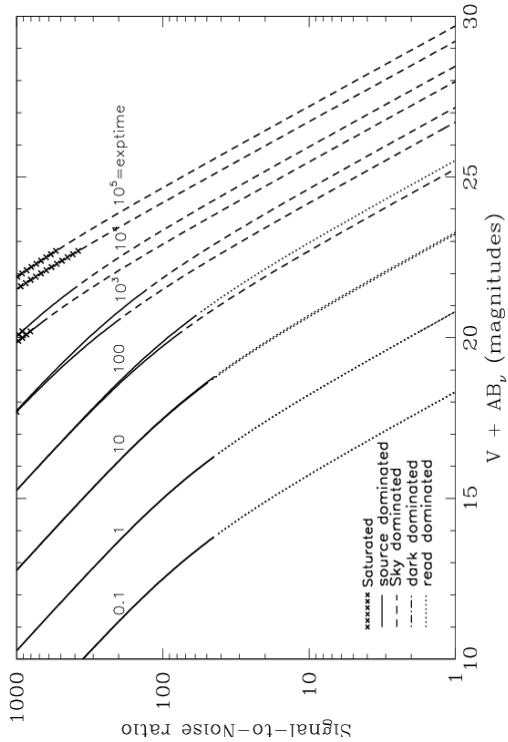
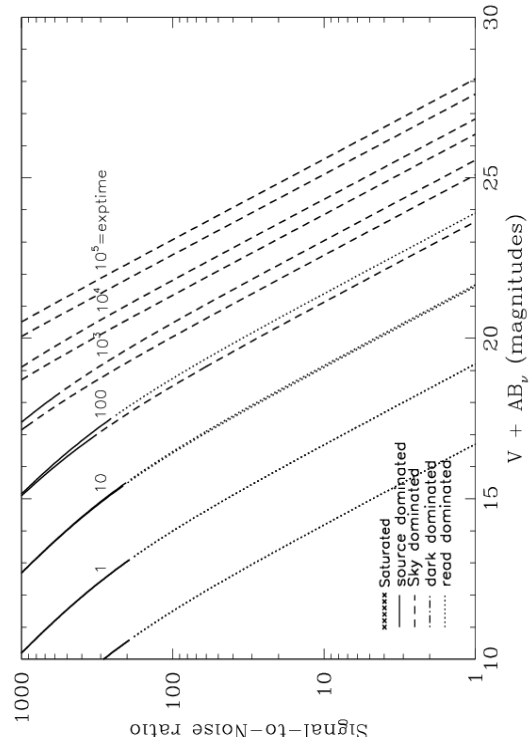


Figure 10.60: Extended source S/N vs. $V+AB_V$ for the HRC/F475W filter. Top curves are for low sky and bottom curves are for average sky for a 1 arcsec^2 area.



HRC/F502N

Description

OIII filter.

Figure 10.61: Integrated system throughput for HRC/F502N.

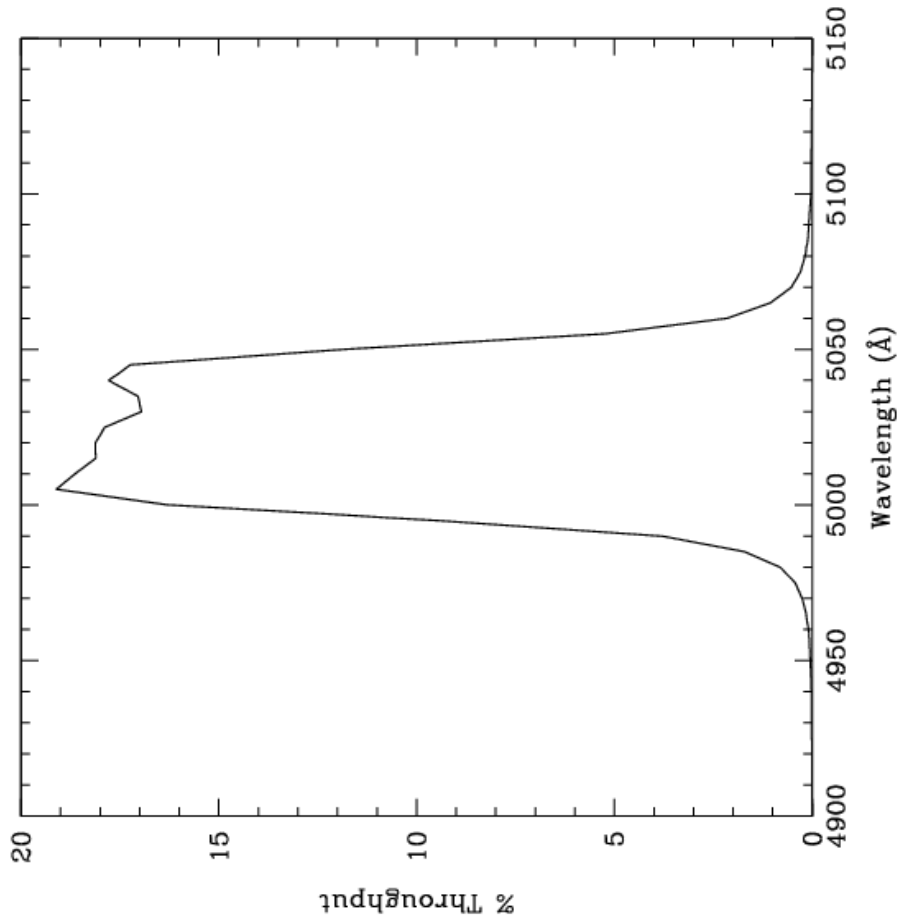


Figure 10.62: Point source S/N vs. $V + AB_V$ for the HRC/F502N filter. Top curves are for low sky; bottom curves are for average sky.

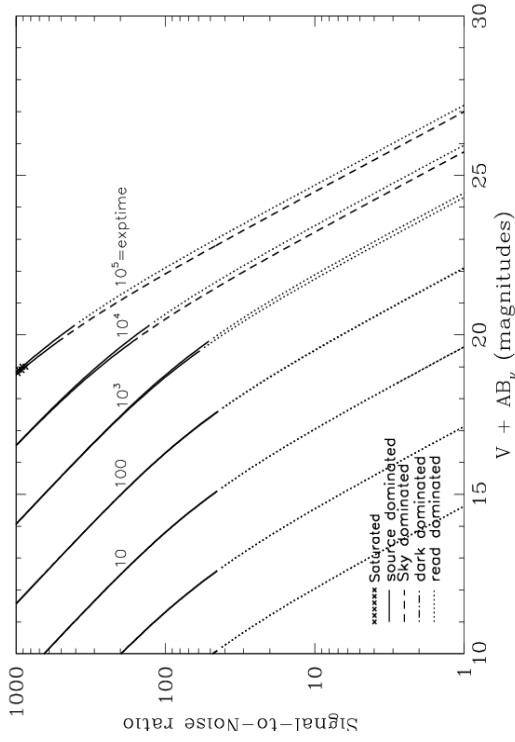
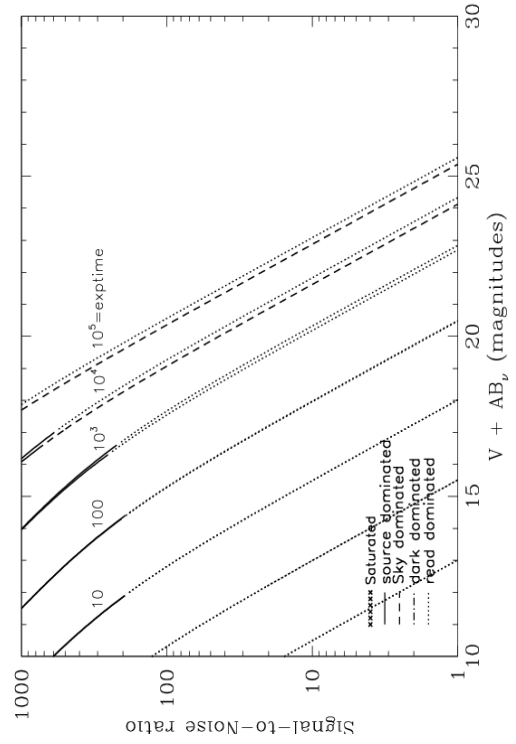


Figure 10.63: Extended source S/N vs. $V + AB_V$ for the HRC/F502N filter. Top curves are for low sky and bottom curves are for average sky for a 1 arcsec^2 area.



HRC/F550M

Description

Narrow V filter.

Figure 10.64: Integrated system throughput for HRC/F550M.

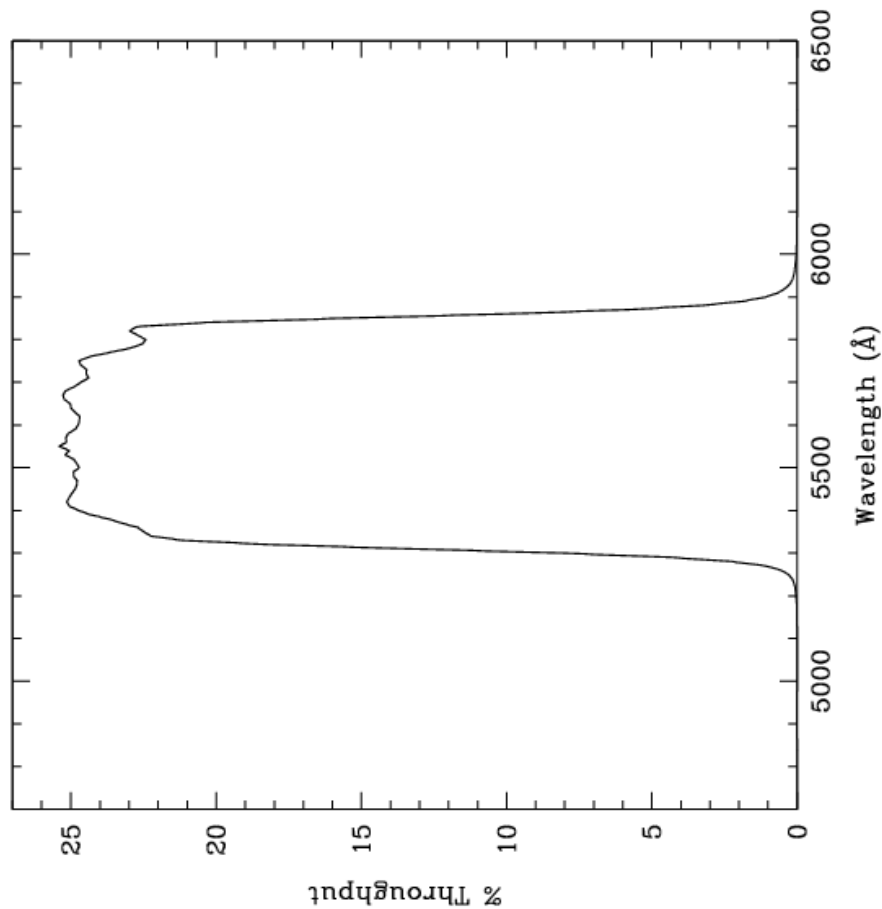


Figure 10.65: Point source S/N vs. $V+AB_V$ for the HRC/F550M filter. Top curves are for low sky; bottom curves are for average sky.

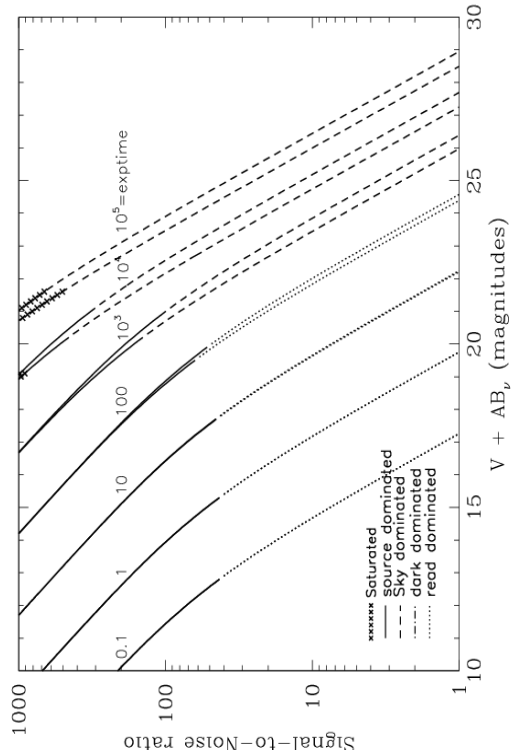
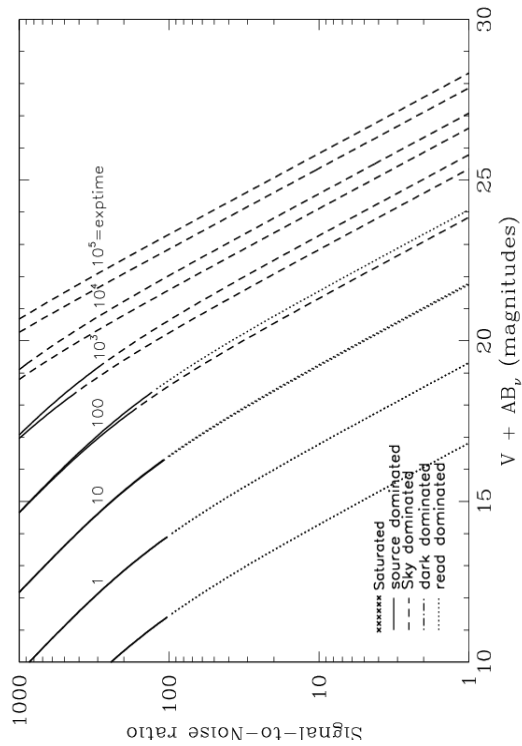


Figure 10.66: Extended source S/N vs. $V+AB_V$ for the HRC/F550M filter. Top curves are for low sky and bottom curves are for average sky for a 1 arcsec^2 area.



HRC/F555W

Description

Johnson V filter.

Figure 10.67: Integrated system throughput for HRC/F555W.

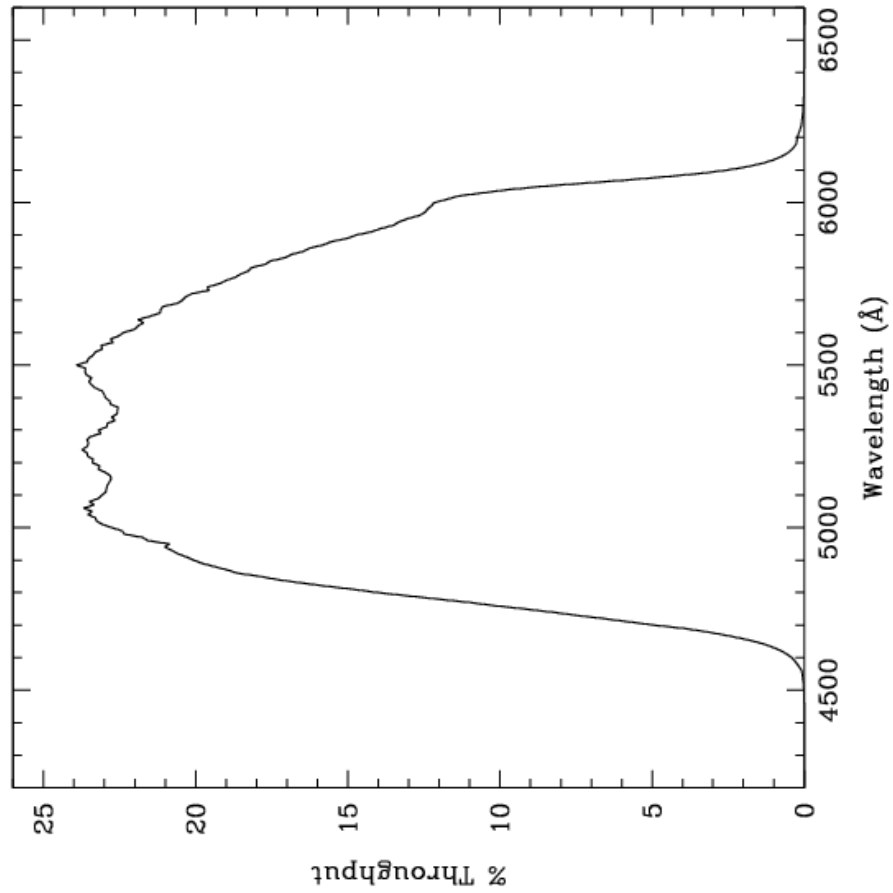


Figure 10.68: Point source S/N vs. $V+AB_V$ for the HRC/F555W filter. Top curves are for low sky; bottom curves are for average sky.

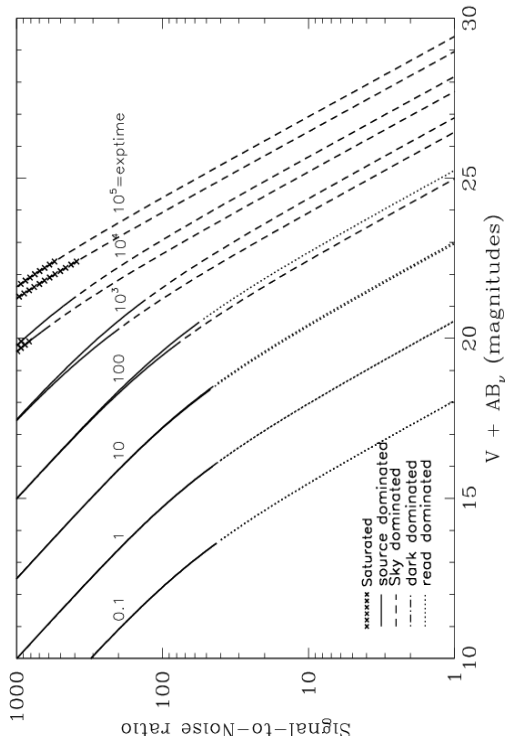
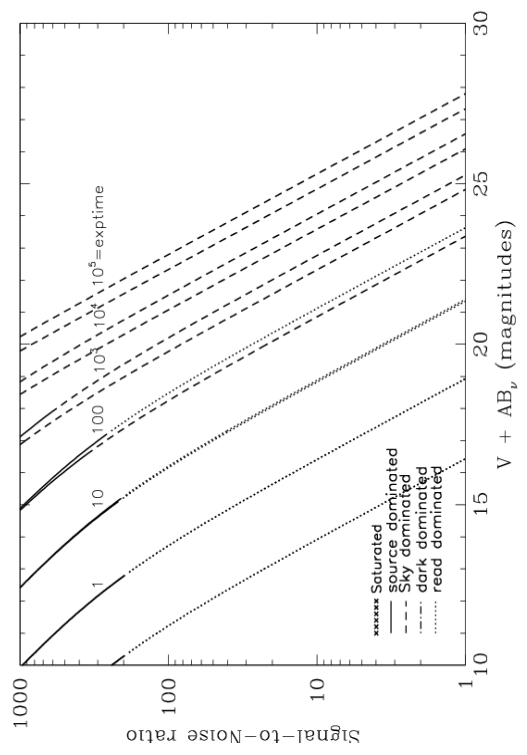


Figure 10.69: Extended source S/N vs. $V+AB_V$ for the HRC/F555W filter. Top curves are for low sky and bottom curves are for average sky for a 1 arcsec² area.



HRC/F606W

Description

Broad V filter.

Figure 10.70: Integrated system throughput for HRC/F606W.

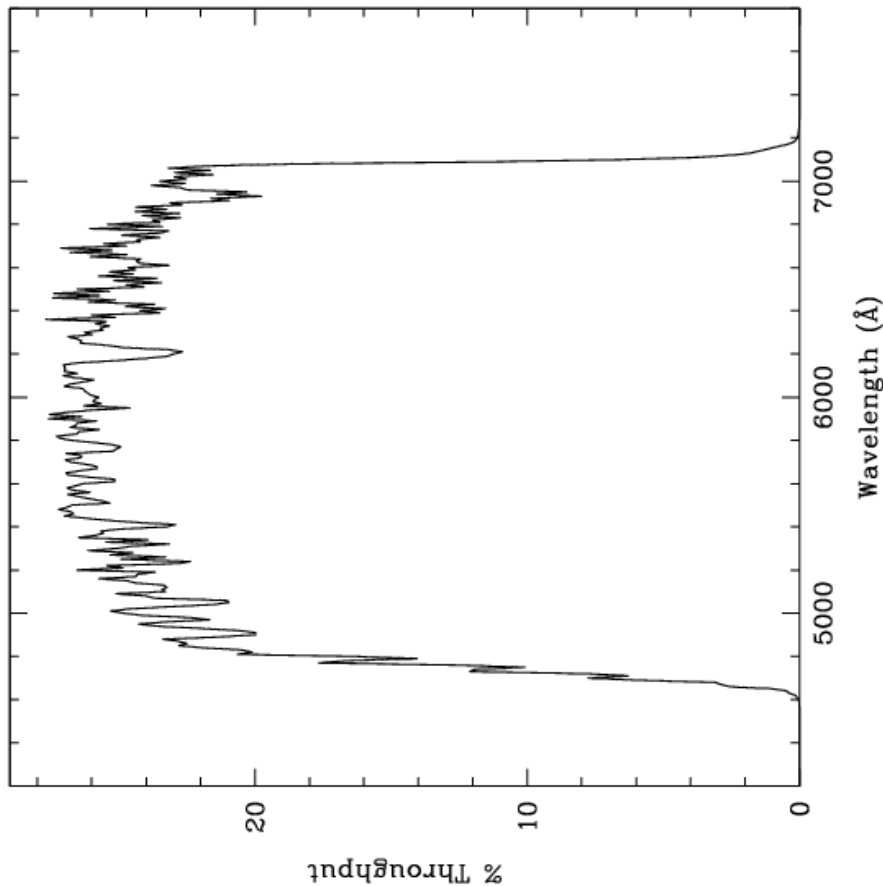


Figure 10.71: Point source S/N vs. $V + AB_V$ for the HRC/F606W filter. Top curves are for low sky; bottom curves are for average sky.

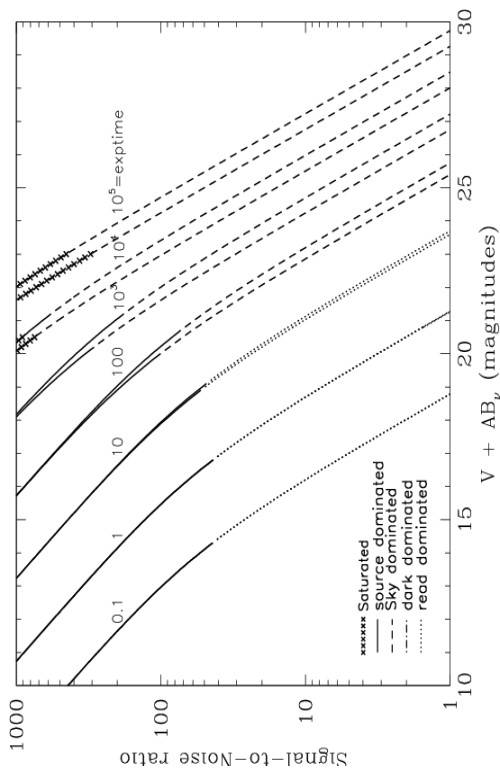
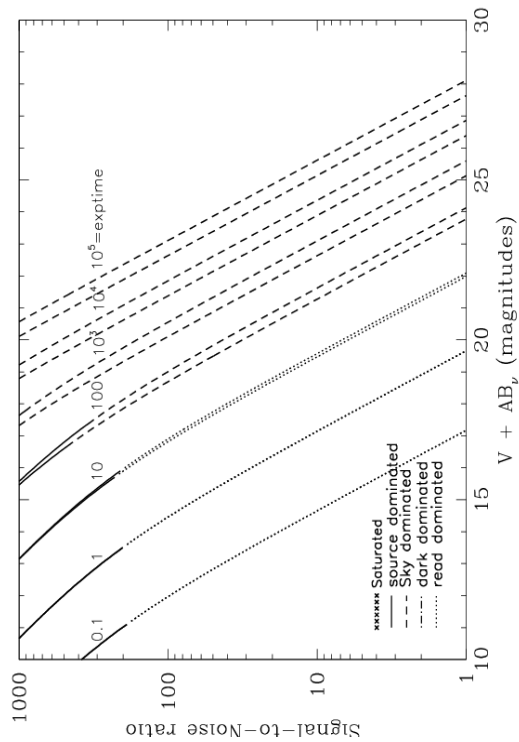


Figure 10.72: Extended source S/N vs. $V + AB_V$ for the HRC/F606W filter. Top curves are for low sky and bottom curves are for average sky for a 1 arcsec^2 area.



HRC/F625W

Description

Sloan Digital Sky Survey r filter.

Figure 10.73: Integrated system throughput for HRC/F625W.

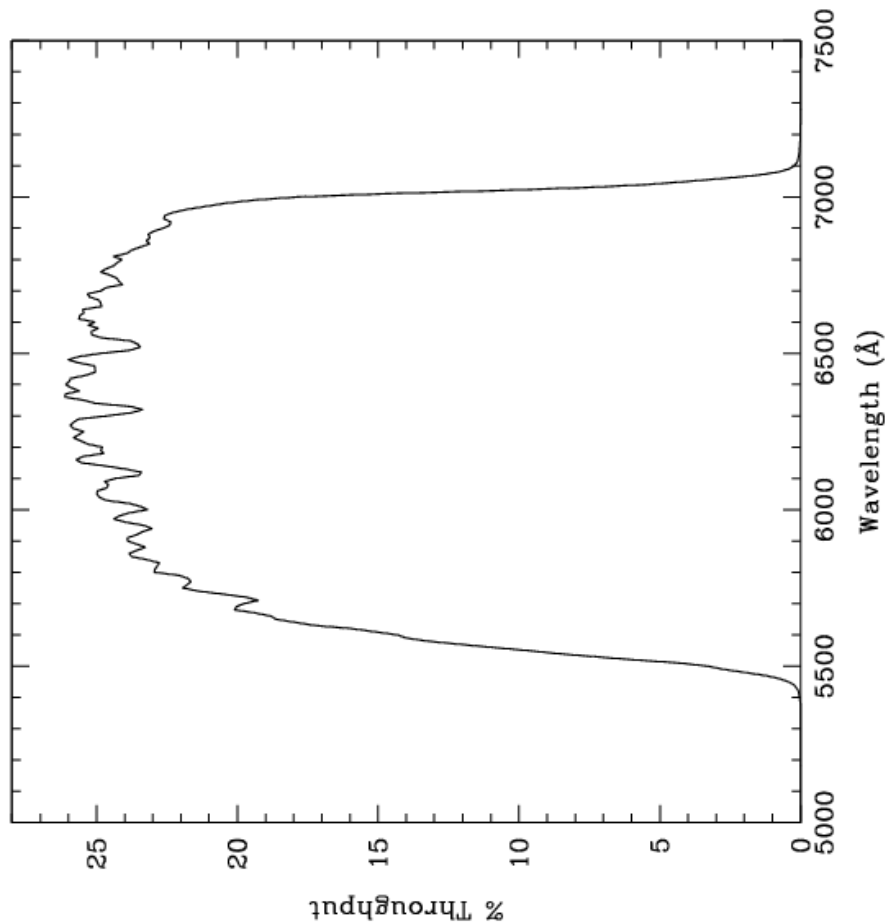


Figure 10.74: Point source S/N vs. $V+AB_V$ for the HRC/F625W filter. Top curves are for low sky; bottom curves are for average sky.

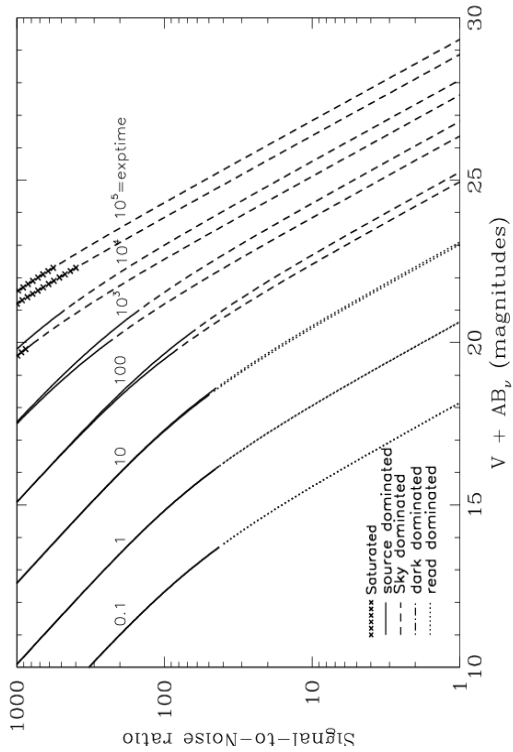
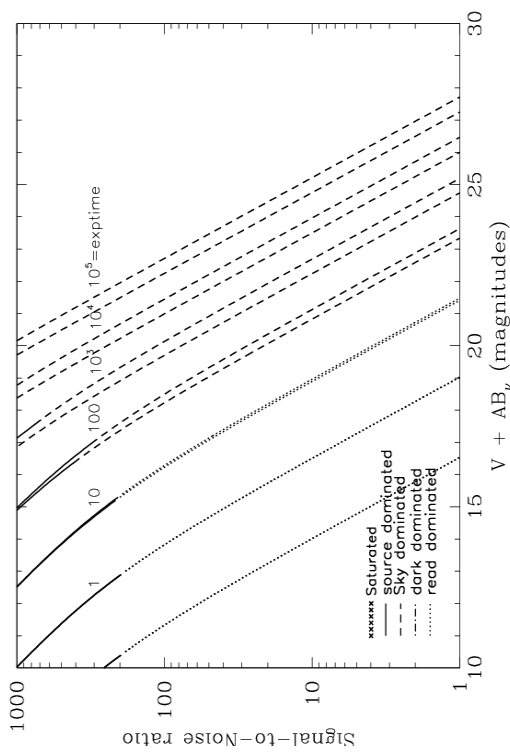


Figure 10.75: Extended source S/N vs. $V+AB_V$ for the HRC/F625W filter. Top curves are for low sky and bottom curves are for average sky for a 1 arcsec² area.



HRC/F658N

Description

H α filter.

Figure 10.76: Integrated system throughput for HRC/F658N.

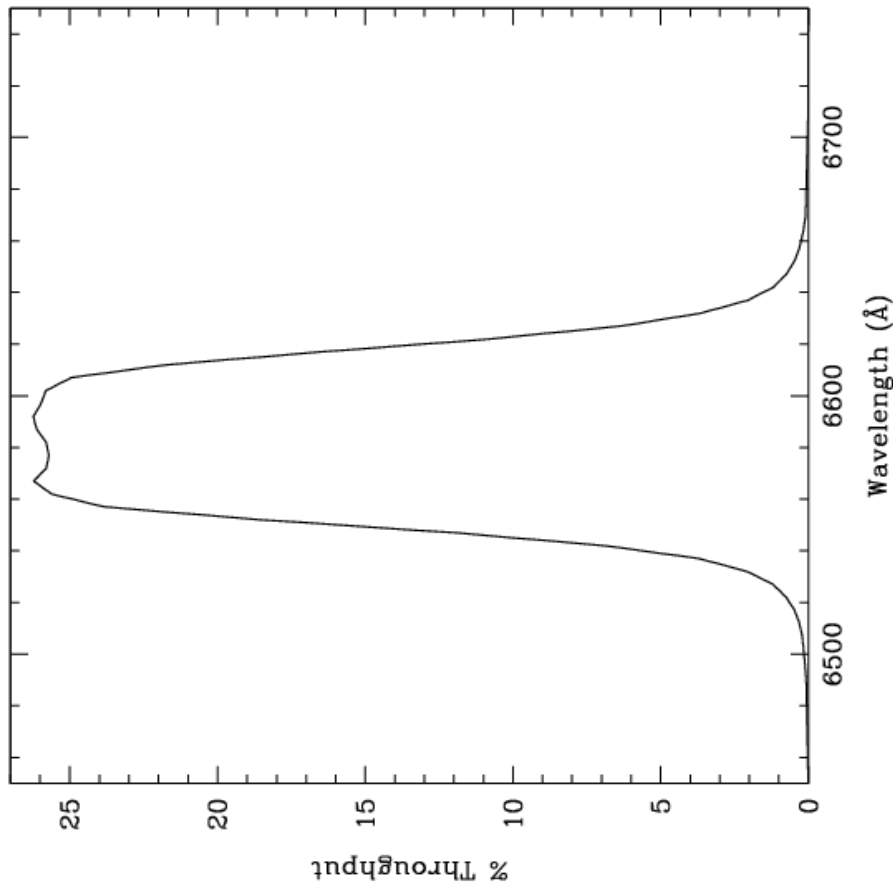


Figure 10.77: Point source S/N vs. $V+AB_V$ for the HRC/F658N filter. Top curves are for low sky; bottom curves are for average sky.

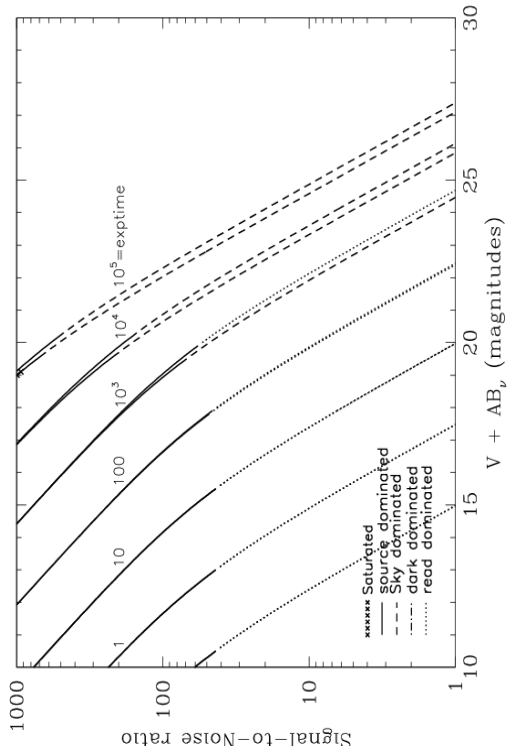
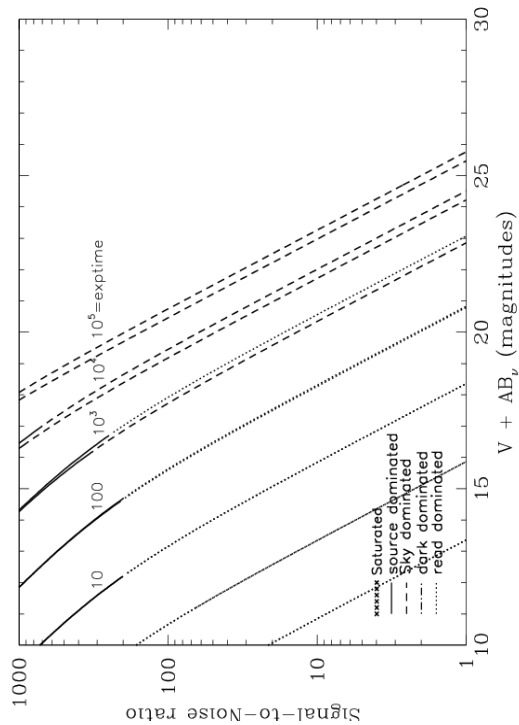


Figure 10.78: Extended source S/N vs. $V+AB_V$ for the HRC/F658N filter. Top curves are for low sky and bottom curves are for average sky for a 1 arcsec^2 area.



HRC/F660N

Description

NII filter.

Figure 10.79: Integrated system throughput for HRC/F660N.

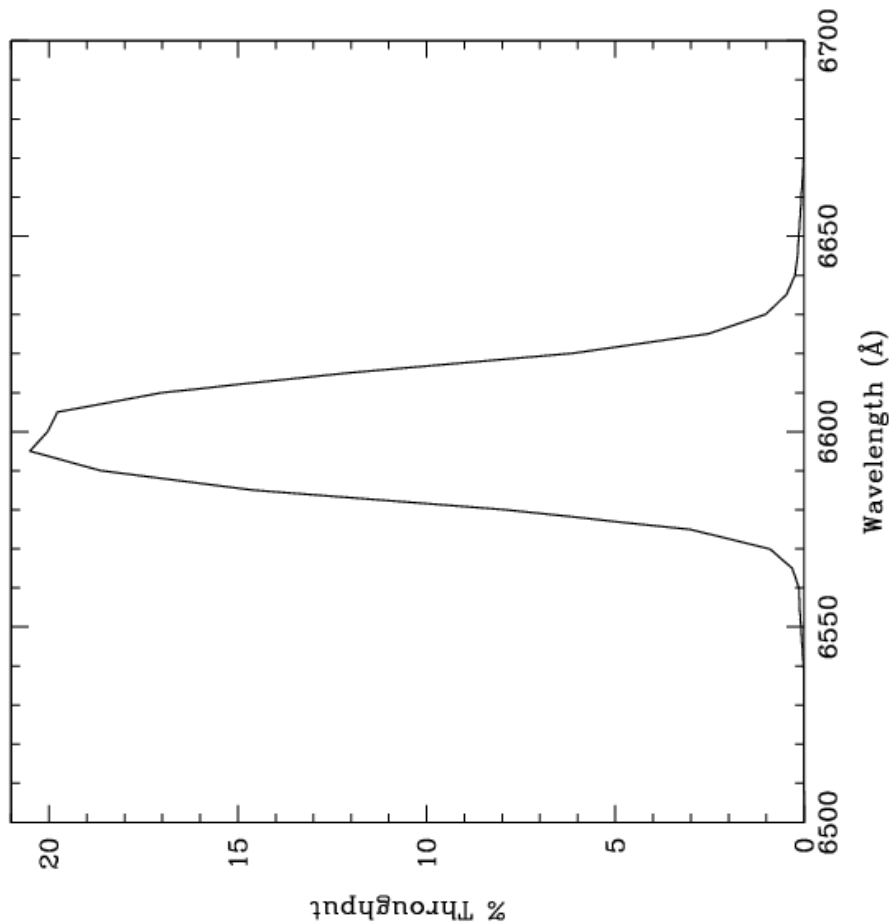


Figure 10.80: Point source S/N vs. $V + AB_V$ for the HRC/F660N filter. Top curves are for low sky; bottom curves are for average sky.

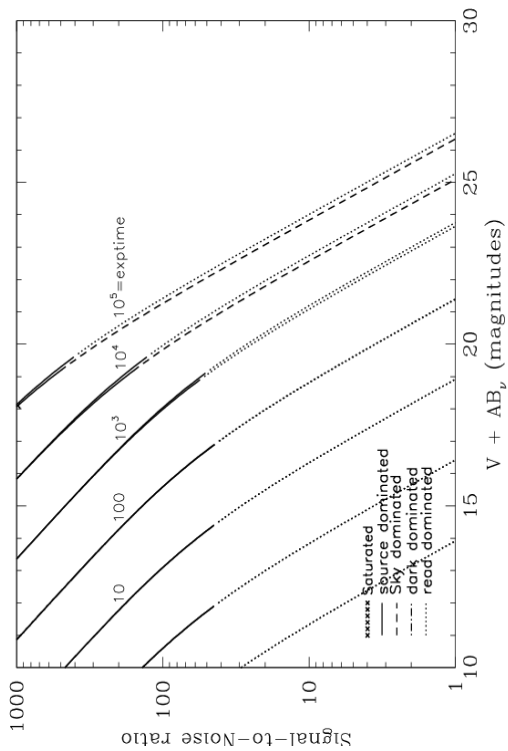
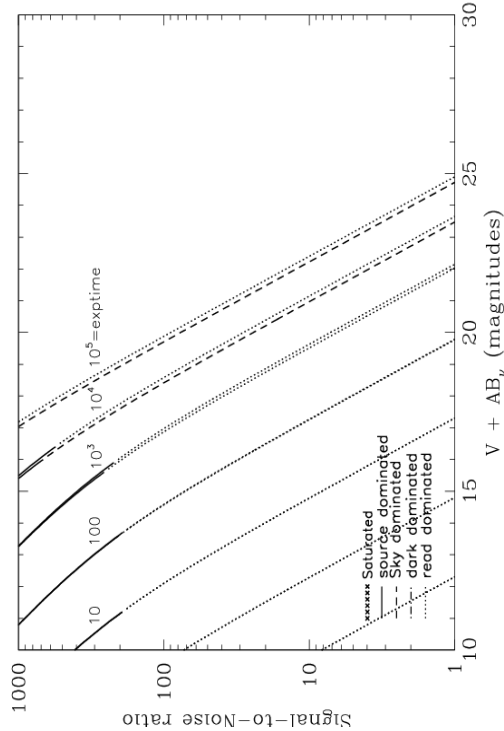


Figure 10.81: Extended source S/N vs. $V + AB_V$ for the HRC/F660N filter. Top curves are for low sky and bottom curves are for average sky for a 1 arcsec² area.



HRC/F775W

Description

Sloan Digital Sky Survey i filter.

Figure 10.82: Integrated system throughput for HRC/F775W.

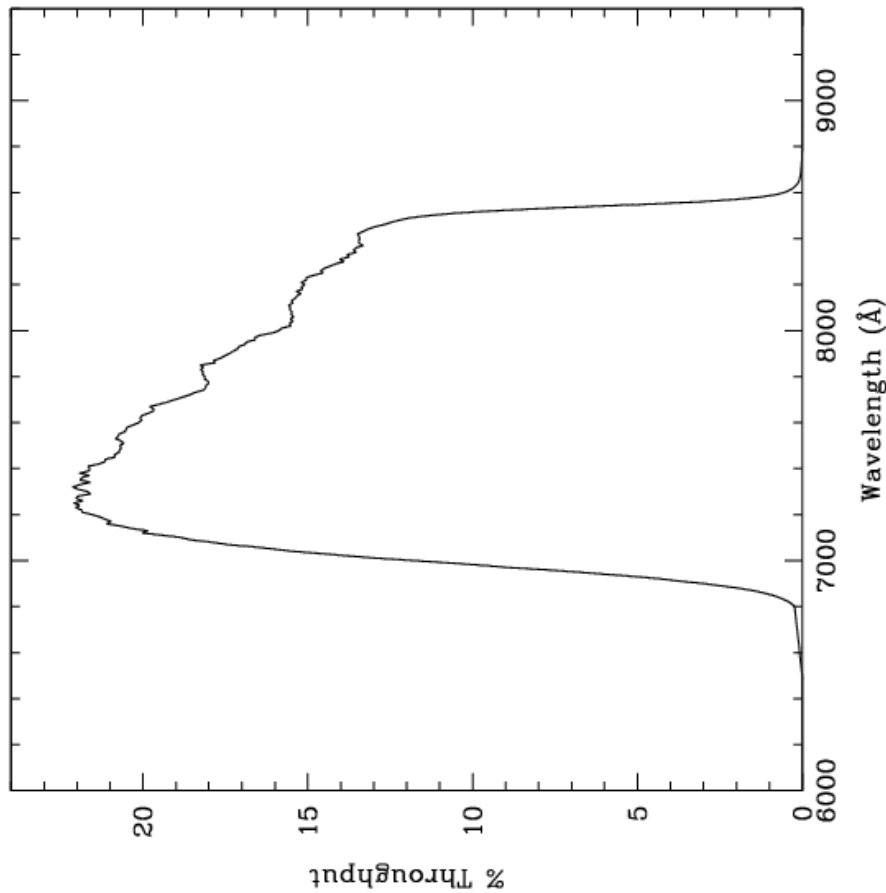


Figure 10.83: Point source S/N vs. $V+AB_V$ for the HRC/F775W filter. Top curves are for low sky; bottom curves are for average sky.

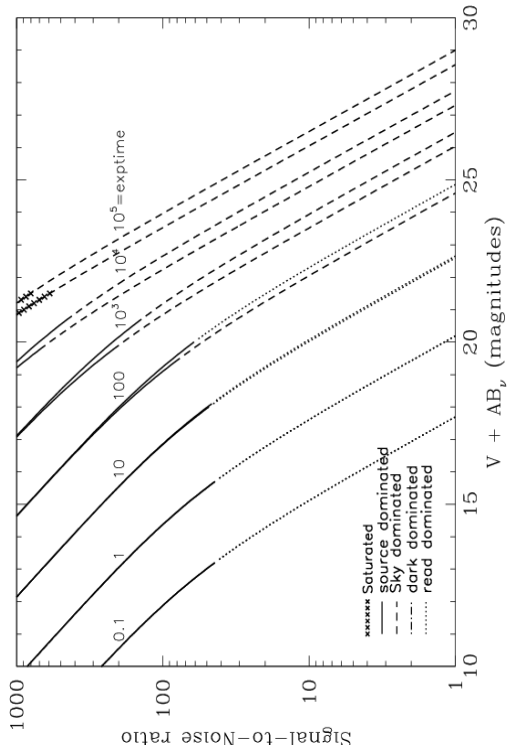
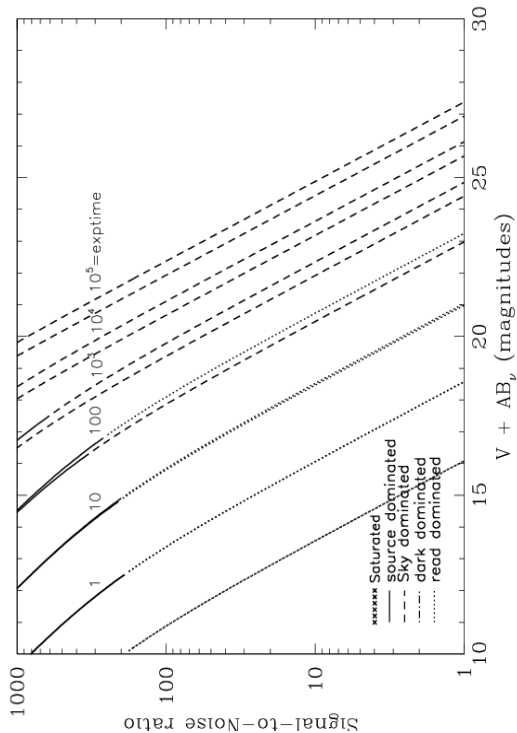


Figure 10.84: Extended source S/N vs. $V+AB_V$ for the HRC/F775W filter. Top curves are for low sky and bottom curves are for average sky for a 1 arcsec^2 area.



HRC/F814W

Description

Broad I filter.

Figure 10.85: Integrated system throughput for HRC/F814W.

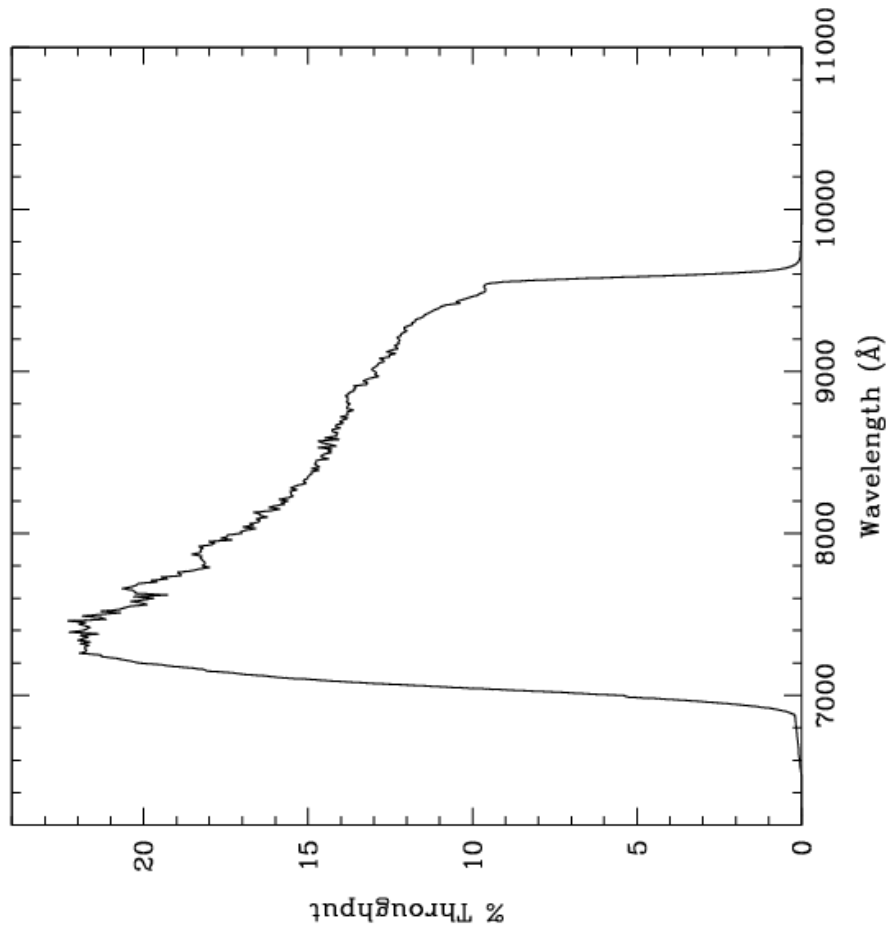


Figure 10.86: Point source S/N vs. $V+AB_V$ for the HRC/F814W filter. Top curves are for low sky; bottom curves are for average sky.

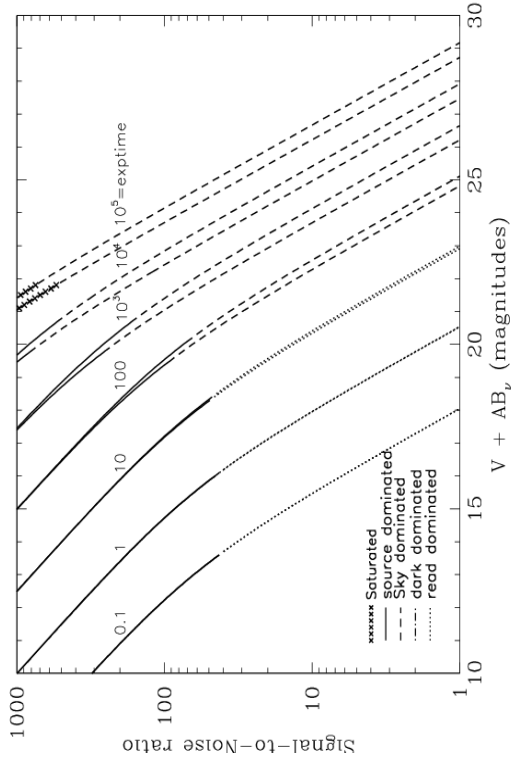
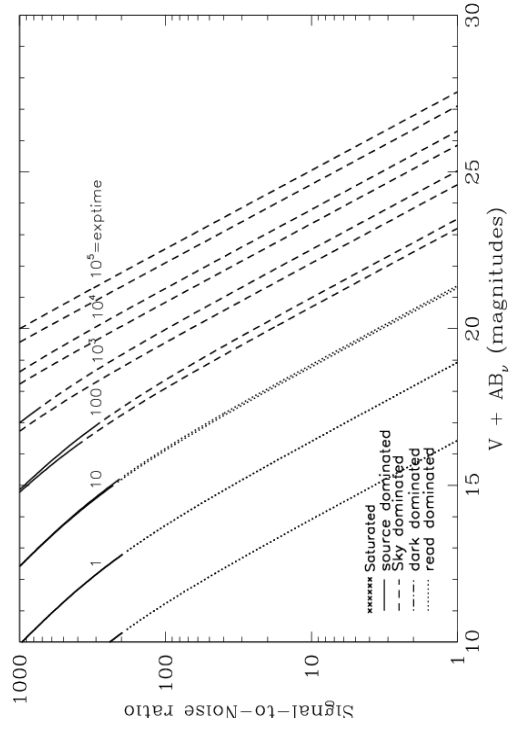


Figure 10.87: Extended source S/N vs. $V+AB_V$ for the HRC/F814W filter. Top curves are for low sky and bottom curves are for average sky for a 1 arcsec² area.



HRC/F850LP

Description

Sloan Digital Sky Survey z filter.

Figure 10.88: Integrated system throughput for HRC/F850LP.

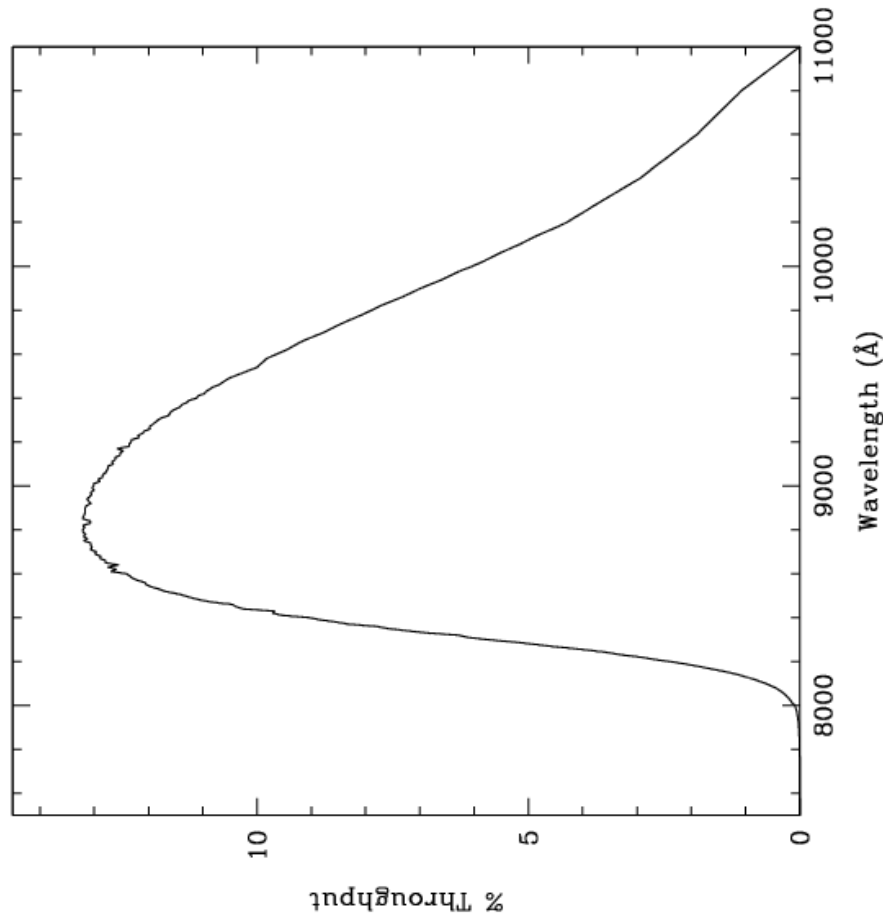


Figure 10.89: Point source S/N vs. $V+AB_V$ for the HRC/F850LP filter. Top curves are for low sky; bottom curves are for average sky.

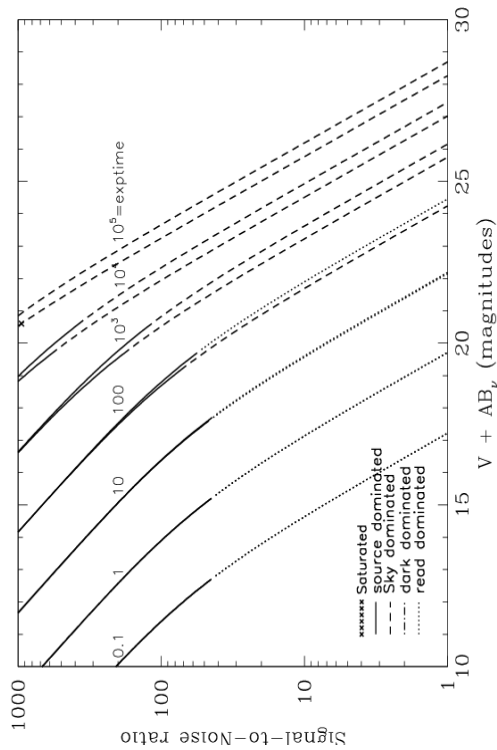
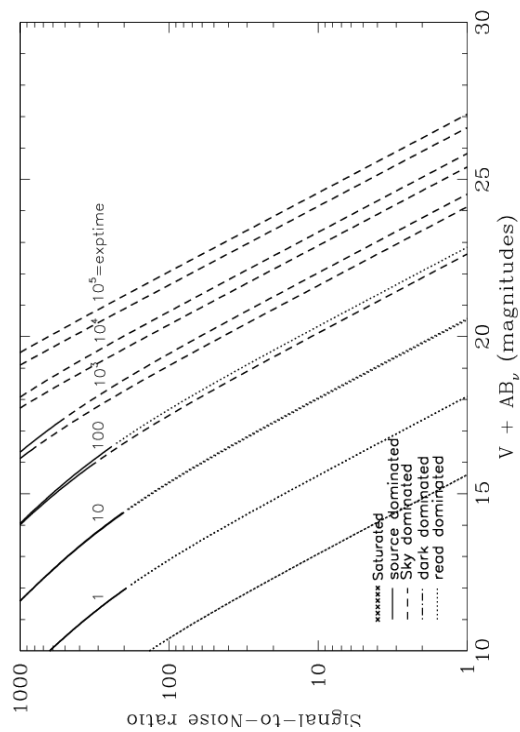


Figure 10.90: Extended source S/N vs. $V+AB_V$ for the HRC/F850LP filter. Top curves are for low sky and bottom curves are for average sky for a 1 arcsec^2 area.



HRC/F892N

Description

Methane filter.

Figure 10.91: Integrated system throughput for HRC/F892N.

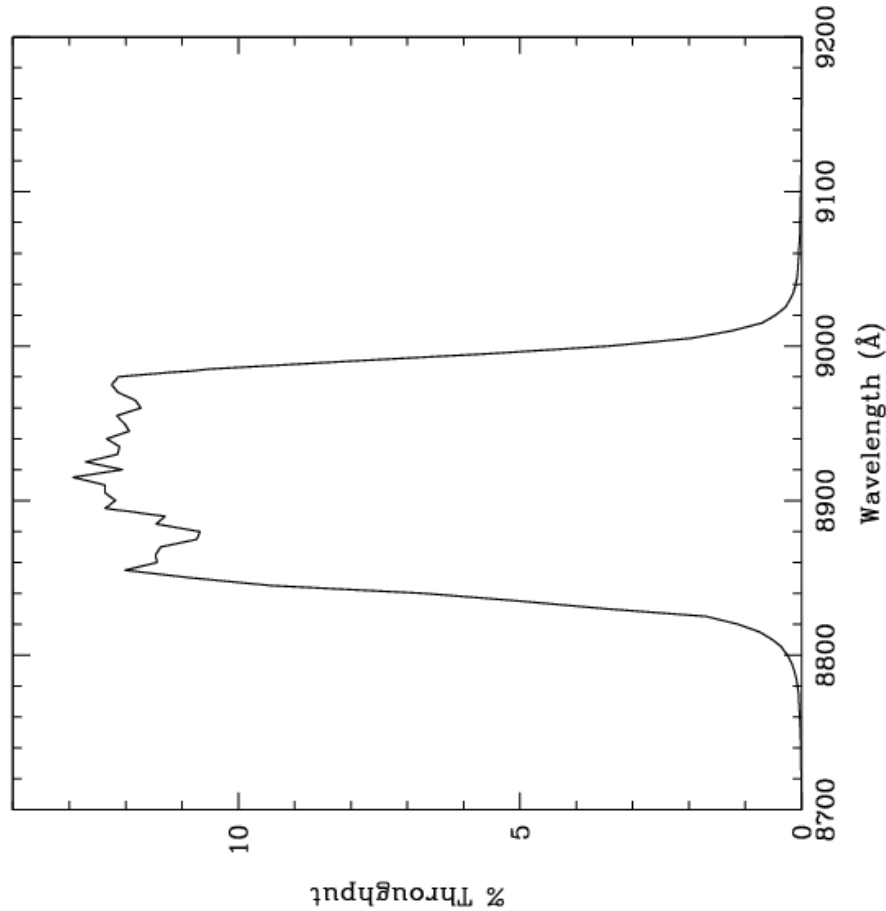


Figure 10.92: Point source S/N vs. $V + AB_V$ for the HRC/F892N filter. Top curves are for low sky; bottom curves are for average sky.

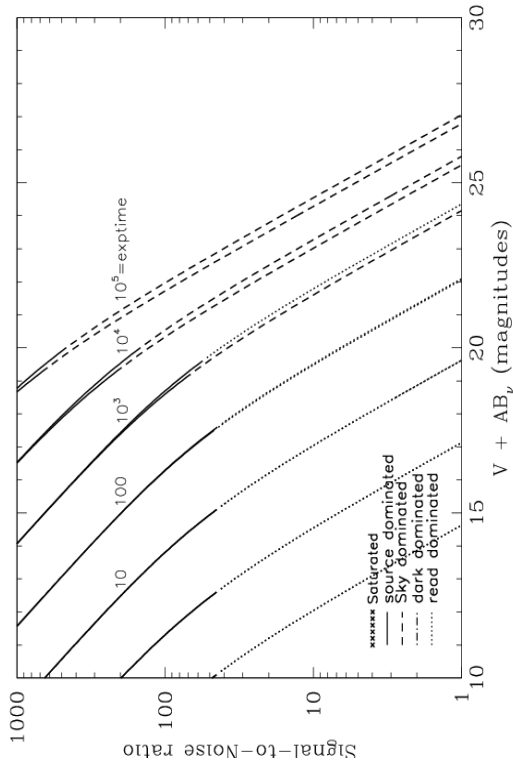
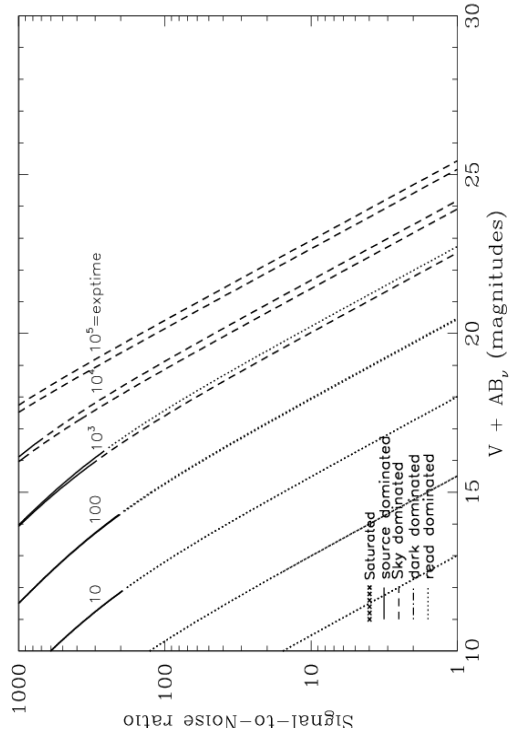


Figure 10.93: Extended source S/N vs. $V + AB_V$ for the HRC/F892N filter. Top curves are for low sky and bottom curves are for average sky for a 1 arcsec^2 area.



HRC/G800L

Description

Grism.

Figure 10.94: Integrated system throughput for HRC/G800L.

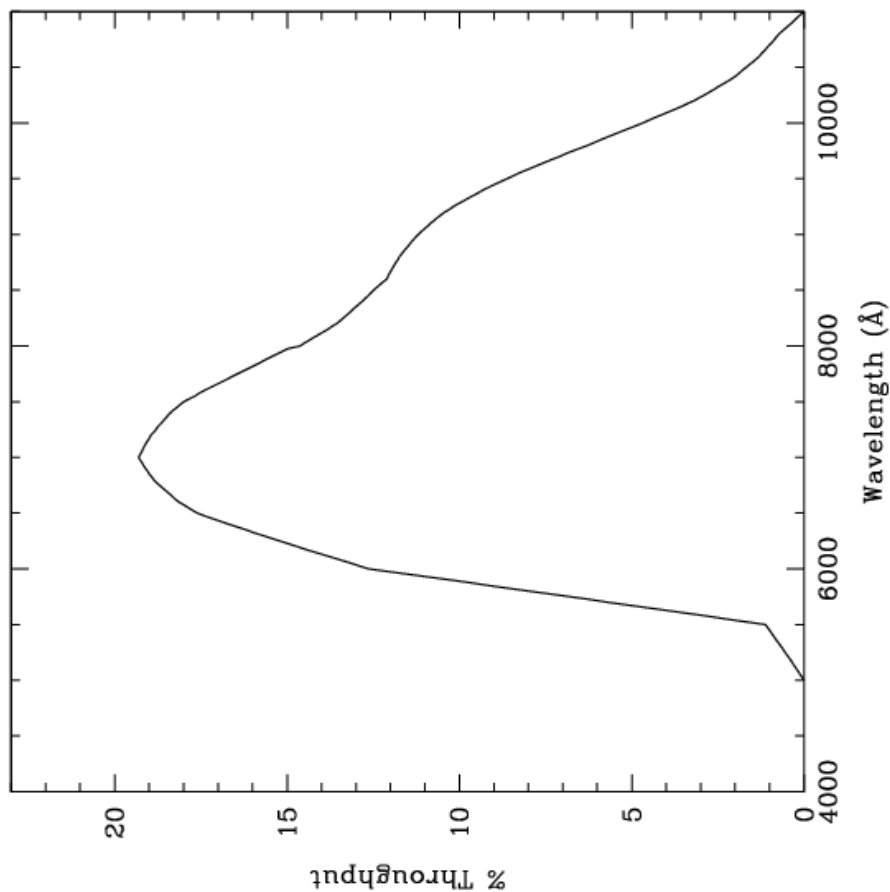


Figure 10.95: Point source S/N vs. $V + AB_V$ for the HRC/G800L filter. Top curves are for low sky; bottom curves are for average sky.

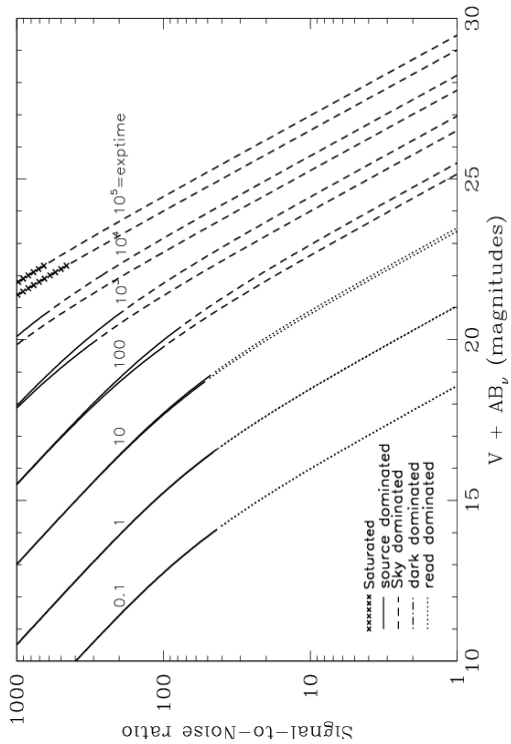
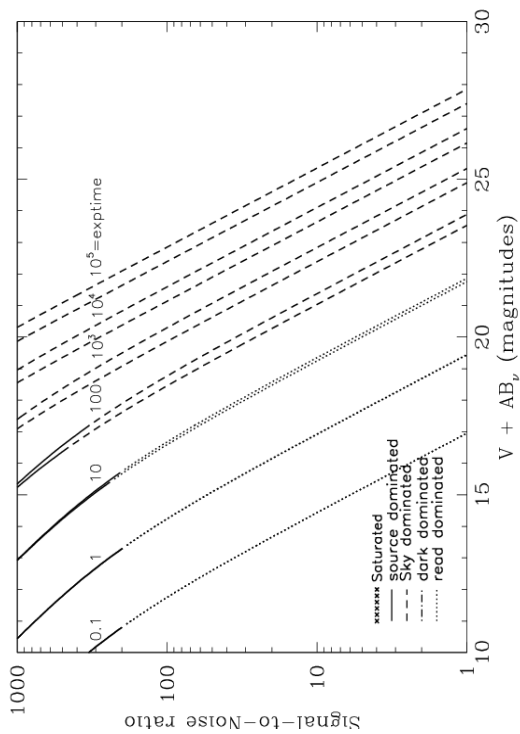


Figure 10.96: Extended source S/N vs. $V + AB_V$ for the HRC/G800L filter. Top curves are for low sky and bottom curves are for average sky for a 1 arcsec^2 area.



HRC/PR200L

Description

HRC Prism.

Figure 10.97: Integrated system throughput for HRC/PR200L.

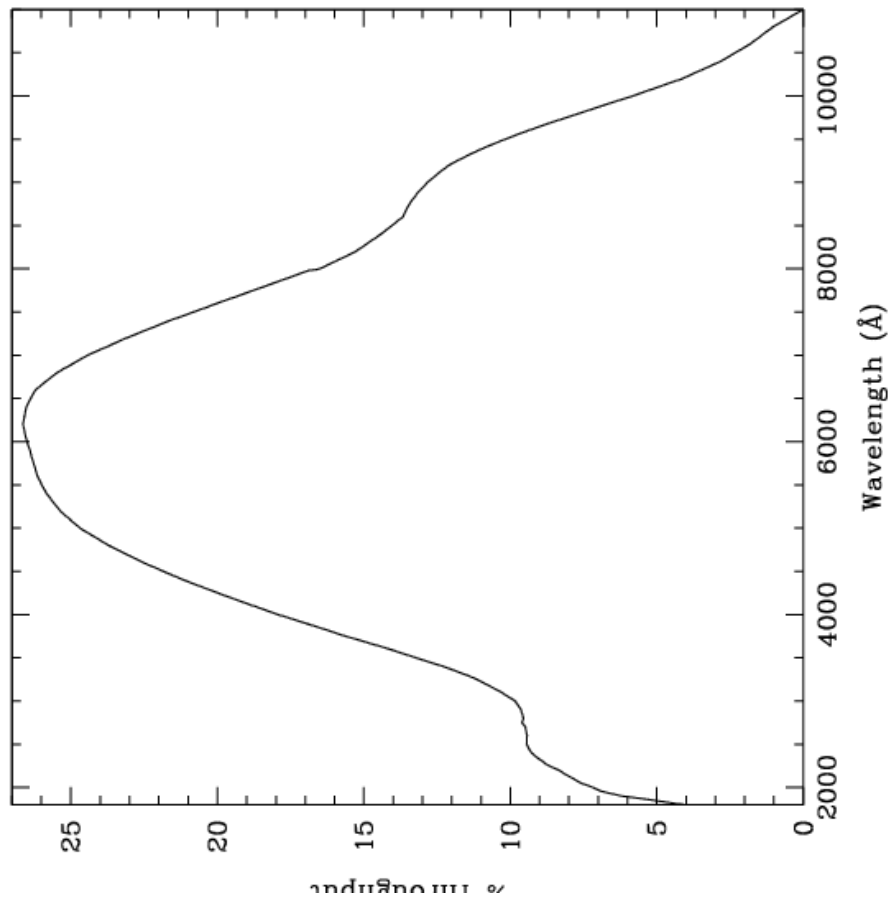


Figure 10.98: Point source S/N vs. $V+AB_V$ for the HRC/PR200L filter. Top curves are for low sky; bottom curves are for average sky.

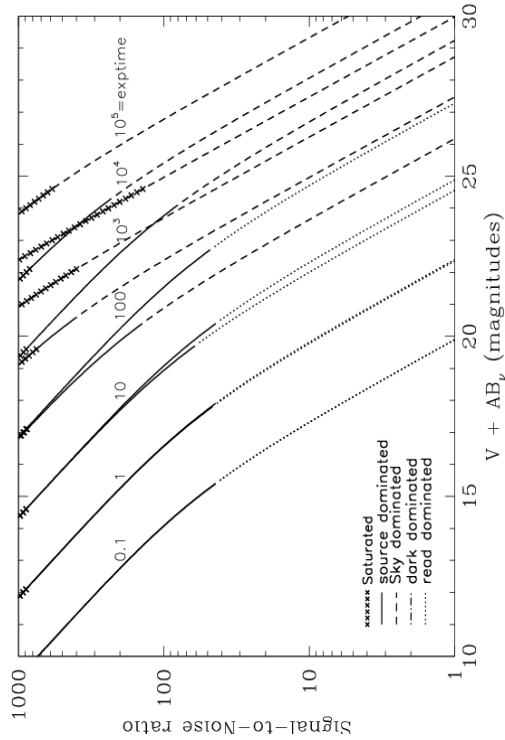
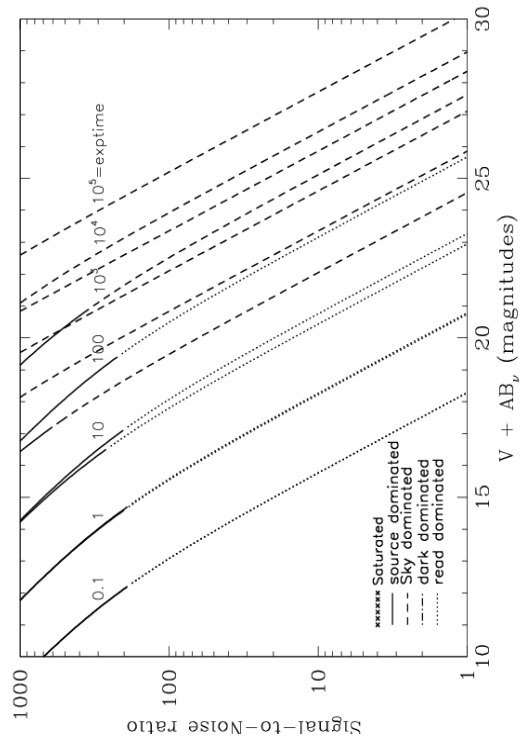


Figure 10.99: Extended source S/N vs. $V+AB_V$ for the HRC/PR200L filter. Top curves are for low sky and bottom curves are for average sky for a 1 arcsec^2 area.



HRC/CLEAR

Description
HRC Clear Filter.

Figure 10.100: Integrated system throughput for HRC/Clear

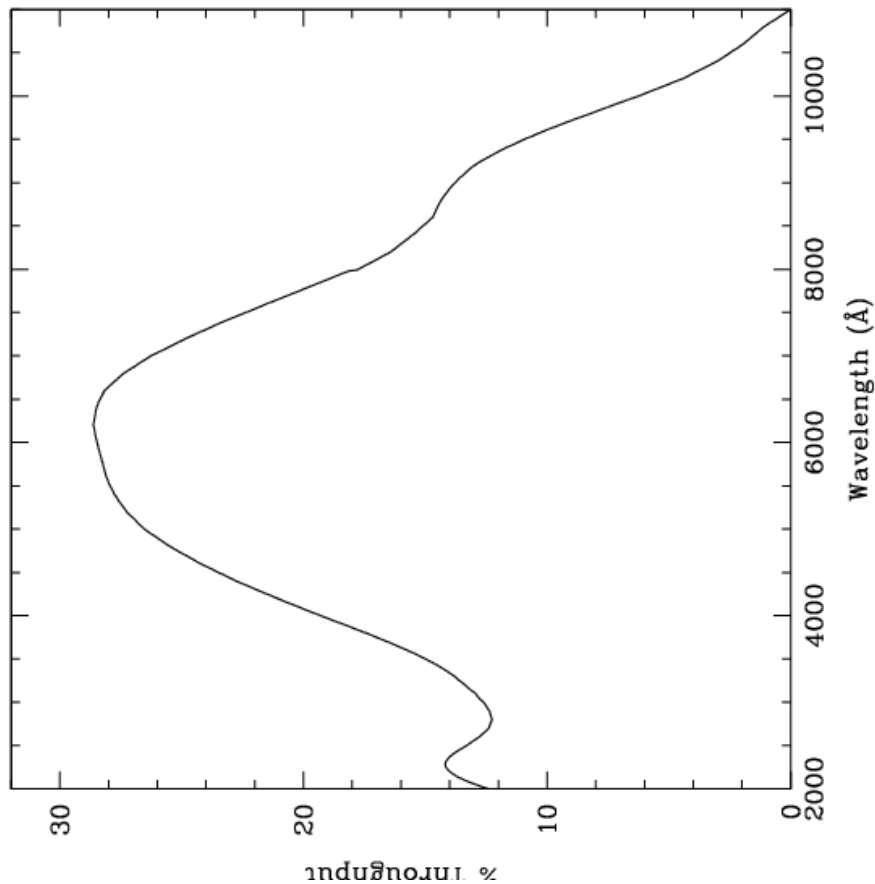


Figure 10.101: Point source S/N vs. $V+AB_V$ for the HRC/Clear filter. Top curves are for low sky; bottom curves are for average sky.

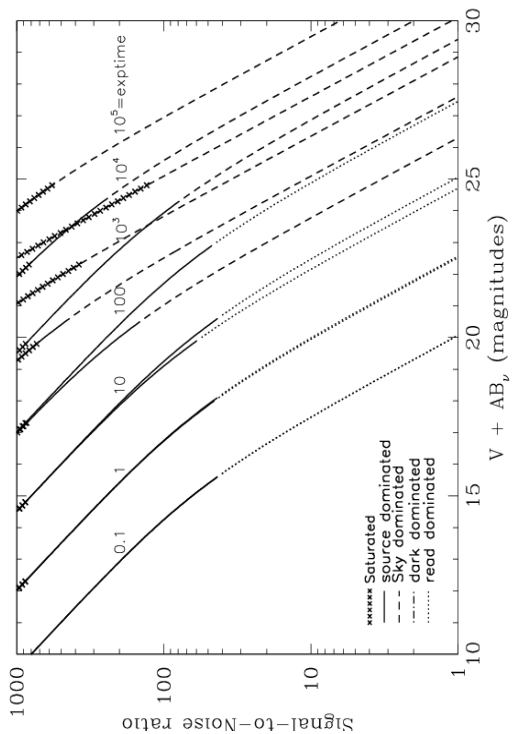
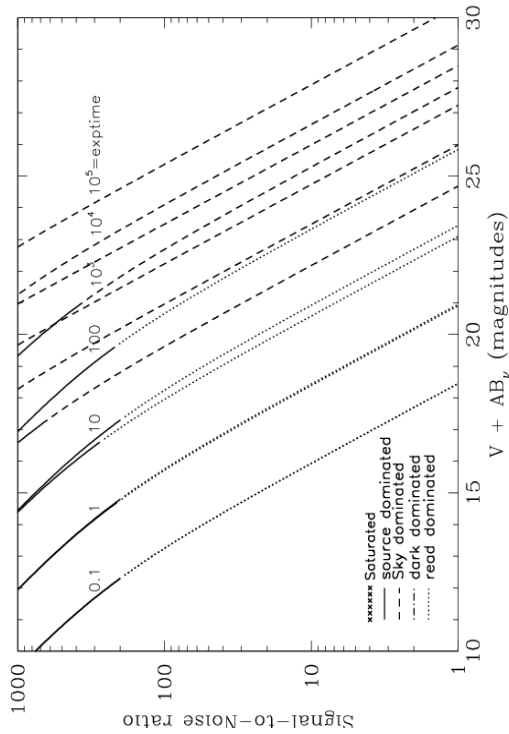


Figure 10.102: Extended source S/N vs. $V+AB_V$ for the HRC/Clear filter. Top curves are for low sky and bottom curves are for average sky for a 1 arcsec^2 area.



SBC/F115LP

Description

MgF₂ filter.

Figure 10.103: Integrated system throughput for SBC/F115LP.

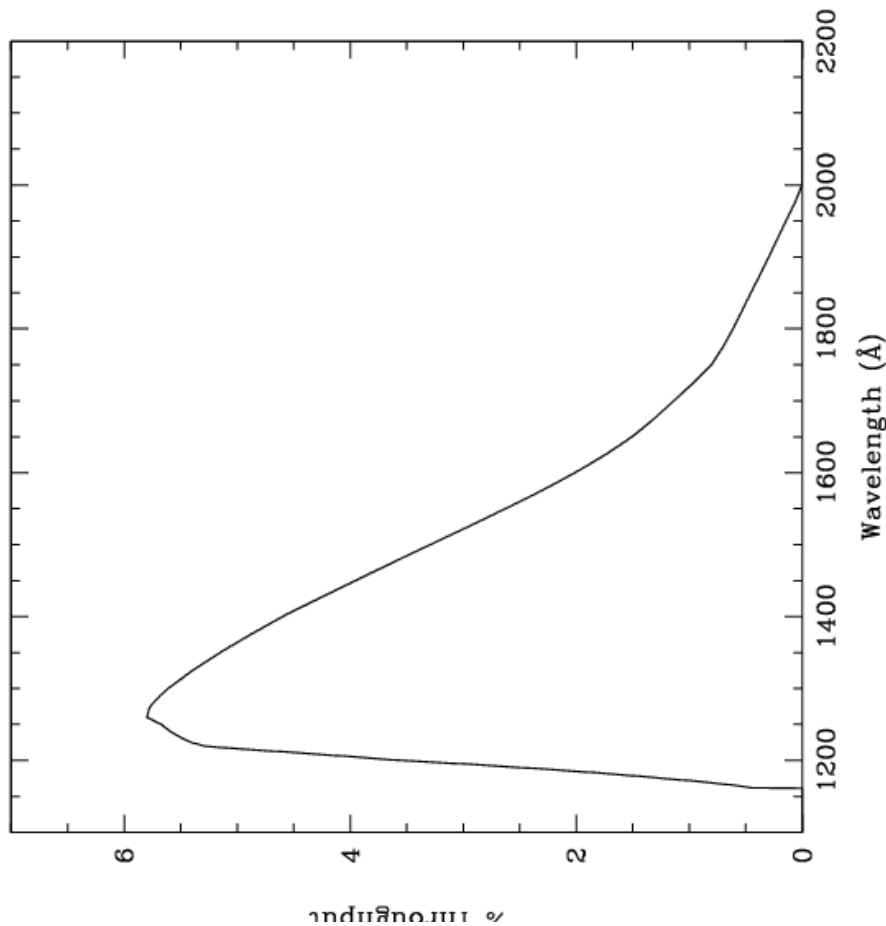


Figure 10.104: Point source S/N vs. $V+AB_V$ for the SBC/F115LP filter. Top curves are for low sky; bottom curves are for average sky.

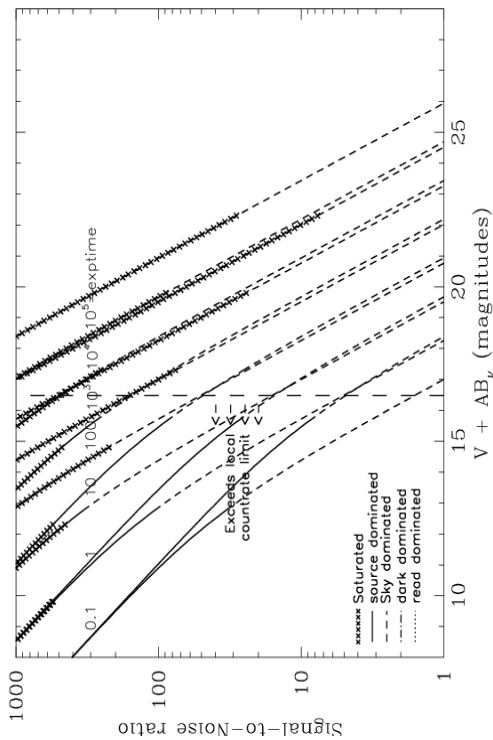
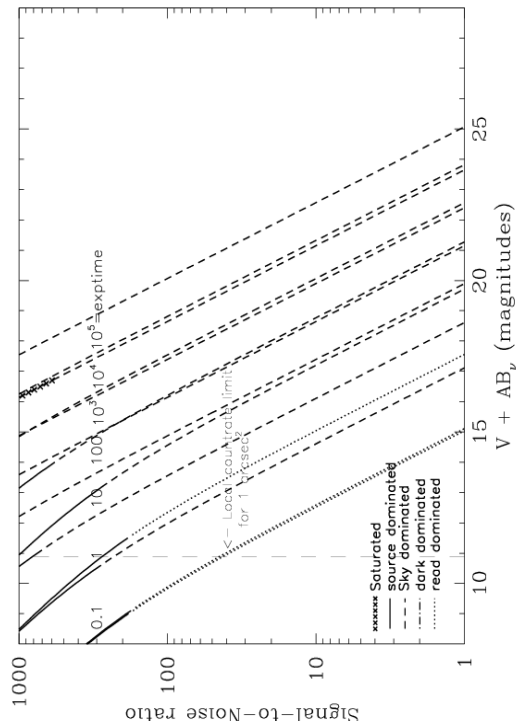


Figure 10.105: Extended source S/N vs. $V+AB_V$ for the SBC/F115LP filter. Top curves are for low sky and bottom curves are for average sky for a 1 arcsec² area.



SBC/F122M

Description

Lyman α filter.

Figure 10.106: Integrated system throughput for SBC/F122M.

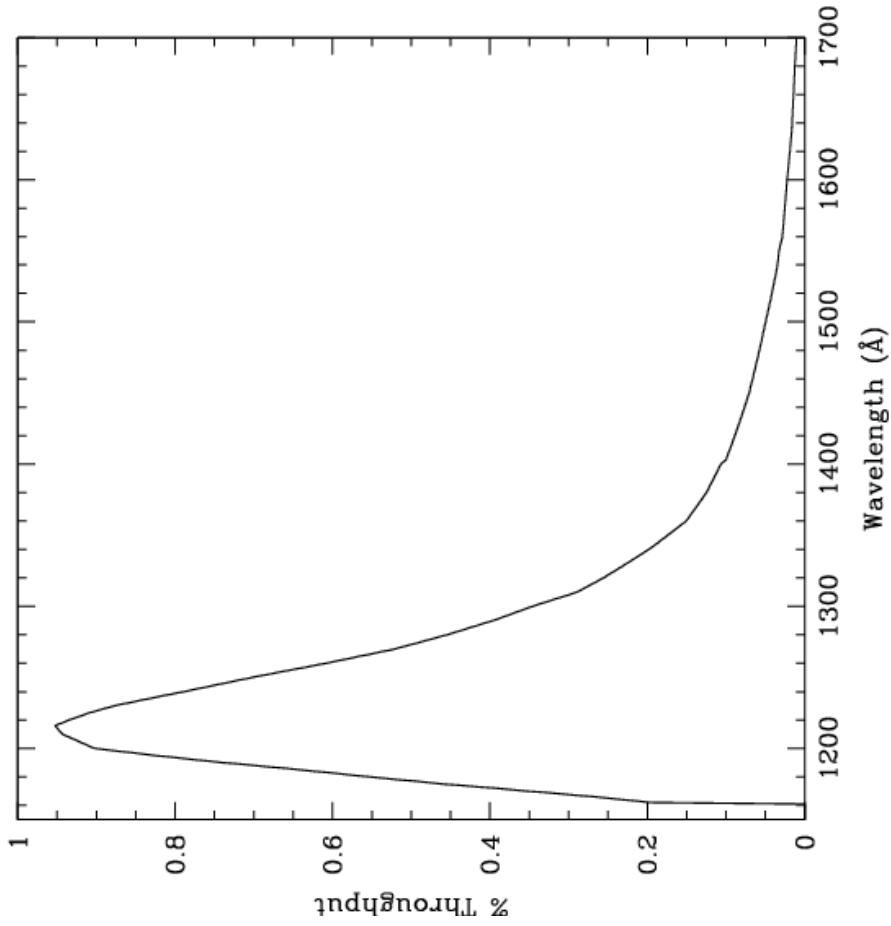


Figure 10.107: Point source S/N vs. $V+AB_V$ for the SBC/F122M filter. Top curves are for low sky; bottom curves are for average sky.

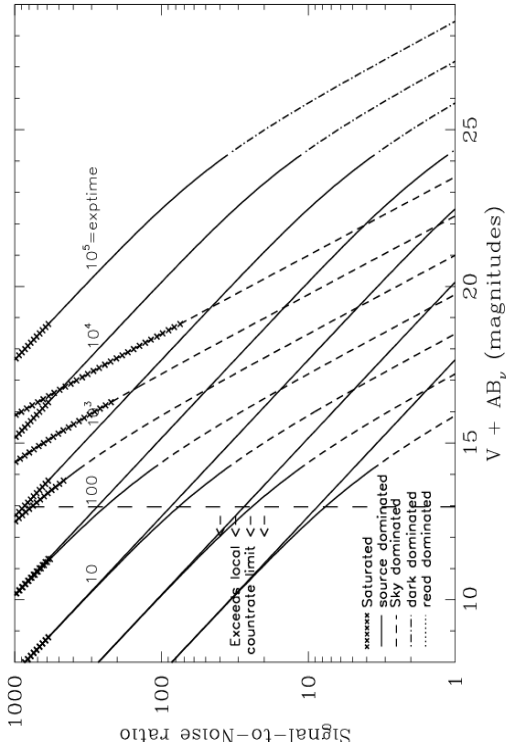
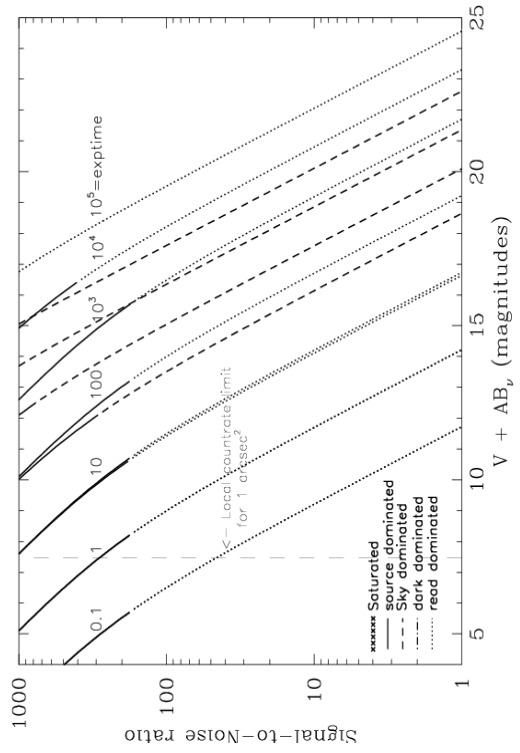


Figure 10.108: Extended source S/N vs. $V+AB_V$ for the SBC/F122M filter. Top curves are for low sky and bottom curves are for average sky for a 1 arcsec² area.



SBC/F125LP

Description

CaF₂ filter.

Figure 10.109: Integrated system throughput for SBC/F125LP.

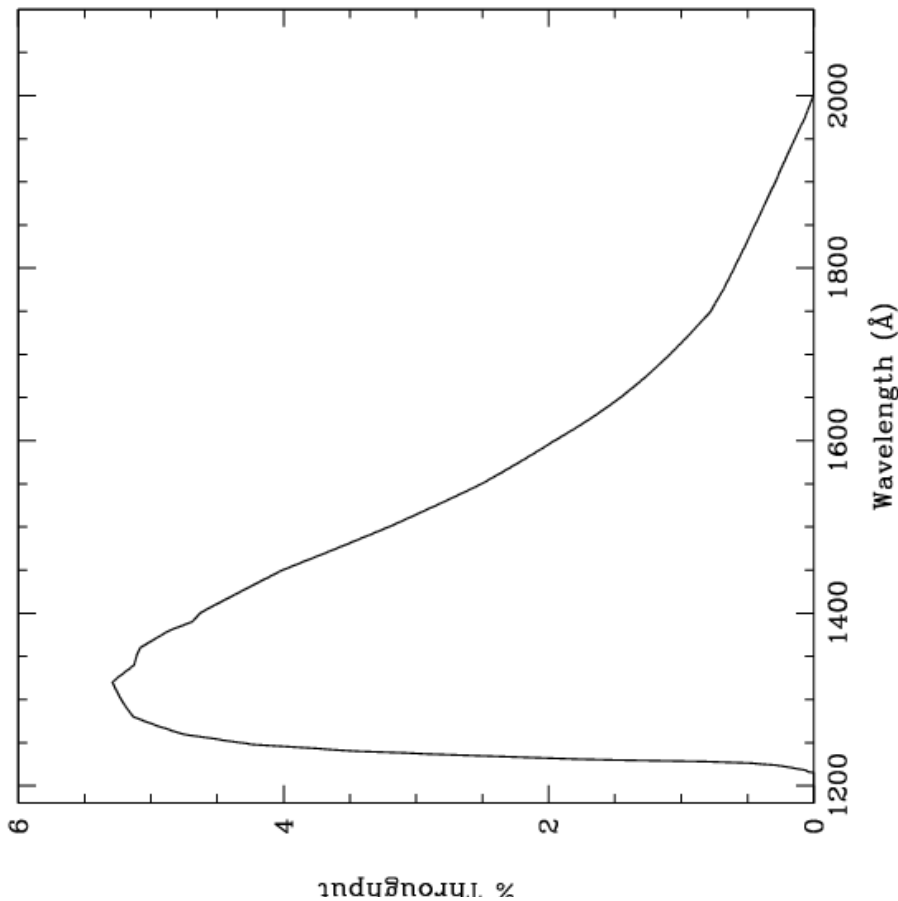


Figure 10.110: Point source S/N vs. $V+AB_V$ for the SBC/F125LP filter. Top curves are for low sky; bottom curves are for average sky.

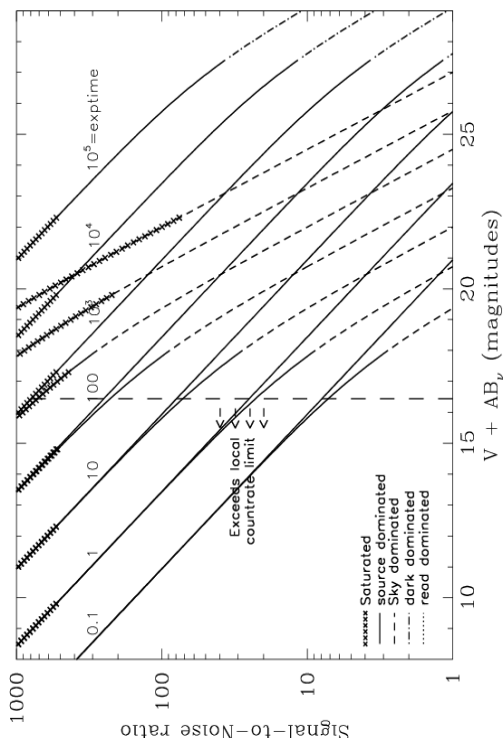
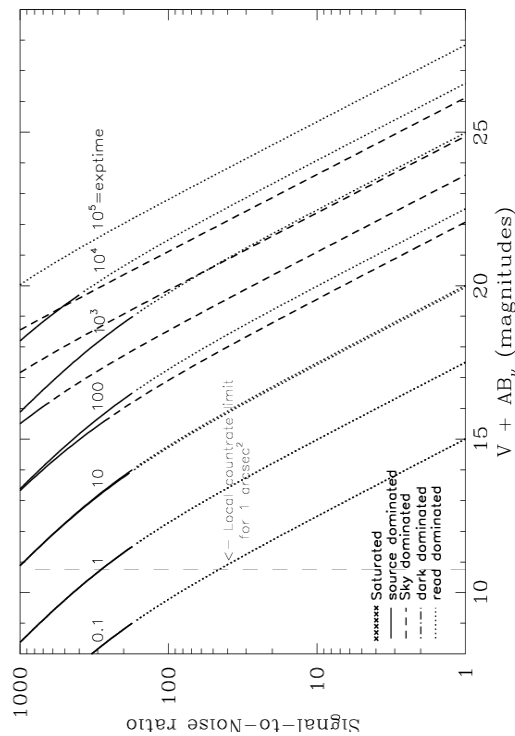


Figure 10.111: Extended source S/N vs. $V+AB_V$ for the SBC/F125LP filter. Top curves are for low sky and bottom curves are for average sky for a 1 arcsec² area.



SBC/F140LP

Description

BaF₂ filter.

Figure 10.112: Integrated system throughput for SBC/F140LP.

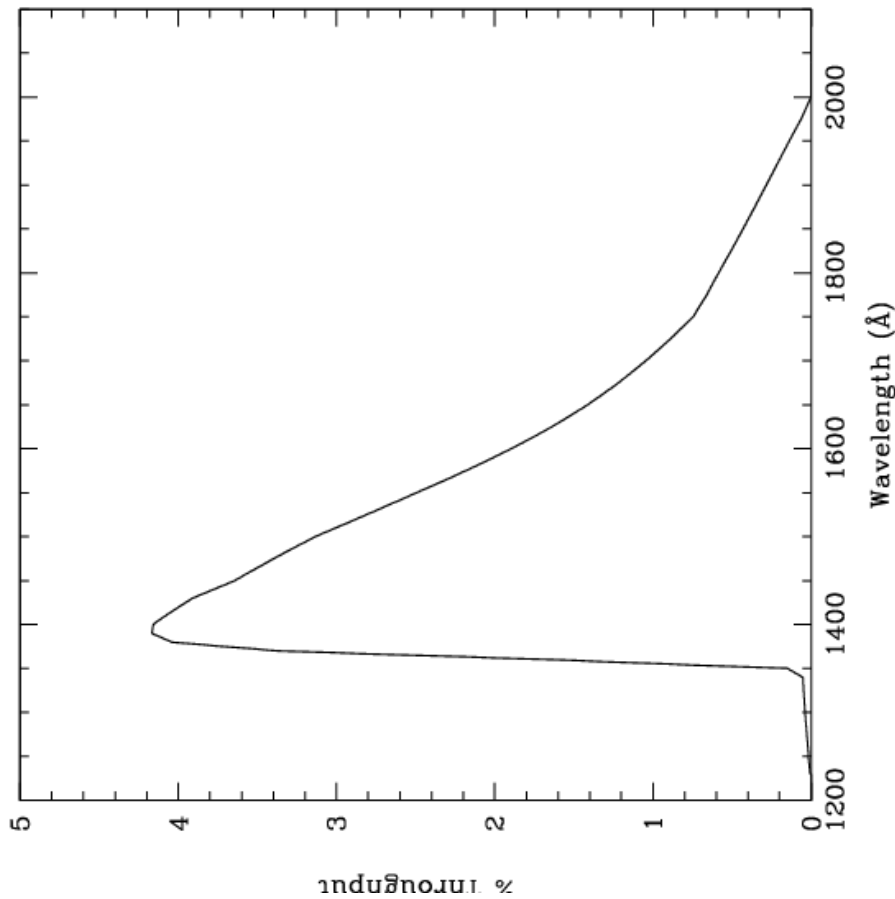


Figure 10.113: Point source S/N vs. $V+AB_V$ for the SBC/F140LP filter. Top curves are for low sky; bottom curves are for average sky.

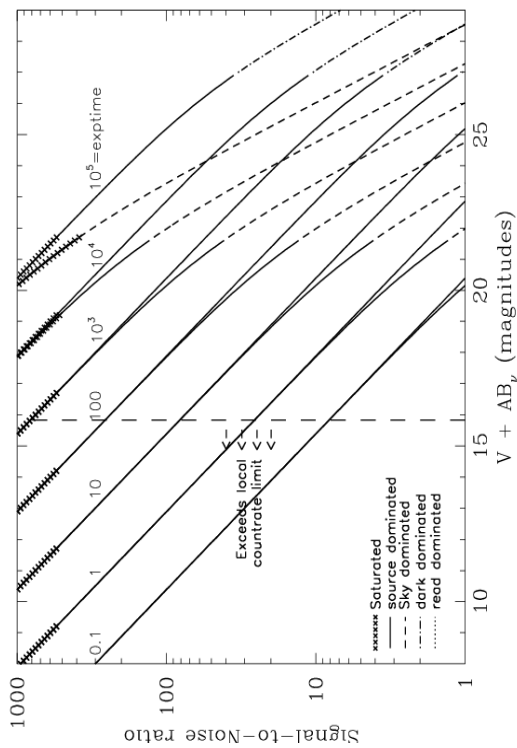
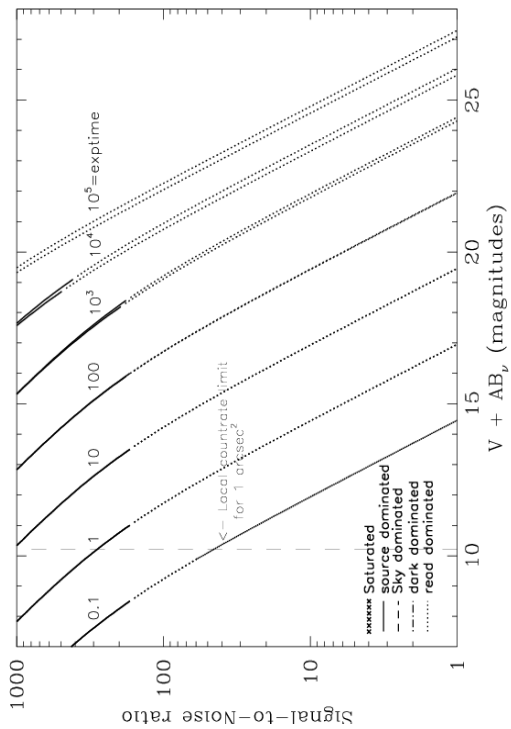


Figure 10.114: Extended source S/N vs. $V+AB_V$ for the SBC/F140LP filter. Top curves are for low sky and bottom curves are for average sky for a 1 arcsec² area.



SBC/F150LP

Description

Crystal Quartz filter.

Figure 10.115: Integrated system throughput for SBC/F165LP.

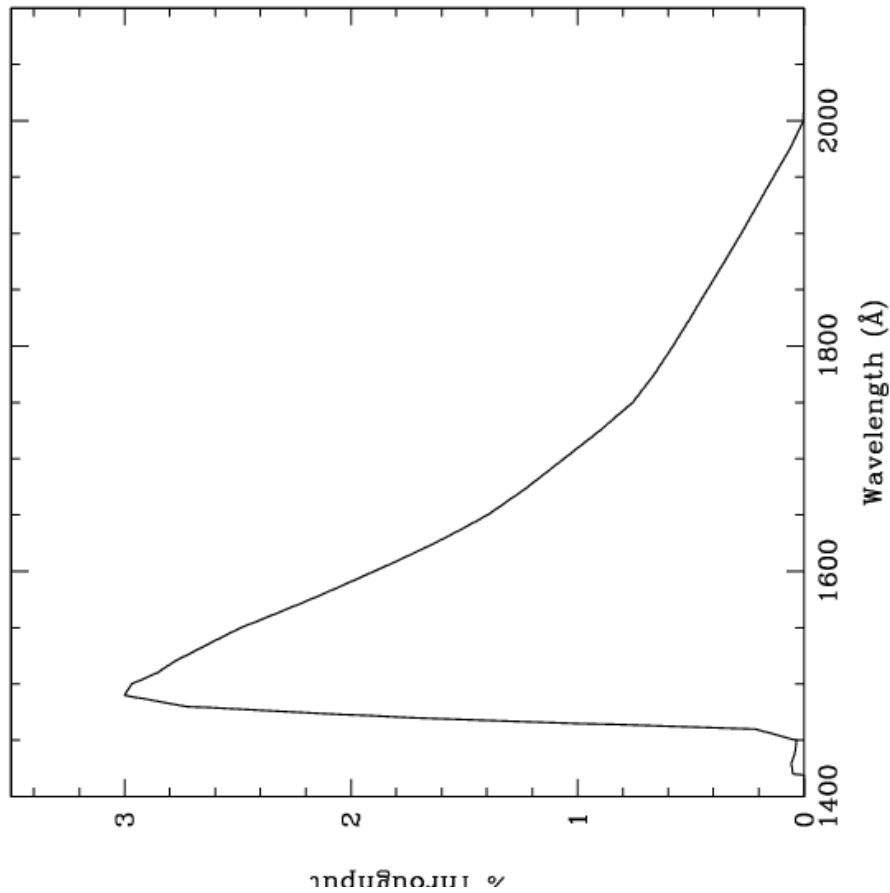


Figure 10.116: Point source S/N vs. $V+AB_V$ for the SBC/F150LP filter. Top curves are for low sky; bottom curves are for average sky.

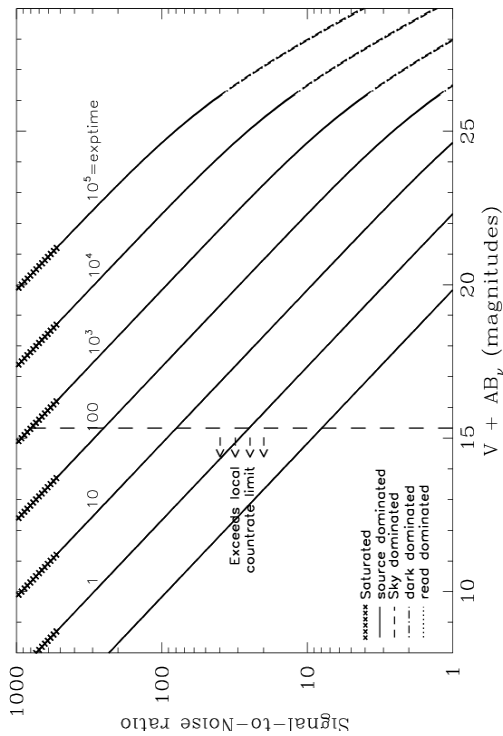
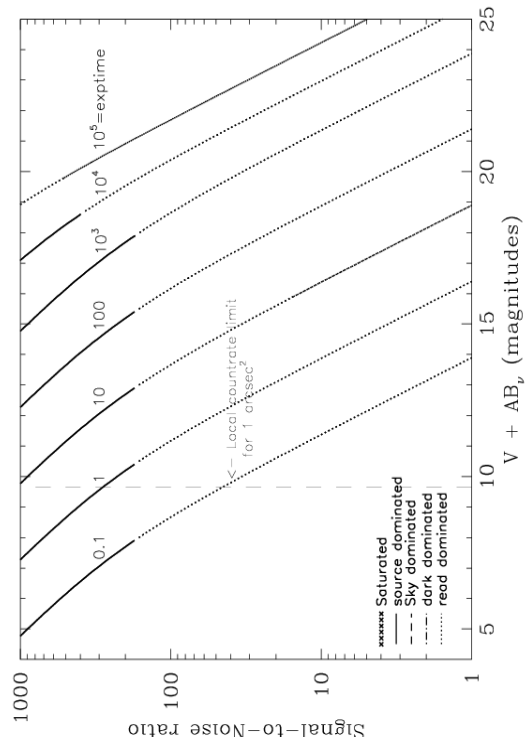


Figure 10.117: Extended source S/N vs. $V+AB_V$ for the SBC/F150LP filter. Top curves are for low sky and bottom curves are for average sky for a 1 arcsec^2 area.



SBC/F165LP

Description

Dynasil filter.

Figure 10.118: Integrated system throughput for SBC/F165LP.

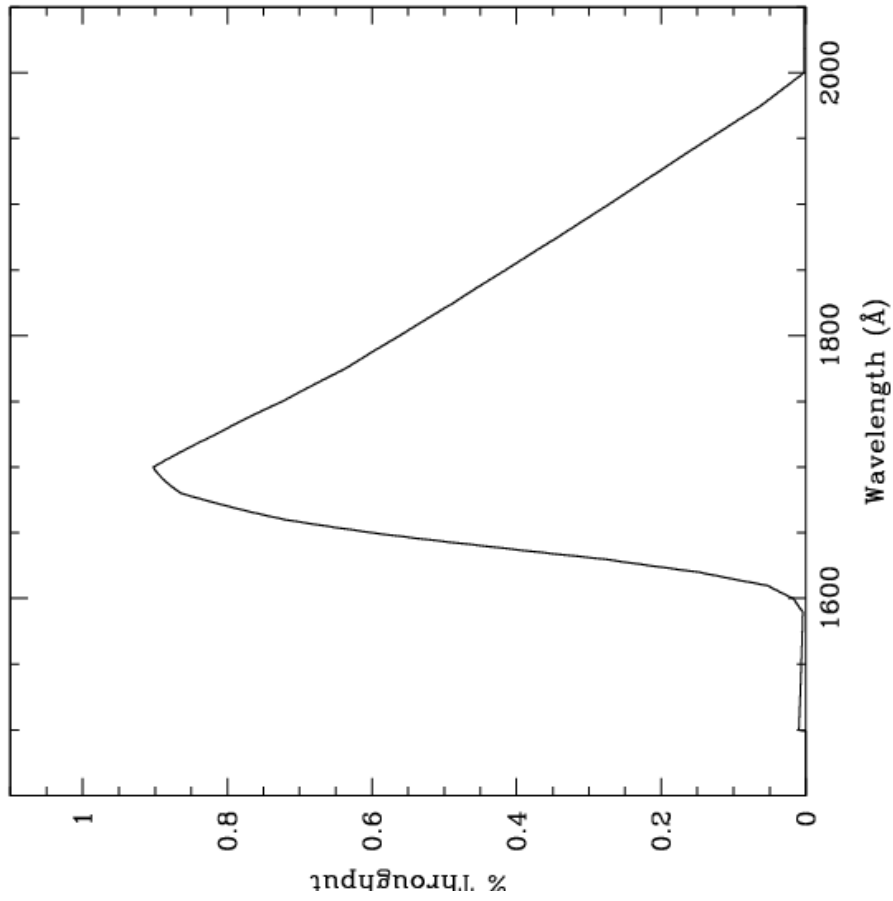


Figure 10.119: Point source S/N vs. $V+AB_V$ for the SBC/F165LP filter. Top curves are for low sky; bottom curves are for average sky.

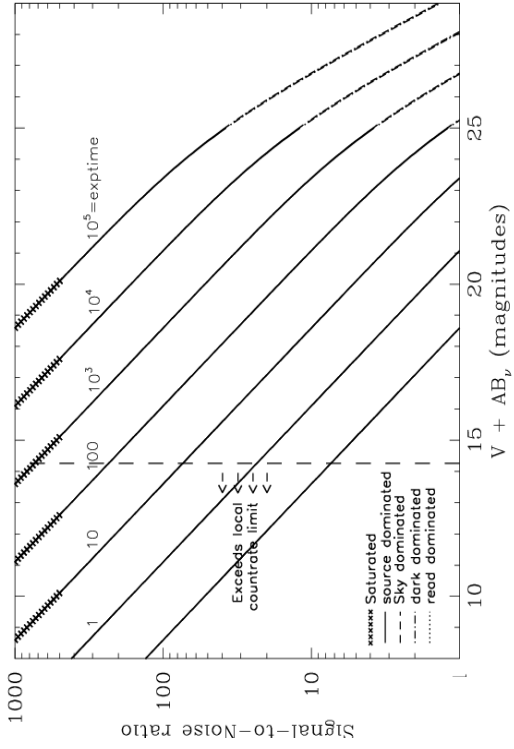
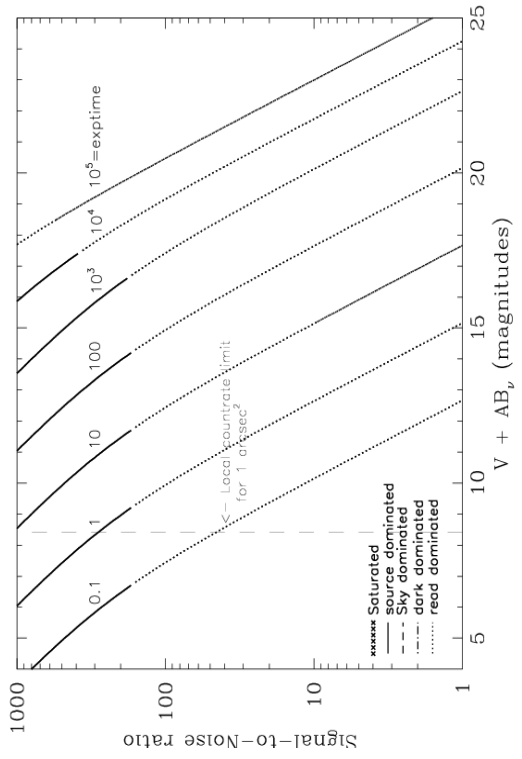


Figure 10.120: Extended source S/N vs. $V+AB_V$ for the SBC/F165LP filter. Top curves are for low sky and bottom curves are for average sky for a 1 arcsec^2 area.



SBC/PR110L

Description

LiF₂ Prism.

Figure 10.121: Integrated system throughput for SBC/PR110LP.

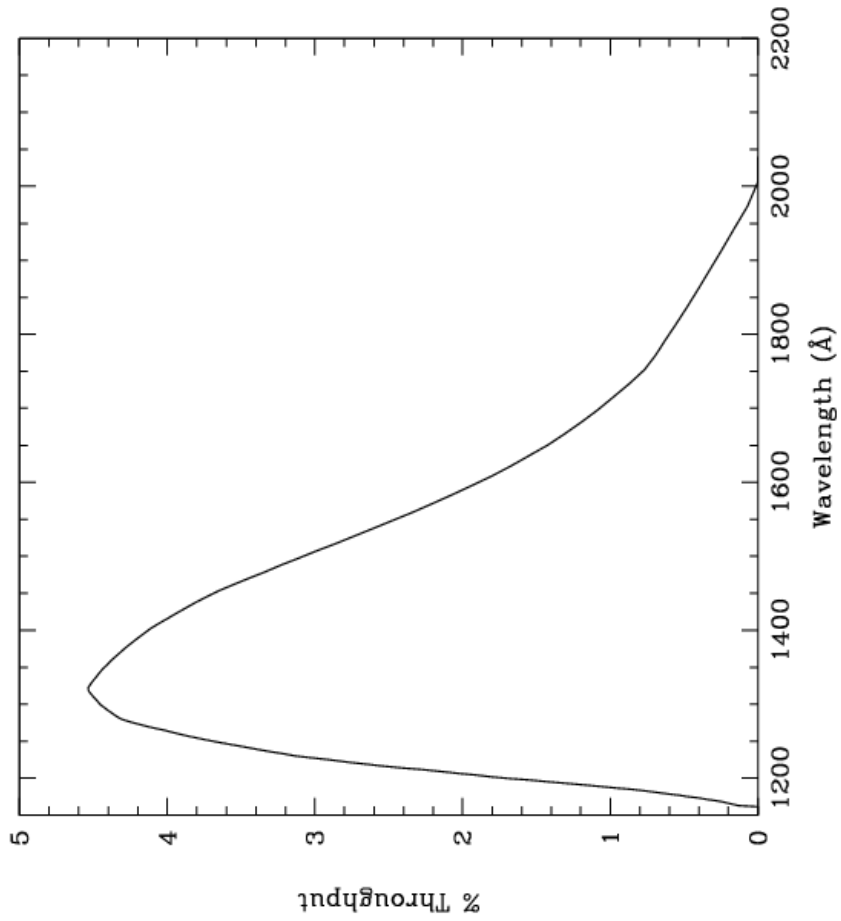


Figure 10.122: Point source S/N vs. $V+AB_V$ for the SBC/PR110LP filter. Top curves are for low sky; bottom curves are for average sky.

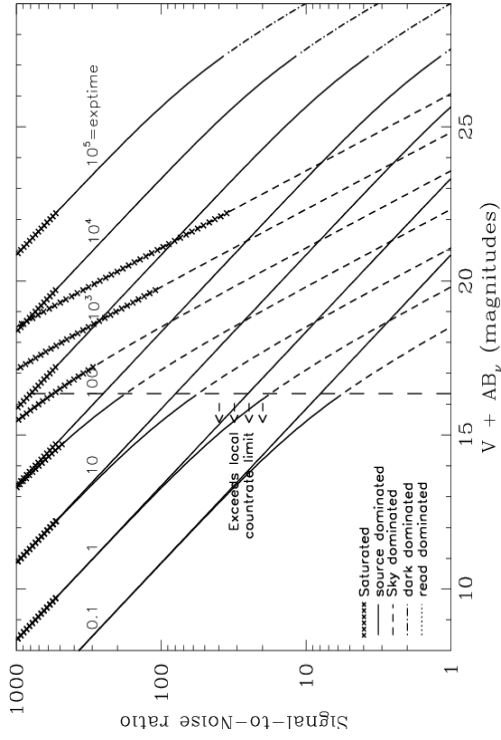
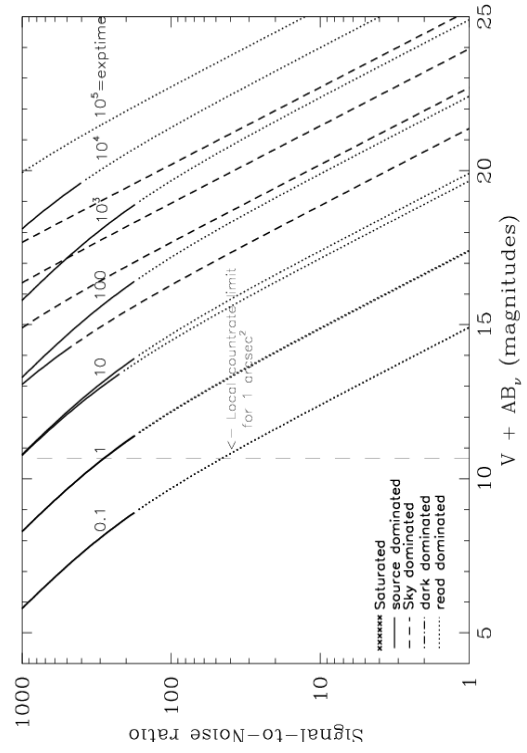


Figure 10.123: Extended source S/N vs. $V+AB_V$ for the SBC/PR110LP filter. Top curves are for low sky and bottom curves are for average sky for a 1 arcsec² area.



SBC/PR130L

Description

CaF₂ Prism.

Figure 10.124: Integrated system throughput for SBC/PR130LP.

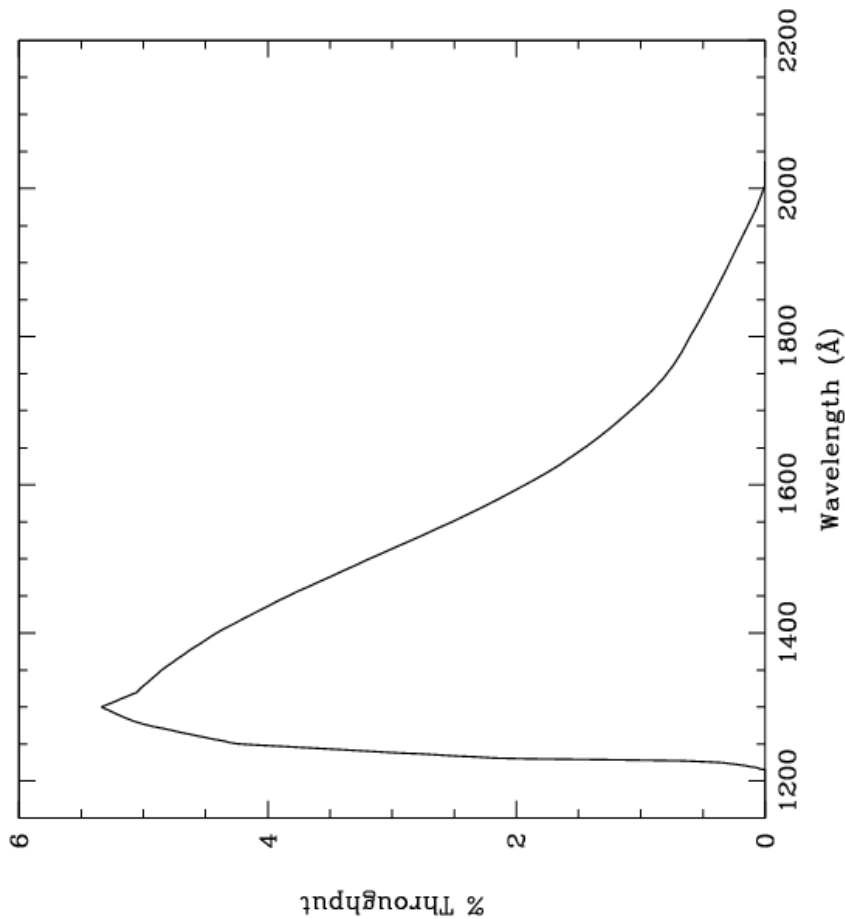


Figure 10.125: Point source S/N vs. $V+AB_V$ for the SBC/PR130LP filter. Top curves are for low sky; bottom curves are for average sky.

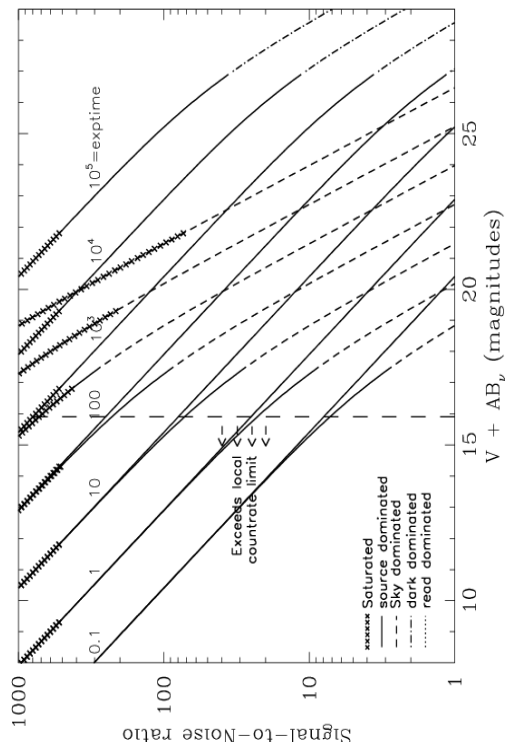


Figure 10.126: Extended source S/N vs. $V+AB_V$ for the SBC/PR130LP filter. Top curves are for low sky and bottom curves are for average sky for a 1 arcsec² area.

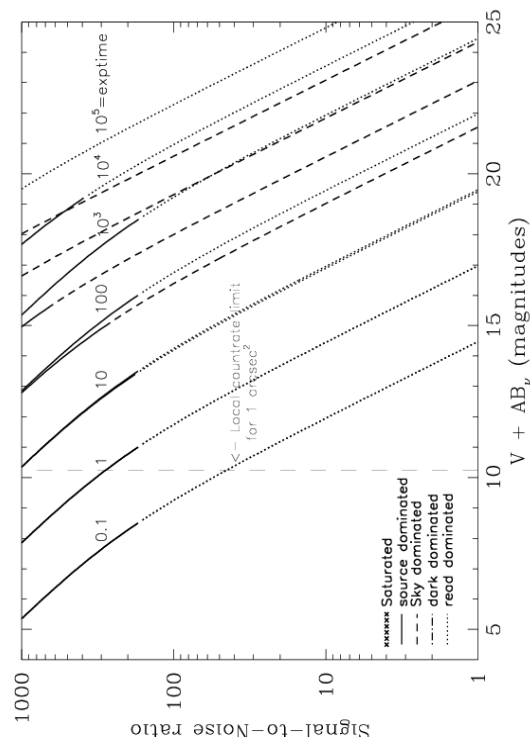


Table 10.1: Color corrections AB_V to go from Johnson V magnitude to AB magnitude for the WFC.

| Spectrum | F435W | F475W | F502N | F550M | F555W | F606W | F625W | F658N | F660N | F775W | F814W | F850LP | F892N | G800L | CLEAR |
|---|-------|-------|-------|-------|-------|-------|-------|-------|-------|-------|-------|--------|-------|-------|-------|
| AvgSky | 0.62 | 0.33 | 0.21 | -0.04 | 0.05 | -0.10 | -0.22 | -0.24 | -0.27 | -0.40 | -0.42 | -0.47 | -0.47 | -0.35 | -0.05 |
| LowSky | 0.52 | 0.26 | 0.14 | -0.03 | 0.03 | -0.07 | -0.15 | -0.18 | -0.20 | -0.26 | -0.27 | -0.30 | -0.31 | -0.23 | 0.00 |
| O5 V | -0.44 | -0.28 | -0.15 | 0.05 | -0.04 | 0.12 | 0.27 | 0.38 | 0.39 | 0.67 | 0.75 | 1.00 | 0.98 | 0.55 | 0.04 |
| B0 V | -0.43 | -0.28 | -0.17 | 0.06 | -0.04 | 0.12 | 0.29 | 0.40 | 0.39 | 0.64 | 0.71 | 0.94 | 0.92 | 0.54 | 0.04 |
| A0 V | -0.07 | -0.08 | -0.07 | 0.02 | 0.00 | 0.08 | 0.15 | 0.33 | 0.29 | 0.35 | 0.39 | 0.48 | 0.48 | 0.29 | 0.14 |
| A5 V | 0.04 | -0.01 | -0.03 | 0.00 | 0.00 | 0.06 | 0.10 | 0.22 | 0.16 | 0.23 | 0.25 | 0.31 | 0.30 | 0.19 | 0.13 |
| F2 V | 0.26 | 0.12 | 0.05 | -0.01 | 0.02 | 0.00 | -0.03 | 0.00 | -0.03 | -0.05 | -0.05 | -0.04 | -0.05 | -0.04 | 0.06 |
| G2 V | 0.54 | 0.28 | 0.14 | -0.03 | 0.04 | -0.07 | -0.16 | -0.16 | -0.17 | -0.30 | -0.31 | -0.34 | -0.34 | -0.26 | 0.00 |
| K0 V | 0.77 | 0.40 | 0.19 | -0.06 | 0.05 | -0.12 | -0.25 | -0.31 | -0.31 | -0.42 | -0.44 | -0.47 | -0.49 | -0.37 | -0.04 |
| M0 V | 1.41 | 0.80 | 0.67 | -0.14 | 0.11 | -0.33 | -0.59 | -0.84 | -0.84 | -1.21 | -1.31 | -1.55 | -1.52 | -1.09 | -0.53 |
| M6 V | 1.72 | 0.89 | 0.71 | -0.18 | 0.12 | -0.40 | -0.66 | -1.17 | -1.15 | -2.11 | -2.34 | -2.80 | -2.74 | -1.96 | -1.27 |
| O7 I | -0.40 | -0.25 | -0.13 | 0.04 | -0.03 | 0.11 | 0.25 | 0.35 | 0.35 | 0.63 | 0.70 | 0.94 | 0.92 | 0.52 | 0.05 |
| B0 I | -0.34 | -0.21 | -0.11 | 0.03 | -0.03 | 0.10 | 0.22 | 0.31 | 0.31 | 0.52 | 0.58 | 0.77 | 0.75 | 0.43 | 0.05 |
| F0 III | 0.19 | 0.07 | 0.00 | 0.00 | 0.01 | 0.01 | 0.01 | 0.06 | 0.03 | 0.06 | 0.06 | 0.07 | 0.05 | 0.04 | 0.10 |
| G0 III | 0.63 | 0.32 | 0.15 | -0.03 | 0.04 | -0.09 | -0.19 | -0.24 | -0.25 | -0.36 | -0.38 | -0.43 | -0.45 | -0.31 | -0.02 |
| K2 III | 1.13 | 0.57 | 0.33 | -0.07 | 0.07 | -0.19 | -0.37 | -0.48 | -0.48 | -0.68 | -0.72 | -0.83 | -0.89 | -0.60 | -0.17 |
| M0 III | 1.56 | 0.80 | 0.56 | -0.12 | 0.11 | -0.33 | -0.58 | -0.74 | -0.75 | -1.24 | -1.35 | -1.59 | -1.62 | -1.12 | -0.55 |
| M6 III | 1.65 | 0.92 | 1.19 | -0.12 | 0.18 | -0.64 | -0.95 | -1.20 | -1.15 | -2.91 | -3.24 | -3.89 | -3.74 | -2.83 | -2.10 |
| Elliptical | 0.95 | 0.51 | 0.34 | -0.07 | 0.07 | -0.19 | -0.36 | -0.48 | -0.48 | -0.81 | -0.92 | -1.07 | -1.18 | -0.72 | -0.27 |
| Sa | 0.80 | 0.45 | 0.30 | -0.06 | 0.07 | -0.18 | -0.36 | -0.54 | -0.51 | -0.75 | -0.84 | -0.94 | -1.05 | -0.66 | -0.24 |
| Sb | 0.81 | 0.44 | 0.27 | -0.06 | 0.06 | -0.18 | -0.34 | -0.50 | -0.48 | -0.75 | -0.85 | -0.97 | -1.09 | -0.66 | -0.24 |
| Sc | 0.08 | 0.00 | -0.71 | 0.07 | -0.03 | -0.17 | -0.26 | -1.76 | -0.84 | 0.40 | 0.77 | 1.67 | 1.26 | 0.20 | 0.08 |
| Starburst E(B-V) 0.51-0.60 | 0.41 | 0.24 | -0.02 | 0.00 | 0.04 | -0.22 | -0.39 | -1.38 | -0.87 | -0.59 | -0.67 | -0.75 | -0.80 | -0.56 | -0.23 |
| Starburst E(B-V)<0.1 | 0.23 | 0.05 | -0.96 | 0.09 | -0.03 | -0.10 | -0.14 | -1.16 | -0.35 | -0.15 | -0.19 | -0.18 | -0.23 | -0.16 | -0.03 |
| Sun | 0.58 | 0.30 | 0.17 | -0.03 | 0.04 | -0.07 | -0.17 | -0.17 | -0.20 | -0.26 | -0.27 | -0.27 | -0.28 | -0.23 | 0.01 |
| Vega | -0.12 | -0.11 | -0.07 | 0.02 | 0.00 | 0.08 | 0.16 | 0.35 | 0.32 | 0.39 | 0.43 | 0.56 | 0.49 | 0.32 | 0.14 |

Table 10.2: Color corrections AB_v to go from Johnson V magnitude to AB magnitude for the HRC.

| Spectrum | F220W | F250W | F330W | F344N | F435W | F475W | F502N | F550M | F555W | F606W | F625W | F658N | F660N | F775W | F814W | F850LP | F892N | G800L | PR200L | Clear |
|----------------------------------|-------|-------|-------|-------|-------|-------|-------|-------|-------|-------|-------|-------|-------|-------|-------|--------|-------|-------|--------|-------|
| AvgSky | 3.56 | 2.58 | 2.01 | 1.89 | 0.63 | 0.32 | 0.21 | -0.04 | 0.05 | -0.09 | -0.22 | -0.24 | -0.27 | -0.30 | -0.42 | -0.47 | -0.47 | -0.35 | 0.21 | 0.29 |
| LowSky | 5.31 | 3.37 | 1.84 | 1.72 | 0.65 | 0.33 | 0.22 | -0.04 | 0.05 | -0.11 | -0.24 | -0.27 | -0.30 | -0.45 | -0.48 | -0.55 | -0.30 | -0.39 | 0.18 | 0.26 |
| O5 V | -1.53 | -1.24 | -0.86 | -0.81 | -0.44 | -0.26 | -0.15 | 0.04 | -0.04 | 0.11 | 0.27 | 0.38 | 0.39 | 0.66 | 0.76 | 1.02 | 0.98 | 0.55 | -0.45 | -0.57 |
| B0 V | -1.16 | -0.98 | -0.72 | -0.69 | -0.44 | -0.27 | -0.17 | 0.06 | -0.04 | 0.11 | 0.28 | 0.40 | 0.39 | 0.63 | 0.72 | 0.96 | 0.92 | 0.54 | -0.31 | -0.41 |
| A0 V | 1.75 | 1.54 | 1.19 | 1.16 | -0.06 | -0.08 | -0.07 | 0.02 | 0.00 | 0.07 | 0.15 | 0.33 | 0.29 | 0.35 | 0.39 | 0.48 | 0.48 | 0.29 | 0.33 | 0.39 |
| A5 V | 2.60 | 2.15 | 1.41 | 1.35 | 0.05 | -0.01 | -0.03 | 0.00 | 0.00 | 0.05 | 0.10 | 0.22 | 0.16 | 0.23 | 0.25 | 0.31 | 0.29 | 0.19 | 0.36 | 0.43 |
| F2 V | 3.49 | 2.52 | 1.45 | 1.35 | 0.27 | 0.11 | 0.05 | -0.01 | 0.02 | 0.00 | -0.03 | 0.00 | -0.03 | -0.05 | -0.05 | -0.04 | -0.05 | -0.04 | 0.31 | 0.38 |
| G2 V | 5.66 | 3.29 | 1.63 | 1.63 | 0.55 | 0.26 | 0.14 | -0.03 | 0.04 | -0.06 | -0.15 | -0.16 | -0.17 | -0.30 | -0.31 | -0.34 | -0.34 | -0.26 | 0.25 | 0.33 |
| K0 V | 6.82 | 4.47 | 2.39 | 2.26 | 0.78 | 0.38 | 0.19 | -0.06 | 0.05 | -0.11 | -0.24 | -0.31 | -0.31 | -0.42 | -0.44 | -0.47 | -0.49 | -0.37 | 0.23 | 0.31 |
| M0 V | 7.73 | 5.93 | 3.90 | 3.76 | 1.40 | 0.76 | 0.67 | -0.14 | 0.12 | -0.31 | -0.58 | -0.84 | -0.84 | -1.20 | -1.32 | -1.57 | -1.52 | -1.09 | -0.24 | -0.15 |
| M6 V | 7.30 | 6.31 | 4.31 | 4.23 | 1.71 | 0.84 | 0.71 | -0.18 | 0.13 | -0.37 | -0.65 | -1.17 | -1.15 | -2.09 | -2.37 | -2.83 | -2.75 | -1.98 | -0.99 | -0.90 |
| O7 I | -0.33 | -0.55 | -0.60 | -0.56 | -0.40 | -0.24 | -0.13 | 0.04 | -0.03 | 0.10 | 0.25 | 0.35 | 0.35 | 0.62 | 0.71 | 0.96 | 0.92 | 0.51 | -0.11 | -0.14 |
| B0 I | -0.72 | -0.69 | -0.55 | -0.54 | -0.34 | -0.20 | -0.11 | 0.03 | -0.03 | 0.09 | 0.22 | 0.31 | 0.31 | 0.51 | 0.59 | 0.78 | 0.75 | 0.43 | -0.15 | -0.21 |
| F0 III | 3.69 | 2.75 | 1.58 | 1.47 | 0.20 | 0.06 | 0.00 | 0.00 | 0.01 | 0.01 | 0.01 | 0.06 | 0.03 | 0.06 | 0.06 | 0.07 | 0.05 | 0.04 | 0.34 | 0.42 |
| G0 III | 6.58 | 4.21 | 2.24 | 2.13 | 0.63 | 0.31 | 0.15 | -0.03 | 0.04 | -0.08 | -0.19 | -0.24 | -0.25 | -0.36 | -0.38 | -0.43 | -0.45 | -0.31 | 0.24 | 0.32 |
| K2 III | 8.43 | 6.56 | 3.78 | 3.56 | 1.13 | 0.54 | 0.33 | -0.07 | 0.07 | -0.17 | -0.36 | -0.48 | -0.48 | -0.67 | -0.73 | -0.84 | -0.89 | -0.60 | 0.11 | 0.19 |
| M0 III | 7.71 | 7.02 | 5.14 | 5.01 | 1.55 | 0.76 | 0.56 | -0.11 | 0.12 | -0.31 | -0.57 | -0.74 | -0.75 | -1.23 | -1.36 | -1.61 | -1.62 | -1.12 | -0.25 | -0.17 |
| M6 III | 6.27 | 6.17 | 4.45 | 4.28 | 1.67 | 0.89 | 1.19 | -0.12 | 0.18 | -0.60 | -0.93 | -1.20 | -1.15 | -2.88 | -3.29 | -3.93 | -3.74 | -2.87 | -1.83 | -1.75 |
| Elliptical | 5.20 | 4.63 | 2.82 | 2.63 | 0.95 | 0.48 | 0.34 | -0.07 | 0.07 | -0.17 | -0.36 | -0.48 | -0.48 | -0.80 | -0.93 | -1.08 | -1.18 | -0.72 | 0.01 | 0.09 |
| Sa | 4.35 | 3.53 | 2.38 | 2.34 | 0.80 | 0.43 | 0.30 | -0.06 | 0.07 | -0.17 | -0.35 | -0.54 | -0.51 | -0.75 | -0.85 | -0.94 | -1.05 | -0.66 | 0.03 | 0.11 |
| Sb | 3.73 | 3.10 | 2.11 | 2.16 | 0.81 | 0.42 | 0.27 | -0.06 | 0.07 | -0.17 | -0.34 | -0.50 | -0.48 | -0.74 | -0.86 | -0.98 | -1.09 | -0.66 | 0.02 | 0.10 |
| Sc | 2.09 | 1.15 | 0.15 | -0.07 | 0.07 | -0.01 | -0.70 | 0.07 | -0.03 | -0.17 | -0.25 | -1.76 | -0.85 | 0.34 | 0.77 | 12.85 | 9.95 | 0.19 | 0.22 | 0.285 |
| Starburst E(B-V) 0.51-0.60 | 1.82 | 1.63 | 1.13 | 1.14 | 0.41 | 0.23 | -0.02 | 0.00 | 0.04 | -0.21 | -0.38 | -1.38 | -0.87 | -0.59 | -0.68 | -0.76 | -0.80 | -0.57 | 0.00 | 0.05 |
| Starburst E(B-V)<0.1 | 0.98 | 0.95 | 0.81 | 0.80 | 0.22 | 0.04 | -0.96 | 0.09 | -0.03 | -0.10 | -0.14 | -1.16 | -0.35 | -0.15 | -0.20 | -0.18 | -0.23 | -0.16 | 0.11 | 0.16 |
| Sun | 5.67 | 3.55 | 1.83 | 1.72 | 0.58 | 0.28 | 0.17 | -0.03 | 0.04 | -0.06 | -0.16 | -0.17 | -0.20 | -0.26 | -0.27 | -0.27 | -0.28 | -0.23 | 0.27 | 0.36 |
| Vega | 1.65 | 1.48 | 1.18 | 1.14 | -0.10 | -0.10 | -0.07 | 0.02 | 0.00 | 0.08 | 0.16 | 0.35 | 0.32 | 0.38 | 0.44 | 0.56 | 0.49 | 0.32 | 0.33 | 0.39 |

Table 10.3: Color corrections AB_V to go from Johnson V magnitude to AB magnitude for the SBC.

| Spectrum | F115LP | F122M | F125LP | F140LP | F150LP | F165LP | PR110L | PR130L |
|---------------------------------------|---------------|--------------|---------------|---------------|---------------|---------------|---------------|---------------|
| AvgSky | 12.00 | 14.41 | 11.83 | 11.23 | 10.60 | 9.25 | 11.81 | 11.81 |
| LowSky | -1.78 | -2.95 | 2.73 | 6.80 | 10.34 | 9.00 | -1.27 | 2.69 |
| O5 V | -2.07 | -2.18 | -2.04 | -1.96 | -1.91 | -1.82 | -2.05 | -2.04 |
| B0 V | -1.64 | -1.53 | -1.69 | -1.67 | -1.63 | -1.54 | -1.66 | -1.69 |
| A0 V | 2.65 | 3.88 | 2.47 | 2.09 | 1.91 | 1.82 | 2.51 | 2.46 |
| A5 V | 5.41 | 7.44 | 5.24 | 4.65 | 4.05 | 3.14 | 5.23 | 5.22 |
| F2 V | 7.91 | 10.17 | 7.74 | 7.14 | 6.51 | 5.18 | 7.72 | 7.71 |
| G2 V | 13.82 | 16.35 | 13.65 | 13.05 | 12.42 | 11.07 | 13.63 | 13.63 |
| K0 V | 10.07 | 10.43 | 10.00 | 9.79 | 9.61 | 9.31 | 10.01 | 9.99 |
| M0 V | 11.58 | 11.94 | 11.50 | 11.29 | 11.11 | 10.81 | 11.51 | 11.49 |
| M6 V | 12.06 | 12.42 | 11.98 | 11.77 | 11.59 | 11.29 | 11.99 | 11.97 |
| O7 I | -0.57 | -0.42 | -0.61 | -0.68 | -0.70 | -0.71 | -0.59 | -0.61 |
| B0 I | -0.80 | -0.61 | -0.87 | -0.83 | -0.78 | -0.75 | -0.82 | -0.86 |
| F0 III | 7.81 | 10.09 | 7.63 | 7.04 | 6.41 | 5.07 | 7.62 | 7.61 |
| G0 III | 9.80 | 10.16 | 9.72 | 9.52 | 9.34 | 9.03 | 9.74 | 9.72 |
| K2 III | 13.32 | 13.68 | 13.24 | 13.04 | 12.86 | 12.55 | 13.26 | 13.24 |
| M0 III | 11.07 | 11.42 | 10.99 | 10.78 | 10.60 | 10.30 | 11.00 | 10.98 |
| M6 III | 10.37 | 10.73 | 10.29 | 10.09 | 9.91 | 9.61 | 10.31 | 10.29 |
| Elliptical | 6.24 | 6.71 | 6.11 | 6.08 | 5.98 | 5.90 | 6.18 | 6.10 |
| Sa | 5.66 | 6.23 | 5.52 | 5.42 | 5.27 | 5.06 | 5.59 | 5.52 |
| Sb | 4.63 | 5.18 | 4.49 | 4.38 | 4.27 | 4.24 | 4.56 | 4.49 |
| Sc | 2.87 | 3.52 | 2.71 | 2.60 | 2.45 | 2.32 | 2.78 | 2.71 |
| Starburst E(B-V) 0.51-0.60 | 2.68 | 3.31 | 2.52 | 2.44 | 2.35 | 2.13 | 2.60 | 2.52 |
| Starburst E(B-V)<0.1 | 1.33 | 1.88 | 1.18 | 1.13 | 1.09 | 1.06 | 1.25 | 1.18 |
| Sun | 12.00 | 11.78 | 12.29 | 11.79 | 11.21 | 10.02 | 12.02 | 12.28 |
| Vega | 2.74 | 3.95 | 2.56 | 2.20 | 2.04 | 1.91 | 2.61 | 2.56 |

10.3 Distortion in the ACS

The ACS detectors exhibit more distortion than previous HST instruments. The principal reason for this is that the optics have been designed with a minimum number of components, consistent with correcting for the spherical aberration induced by the OTA, without introducing coma. The result is a high throughput, but focal surfaces far from normal to the principal rays. The WFC detector is tilted at 22° , giving an elongation of 8% while the HRC and SBC have a 25° tilt leading to an elongation of 12%. In each case, the scales in arcseconds per pixel are smaller along the radial direction of the OTA field of view than along the tangential direction.

The orientations of the ACS detector edges are approximately in line with the V2 and V3 coordinate axes of the telescope. Consequently, the eigenaxes of the scale transformation are along the diagonals for WFC, and the apertures and pixels appear non-rectangular in the sky projection. For the HRC and SBC the situation is even more irregular because the aperture diagonals do not lie along a radius of the HST field of view. Figure 7.8 shows the ACS apertures in the telescope's V2V3 reference frame. For a telescope roll angle of zero this would correspond to an on-sky view with the V3 axis aligned with North and the V2 with East.

If these were the only distortions they would not really present much difficulty. Their impact on photometry and mosaicing, or dithering could be simply computed. A more problematic effect is the variation of scale across each detector. For the WFC this amounts to a change of 10% from corner to corner. For the HRC and SBC this variation is only about 1% as they cover much smaller fields of view. The area on the sky covered by a WFC pixel varies by about 18% from corner to corner, allowance for which must be made in photometry of extended objects. Dithering and mosaicing are complicated by the fact that an integral pixel shift near the center of the detector will translate into a non-integral displacement for pixels near the edges. Even this is not a fundamental difficulty, but will imply some computational complexity in registering images and will depend on an accurate measurement of distortions.

The results presented here are derived from on-sky measurements. For WFC and HRC multiple pointings of 47 Tucanae were taken through the F475W filter, resulting in several thousand star location measurements. These were analyzed to express the distortion as quartic polynomials. The residuals of the fit to these polynomials are of order 0.2 pixels, much larger than the errors. Correction images describing these residuals are now supplied and used in *calacs* to bring the final errors down to about 0.01 pixels. Additionally, an area of open cluster NGC188, for which astrometric data are available, was used to establish the exact location and orientation of the aperture in telescope coordinates. At the same time, the

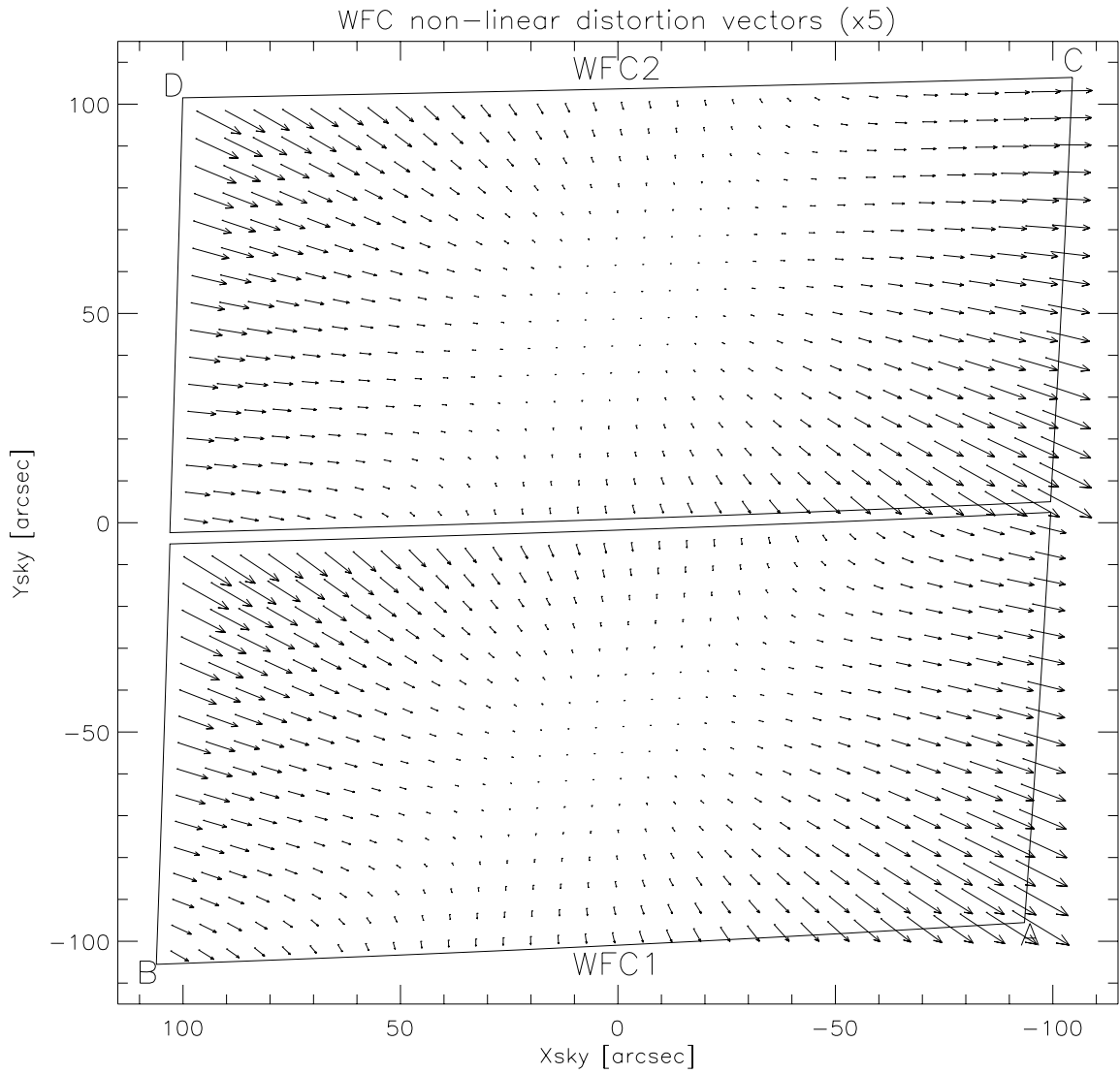
scale factors were confirmed. For the SBC, the distortion measurement used the target NGC6681 and filter F125LP. The alignment was established by observing this same target with the HRC and SBC consecutively to establish the relative locations. The SBC position was thereby derived from the HRC position.

10.3.1 WFC

The rhombus shape of the WFC is evident in Figure 7.8. The angle between the x and y axes is 84.9° for WFC1 and 86.1° for WFC2. The WFC distortion is illustrated in Figure 10.127, a vector displacement diagram which shows the contribution of the non-linear part of a quadratic fit to the data. The vectors represent the displacements and have been scaled up by a factor of 5 for display. The corner displacements are about 82 pixels. The principal effect is the diagonal variation of scale.

At the center of chip WFC1 the scale in the x direction is 0.0493 arcseconds/pixel, and 0.0486 arcseconds/pixel in the y direction. For WFC2 these figures are 0.0498 arcseconds/pixel, and 0.0503 arcseconds/pixel. Between the corner of WFC nearest to the V1 axis and the diagonally opposite corner, the overall scale increases by 10%. WFC1 forms a slightly distorted rectangle 201 by 100 arcseconds in size while WFC2 is 203 by 103 arcseconds. There is a 2.5 arcsecond gap between the two chips.

Figure 10.127: Non-linear component of the WFC Distortion.



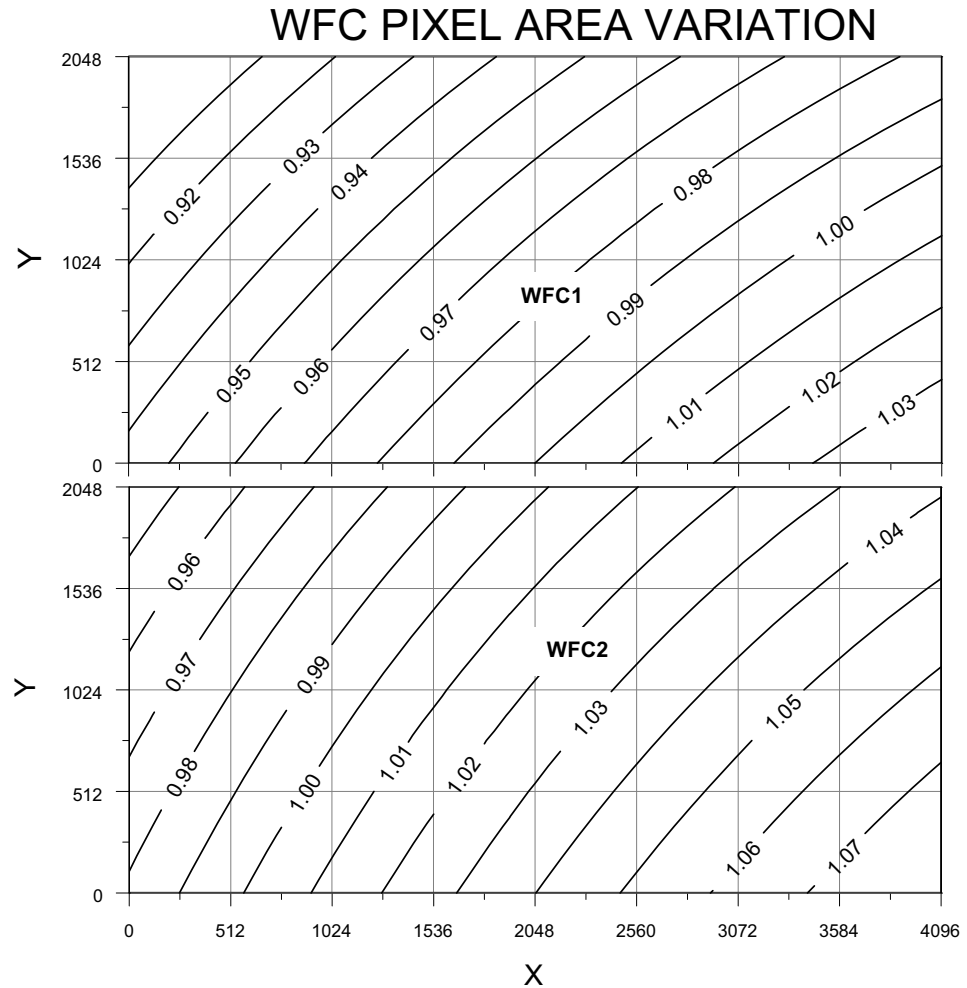
Note that this figure is rotated 180° with respect to the pipeline calibration products, where WFC2 is the lower half of the detector.

The resulting variation of the projected pixel area on the sky requires corrections to the photometry of point objects. A contour plot of relative pixel size across the WFC normalized to the central pixel, is shown in Figure 10.128. The range of area is from 0.89 to 1.08 times the central value.

10.3.2 HRC

The High Resolution Channel has its edges aligned approximately along the V2 and V3 axes. In this case, the center of the aperture lies on a line passing through the V2V3 origin and making an angle of 22° with the V3 axis. The diagonal of the aperture does not correspond to a radius of the HST field of view. So the distortion has no particular symmetry with respect to the detector axes. Again, because the focal plane, and therefore the detector plane is 25° away from the plane normal to the light path, the scales along the axes differ by 14%. However, since the HRC is less than 30 arcseconds across, the scale variation over the field is much less than for the WFC, being about 1%. At the center the x and y scales are 0.0284 and 0.0248 arcseconds/pixel respectively. The average scales across the middle of the detector are 0.02842 and 0.02485 arcseconds/pixel making the x and y widths 29.1 and 25.4 arcseconds. The slightly non-square projected aperture shape is evident in Figure 7.8. The angle between the x and y axes on the sky is 84.2° . A vector plot of the deviation from linearity is given in Figure 10.129 in which the deviations have been magnified by a factor of 10 for illustrative purposes. The largest deviation is 4.9 pixels in the top left corner and corresponds to about 0.1 arcseconds. The variation of pixel size across the HRC to be used for photometric correction of point sources is shown in Figure 10.130. The maximum deviation from the central value is just over 2%.

Figure 10.128: Variation of the WFC effective pixel area with position in detector coordinates.



10.3.3 SBC

The Solar Blind Channel contains the MAMA detector. It is centered close to the HRC position in the V2V3 plane and has a slightly larger field of view, about 35 by 31 arcseconds. The scales and distortions have now been measured directly. The maximum distortion displacement is about 2 pixels or 0.06 arcseconds. The HRC and SBC both have much smaller areas than the WFC. In the x direction the scale is 0.0338 arcseconds/pixel while in the y direction it is 0.0301 arcseconds/pixel. Like the HRC, the SBC exhibits a 13% difference between x and y scales with a variation across the aperture of a little over 2%.

Figure 10.129: HRC distortion.

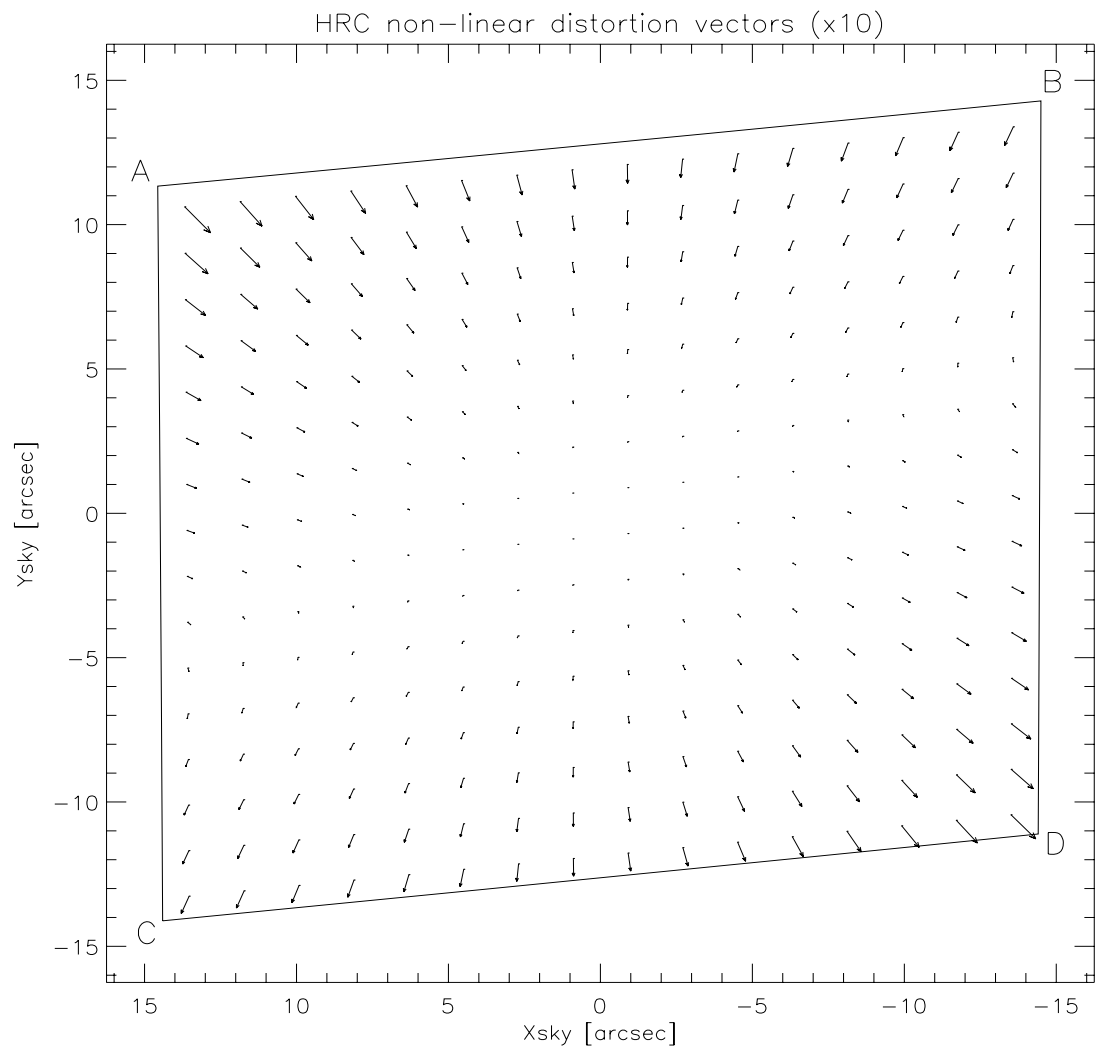
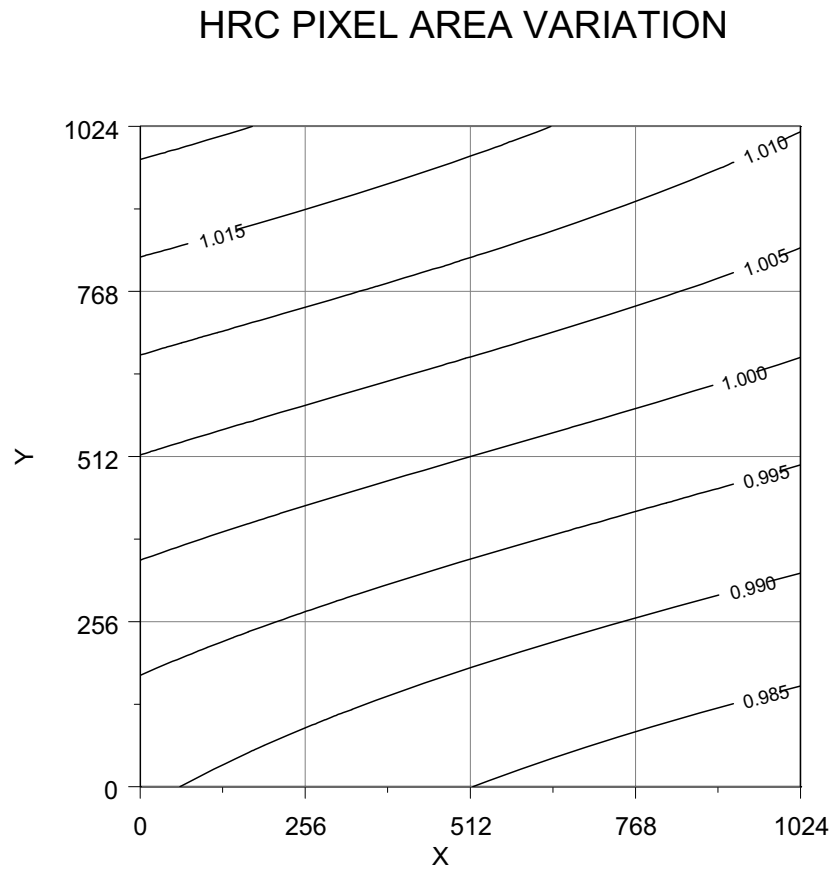


Figure 10.130: Variation of the HRC effective pixel area with position in detector coordinates.



10.3.4 Summary

All values presented here are based on in-flight measurements taken during SMOV. Formerly they were based on Ball Aerospace optical simulator measurements. The new values are quite close to the previously published numbers in that scale factors have changed by less than 1% and the aperture locations moved by only a few arcseconds.

Glossary

The following terms and acronyms are used in this Handbook.

ADC: Analog to digital

ABMAG: $-2.5 \log (F_{\nu}) - 48.60$ where F_{ν} is the flux from the source in $\text{erg cm}^{-2} \text{sec}^{-1} \text{Hz}^{-1}$

AB_ν: Correction to ABMAG to account for the fact that the source spectrum is not constant in F_{ν} ($\text{ABMAG} = V + \text{AB}_{\nu}$)

ACS: Advanced Camera for Surveys

APT: Astronomer's Proposal Tool

aXe: Spectroscopic Data Extraction Software

BOP: Bright Object Protection

calacs: ACS calibration pipeline software

CCD: Charge Coupled Device. Solid-state, light detecting device

CMD: Color Magnitude Diagram

CP: Call for Proposals

CR: Cosmic ray

CR-SPLIT: Division of a CCD exposure into shorter exposures to be used for cosmic ray rejection

CTE: Charge transfer efficiency

CVZ: Continuous viewing zone

DN: Data number

ETC: Exposure Time Calculator. ETCs are Web-based tools which can be accessed through the ACS Web pages.

ERO: Early release observations

FGS: Fine Guidance Sensors

FOS: Faint Object Spectrograph

FOV: Field of view

FTP: File Transfer Protocol. Basic tool used to retrieve files from a remote system. Ask your system manager for information about using FTP.

FUV: Far ultraviolet (~ 912 to 2000 \AA)

- FWHM***: Full width at half maximum
- GALEX***: Galaxy Evolution Explorer
- GHR***: Goddard High-Resolution Spectrograph
- GO***: General Observer
- GSC***: Guide Star Catalog
- GSCII***: Guide Star Catalog II
- GTO***: Guaranteed Time Observer
- Help Desk***: Facility for getting help on HST related topics via email.
help@stsci.edu.
- HRC***: High Resolution Channel
- HST***: Hubble Space Telescope
- IDT***: Investigation Definition Team
- IR***: Infrared
- IRAF***: Image Reduction and Analysis System. The environment in which STSDAS operates.
- ISR***: Instrument Science Report
- IUE***: International Ultraviolet Explorer Satellite
- K***: Degree Kelvin
- L-flats***: Low Frequency Variations Flats
- LMC***: Large Magellanic Cloud
- MAMA***: Multi-Anode Microchannel Array
- MCP***: Microchannel Plate
- MPP***: Multi Pinned Phased, a CCD mode that reduces dark current rate
- NICMOS***: Near-Infrared Camera and Multi-Object Spectrograph
- NUV***: Near ultraviolet (~2000 to 4000 Å)
- OTA***: Optical Telescope Assembly
- PASP***: Publications of the Astronomical Society of the Pacific
- PC***: Program Coordinator
- Phase I proposal***: A proposal for observing time on HST
- Phase II program***: An approved HST program; includes precise detail of how program is to be executed
- PI***: Principal investigator
- P-flats***: pixel-to-pixel high-frequency flats
- PRF***: Pixel Response Function
- PSF***: Point-spread function.
- PyRAF***: version of IRAF implemented in the Python language

QE: Quantum Efficiency

QEH: Quantum Efficiency Hysteresis

Quadrant: Section of detector that is read-out by an amplifier. For WFC, there are 4 amplifiers, two for each detector, so each amplifier reads one 2048 x 2048 pixel quadrant.

RA: Right Ascension

RAS: HST simulator used in ground tests to accurately simulate the full field OTA illumination, and is used to calibrate HST instruments. Also known as RAS/HOMS, the Refractive Aberrated Simulator/Hubble Opto-Mechanical Simulator.

reference file: data file containing ACS parameters or calibration information which is used by the calibration pipeline

rms: Root mean square

RQE: Responsive Quantum Efficiency

SAA: South Atlantic anomaly

SBC: Solar-Blind Channel

SDSS: Sloan Digital Sky Survey

SITe: Scientific Image Technologies; company that designed the ACS CCDs

SLIM: Slitless Spectroscopy Simulator

SMOV: Servicing Mission Observatory Verification

S/N: Signal-to-noise ratio

SNAPSHOT: Short exposures taken during unused blocks of telescope time.

ST-ECF: Space Telescope European Coordinating Facility

STAN: Space Telescope Analysis Newsletter

STIS: Space Telescope Imaging Spectrograph

STScI: Space Telescope Science Institute

STSDAS: Space Telescope Science Data Analysis System. The complete suite of IRAF data analysis and calibration routines used to process HST data.

synphot: STSDAS synthetic photometry (IRAF) software package

TAC: Telescope Allocation Committee

TECs: Thermal Electric Coolers

Tiny Tim: PSF simulation software developed by John Krist & Richard Hook

URL: Uniform resource locator. Address for WWW.

UV: Ultraviolet

VTT: a tool in APT that displays HST instrument apertures superimposed on FITS format sky images.

WFC: Wide-Field Channel

WFPC2: Wide Field Planetary Camera-2. Replacement for WF/PC installed during first servicing mission of December 1993.

WWW: World Wide Web. Hypertext-oriented method for finding and retrieving information over the Internet.

Index

A

AB(nu) 170, 189, 233
Aberrated Beam Coronagraph 82
Aberration Correction 11
ABMAG 167, 189
ACCUM mode
 HRC 129
 SBC 130
 WFC 126
ACQ mode
 effective neutral density filters 131
 HRC 130
Apertures
 available-but-unsupported 117, 136
 coronagraph/acqs 85, 143
 HRC 129, 142, 143
 polarizers 140
 ramps 137, 141
 SBC 144
 small filters 139, 140
 subarrays 128, 140
 WFC 127, 136, 140
A-to-D Converter
 HRC 27, 129
 WFC 27, 126
Auto-Parallels 150, 153

B

Bandpass 52, 191
Blooming 27
BOP
 screening 121
 solar system objects 124

Bright Object Protection 49
 global limit 48, 122
 limiting V magnitudes 120
 local limit 48, 122
 policy 126
 global limit table 122
 parallels 125
 Phase I 121
 Phase II 121
 safety 49
Buffer
 compression 127
 HRC 130
 internal memory 14
 overheads 127
 SBC 130
 SBC 16 bit 45
 WFC 127

C

CALACS 68
Calibration
 accuracies 15
 lamps 13
 non-science exposures/GO obtained 118
 polarizers 75
CCDs
 HRC. See HRC
 WFC. See WFC
Charge Transfer Efficiency 38
 background considerations 39
 parallel measurement/table 39
 predicted/expected losses 40, 120
 science applications 40

- serial measurement/table 39
- utilizing POS TARGETS 40
- Coordinated Parallels 149
- Coronagraphy
 - coronagraph design 82
 - exposure time calculation 97
 - Lyot stop 82
 - occulting finger 84
 - occulting masks 82
 - PSF 95
 - target acquisition 130
- Cosmic Rays
 - CR-splitting 35
 - HRC 37
 - WFC 37
- Count Rate Limits
 - SBC 43, 49
- CR-SPLIT 132, 150, 158
- CTE 38

D

- Dark Current
 - SBC 43
- Dark Frames
 - HRC/WFC 30
- Data Number (DN) 24, 126, 129
- Data Storage
 - buffer dumps 14, 127
 - buffer size 14
 - data transfer rate/overheads 14
 - data volume 118
- Detectors
 - HRC. See HRC
 - SBC. See SBC
 - WFC. see WFC
- Dithering
 - cosmic rays 35
 - goals 131
- Drizzle/Multidrizzle 133
- Dynamic Range 135

E

- Earthshine 177, 185
- Encircled Energy

- models 67
- Exposure Time Calculations 165
 - bright object limits 120
 - ETC 165
 - examples 181
 - sky backgrounds 185
 - useful quantities tables 167
- Exposures
 - minimum/maximum exposure time 10, 130
 - overheads 158
 - target-acquisition 118
- Extinction 180

F

- Field of View (FOV)
 - HRC 142
 - ramps 138
 - SBC 144
 - WFC 136
- Filter Wheel
 - SBC 13
 - WFC/HRC 13
- Filters 16, 166
 - HRC/F220W 204, 205
 - HRC/F250W 206
 - HRC/F330W 207
 - HRC/F344N 208
 - HRC/F435W 209
 - HRC/F475W 210
 - HRC/F502N 211
 - HRC/F550M 212
 - HRC/F555W 213
 - HRC/F606W 214
 - HRC/F625W 215
 - HRC/F658N 216
 - HRC/F660N 217
 - HRC/F775W 218
 - HRC/F814W 219
 - HRC/F850LP 220
 - HRC/F892N 221
 - HRC/G800L 222
 - HRC/PR200L 223
 - Johnson-Cousins 60
 - narrow-band 61
 - Ramp Filters

- HRC 62
- WFC 61
- SBC Summary Table 54
- SBC/F115LP 225
- SBC/F122M 226
- SBC/F125LP 227
- SBC/F140LP 228
- SBC/F150LP 229
- SBC/F165LP 230
- SBC/PR110LP 231
- SBC/PR130LP 232
- Sloan Digital Sky Survey 61
- WFC/F435W 191
- WFC/F475W 192
- WFC/F502N 193
- WFC/F550M 194
- WFC/F555W 195
- WFC/F606W 196
- WFC/F625W 197
- WFC/F658N 198
- WFC/F660N 199
- WFC/F775W 200
- WFC/F814W 201
- WFC/F850LP 202
- WFC/G800L 203
- WFC/HRC Summary Table 53
- Flat Field
 - HRC 25
 - WFC 25
- Fringing 23
- Full Well 27
- G**
- Gain
 - ACCUM default 57
 - ACQ default 57
 - available-but-unsupported 25
 - default 25
 - HRC 24, 129
 - selection 25
 - WFC 24
- Geocoronal emission 179
- Geometric Distortion
 - HRC 239
 - PSF 68
- temporal changes 132
- WFC 60
- H**
- Hot Pixels
 - anneal cycles 33
 - creation rate table 32
 - data quality array 35
 - dither pattern 35
 - permanent growth table 35
 - shot noise 35
 - spontaneous healing 35
 - warm pixels definition 32
- HRC
 - ACCUM 129
 - ACQ 130
 - apertures 129, 142
 - A-to-D converter 129
 - buffer 130
 - characteristics 62
 - coating 22
 - cosmic rays 37
 - dark count 15, 22
 - detector architecture 10
 - field of view 15, 22
 - flat field 25
 - fringing 23
 - full well 27
 - full width half maximum (FWHM) 62
 - gain 129, 135
 - multiple electron events 41, 63
 - operating temperature 22
 - performance characteristics table 22
 - physical overscan 24
 - pixel size 15, 22
 - plate scale 148
 - point spread function 67
 - QE hysteresis 23
 - quantum efficiency 22
 - ramp filters 129
 - read noise 15, 29
 - readout 24
 - red leaks 63
 - saturation 27
 - subarrays 130

virtual overscan 24

I

Imaging

BOP 120
 HRC detector 62
 limiting magnitude 58
 saturation 60
 SBC detector 64
 signal-to-noise 59
 throughput 58
 WFC detector 60

Imaging caveats 56

filters see filters 56

Integrated System Throughput 58

L

Lamps

deuterium 13
 tungsten 13

Light Paths 12

Limiting Magnitudes 58

Linearity

CCDs 135
 SBC 48

LOW-SKY 179, 182

Lyot Stop 82

M

MAMA. See SBC

Memory. See Buffer

Multidrizzle/Drizzle 133

O

Optical Path

HRC/SBC 12
 WFC 12

Optics

coronagraph 11
 corrective optics 11
 fold mirror 11
 HRC/SBC 11
 spherical aberration 11

WFC 11

Orbit-Time Determination 156

Orientation

computing 144
 ORIENTAT 146
 PA_APER 146

Overheads

buffer dumps 127, 158
 buffer size 158
 examples 160
 guide star ACQ/reACQ 156
 HRC/SBC toggle 159
 observatory level 156
 readout 157
 science exposure level 157
 spectroscopy 158
 subarrays 159
 table 157
 target acquisition 157
 WFC parallel buffer dumps 159

P

Parallel Observations

auto-parallels 150
 coordinated parallels 149
 pointing 149
 pure parallels 153
 SBC in parallel 125
 visual target tuner 149

Patterns 131

Phase I

bright object limits 121
 preparation 3, 113

Phase II

bright object limits 121

Photometry

encircled energy 67, 167
 zero point 167

Pivot Wavelength 167

Plate Scale 131, 148

Polarimetry

Calibration 75
 filters 78, 80
 FOV 78
 throughput 76

Post-flash 13, 120

PSF

- coronagraphy 95
- encircled energy 67
- geometric distortion 68
- HRC 67
- HRC halo 62
- models 66
- pixel response function 65
- residual aberrations 72
- undersampling 60, 62
- WFC 67

Pure Parallel Program 153

Q

Quantum Efficiency Hysteresis 23

R

Ramp Filters

- aperture location 129
- apertures 137

Readout Time 10, 157

Red Leaks

- HRC 63
- SBC 64

S

Saturation

- CCDs 27
- SBC 45

SBC

- ACCUM mode 41, 130
- apertures 144
- BOP 125
- buffer 130
- characteristics 43, 64
- flat field 47
- global count rate 48
- limiting count rates 50
- local count rate 48
- MAMA detector
- non-linearity 48
- optical path 12
- physical description 10
- plate scale 15

policy 11, 125

PSF 44

red leaks 64

repeller wire 42

signal to noise limitation 47

spectral response 43

Scheduling

SBC considerations 45

Sensitivity

HRC/G800L 104, 105

HRC/PR 200L 105

WFC/G800L 102, 103

Shutter 28

Signal-to-Noise 172

sky background 185

Solar System Objects 124

South Atlantic Anomaly 45

Spectral Response. See Imaging throughput 58

Spectroscopy

HRC 104

SBC 107

WFC 102

STIS 45

Subarrays

amplifier 128

coronagraph 130

data volume 128

HRC 130

overscan 128

Synphot 166

T

Target ACQ

accuracy 13

aperture 13

coronagraph 13

ramp filters 13

Tiny TIM 66

Transmission Curves

broad-band filters 54

medium-band filters 55

narrow-band filters 55

SBC filters 55

SDSS filters 54

W

WFC

- ACCUM 126
- apertures 127, 136
- characteristics 60
- cosmic rays 37
- dark count 15, 22
- detector architecture 10
- field of view 15, 22
- flat field 25
- fringing 23
- full well 27
- full width half maximum (FWHM) 60
- gain 126, 134
- non-repeatability 28
- operating temperature 22
- performance characteristics table 22
- pixel size 15, 22
- plate scale 148
- point spread function 67
- QE hysteresis 23
- quantum efficiency 22
- ramp filters 129
- read noise 15
- readout 24
- saturation 27
- virtual overscan 24

Z

Zodiacal Light 185